Autoignition in Turbulent Flows

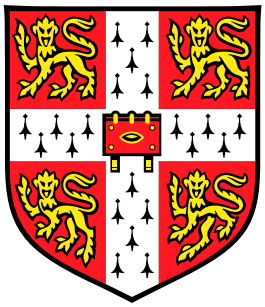

Department of Engineering
University of Cambridge

This dissertation is submitted for the degree of
Doctor of Philosophy

by:

Christos Nicolaos Markides

Clare College

Wednesday, 29$^{\underline{\text{th}}}$ of June, 2005

Dedicated to,

My brother,

Pearl Jam

"i will hold the candle till it burns off my arm"

and

ΠΥΞ ΛΑΞ

"ο'τι αξιζει ποναει κι ειναι δυσκολο"

Acknowledgements

On arriving at the Hopkinson Laboratory for the Ph.D. I was greeted by a bare, square cell with 4 m-high black, windowless steel walls. The transformation of this cell into a laboratory, including the supply of electricity, water, compressor air, exhaust gas extraction and the selection, purchasing and setting-up of measurement and data-logging equipment, along with all aspects of the autoignition experiment; from manufacture, development and testing, were entirely done by the author, with occasional assistance from the supporting technical staff: Messrs. Mick Underwood, Trevor Parsons, Robert Leroy, John Harvey and Roy Slater. Special thanks go out to Mr. Underwood, with the help of whom many an obstacle have been overcome and Mr. Peter Benie, the computer wizard. Dr. Epaminondas Mastorakos' ideas concerning the initial experimental concept are acknowledged with appreciation, as are his suggestions during its initial development and recommendations for the presentation of many of the results. The methods of measurement, processing (filtering and calculations) and analysis were also all completely developed by the author, with the exception of parts of the denoising algorithm for the PLIF images that were originally developed by Portilla et al. [2003].

I would like to thank Dr. Mastorakos for his guidance and for reading through the thesis and providing comments. Thanks also to Drs. Ivor Day, Alex Riley, Tim Nickels and Karthik Balachandran, and, Messrs. Ramanarayanan Balachandran and Haakon Pedersen-Mjaanes, for lending equipment and/or being around and helping with the gas chromatograph, hot wire, PLIF, PMT and microphone measurements; Mr. Giorgio De Paola for his generous time and interesting discussions, but also for providing the 0-D CMC calculations that are mentioned in the thesis, Mr. Tom Smith for his ideas during the re-design of the heaters, Mr. Stelios Karagiorgis for his assistance with the heater controller tuning and Mr. Ik Soo Kim for his company.

The years of research carried out for the Ph.D. have been marred by the friends that I have lost. Even though they are now away, I would like to mention and extend my warmest gratitude towards Drs. Fernando Siso-Nadal, George Biskos and Marina Neophytou. A heartfelt thank you goes out to all my friends in the department, the laboratory, in college, at home and to all those that I am forgetting to mention that have stayed by my side. Last, but certainly not least, I express my gratitude towards my parents, Dr. and Mrs. Markides, who never doubted and always supported me.

This work was made possible with the financial assistance of the Ministry for Finance of the Government of Cyprus, the Cambridge Commonwealth and Overseas Trusts (and specifically Dr. Anil Seal), the Leventis Foundation, Ford and EPSRC.

Hopkinson Laboratory, Cambridge
Wednesday, 29$^{\underline{\text{th}}}$ of June, 2005 *Christos Markides*

Publications

In chronological order, the work that is the subject of this thesis and results from the experiments have appeared, or are being currently prepared for publication, in:

1. The Conference on Modelling Fluid Flow, 12^{th} International Conference on Fluid Flow Technologies in Budapest, organized by EM2C-CNRS, 2003.
2. The European Combustion Meeting in Orléans, organized by the French Section of the Combustion Institute and CNRS-LCSR, 2003.
3. The 30^{th} International Symposium on Combustion, organized by the Combustion Institute and University of Chicago, [Markides and Mastorakos, 2005].
4. The European Combustion Meeting in Louvain-la-Neuve, organized by the Belgian Section of the Combustion Institute and Université Catholique de Louvain, 2005.
5. The 4^{th} Mediterranean Combustion Symposium in Lisbon, organized by the Institute Superior Technico, 2005. Also selected for publication in *Exp. Therm. Fluid Sci.*, 2006.
6. The Fluid Mixing $VIII$ Conference in London, organized by the Institution of Chemical Engineers and Kings College, 2006. Also selected for publication in *Chem. Eng. Sci.*, 2006.
7. The 51^{st} Turbo Expo Gas Turbine and AeroEngine Technical Congress & Exposition in Barcelona, organized by ASME, 2006. Also selected for publication in *J. Eng. Gas Turb. Power*, *Trans. ASME*, 2006.
8. Markides, C.N. and Mastorakos, E., Experiments of Autoignition in Turbulent, Confined Axisymmetric Co-flows, *Combust. Flame*, 2006.
9. Markides, C.N. and Mastorakos, E., Characteristics of Autoignition Sites in Turbulent Non-Premixed Flows, *Combust. Flame*, 2006.
10. Markides, C.N. and Mastorakos, E., On the Influence of Turbulent Mixing on the Location of Autoignition in Turbulent Flows, *Combust. Flame*, 2006.
11. The 5^{th} International Symposium on Turbulence, Heat and Mass Transfer in Dubrovnik, organized by ICHMT, 2006.
12. Markides, C.N. and Mastorakos, E., Scalar Mixing in Turbulent, Confined Axisymmetric Co-flows with Acetone PLIF, *J. Fluid Mech.*, 2006.

Details and copies of some of these papers and/or slides, where made possible by copyright laws, are available at *http://www2.eng.cam.ac.uk/∼cnm24/archive.htm*. Details of the project can also be found at various locations on the Engineering Department Energy Group pages at *http://www-g.eng.cam.ac.uk/energy/index.html*.

Hopkinson Laboratory, Cambridge
Wednesday, $29^{\underline{\text{th}}}$ of June, 2005 *Christos Markides*

Declaration

This dissertation is the result of my own work and includes nothing which is the outcome of work done in collaboration except where specifically indicated in the text. The dissertation contains approximately **65,000** words, **115** figures and **10** tables.

Hopkinson Laboratory, Cambridge
Wednesday, 29$^{\underline{\text{th}}}$ of June, 2005 *Christos Markides*

Abstract

Current development of combustors for Diesel and HCCI engines depends mainly on an improved understanding and ability to predict the controlling phenomenon of autoignition. In these applications autoignition occurs in the presence of inhomogeneities and strong turbulence, which cannot be neglected and whose effect must be understood. The study of autoignition is also critical in applications where unwanted manifestations of this phenomenon are to be avoided, such as in the premix ducts of LPP gas turbines, SI engines and flammable material storage areas. In parallel, there is great academic interest in fundamental questions surrounding turbulent reactive flows where the chemical and fluid-mechanical timescales are of the same order, whence the mixing has a direct effect on the chemistry. With few exceptions, experimental autoignition investigations have concentrated on homogeneous mixtures, driven by the desire to understand the complex chemical kinetics of this phenomenon. Yet, our present understanding leads one to reason that autoignition in the turbulent, inhomogeneous case cannot be understood at the fundamental level by extrapolation from homogeneous, or even laminar inhomogeneous studies.

In the experiments described in this thesis, gaseous fuels were injected, continuously and concentrically, into high-temperature, turbulent co-flows of air, confined inside a quartz tube. The flow and mixing fields in the tube were characterized with thermocouples, hot wires and acetone fluorescence. Original phenomena are reported concerning the emergence of autoignition 'spots', unsteady flame propagation and extinction or possible flashback. The observed phenomena are classified into operation regimes, the boundaries between which are explored paying attention to flashback conditions. The frequency of appearance of the autoignition 'spots' was also measured, together with the sound and spectral signature of chemiluminescence produced during autoigniting conditions. Optical measurements of autoignition were made from which the location of autoignition was measured and used to estimate mean 'delay times' from injection. As would be expected by considerations of simple chemical kinetics and the mean scalar field, higher air temperatures and lower jet velocities were found to move autoignition closer to the injector. A more involved conclusion is that as the air velocity and hence turbulent fluctuations were increased, the scalar dissipation rate increased and autoignition was both shifted downstream and delayed. As autoignition moved downstream, the autoignition frequency and sound intensity decreased. Situations are presented that cannot be explained in terms of homogeneous delay time arguments and where the importance of the mixture fraction and of the conditional scalar dissipation rate are highlighted.

Table of Contents

List of Figures

List of Tables

Chapter 1

Introduction

1.1 Introduction Chapter Objectives

The purpose of this chapter is two-fold: to explain the motivation for and aims of the work described in this thesis, and, to provide a brief outline of the structure of the thesis itself. In the first section, **Section 1.2**, a general overview of autoignition background theory is given; from early knowledge and observations of the phenomenon, to the most recent advances in the more complex, turbulent inhomogeneous case (the autoignition of two-phase flows is not treated) that is the subject of this study. Where necessary, attention will be drawn towards specific issues that are of direct relevance to this investigation, but overall, an attempt has been made to keep the overview as general as possible, within the limitations in space. A variety of previous autoignition studies are appraised, from the theoretical treatment of homogeneous, stagnant mixtures with simple chemistry, to Direct Numerical Simulations (DNS) and experiments of inhomogeneous counterflows and co-flows. **Section 1.3** consolidates the main points of **Section 1.2** and continues to state the purpose of this study. This leads to **Section 1.4**, which outlines the way in which this document has been organized, so as to best convey the stated objectives.

1.2 Autoignition Background

The earliest investigations of autoignition, during the late 19^{th} century, were aimed at determining the 'autoignition temperature' of a combustible mixture. From the mid-1950s and following the important result that there can be no single, absolute 'autoignition temperature', attention was directed towards the 'autoignition delay time' associated with a set of initial conditions for temperature (T), pressure (p) and composition (e.g. mass fractions Y). This has remained the 'traditional' form in which autoignition is studied, with the bulk of recent experiments and analyses continuing to be aimed towards understanding the chemical kinetics of oxidation of various fuel–oxidizer systems in *homogeneous* reactors. Much work is required before it can be claimed that a complete understanding of oxidation kinetics has been attained and the community still struggles to come to a consensus over several issues. Still, knowledge of these chemical processes has been greatly enhanced.

In the aftermath of the advent of the Homogeneous Charge Compression Ignition (HCCI) engine and Lean Premixed Pre-vaporized (LPP) gas turbine concepts and the increasingly strict emission regulations for diesel engines, the immediate practical needs concerning autoignition in the presence of strong turbulence and mixture inhomogeneities served as a renewed driving force for research in this field, with inhomogeneities making their first, reluctant appearance. Initially, the 'conventional' approach towards inhomogeneous autoignition resulted directly from the pre-existing work concerning autoignition delay times in the various homogeneous configurations, on account of the considered increased importance of the chemistry [Henein and Bolt, 1972, Pedersen and Qvale, 1974]. An argument was put forward that attempted to explain inhomogeneous autoignition once again in terms of a residence time and envisaged the possibility of separating the total autoignition delay time into a fluid-mechanical 'mixing time' (set by turbulent mixing) and a 'chemical delay time' (set by the chemistry as before), the latter of which was believed to

be the most important, or 'controlling', parameter [Wentzel, 1936]. According to this idea, the initially inert inhomogeneous mixture will need some 'mixing time' before becoming a reactive homogeneous mixture, after which it will need a further (homogeneous) 'chemical delay time' to autoignite. As a consequence of this simple decoupling much of the early literature is filled with studies that report only on an 'autoignition delay time' in:

1. A wide variety of unsteady/transient flow configurations such as shock tubes, jet stirred reactors, constant volume vessels or other diesel-like combustion chamber environments, rapid compression machines, etc., in which:
   (a) Mixture inhomogeneities were not present.
   (b) Mixture inhomogeneities and turbulence were present, but could not be properly characterized due to the chosen nature of the flow and/or were until recently considered unimportant.
2. Continuous flow reactors/configurations that (potentially) allowed measurements of turbulence quantities and characterization of the inhomogeneities, but in which:
   (a) The mixture inhomogeneities were purposefully minimized (for example by promoting intense turbulent mixing between the fuel and oxidizer early on and in the minimum time possible by specially designed injection schemes) in order to study other effects [Burwell and Olson, 1965, Cowell and Lefebre, 1987].
   (b) The mixture inhomogeneities were present, but whose effect was overlooked/not measured, or were present, were measured but whose effect was investigated only qualitatively [Ducourneau, 1974, Spadaccini, 1977, Spadaccini and TeVelde, 1982].

(c) The presence of inhomogeneities was linked with the two-phase physics of liquid fuel spray evaporation in complex mixing fields, such as the steady and unsteady/transient cross-streamwise (perpendicular) injection of a fuel spray into a heated air stream [Mizutani and Takada, 1999, Stringer et al., 1969].

Even in the work of the last two references, where the turbulent flow field was relevant and inspected (the authors measured the turbulence intensity) together with the measurements of autoignition, direct measurements of the mixing fields were not made and a consensus regarding the effects of turbulent mixing cannot be reached since the authors diametrically disagreed on the true effects of turbulence on their results. Stringer et al. [1969] concluded that the influence of turbulence was insignificant and Mizutani and Takada [1999] that autoignition delay times were increased by strong turbulence, at least for a certain temperature range.

Currently, the autoignition of a turbulent mixing flow is a problem of great fundamental importance and practical interest. The further development of combustors for HCCI engines and LPP gas turbines, in terms of improved performance and efficiency and reduced emissions, can be significantly aided by a better understanding and ability to predict the phenomenon of autoignition in the presence of considerable fluctuations of velocity, composition and temperature, whose effect must be understood. In parallel, turbulent autoigniting flows in which the chemical and fluid-mechanical timescales are of the same order (such as in the current experiments), are a theoretically challenging problem due to the non-linear coupling between complex chemistry and turbulent mixing that is interesting to explore. The phenomenon (and hence any successful theory) of inhomogeneous, turbulent autoignition involves the dynamic interplay between several underlying mechanisms, such as:

- the turbulent, fluid-mechanical mixing processes that bring the oxidizer and fuel together,

- the chemistry of the slow pre-ignition reactions between the reactants, and,
- the thermodynamical fate of the heat released from these reactions, leading to thermal runaway in localized sites called autoignition kernels.

With each one carrying equal importance, the convenient assumptions of scale-separation cannot be applied and so it can be said, that turbulent inhomogeneous autoignition truly stands on the boundaries where the disciplines of chemistry, fluid mechanics and thermodynamics meet. These phenomena can be complicated and immensely diverse, highlighting the many possibilities for non-linear interaction between the equally important aspects. Measurements of the phenomena that are the subject of this study can serve as excellent test-beds for testing both Computational Fluid Dynamics (CFD) and chemistry models, since they are by definition the outcome of *de rigeur* turbulence–chemistry interactions.

The major advances in this field have come from all aforementioned disciplines. They have been borne out of experimental, theoretical and computational approaches and by considering a wide variety of configurations: homogeneous and inhomogeneous, gaseous fuels and evaporating sprays, simple and complex chemistries, constant volume/pressure vessels and continuous flows; laminar and turbulent, two- and three-dimensional. In each of these configurations it has been possible to isolate and treat different aspects of the phenomenon, from the chemistry to the mixing patterns of passive scalars in turbulent flows, but also to progressively examine more complex cases of autoignition in a turbulent reacting flow. For a brief presentation of the latest theories and observations of autoignition, it is necessary to go back to the simple case of the constant volume or pressure vessel and this is done below.

1.2.1 Homogeneous Autoignition

The simplest relevant analysis is the treatment of the thermal explosion of a homogenous mixture in a closed vessel (bomb). In this, a uniform combustible mix-

ture undergoes either an isochoric or isobaric process of autoignition, assuming no heat losses and one-step Arrhenius chemistry described by an exponential reaction rate term proportional to $exp\Big\{-\frac{T_{act}}{T}\Big\}$. The numerator is a constant termed the 'activation temperature' and is related to the 'activation energy' of the reaction via $T_{act} \equiv \frac{E_{act}}{\overline{R}}$, with $\overline{R}$ the Universal Gas Constant. Given this theoretical, one-step exothermic chemistry model, with finite reaction rate, autoignition always occurs after an 'autoignition delay time' (τ_{IGN}), during which the rate of change of all scalars is exponential. This is important since it reveals that initially the evolution of the chemistry is very slow and the temperature (and reactant concentrations) can be idealized as being approximately constant, whereas at later times autoignition has a strongly self-accelerating character, termed 'thermal runaway'. Denoting by the subscripts '*fu*' the fuel and '*ox*' the oxidizer and by the superscript '0' initial conditions, the main results for the isobaric autoignition process are that τ_{ign}:

- Decreases very quickly with increasing initial temperature and is inversely proportional to the initial density, and thus, the initial pressure.
- Is minimized when $Y_{fu}^0 = Y_{ox}^0 = 0.5$ and increases for leaner or richer initial mixture compositions. Note that Arrhenius (unlike real) chemistry does not set lean/rich composition limits outside which reaction is not possible.

For complete combustion the temperature in the vessel always reaches the adiabatical flame temperature after autoignition.

The next step in complexity is to allow for a relaxation of the adiabatic constraint. The main result concerns the importance of the balance between:

- the heat release from the proceeding exothermic chemical reaction, and,
- the heat losses from the system through the walls of the container

and is a fundamental consideration for autoignition in general. Depending on the magnitude of the heat losses relative to the non-linear generation of heat due to the

chemical reaction, the following scenarios are possible:

- For low heat losses, the generation of heat is larger than heat loss from the vessel. Autoignition will always occur as in the case of no heat losses, yet the autoignition delay time increases relative to the adiabatic case and the eventual temperature is now lower than the adiabatic flame temperature.
- For excessive heat losses, a stable, slow reacting, or 'cool-flame', solution is found. The heat generation and loss terms balance and thermal runaway does not occur. The vessel keeps reacting, at very low rate, yet the heat of the reaction is lost as soon as it is generated. The temperature rise is small and the system no longer experiences an exponential explosion as before.

The analytical analyses mentioned so far have been concerned with stagnant, homogeneous mixtures and the simple, one-step chemistry of thermal explosions and as such, cannot give insight to the effects of turbulence, inhomogeneities or real chemistry on autoignition. In order to understand the individual processes that constitute a complex phenomenon such as this and their possible interactions, it is common practice to begin by observing and studying isolated aspects of the overall phenomena where possible. The insight gained in each of the more elementary treatments is always instructive and could lead in some ways to the understanding of the more sophisticated ones. Nevertheless, it is generally dangerous to extrapolate results and conclusions outside the bounds of the physical processes for which they were reached and it does not always follow that knowledge from the simplified cases can be applied blindly to the more complex ones.

Qualitatively different phenomena of homogeneous autoignition, that rely on deviations from the high activation energy (or temperature) single-step Arrhenius description of thermal explosions, have traditionally dominated autoignition studies [Benson, 1981, Griffiths and Scott, 1987, McKay, 1977]. For a recent review of work carried out post-1994 see also Simmie [2003]. In these studies emphasis rests on the

study of the slow chemical paths and shifting explosion limits of the so-called 'multiple ignitions' and 'cool flames'. These phenomena are observed at relatively lower temperatures and are associated with weaker luminescence, lower heat release and negative temperature coefficients. In the experimental work that is the subject of this thesis, real chemistry effects are of course present as a matter of fact. Attention is placed on the investigation of the effects of turbulent mixing on this chemistry.

The phenomenon of turbulent inhomogeneous autoignition is dominated by turbulent scalar mixing, set up by the non-uniformities and turbulent flow. In the governing equations for the turbulent fluctuations of species and temperature, the only source terms come from the chemistry, with turbulent transport terms playing a 'balancing' role. Seen otherwise, scalar fluctuations can be 'transported', but not created by turbulence. For the autoignition of a homogeneous mixture in the absence of temperature fluctuations, the fluctuations of the velocity field cannot give rise to scalar fluctuations. Hence, this case is of little fundamental importance. In the turbulent autoignition of homogeneous mixtures, even the inclusion of temperature fluctuations is of reduced fundamental importance. In the absence of turbulent mixing, which is by definition non-existent for a homogeneous mixture, an important part of the turbulent transport processes is not treated. A true understanding of turbulent autoignition in the presence of mixture inhomogeneities should come from dealing with the full, turbulent inhomogeneous situation. For this reason, the experiments presented in this thesis were designed to physically model the case in which fluctuations exist in the velocity and all scalars, with (length and time) scales chosen to be similar to those of the chemistry and thus of autoignition itself. Knowledge concerning the effects of scalar mixing on autoignition has come from the theoretical treatment of autoignition in laminar inhomogeneous flows and more recently from experiments, DNS and modelling of autoignition in turbulent inhomogeneous flows. The following two sections, **Sections 1.2.2** and **1.2.3**, are a brief introduction to inhomogeneous autoignition in laminar and turbulent flows respectively.

1.2.2 Laminar Inhomogeneous Autoignition

Laminar inhomogeneous autoignition includes the classical problems of the laminar (most commonly planar) co-flowing mixing layer and strained counterflow. Due to its simplicity, the former has been approached mostly from an analytical and theoretical point of view. On the other hand, the autoignition of non-uniform counterflow mixing layers has been explored analytically, experimentally and with simulations. In both cases the character of the solution depends on the pre-ignition chemistry, which can, in general, give rise to a thermal or chain-branched explosion. As mentioned in Varatharajan and Williams [2000], many investigators have tended to treat these two as completely different processes, based on the fundamental difference of the dynamic build-up before the explosion. Specifically, thermal explosions exhibit thermal runaway at a finite time (as in **Section 1.2.1**), whereas for chain-branched explosions radical concentrations evolve exponentially and mathematically approach infinity only at infinite times.

Laminar Co-flowing Mixing Layers:

The autoignition of two, initially separated, streams of fuel and oxidizer downstream of a splitter-plate in a planar (two-dimensional) flow geometry, with a one-step Arrhenius chemistry model and high energy asymptotics was first investigated by Liñán and Crespo [1976]. This work was extended by Sánchez [1997], to take into account the wake formed by the shedding of the boundary layers on the walls of the splitter-plate into the merging region of the main flow. In both cases the results revealed that initially the reactants mix in a nearly 'frozen' flow and reaction is slow, with low heat release and temperature rise. This is always overtaken by a sudden thermal-runaway behaviour that clearly identifies the location of autoignition.

The laminar, inhomogeneous mixing layer is mathematically a parabolic, or initial-value, problem and can be understood in the following way. The initial con-

ditions of the problem, together with the mixture fraction, or normalized conserved scalar (ξ) at a point in the flow, completely determine the state of mixing. For a constant temperature domain, as the mixing layer evolves from an initial state in which the fuel and oxidizer were separated, the probability density function (pdf) of mixture fraction spreads from initial delta functions to occupy a range of values in mixture fraction space. Seen differently, as the fuel and oxidizer mix, fluid particles with a range of different mixture compositions appear. Each fluid particle can be roughly thought of as a homogeneous reactor, reacting based on its composition, in a similar way to that described for a homogeneous mixture in a closed vessel (**Section 1.2.1**). Then, in terms of the mixture fraction field, the conditional reaction rates are a function of mixture fraction. Fluid particles with the 'right' composition will have the maximum reaction rate allowable by the temperature and will autoignite first, since they will be associated with the shortest τ_{IGN}. These are the 'most reactive' conditions and are associated with the most reactive mixture fraction, ξ_{MR}. For one-step chemistry and a constant temperature throughout the domain $\xi_{MR} = 0.5$, while ξ_{MR} will shift to leaner values as T_{ox} increases relative to T_{fu}.

A very important graph for inhomogeneous autoignition that was arrived at by the treatment of the laminar mixing layer is the curve of temperature, or heat release, versus Damköhler number. The non-dimensional Damköhler number, $\mathcal{D}a = \frac{\tau_{res}}{\tau_{chem}}$, is the ratio of a representative physical timescale, such as a residence time (τ_{res}), to a representative chemical timescale (τ_{chem}). **Figure 1.1**, with the sharp rise indicating thermal runaway at τ_{ign} (and corresponding $\mathcal{D}a_{ign}$) is characteristic of autoignition. The lower left portion of the curve corresponds to the slowly reacting state prior to autoignition, when τ_{res} are much shorter than the large timescales of slow chemistry. As the chemistry becomes faster or τ_{res} increases, so does $\mathcal{D}a$ until the autoignition point is reached. For $\mathcal{D}a$ values greater than this, explosive ignition leads to fully-fledged combustion with its associated high temperatures, e.g. the adiabatic flame temperature for complete combustion.

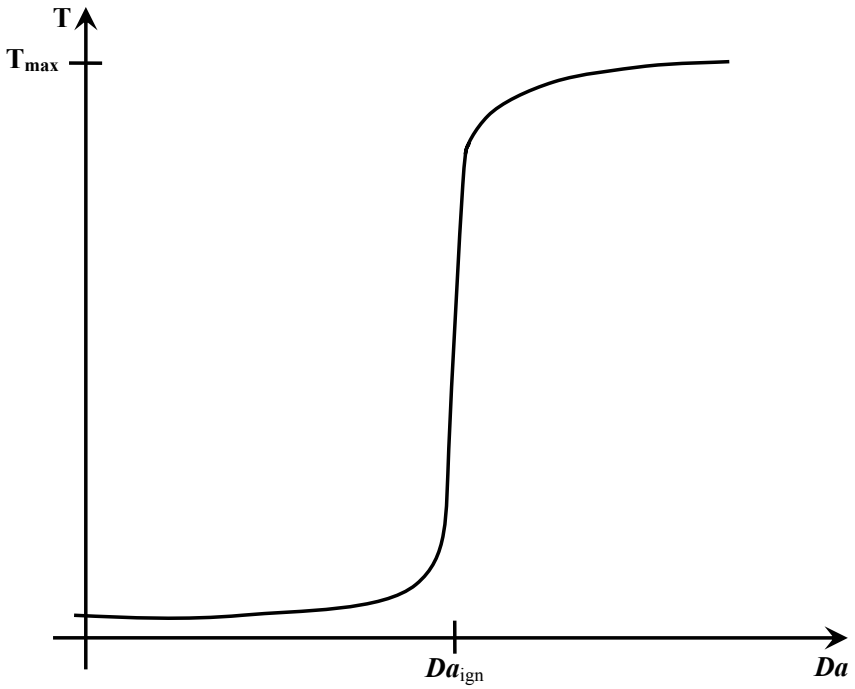

Figure 1.1: Maximum Flame Temperature versus Damköhler Number for Parabolic Autoignition

Indirectly, **Figure 1.1** also demonstrates that as long as there is no restriction to τ_{res}, no excessive heat losses from the system and the chemistry allows the reaction to proceed, there is no theoretical reason for autoignition not to occur, because, as with the homogeneous bomb, the reaction rate is always finite and any heat released from the reaction will inevitably lead to an increase in temperature and an acceleration in the reaction rate.

In addition, **Figure 1.1** has important implications for the turbulent case. The chemical reactions that take place at high temperatures, e.g. in flames, are nearly always fast compared to all turbulent timescales, whereas at the low temperatures of low $\mathcal{D}a$, the chemistry is usually slow relative to the turbulence. Hence, in both cases the length and timescales of the chemistry and turbulence may be separated. However, just prior to autoignition, the chemical timescales are of the same order as those of the turbulence and any assumptions of scale-separation are no longer valid.

In recent years chain-branching autoignition in the co-flow mixing layer has also been approached analytically [Ju and Niioka, 1994, Sánchez et al., 1997, 1999, Treviño and Liñán, 1995]. Hydrogen chemistry has been very much at the centre of attention, due to its fundamental role in hydrocarbon combustion, relative simplicity and interesting behaviour near the crossover temperature (T_c) [Trevino, 1991], at which the rate of the main three-body, exothermic chain-terminating reaction $H + O_2 + M \rightleftharpoons HO_2 + M$ is balanced by the rate-controlling chain-branching reaction $H + O_2 \rightleftharpoons OH + O$. At temperatures higher than T_c the recombination reactions responsible for the heat release are overtaken by the branching reactions due to the lower T_{act} and pre-exponential (frequency) factor of the former. Hence, initially, the mixing layer achieves a thermally-frozen state. A short chain-initiating region is followed by a long autocatalytic region of weakly exothermic chain-branching in which the radical-pool builds up exponentially before the point of autoignition. It has also been determined that initial radical build-up cannot be guaranteed unless chain-initiating steps such as $H_2 + O_2 \rightleftharpoons 2OH$ are taken into account, even though these reactions are slow. The effect of the wake from the boundary layers of the separating plate has been treated, with similar conclusions [Sánchez et al., 1998].

Laminar Counterflows:

Steady and un-steady counterflows of cold fuel and hot oxidizer have been extensively studied both analytically and numerically. Analytic, asymptotic approaches include those of Liñán [1974] for large activation energy thermal autoignition, and, Helenbrook et al. [1998] and Mellado et al. [2000] for chain-branching autoignition. Generally, the literature, as with the co-flow mixing layer, focuses on hydrogen chemistry. Yet, unlike for the co-flows, numerous experimental investigations have been performed, for a variety of hydrocarbon fuels and hydrogen and over a wide range of conditions. Another situation that has been considered is that of a premixed fuel–oxidizer stream being ignited by an inert, opposed hot nitrogen flow.

The counterflow, or strained mixing layer, is a boundary-value problem and as such can be described by an elliptic set of partial differential equations. Conveniently, for the velocity field diffusion can be neglected. A potential (inviscid) flow stream-function transformation can be used, based on an aerodynamic strain rate (γ), such that $\psi \equiv \gamma xy$; effectively $u_x = \gamma x$ and $u_y = -\gamma y$. For the species in steady counterflow mixing layers diffusion is balanced by species advection that brings the reactants together in the mixing zone. Mathematically for species σ:

$$u_x \frac{\partial Y_\sigma}{\partial x} + u_y \frac{\partial Y_\sigma}{\partial y} - \mathcal{D}_\sigma \Big(\frac{\partial^2 Y_\sigma}{\partial x^2} + \frac{\partial^2 Y_\sigma}{\partial y^2} \Big) \quad = \quad \frac{\dot{\omega}}{\varrho} \tag{1.1}$$

with $\mathcal{D}_\sigma$ its diffusion coefficient. It becomes straightforward to define two characteristic timescales; one for the fluid-mechanics (left-hand-side) and sometimes called the 'diffusive time', and, one for the chemistry (right-hand-side). A Damköhler number can be defined as before, based on the ratio of these scales and it can be seen, directly from the definition of γ, that $\mathcal{D}a$ is proportional to γ^{-1}. Going a step further, an equivalent $\mathcal{D}a$ can also be defined from the inverse of the scalar dissipation rate (χ) since in this flow, γ is proportional to χ (but depends also on the position across the flamelet) according to $\chi = \frac{\gamma}{\pi} exp\{z^{-2}\}$, with z a non-dimensional length [Liñán, 1974]. Seen otherwise, γ acts as a 'scaling parameter' for the conditional χ, $\chi|\xi = \frac{\gamma}{\pi} exp\{-2[erfc^{-1}(2\xi)]^2\}$, where $erfc^{-1}$ is the inverse of $erfc$ [Peters, 2000].

Liñán [1974] obtained solutions of the form of an S-shaped curve, as illustrated in **Figure 1.2** and studied the ignition regime at lower $\mathcal{D}a$ (higher γ and χ). He found that critical straining conditions exist, beyond which a low temperature, frozen solution is not possible and a diffusion flame temperature exists instead. This means that autoignition (i.e. transition to flame in this context) can occur only if $\mathcal{D}a$ is above a certain value, whereby the mixing rate is below a critical value. The autoignition delay time, τ_{ign}, was found to increase with increasing mixing rate [Liñán and Williams, 1993]. Theory, numerical simulations and experiments have

indicated, that indeed, autoignition is not possible for $\chi > \chi_{crit}$. This result has important implications for the effects of turbulence. If extrapolation were possible, it would have meant that autoignition would be expected to occur later if the mixing rate was increased and possibly not at all. This would seem contrary to empirical knowledge of autoignition, for example in engines, where it is empirically known that 'faster mixing' in fact results in earlier autoignition. Actually, the discrepancy is not as clear as it seems and partly arises due to the fact that empirical knowledge of autoignition based on 'mixing' and 'chemical' times can be misleading. This will be discussed in the light of the results of in **Chapter 8**.

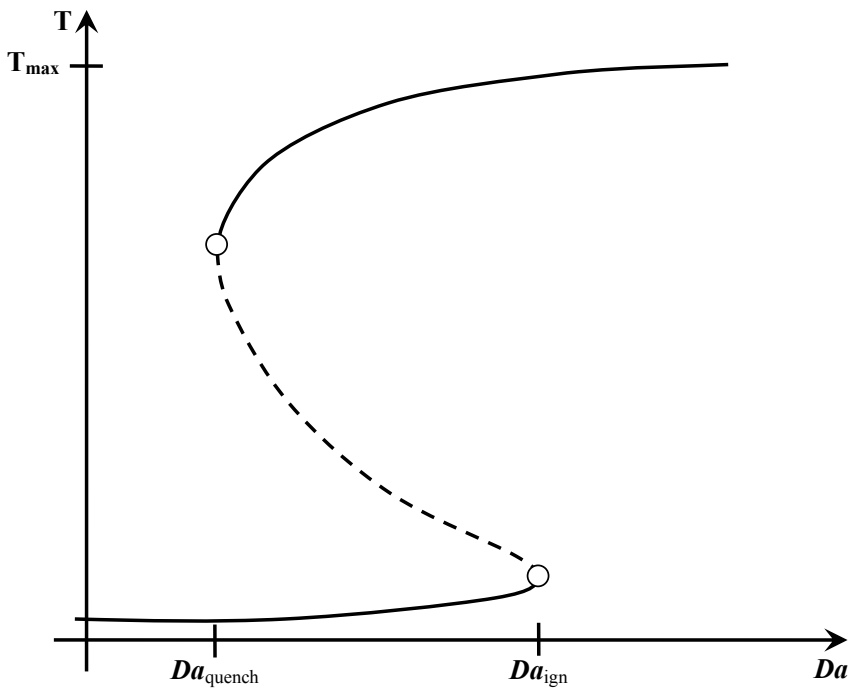

Figure 1.2: Maximum Flame Temperature versus Damköhler Number for Elliptic Autoignition

More detailed treatment of the hydrogen autoignition chemistry in the laminar counterflow configuration was possible by computational [Kreutz and Law, 1996, 1998, Kreutz et al., 1999, Mason et al., 2002] and experimental/computational [Fotache et al., 1998, Zheng et al., 2002, Zheng and Law, 2004] investigations. Various

hydrocarbons such as methane, ethylene, ethane, propene, propane, butane and n-heptane have also been investigated, with numeric studies [Liu et al., 2004] and experiments/simulations [Fotache et al., 1997a, 1999, Humer et al., 2002]. These studies have provided an excellent understanding of autoignition chemistry in the presence of strain rate and have revealed the existence of complex thermokinetic/diffusive effects based on which reduced chemical kinetic mechanisms have been developed.

In laminar inhomogeneous autoignition the existence of critical conditions, in terms of a strain-rate, scalar dissipation rate or Damköhler number, has been verified. The observed influence of the non-uniform flow on the emergence of autoignition highlights the fact that, on a fundamental level, autoignition does not follow directly from expectations based on the homogeneous case [Humer et al., 2002].

1.2.3 Turbulent Inhomogeneous Flows

An appreciation of the fundamental issues of turbulent autoignition must come from truly dealing with the turbulent case [Mastorakos, 2002]. Theoretical approaches are extremely difficult because of the complex chemical kinetics of the slower chemistry of autoignition, the turbulent closure problem and the coupling of the chemistry and turbulence. Experimentally there has been a lack of interest in treating this problem, perhaps inhibited by the difficulty of performing well-characterized measurements in the 'hostile', and immensely sensitive to conditions, turbulent autoignition environment. It is well known that the underlying physical and chemical processes of this phenomenon and their mutual cross-interference is sensitive to initial conditions. As a result, there is currently little data available concerning the effect of the local turbulence character on autoignition. It is only recently, with the increase in residence times, τ_{res} and consequently $\mathcal{D}a$ associated with the low emission LPP industrial turbines and the increased interest in controlling the autoignition timing in HCCI engines, that this issue has become relevant. Improved understanding of

turbulent autoignition has come from Direct Numerical Simulations (DNS), even though there are the issues of the low Reynolds numbers that have been examined and/or the simplified description of the chemistry. Moreover, and crucially, the validity of the DNS results has not been experimentally verified.

Stagnant Mixing Layers:

Knowledge in this field has been recently expanded with the help of DNS [Domingo and Vervisch, 1996, Echekki and Chen, 2003, Hilbert and Thevenin, 2002, Im et al., 1998, Mastorakos et al., 1997a, Sreedhara and Lakshmisha, 2000, 2002], which have amply emphasized the importance of the mixture fraction field in determining the location of autoignition. Current, 'state of the art', understanding of the autoignition of an inhomogeneous mixture, in a turbulent flow, stemmed from the observation of Mastorakos et al. [1997a], who re-examined autoignition in isotropic, homogeneous, decaying two-dimensional turbulence in a shear-less mixing layer with a simple chemistry model, in terms of the original observations of Liñán and Crespo [1976] for the laminar mixing layer and concluded that:

1. Autoignition always occurred at a well-defined mixture fraction ξ_{MR}, termed the *most reactive mixture fraction*. The value of ξ_{MR} could be (approximately [Mastorakos et al., 1997b]) determined *a priory* from knowledge of the initial conditions and the chemistry. At any instance, there were many such possible locations in the layer.

2. The fluid particles that eventually autoignited were the ones associated with small gradients of the mixture fraction ξ, i.e. experienced lower values of conditional scalar dissipation rate, $\chi|\xi = \xi_{MR}$. Plots of the reaction rate (or even the 'reactedness' $\mathcal{B}_{auto}$; i.e. the non-dimensional temperature increment from the initial condition) versus $\chi|\xi = \xi_{MR}$ were demonstrated to be very well correlated as far as the first autoignition location was concerned.

Since then, evidence to support these findings has come from simulations with different codes [Sreedhara and Lakshmisha, 2000] and with detailed chemical mechanisms for hydrogen and a reliable four-step reduced mechanism for n-heptane. An extension has been made to three-dimensional simulations with complex hydrocarbon chemistry [Sreedhara and Lakshmisha, 2002], agreeing fully with the earlier results.

It is significant to mention that, according to the latest understanding, a residence time until autoignition cannot fully define the problem in the absence of information on the mixture fraction field. It is surprising that even today, the number of autoignition experiments that are being performed in turbulent flows for which the mixture fraction field has been directly characterized, or at least for which an attempt has been made to estimate the mixing quantities based on accurate turbulence measurements, are very scarce indeed. In **Chapters 4** and **6** the importance of information on the mixture fraction is further justified, viewed in the light of results concerning the various phenomena that have been observed in this study.

A point is being reached, whereby the location of autoignition can be reasonably predicted, but these predictions can only be confirmed by experiment. On the other hand, the effect of the turbulence character, length and timescales on the magnitude and randomness of τ_{ign} is far from understood. For the purposes of the current study, the exploration of the sensitivity of autoignition to the aforementioned parameters, is best attempted in conditions in which the chemical timescales are of the same order, or close to the order, of the fluid-mechanical/turbulent timescales; whence the direct effect of turbulent mixing is most significant.

Turbulent Counterflows:

Recently, experiments of autoignition in the counterflow configuration have been extended to turbulent counterflows of hydrogen [Blouch and Law, 2003, Blouch et al., 1998]. These experiments and successful Probability Density Function (PDF)

modelling [Blouch et al., 2003] have produced the very interesting result that, as with the laminar counterflows, depending on the temperature of the air stream autoignition may not occur at all (at least during the residence time available, as determined by the mean bulk strain rate).

The existence of critical conditions in the case of the counterflow is an interesting outcome, in that the DNS have not shown that such a limit exists for autoignition in turbulent mixing layers. This is not altogether surprising, since the decaying turbulence and hence χ meant that high values of this variable could not be sustained for long, eventually leading to right (in the sense of low $\chi|\xi = \xi_{MR}$) conditions for autoignition. Going back to the laminar mixing layers, both co-flow and counterflow, τ_{res} is completely determined by χ and *vice versa*. For example, for equal velocity everywhere, the cross-streamwise profile of χ in the co-flow is identical for equal τ_{res} and independent of the bulk flow velocity. Yet for the co-flow, unlike the counterflow:

1. τ_{res} (and hence $\mathcal{D}a$) can always be made arbitrarily long, and,
2. χ always decays downstream, rather than remaining constant as the reactants flow radially outwards,

such that the solution will always jump to the burning temperature (**Figure 1.1**).

The novelty of the turbulent case is that χ does not completely determine τ_{res}. For the counterflow it is known that the criticality holds, but then the allowable τ_{res} is not arbitrary *and* it is relevant to approach the problem in terms of a consistently high bulk χ that can be achieved in practice by having high bulk strain rates. On the other hand, for the co-flow τ_{res} can still be arbitrarily long. This means that it is possible to have a 'hypothetical' situation in which χ is sustained above a critical value (for all τ_{res}) such that autoignition fails (for any τ_{res}). Physically this would mean that the flow always has the ability to diffuse heat and radicals away from

the reaction zone, promoting heat losses and depleting the radical pool and thus precluding autoignition.

This possibility of critical conditions is interesting and has been theoretically demonstrated, albeit for artificially sustained (constant) high levels of dissipation with zero-dimensional (0-D) Conditional Moment Closure (CMC) [Mastorakos and Bilger, 1998, Mastorakos et al., 1997b]. Nevertheless, it must be said that in parabolic flows, χ will *always* decay with increasing τ_{res} in the absence of sources, such as droplets (as is the situation that has been investigated in this work). Furthermore, the CMC approach was a modelling-based effort to predict autoignition in these flows and hence, the subsequent conclusions are subject to an uncertainty arising from the simplifications made for closure. Experimentally such an outcome has not been explored for parabolic flows and so the question is as yet open.

For the turbulent counterflow it was also shown experimentally, that increased turbulence in the air stream resulted in a higher critical temperature necessary for autoignition, suggesting a delaying effect of turbulence on the pre-ignition reactions. This finding is in subtle contrast to the DNS, that have shown that turbulence may accelerate autoignition. This discrepancy is most interesting and so the reasons behind the DNS finding will be reflected on briefly. It has been stated above that the DNS results have revealed that, locally, autoignition occurs at ξ_{MR} and at regions with low values of $\chi|\xi = \xi_{MR}$. The simulations did not last very long relative to the turbulence turnover time and also had to resolve the fuel–air interface. Hence, the autoignition time was found to depend strongly on the initial condition (i.e. the initial value of χ), with the turbulence affecting autoignition time only insofar as it affected the emergence of the lowest value of the conditional $\chi|\xi = \xi_{MR}$. Therefore, autoignition was promoted by fast mixing, due to the earlier emergence of well-mixed ξ_{MR} spots. It becomes essential to experimentally clarify this disparity and to validate or not the theoretical results from DNS regarding turbulent autoignition in parabolic flows.

1.3 Aims

It has been mentioned that although the problem of autoignition has been approached from many angles, the effect of turbulent mixing on autoignition chemistry and the statistical nature of the random appearance of the phenomena in the turbulent inhomogeneous case remain unclear. This situation is compounded by the facts that, on the one hand, the most important underlying processes of this phenomenon, namely oxidation kinetics and turbulence, cannot be said to be closed problems in themselves, and on the other, in most applications of interest autoignition occurs in situations where the two processes cannot be decoupled and in which the final outcome is a compounded result of so-called 'chemistry–turbulence interactions', or placed more simply, of their 'mutual interference'. Accurate predictions of autoignition can only be made for a limited (and special) number of cases.

This document presents results from an experimental effort to observe autoignition in a turbulent inhomogeneous flow of a parabolic nature. The thesis will describe experiments in which various pure, or diluted, gaseous fuels were injected concentrically and continuously into a co-flow of preheated, turbulent air. Hydrogen, acetylene (ethyne), ethylene (ethene) and prevaporized n-heptane have been used. With the exception of the more complex situation of evaporation and mixing of liquid fuel sprays that are not considered here, this study has been specifically designed to consider the problem from the most generalized point of view; that in which the phenomenon occurs as a consequence of turbulent mixing, real chemistry and such that the chemical and turbulent timescales are of the same order.

It will be shown that a variety of autoignition phenomena are possible, as are related phenomena such as post-ignition flame propagation and flashback or extinction, that are not necessarily the same for all fuels. Furthermore, it will be demonstrated that for a certain, relatively wide range of conditions, autoignition appears in the form of random events, or 'spots', that manifest both visually and

acoustically in a well-defined manner. It will be shown that the randomness of these spots cannot be neglected and that for a complete description both the mean behaviour and statistical fluctuations must be considered. In this study autoignition will been examined in terms of:

1. The mean location of its appearance relative to injection, as well as an estimated mean residence/delay time associated with this location. The effects of the choice of fuel, the degree of fuel dilution with nitrogen, the temperature and velocity, and of the flow geometry will be examined, with specific reference to the discrepancy between the DNS and counterflow experiments concerning the effect of turbulent mixing on autoignition chemistry.

2. The randomness, or spread, in the location and delay time of autoignition.

3. Topological and spatial details of the manifestation of the instantaneous, explosive autoignition spots, as well as details of the temporal evolution of the resulting autoignition spots into propagating flames and the fate of these post-ignition flames.

4. The frequency of appearance of the random spots and its relation to the autoignition location.

5. The spectral and acoustic signature of the spots. The former will be investigated with spectroscopy and the latter with acoustic measurements.

6. Possible differences in the overall behaviour between the various fuels.

To the best knowledge of the author experiments investigating these aspects of autoignition have not been previously reported in the literature. Similar configurations have been explored, but in those experiments the phenomena were either additionally affected by such issues as the two-phase physics of liquid fuel spray evaporation and/or were done in more complex and less well-known mixing fields than the steady,

axisymmetric, plume-in-co-flow chosen in this work. More importantly, all earlier studies reported a delay time only, with no reference to the location of autoignition relative to the turbulent mixing field, or a proper characterization of the this field to ascertain any effects of relevant mixing quantities on the phenomena.

The statistics of autoignition have not been previously explored experimentally and could be the outcome of calculations, such as those by PDF or Large Eddy Simulation (LES) methods. Therefore the present data can serve as an ideal test-bed for the validation of advanced CFD and turbulent reacting flow models. Hence, in addition to the previously mentioned points and from a more practical point of view, the work that is reported in this thesis, aims to:

1. Provide well-characterized data of autoignition lengths and delay times for various fuels in the presence of velocity fluctuations and mixture inhomogeneities for the purposes of modelling.

2. Uncover any connection between the ensemble-mean behaviour (e.g. the average ignition timing measured from many cycles in a diesel engine) and the possibility of relatively rare events causing dangerous autoignition (e.g. in a gas turbine premix duct).

3. Provide information on the chemiluminescence emissions and sound characteristics of phenomena that arise.

1.4 Thesis Structure

Chapter 2 that follows immediately presents the experimental apparatus, measurement equipment and methods used, both for experiments whose purpose was to characterizing the background flow, in terms of temperature, velocity and mixture fraction, and for the autoignition experiments. This is succeeded by **Chapter 3**, which

describes the apparatus in terms of accumulated knowledge concerning the velocity, temperature and mixing fields. **Chapters 4**, **5**, **6** and **7** present the main results from this work in terms of the above stated objectives. More specifically, **Chapter 4** introduces, mostly qualitatively but where applicable quantitatively, general observations concerning the spatial and temporal features of the phenomenon. In this chapter there is also an attempt to convey, empirically, a broader description of the experiences gained during the course of these experiments. **Chapter 5** reports on the frequency of the autoignition events and the acoustic signature recorded during autoigniting conditions. **Chapter 6** and **7** are the main results chapters. There, information will be available on the measured location and estimated delay time of autoignition respectively, including the effects of the various parameters, such as the fuel, fuel dilution with nitrogen, temperature, velocity, flow geometry and turbulence quantities. Finally, **Chapter 8** briefly reiterates the main conclusions from the perusing results chapters, remarks on an underlying explanation for the majority of phenomena and trends that have been observed and highlights wider implications concerning autoignition in these flows that arise from this work.

It is noted that throughout this thesis S.I. units are used, unless specifically stated.

Chapter 2

Experimental Methods

2.1 Methods Chapter Objectives

This chapter describes the experimental apparatus, along with the method of its operation. All experimental techniques will be stated, including the equipment used and their specifications. The experimental methods refer to both:

- Those used for the characterization of the conditions in the experiment, and,
- Those used for the autoignition measurements themselves, with the exception of optical measurements.

In the case of the optical autoignition measurements and because certain concepts relating to the spatial appearance of autoignition have not yet been introduced, the methods of two-dimensional optical (cameras only) data generation and processing thereof will be kept for **Section 4.4**, after the autoignition phenomena have been introduced (**Chapter 4**) in order to facilitate the reader.

The chapter begins with a detailed presentation of the apparatus (**Section 2.2**), which includes the original experimental concept, the key problems that were faced during the development phase and their solutions. Throughout the thesis a number of variables that were measured, such as the temperature at the inlet

location and the flow rates of the air and fuel streams, will be used to describe the conditions in the quartz tube during autoignition. These variables are also defined in the current chapter. The equipment and experimental methods used to measure the inlet variables and supply the characterization data of **Chapter 3** can be found in **Section 2.3**, whereas those used for the autoignition measurements and to supply the main results of **Chapters 5** to **7** are outlined in **Section 2.4**.

Finally, it was desirable to inspect the data in terms of a mean residence time until autoignition and attempt to compare this with other measurements of autoignition delay time available in the literature. The method of estimation of an average autoignition 'delay time' corresponding to the various measures of autoignition length is discussed in **Section 2.4.3**.

2.2 Apparatus

The 'Autoignition in Turbulent Flows' laboratory was erected in the Hopkinson Laboratory, in the Inglis Building of the Department of Engineering, in September 2001 especially for the autoignition experiments that are the subject of this thesis. In terms of the development of the experiment the author has found help, to a certain degree, from other autoignition experiments in the literature in related configurations. Yet, because none of these experiments were performed with the particular approach adopted here, many problems had to be solved 'from first principles'. He would like to emphasize the fact that the evolution of this experiment to the stage at which it currently exists proved time consuming and was not a simple affair. Delays were initially encountered in providing the laboratory with the necessary high power electrical supply, completed by April 2002. This allowed the first successful realization of autoignition in the apparatus to be achieved in July 2002, but severe problems with the low-cost commercial heaters failing at higher temperatures meant that the experiment was not robustly operational until March 2003.

This section describes the apparatus. **Section 2.2.1** begins by stating, broadly, the experimental concept that resulted from the considerations of **Section 1.3**. This leads to a presentation of the final form of the apparatus, as used in the experiments (**Section 2.2.2**). This is the main section, in which the apparatus is described. Various modified versions of the basic configuration were used. For example 'injector extensions' was used in order to perform experiments with smaller injector nozzle diameters. In some experiments a heat exchanger was used to further insulate the quartz tube, whereas in others, conically shaped bluff-bodies were placed at the injector nozzle to investigate the effects of a recirculation zone, higher turbulence intensities and more vigorous mixing on the phenomena. These modifications to the basic design are presented in **Section 2.2.3**. Turbulent autoignition is a phenomenon extremely sensitive to initial conditions. Particular attention has been paid to the accurate reporting of the measured quantities, both in minimizing and quantifying all experimental uncertainties. **Sections 2.2.4** and **2.2.5** detail, respectively, the corrections made to the (most important) temperature measurements and the resulting uncertainties in the rest of the variables reported in this thesis.

2.2.1 Experimental Concept and Key Design Issues

A sketch of the experimental concept can be seen in **Figure 2.1**. A concentrically placed injector releases cold, nitrogen-diluted fuel into a uniform, turbulent co-flow of hot air flowing in a well-insulated tube. Downstream of injection the fuel and air mix and at some length from the nozzle the reactive mixture autoignites. In this basic form the configuration will be referred to as the 'Confined Turbulent Hot Co-Flow' (CTHC). For certain experiments the use of a bluff-body was made and in this case the flow configuration will be termed a 'Confined Turbulent Hot Annular Jet' (CTHAJ), where the annular jet refers to the flow of air in the annular area described by the inner wall of the quartz tube and the radial extent of the bluff-body at its most downstream end, on the injector nozzle.

Pre-heating by electrical means has advantages over using high temperature, vitiated air (i.e. combustion products), as employed by Cabra et al. [2002] for example, mainly due to: (i) the elimination of uncertainties in inlet conditions of the chemistry, introduced by the presence of post-flame radicals, and, (ii) increased controllability. Due to financial limitations it was decided early on to opt for commercial, low-cost electrical 'air process' heaters. These heaters come in various sizes, with the smaller sizes usually being capable of slightly higher final temperatures due to marginally improved heat transfer from the heated wires to the flowing air. Given the necessity for as high a temperature capability as possible and the further desire for a flexibility with higher pressure, a relatively small sized, stainless steel heater was chosen, namely the 3/8" Osram Sylvania, Threaded Inline model. The heater has a cylindrical shape, with a length of 0.3 m and an outer diameter of 2 cm. For manufacturer's drawings see **Figure 2.2**.

According to factory specifications it can be operated with inlet pressures up to 10 bar. Its maximum power is rated at 1.6 kW, with a maximum drawn current of 9.4 A at a root-mean-square (rms) voltage of 170 V_{rms} (the resistance of the heating element is about 18 Ω). Most importantly the manufacturer specifies that the heaters are capable of temperatures up to 760°C and that two heaters can be operated in series with one another, thus achieving final temperatures up to 1038°C. This was the highest air temperature that any manufacturer specified for such a heater. Unfortunately, serious problems were encountered when two heaters were run in series, leading to an inability to achieve overall temperatures higher than about 800°C. It was decided to completely re-design and manufacture all four heaters in-house in order to avoid the performance and reliability issues of the commercially available models. **Figure 2.3** shows the new design and a comparison with the performance of the original heater. In this figure, due to limited data concerning the original heaters, only results with the first heater rms voltage at 120 V_{rms} are shown. The revised heaters have also been operated with up to 145 V_{rms} across

the first heaters and at much higher air temperatures than those allowable by the original design. A log book with the operational life of the new heaters has been kept documenting more than 1000 hours without failure.

Larger quartz tube sections were favoured so as to minimize boundary layer effects, and provide more uniform flow and mixing fields in the quartz tube. Together with the need to establish sufficiently high Reynolds number turbulent flows, this meant that relatively high flow rates of air were required. Achieving the specified high temperatures, given the small size of the chosen Osram Sylvania heater, involved flow rates that could only have been achieved with four heaters, arranged in two sets of two heaters in series.

Due to the decision to go with two sets of heaters, problems were also encountered with differential flow rates in the two heater streams. Initially, a simple Y-fitting was used to split the flow into two. At cold conditions and for a fixed total mass flow, each stream experienced a certain (but similar) pressure drop through the heaters, but dissimilar flow rate. This was unavoidable as no two heaters are manufactured in precisely the same way and is worsened by the fact that the serpentine heating elements inside the heaters occupy most of the cross-section available to the flow, thus resulting in large pressure drops (up to 4 bar) through the heaters. So as to generate the same temperature rise at the heater exits, the voltage was set slightly higher on the heaters in the stream with the highest flow. At low temperatures this voltage discrepancy was small, but with the increasing voltages necessary to provide higher temperatures this effect became more acute. In the experiment, this resulted in the straining of the higher flow heater pair and ultimately in complete failure by burn-out. The need to regulate this problem resulted in the 'heater flow equalization valve assembly', whose purpose was to create an additional counteracting pressure drop across both parallel streams. The assembly ensured that the air mass flow was divided equally, irrespective of any difference in heaters themselves, and thus, also ensured that the temperature rise of each heater flow was equal.

2.2.2 A Brief Presentation of the Final Design

The forerunning section was preoccupied with the basic idea behind the autoignition burner and stated challenges faced during the design and testing phases relating to the continuous supply of high temperature air. The final design, as used for the experiments, is now presented. **Figure 2.8** shows definitions of the geometry and measurement variables that will be used throughout this thesis.

Air Supply:

Figure 2.4 outlines the air supply arrangement. Compressor air was supplied to a two-stage preparation arrangement, comprising of a regulator/pre-filter combination and a coalescing filter. The regulator was used along with a pressure gauge to adjust and maintain the back pressure at 10.0 bar(g). The first stage pre-filter acted as a high efficiency dryer and particulate purifier, removing water droplets, residual humidity and particles down to 25 μm according to manufacturer's specifications. The second stage filter contained an activated carbon element and acted as an oil droplet and vapour oil purifier. It was also used to remove any hydrocarbon odour traces. Its rated maximum oil content and particle removal in the outlet was 0.003 ppm and 10 nm respectively.

The air mass flow ($\dot{m}_{air}$) was measured directly with a Bronkhorst High-Tech digital, thermal mass flow controller (AIR-MFC) calibrated to operate at inlet gauge pressures of 10.0 bar. The AIR-MFC* was factory calibrated with air, had a maximum flow rate of 500 l/min at normal conditions (i.e. 0°C and 1 atm., or 1.01325 bar) and actually indicated volumetric mass flow rates at normal conditions. Mass flow rates were calculated by multiplying the indicated volumetric flow rates with the density of air at normal conditions. It had the following technical specifications: an accuracy of ±0.5% of reading plus ±0.1% full-scale (based on actual factory calibra-

*Can be found at *http://www.bronkhorst.com/*, as can the FUEL-MFC.

tion), a reproducibility of 0.1% full-scale, a repeatability of 0.2% reading, pressure and temperature sensitivities of 0.1%/bar and 0.05%/°C respectively, a turndown control range of 100 – 2% and a control stability of <0.1% full-scale. Note that, the subtle difference between 'repeatability' and 'reproducibility' is that 'repeatability' includes neither drift (repeated measurements over any length of time) errors nor hysteresis, whereas 'reproducibility' includes drift, hysteresis, and repeatability.

Downstream of the AIR-MFC the air was divided into two streams of equal flow rate by means of the 'heater flow equalization valve assembly' (see end of **Section 2.2.1** and **Figure 2.4**), with incorporated monitor flow meters and pressure gauges. Each branch of the assembly supplied two inline electrical resistance heaters operated in series. The temperature of the air was measured at the exit of each heater pair with 1.5 mm diameter Pyrosil D® sheathed, mineral insulated N-Type (Nicrosil/Nisil) thermocouples. Note that conductor combinations are written in this thesis as "+ve wire leg/-ve wire leg". These measurements were employed as negative feedback inputs into a 'heater controller unit' rated at up to 30 kW, that was again completely custom designed and manufactured in-house to save cost. The 'heater controller unit' contained amongst other: two burst/phase angle microprocessor power controllers, two solid state power regulators, two commercially available Proportional-Integral-Derivative (PID) temperature controllers, thermocouple circuitry (including signal amplification and hardware correction) and real-time rms voltage, power and temperature displays.

After the second stage heaters a custom-made, 303 grade stainless steel 'air mixer' merged the two hot streams as shown in **Figure 2.5**. The 'air mixer' was used to promote uniform velocity and temperature conditions leading into the main experiment flow section. It also contained a perforated plate for turbulence generation with $M = 3.0$ mm diameter holes and 44% solidity. Its final section consisted of a 35.0 mm contraction length. This was designed to create favourable pressure gradients, inhibit boundary layer growth and thus minimize flow separations and

unsteadiness. In addition, the inner walls of the mixer and of the quartz tube were designed to met to within 0.5 mm, taking into account the differential expansion between stainless steel and quartz at the elevated temperatures. The complete heater and mixer assembly were heavily insulated with a 0.15 m thick lagging layer of non-refractory ceramic blankets along its whole length in order to keep heat losses to a minimum. A 1.0 mm diameter Pyrosil D® sheathed, mineral insulated N-Type thermocouple was embedded in the walls of the mixing block in order to measure temperature and assess the overall thermal state of the apparatus. This thermocouple measurement (T_{mixer}) proved useful in confirming that the apparatus had reached thermal equilibrium during the lengthy (1 – 2 hours, see **Section 2.4.1** for more details) heating up process before each experiment and for corrections to the raw thermocouple measurement of the air temperature.

From the mixer the hot air passed directly into a quartz tube with an open-ended exit, such that the pressure in the tube was ambient. The air temperature (T_{air}) was measured at the 'inlet' of the tube, which was 26±1 mm upstream of the injector with a twin-bore 0.20 mm diameter ceramic (re-crystallized alumina) sheathed bare-wire, butt-welded R-Type (Pt&13%Rh/Pt) thermocouple. Here, Pt&13%Rh denotes an alloy of Platinum and 13% Rhodium. The thermocouple had a total length 0.10 m, was embedded in the mixer wall and protruded by 9±1 mm into the flow with horizontal orientation. An additional twin-bore, 0.20 mm diameter ceramic (aluminous porcelain) sheathed bare-wire, butt-welded N-Type thermocouple was placed at the exit of the tube to monitor heat losses along the length of the tube and to detect combustion. The reading from this thermocouple (T_{exit}) was also used for temperature corrections due to radiative heat losses from the raw T_{air}. The whole apparatus, including the quartz tube, was supported by a steel 'alignment table' that was used to set its orientation to 0.5 degrees with the aid of levels.

Finally, 45° conically shaped bluff-bodies were placed at the injector nozzle to investigate the effects of higher turbulence intensities and more vigorous mixing on

the phenomena, but also to examine the possibility of interactions of the phenomena with the recirculation zone. The presence of the bluff-body created an annular region between its circumference and the inner wall of the quartz tube (see **Figures 2.1** and **2.8**). Hence, this will be referred to as the CTHAJ burner configuration. Experiments with the CTHAJ burner were done only with ethylene.

Nitrogen-Diluted Fuel Supply:

The fuel (hydrogen, acetylene or ethylene) was supplied from a compressed cylinder at 99.999% vol/vol purity and regulated cylinder gauge pressure of 10.0 bar (only 1.5 bar for acetylene). It passed through a Bronkhorst High-Tech digital thermal mass flow controller (FUEL-MFC) before entering a 'fuel mixer' block farther downstream whose purpose was to promote mixing between the fuel and nitrogen streams. The FUEL-MFC had a maximum flow rate of 15 l/min at normal conditions (0°C and 1 atm.) and the same specifications (and accuracy) as the AIR-MFC, but was actually calibrated for use with methane. Any number of compatible gases could be used as long as the raw readings were corrected with the use of a conversion factor. The conversion introduces an additional uncertainty in the absolute (or determinate) accuracy of the fuel mass flow rate ($\dot{m}_{fuel}$), which is worsened by 2.3%. On the contrary, it does not introduce extra uncertainty to the 'relative accuracy' of the instrument, i.e. the indeterminate (random) error, or the rest of the specifications such as the reproducibility, repeatability, the sensitivities etc.

In addition to these fuels, n-heptane was also used. At room temperature and pressure n-heptane is a liquid and so for these experiments had to be prevaporized. A pre-calibrated positive displacement peristaltic pump and small electric heater (**Figure 2.6(e)**) were used for this purpose. Calibration was performed by measuring, at room conditions, the weight of liquid n-heptane with a high-accuracy ($\pm$0.005 g) balance and hand-held stopwatch, as a function of the setting on the peristaltic pump. The capability of the peristaltic pump to set the mass flow rate of

n-heptane ($\dot{m}_{n-C7H16}$) was associated with a worst case error of ±6% at the lowest flow rates (0.020x10^{-3} kg/s), improving to ±4% at the highest (0.100x10^{-3} kg/s). Temperatures of 150°C proved sufficient for evaporation. To improve accuracy in these experiments, the FUEL-MFC was used to control the mass flow of nitrogen ($\dot{m}_{N2}$) instead of the rotameter in the basic gaseous fuel arrangement (**Figure 2.5**).

Nitrogen at 99.9995% vol/vol purity was supplied from a compressed cylinder regulated at 4.0 bar. Its flow rate ($\dot{Q}_{N2}$) was adjusted by a pair of suitably ranged, coarse/fine pre-calibrated rotameters with pressure gauges at their exits for flow measurement corrections due to density. In order to keep the experimental error in the fuel stream flow rate to a minimum, nitrogen rotameters with different ranges were utilized depending on the flow rates used. The rotameter readings were converted to mass fluxes in (kg/s) by the following expression:

$$\begin{aligned} \dot{m}_{N2} &= \rho_{N2}\dot{Q}_{N2} = \rho_{N2}\dot{Q}^{ind}_{N2}\sqrt{\frac{\rho^{cal}_{N2}}{\rho_{N2}}} \\ \Rightarrow \dot{m}_{N2} &= \dot{Q}^{ind}_{N2}\sqrt{\rho^{cal}_{N2}\rho_{N2}} \end{aligned} \tag{2.1}$$

where $\dot{Q}_{N2}$ and $\dot{Q}^{ind}_{N2}$ are the corrected and raw nitrogen rotameter readings in (m^3/s) respectively, ρ^{cal}_{N2} the density of nitrogen at the conditions at which the rotameter tube was calibrated (usually 20°C and 1 atm.) and ρ_{N2} the best estimate for the actual density in the rotameter tube during the taking of the $\dot{Q}^{ind}_{N2}$ measurement. For the best possible measure of ρ_{N2} the pressure in the rotameter flow tubes was measured with 63 mm diameter dial size, analogue, general purpose pressure gauges consisting of a phosphor bronze pressure element and helical spring. The gauges ranged up to 1 bar(g) and were factory certified to an accuracy of ±1.6% full-scale.

The basic injector consisted of an 11 gauge (0.1170" outer and 0.090" inner diameter) stainless steel hypodermic tube. This is a manufacturer designated size. The actual diameters were measured (see **Section 2.2.3**). Pure fuel or the diluted

fuel/nitrogen mixtures were injected axially and continuously through the injectors at ambient pressure. *Throughout this thesis the pure or nitrogen-diluted fuel stream will be referred to as 'fuel stream' or simply as 'fuel'.* The dilution of the fuel is described by the mass fraction of fuel in the diluted-fuel stream (Y_{fuel}). For most of its length the injector was encased in a 2.0 mm thick-walled ceramic sheath in order to insulate the fuel from the hot air, keep it at a cooler temperature and inhibit fuel decomposition prior to injection. The nozzle was located a certain distance downstream of the perforated plate to allow the turbulence to develop (see **Table 2.2**). An 'injector alignment mechanism' ensured that the injector was located at the centreline of the tube to 0.5 mm and that it was correctly aligned with its axis.

A 500 mm long and 0.25 mm diameter 321 grade stainless steel sheathed, mineral insulated K-Type (Chromel/Alumel) thermocouple was placed through the injector tube all the way to 1 – 2 mm from the injector nozzle (exit) and allowed a real time measurement of the fuel injection temperature (T_{fuel}). It should be noted that the fuel injection temperature was not an independent parameter is these experiments, but depended on the heat transfer through the injector wall, from the hot co-flowing air to the fuel flowing inside the injector. For certain experiments a further small heater (**Figure 2.7(f)**) was used to slightly pre-heat the fuel/nitrogen mixtures just before the injector. In this way a certain degree of control of the fuel injection temperature was possible. An idea for a water or gas cooled injector was rejected as this would have thickened the temperature boundary layer developing on the injector walls going into the quartz tube.

To investigate the effect of the injector nozzle diameter it was decided to manufacture 'injector extensions' that could be inserted and push-fit secured into the basic injector, as in **Figure 2.5**. In this way it was ensured that, as long as the extensions were sufficiently well streamlined, the flow and temperature profiles of the air stream would not be significantly altered across the experiments, except inside the jet or wake downstream of injection. The 'small' injector experiments were performed only

with acetylene. During these experiments the relative error in setting the acetylene flow rate would have been greatly worsened by using the same FUEL-MFC as for the experiments with the larger injector. A low flow rate (20 – 200 ml/min) Alicat Scientific laminar volumetric flow meter (FUEL-VFM) was employed in place of the FUEL-MFC to measure the acetylene flow rate ($\dot{Q}_{C2H2}$). The FUEL-VFM had an accuracy of ±1% full-scale, a repeatability of ±0.5% full-scale, pressure and temperature sensitivities of 0.02%/bar and 0.02%/°C and a turndown ratio of 100 – 1%. It was certified as have been calibrated before delivery with (20°C and 1 atm.) nitrogen at three flow rates spanning its full range with an error inside ±0.1% full-scale.

2.2.3 Specifics

Table 2.1 describes the three quartz tubes that were used in the experiments.

Quantity (Dimension) ± ***Error***	'Jacketed' Tube	'Blanket-Insulated' Tube	'Large Ø' Tube
Outer Diameter (mm)	27.91 ±0.02	28.10 ±0.03	— —
Inner Diameter (mm) D_{TUBE}	24.78 ±0.02	25.00 ±0.03	33.96 ±0.02
Length (m) L_{TUBE}	0.5 —	1.5 —	0.3 —
Used in CTHC	Yes	Yes	No
In CTHC w/ Heat Exchanger	Yes	No	—
Used in CTHAJ	Yes	No	Yes
Additional Insulation Type	No	Blanket	Blanket
Quartz Type	Synthetic Quartz	Synthetic Quartz	Synthetic Fused Silica
PLIF Measurements	No	No	Yes

Table 2.1: Quartz tubes used for autoignition experiments. The 'jacketed' tube has been used more extensively than the others. The main difference between this and the 'blanket-insulated' tube is the method of insulation.

The 'jacketed' (two sealed concentric) quartz tube configuration incorporated a pre-evacuated annular volume so as to reduce heat losses and establish a temperature field as uniform as possible within the tube. This tube provided full optical access and required no additional insulation. The tube diameters were measured with a digital Vernier caliper with resolution ±0.01 mm and accuracy ±0.02 mm.

The injectors used in the experiments are listed in **Table 2.2**.

Dimension ± Error	'3 mm' Injector	'Small' Injector
Outer Diameter $- d_{OUT}$ ***(mm)***	2.96±0.02	—
Inner Diameter $- d_{IN}$ ***(mm)***	2.24±0.03	1.027 & 1.185±0.005
Length from Grid $- z_M$ ***(mm)***	63	(63 + 8 =) 71
Normalized Length from Grid $- \frac{z_M}{L}$	21.0	23.7
Turbulent Time from Grid $- \frac{z_M}{L}\frac{\sqrt{\overline{u'^2_{air}}}}{U_{air}}$	2.1	2.4
Used in CTHC	Yes	Yes
Used in CTHC w/ Heat Exchanger	Yes	No
Used in CTHC w/ Fuel Heater	Yes	Yes
Used in CTHAJ	Yes	No
Used in CTHAJ w/ Fuel Heater	Yes	—
Stainless Steel Grade	304	321
PLIF Mixing Measurements	Yes	Yes

Table 2.2: Injectors used for autoignition experiments. Turbulent time is in term of eddy turnovers.

The default injector was made from thin-walled 304 grade stainless steel tubing, had an 2.24±0.03 mm internal diameter, an outer diameter of 2.96±0.02 mm, and a wall thickness of 0.36 mm. The diameters were measured at ambient conditions with the same digital Vernier caliper used for the quartz tubes. In the calculations for U_{air} and U_{fuel} (see **Section 2.2.5**) based on the air and diluted fuel (fuel plus nitrogen) flow rates, the cross-sections took into account the expansion of the stainless steel at the high temperatures during operation. Typically, with a coefficient of thermal expansion of 18.8±0.5 μm.m^{-1}.K^{-1}, the diameter will increase by up to

1.7% during operation at higher air temperatures, such as 1200 K. This injector will be everywhere referred to as the '3 mm injector'. It was also used in the CTHAJ.

In the CTHAJ configuration a bluff-body was placed at the end of the 3 mm injector, as in **Figures 2.1** and **2.5**. A divergent 45° cone shaped bluff-body was used. It was placed so that axially its flat face was level with the end of the injector and perpendicular to the flow direction, such that the distance from the grid to the bluff-body flat face was $z_{BLUFF} = z_M = 63$ mm. Two quartz tube/bluff-body combinations have been used in the experiments with the CTHAJ burner, chosen such that the blockage ratio was kept approximately the same. Denoting the inner quartz tube diameter by D_{TUBE} and the bluff-body flat face diameter by D_{BLUFF}, the combinations were as per **Table 2.3**.

Dimension* ± *Error	Low $\mathcal{R}e$	High $\mathcal{R}e$
Quartz Tube Diameter* – D_{TUBE} *(mm)	'Jacketed' 24.78±0.02	'Large Ø' 33.96±0.02
Bluff Body Diameter* – D_{BLUFF} *(mm)	10.00±0.02	13.99±0.02
***Blockage Ratio* – $(\frac{D_{BLUFF}}{D_{TUBE}})^2$**	0.163	0.170
Length from Grid* – $z_{BLUFF} = z_M$ *(mm)	63	63
***Normalized Length from Grid* – $\frac{z_M}{L}$**	21.0	21.0
***Turbulent Time from Grid* – $\frac{z_M}{L}\frac{\sqrt{u'^2_{air}}}{U_{air}}$**	2.1	2.1
Used w/ Fuel Heater	Yes	—
Stainless Steel Type	321	321
PLIF Mixing Measurements	No	Yes

Table 2.3: Quartz tube/bluff-body combinations used in CTHAJ experiments. Turbulent time is in term of eddy turnovers.

In **Tables 2.2** and **2.3** a value of 0.1 was used for the turbulence intensity $\frac{\sqrt{u'^2_{air}}}{U_{air}}$. The actual values of $\frac{\sqrt{u'^2_{air}}}{U_{air}}$ were measured (see **Section 3.2**) and found to be around 0.14 at the injector for a wide range of flow conditions. Closer to the grid the values are even higher, so that the turbulent turnover times provided in these tables underestimate the true values. Also, it has been assumed, as is common in grid

turbulence at relative closeness to the grid, that the size of the characteristic large-scale turbulent eddy size can be approximated by $L \approx M$. The longitudinal integral lengthscale, L_{turb}, has been measured directly (**Section 3.2**) and the measurements confirm this assumption. Generally in this thesis, where L_{turb} is given, this will be from measurement except where specifically stated.

Two Reynolds numbers were defined for the CTHC, termed 'macroscale' and 'turbulent' $\mathcal{R}e$:

$$\mathcal{R}e_{air}|_{CTHC} = \frac{U_{air}D_{TUBE}}{\nu_{air}} = \frac{\frac{\dot{m}_{air}}{A_{air}}D_{TUBE}}{\mu_{air}} \tag{2.2}$$

$$\mathcal{R}e_{turb}|_{CTHC} = \frac{\sqrt{\overline{u'^2_{air}}}L_{turb}}{\nu_{air}} \approx \frac{\rho_{air}(0.1U_{air})M}{\mu_{air}} = 0.1\frac{\frac{\dot{m}_{air}}{A_{air}}M}{\mu_{air}} \tag{2.3}$$

In these definitions U_{air} is a 'bulk' velocity; it is the volumetric flow velocity, averaged over the area defined by the outer extent of the injector and inner extent of the quartz tube (A_{air}).

For the CTHAJ the macroscale Reynolds number was again based on the 'bulk' velocity, this time averaged over the annular area, $A_{H/R}$, defined by the 'hydraulic diameter' ($D_{H/R} = D_{TUBE} - D_{BLUFF}$), which is the minimum radial clearance between the bluff-body and the quartz tube inner wall. For the same quantity the relevant scaling lengthscale was the 'hydraulic diameter':

$$\mathcal{R}e_{air}|_{CTHAJ} = \frac{U_{air}D_{H/R}}{\nu_{air}} = \frac{\frac{\dot{m}_{air}}{A_{H/R}}D_{H/R}}{\mu_{air}} \tag{2.4}$$

Finally, the turbulent Reynolds number does not change from the CTHC to the CTHAJ, $\mathcal{R}e_{turb}|_{CTHAJ} = \mathcal{R}e_{turb}|_{CTHC}$, as it is again defined based on $\sqrt{\overline{u'^2_{air}}}$ and L_{turb} just upstream of (behind) the bluff-body. It is assumed that these quantities are not significantly affected by the presence of the bluff-body at this location.

2.2.4 Thermocouple Temperature Measurements

The raw temperature measurements were corrected for radiation and conduction losses in the case of the air thermocouple and for radiation only in the case of the fuel thermocouple (see **Figure 2.9**). **Equations 2.5** and **2.6** are the main results from **Appendix A** relating the raw and corrected temperatures:

$$\begin{aligned} T_{air}^{corr} &= T_{air}^{raw} \\ &\quad + \underbrace{\frac{\sigma\epsilon}{h}\Big\{(T_{air}^{raw})^4 - \overbrace{\Big[\frac{3}{4}(T_{steel})^4 + \frac{1}{4}(T_{quartz})^4\Big]}^{F_{t/c-steel}(T_{steel})^4 + (1-F_{t/c-steel})(T_{quartz})^4}\Big\}}_{\Delta T_{rad}} \\ &\quad + \underbrace{\frac{T_{air}^{raw} - T_{mixer}}{[\cosh(mL_{t/c}) + (\frac{h}{mk_{metal}})\sinh(mL_{t/c})] - 1}}_{\Delta T_{cond}} \end{aligned} \tag{2.5}$$

$$m = 2\sqrt{\frac{h}{k_{metal}d_{t/c}}}$$

$$T_{fuel}^{corr} = T_{fuel}^{raw} + \frac{\sigma\epsilon}{h}\Big[(T_{fuel}^{raw})^4 - (T_{injector})^4\Big] \tag{2.6}$$

where $L_{t/c}$, $d_{t/c}$ are the immersed length and conductive diameter of the thermocouple wire, σ is the Stefan–Boltzmann constant (equal to 5.669x10^{-8} W.m^{-2}.K^{-4}), and ϵ, k_{metal} are the emissivity and thermal conductivity of the thermocouple material. The second and third terms on the right-hand-side of **Equation 2.5** are defined as the air thermocouple radiation and conduction 'temperature correction terms': ΔT_{rad} and ΔT_{cond}. Collectively they will be referred to as the 'temperature correction term' for the air thermocouple, $\Delta T_{t/c}$. The second term on the right-hand-side of **Equation 2.6** is defined as the fuel thermocouple radiation 'temperature correction term', ΔT_{rad}, and is the total 'temperature correction term', $\Delta T_{t/c}$, for this thermocouple that is not corrected for conduction losses.

A breakdown of $\Delta T_{t/c}$ in the case of T_{air} can be found in **Table 2.4**.

Thermocouple Size, Type	$\frac{\Delta T_{rad}}{T_{air}}$ @ T_{air}	$\frac{\Delta T_{cond}}{T_{air}}$ @ U_{air}
0.20 mm, R-Type	0.2% @ 800 K 0.4 – 0.5% @ 1100 K	0.2 @ $>$ 20 m/s 0.3 – 0.4 @ $<$ 20 m/s

Table 2.4: Normalized magnitude of thermocouple temperature corrections due to radiation (ΔT_{rad}) and conduction (ΔT_{cond}).

The uncertainty in $\Delta T_{t/c}$ is specified conservatively from a '1-in-20' chance of being outside the bound $mean(\Delta T_{t/c}) \pm uncertainty(\Delta T_{t/c})$, or a 95% confidence level, or a confidence interval of 2 standard deviations, also equal to $rms(\Delta T_{t/c})$. The discrepancies between the corrected temperatures from the air and fuel thermocouples and the temperatures of a fine (0.076 mm) K-Type wire (representing the closest measurement of T_{corr} to within 0.1%), δT_{corr}, were as in **Table 2.5**.

Thermocouple Configuration	$2 \times rms(\delta T_{corr})$	$2 \times rms(\frac{\delta T_{corr}}{T_{corr}})$
T_{air} Embedded in Mixer Wall	±7 K	±0.9%
T_{fuel} Inside Injector	±6 K	±0.8%

Table 2.5: Thermocouple discrepancies after radiation and conduction corrections in co-flow air temperatures up to 1000 K.

Table 2.5 reports *total* discrepancies between two corrected thermocouple readings of the same temperature. **Table 2.6** shows an estimate of the error due to the correction ($\Delta T_{t/c}$) alone, ignoring the error in T_{raw} from the equipment.

Thermocouple Configuration	$2 \times rms(\Delta T_{t/c})$	$2 \times rms(\frac{\Delta T_{t/c}}{T_{air}})$
T_{air} Embedded in Mixer Wall	±5 K	±0.6%
T_{fuel} Inside Injector	±5 K	±0.7%

Table 2.6: Radiation and conduction thermocouple corrections: quantification of temperature uncertainty. Showing both absolute (in K) and relative (in %) error.

Finally, for T_{air} it was deemed desirable to account for both the random and systematic contributions to the uncertainty. A further method of uncertainty calculation, by sequential result perturbation was used [Holman, 2001, Moffat, 1988]. According to this analysis, the uncertainty in T_{air}^{corr} due to worst-case uncertainties in the values of all parameters in **Equation 2.5**, including the approximations made for h and the temperatures T_{steel}, T_{quartz} and $T_{injector}$, amounts to 0.6% at the highest measured temperatures of this work. This agrees well with the result shown in **Table 2.6** from direct measurements. The analysis also revealed that the 0.6% discrepancy can be broken down into 0.3% random and 0.5% systematic contributions. Note that the total uncertainty squared is equal to the sum of squares of these contributions.

2.2.5 Quantifying Variables and Measurement Allowance

The seven key measured variables have already been mentioned in the description of the apparatus above. Recaping, these were the:

1. Raw temperature of the air and fuel streams: T_{air}^{raw} and T_{fuel}^{raw}
2. Mass flow rate of air from the AIR-MFC: $\dot{m}_{air}$
3. Flow rates of fuel from the:
   (a) FUEL-MFC normally: $\dot{m}_{fuel}$, or,
   (b) FUEL-VFM for the small injector acetylene experiments: $\dot{Q}_{C2H2}^{ind}$, or,
   (c) Peristaltic pump for the n-heptane experiments: $\dot{m}_{n-C7H16}$
4. Flow rates of nitrogen from the:
   (a) Rotameters usually: $\dot{Q}_{N2}^{ind}$, or,
   (b) FUEL-MFC for the n-heptane experiments: $\dot{m}_{N2}$

together with the ambient room temperature (T_{amb}) and the pressure (p_{bar}) on the laboratory barometer. The ambient room temperature was measured with a calibrated thermometer with reading sensitivity to within ±0.05°C and similar accuracy. The barometer had a sensitivity of ±0.05 mbar, but the accuracy of the instrument was worsened to ±0.1 mbar due to a correction that had to be performed to the raw reading to account for the effect of ambient temperature.

Also mentioned were the two auxiliary thermocouple measurements that were used for radiation and conduction corrections to the raw air temperature reading. Ultimately, the following five quantities were calculated and reported for each experimental condition (see also **Figure 2.8**): bulk air temperature and velocity, T_{air} and U_{air}, bulk fuel temperature and velocity, T_{fuel} and U_{fuel}, and the nitrogen-diluted fuel mass fraction, Y_{fuel}. For each autoignition experiment these quantities allow for a description of the conditions inside the quartz tube.

Bulk Air Temperature – T_{air}:

In all but the small injector CTHC experiments the raw measurement of the air temperature was made 26±1 mm (or 8.7±0.3 M) upstream of the injector and at a radial distance of 9±1 mm from the inner surface of the quartz tube wall (or $0.3R_{TUBE}$ from the centreline, where $R_{TUBE} = \frac{D_{TUBE}}{2}$). After correction for radiation and conduction losses from the wire T_{air} is the most accurate measure of the air temperature at $\frac{r}{R_{TUBE}} = 0.3$ and $\frac{z}{M} = -8.7$, $T_{air} = T(\frac{r}{R_{TUBE}} = 0.3, \frac{z}{M} = -8.7)$. In the small injector experiments with the CTHC burner the axial distance of the measurement from the injection location increased by the additional length of the 'injector extension', i.e. 8 mm (see **Table 2.2**), so that: $T_{air} = T(\frac{r}{R_{TUBE}} = 0.3, \frac{z}{M} = -11.3)$. The uncertainty of this measurement was investigated in **Section 2.2.4**. Summarizing, the random and systematic errors in T_{air} are 0.3% and 0.8%, resulting in a total error of 0.9%.

Bulk Air Velocity – U_{air}:

The AIR-MFC gives direct readings of mass flow rate ($\dot{m}_{air}$) and requires no correction. Based on the mass flow rate of the AIR-MFC, the bulk air velocity, U_{air}, is the average velocity over the annular flow area defined by the inner quartz tube wall, D_{TUBE}, and either the injector outer diameter (in CTHC), d_{OUT}, or bluff-body diameter (in CTHAJ), D_{BLUFF}, at T_{air} and the measured ambient pressure. For the CTHC:

$$\begin{aligned} U_{air} &= \frac{\dot{m}_{air}}{\rho_{air}} \frac{4}{\pi D^2} \\ D^2 &= D_{TUBE}^2 - d_{OUT}^2 \end{aligned} \tag{2.7}$$

The method of uncertainty analysis used throughout this thesis was taken from Taylor [1997]. The error in U_{air} is as follows:

$$\frac{\delta U_{air}}{U_{air}} = \sqrt{\left(\frac{\delta \dot{m}_{air}}{\dot{m}_{air}}\right)^2 + \left(\frac{\delta \rho_{air}}{\rho_{air}}\right)^2 + 4\left(\frac{\delta D}{D}\right)^2} \tag{2.8}$$

where all terms have already been described in previous sections. It is clear why an accurate measurement of the geometry is necessary for the minimization of the uncertainty in reporting this variable. For the density term:

$$\left(\frac{\delta \rho_{air}}{\rho_{air}}\right) = \sqrt{\left(\frac{\delta p_{bar}}{p_{bar}}\right)^2 + \left(\frac{\delta T_{air}}{T_{air}}\right)^2 + (\varepsilon_\rho|_{air})^2}$$

The pressure term is negligible (0.01%), whereas the error in T_{air} is 0.9% and $\varepsilon_\rho|_{air}$, the error associated with the method of calculation of the density of air, is 0.1%. Thus, $\frac{\delta \rho_{air}}{\rho_{air}}$ is 0.9% to one significant figure.

The geometry term can be approximated by:

$$\left(\frac{\delta D}{D}\right)^2 \approx \left(\frac{D_{TUBE}}{D}\right)^2\left(\frac{\delta D_{TUBE}}{D_{TUBE}}\right)^2 + \left(\frac{d_{OUT}}{D}\right)^2\left(\frac{\delta d_{OUT}}{d_{OUT}}\right)^2$$

with $\delta D_{TUBE} = 0.03$ mm (worst case for the 'blanket-insulated' tube) and $\delta d_{OUT} = 0.02$ mm, so that $\frac{\delta D}{D} \approx 0.2\%$.

Finally, the term $\frac{\delta \dot{m}_{air}}{\dot{m}_{air}}$ is the accumulated error from: the ±0.5% of reading plus ±0.1% of full-scale accuracy, the sensitivity of the instrument to the ambient conditions of 0.1%/bar and 0.05%/°C (possible ambient variations of ±20 mbar and ±5°C are typical) and the ±0.1% uncertainty from the variations to the supply (inlet) pressure and temperature. This is plotted as a function of mass flow rate in **Figure 2.10**, together with the total error in U_{air} as given by **Equation 2.8**. The range of $\dot{m}_{air}$ corresponds to 15 – 60% of the full-scale of the instrument and covers the full range used in the experiments.

Hence, U_{air} is the most accurate measure of the air 'bulk' velocity at $\frac{z}{M} = -8.7$ (or -11.3 in the case of the small injectors). 'Bulk' implies cross-section averaged, based on the flow rate. The relative error associated with U_{air} is at most 1.5%. Note that this is a total quantity; the random component is expected to be lower.

Bulk Fuel Temperature – T_{fuel}:

The raw measurement of the fuel injection temperature was made 1 – 3 mm upstream of the injection location. After correction for radiation losses from the wire, T_{fuel} is the most accurate measure of the fuel temperature just prior injection, $T_{fuel} = T(\frac{r}{R_{TUBE}} = 0, \frac{z}{M} = -0.5)$. The uncertainty of this measurement was also investigated in **Section 2.2.4** and it was found that the errors for this measurement amount to ±0.8%. For the small injectors the measurement was made an additional 8 mm from the injector nozzle (i.e. 9 – 11 mm), or, $T_{fuel} = T(\frac{r}{R_{TUBE}} = 0, \frac{z}{M} = -3)$.

Furthermore, the error is worsened to 2% because the calibration results, which were obtained without the 'injector extensions', are no longer applicable.

Bulk Fuel Velocity – U_{fuel}:

Based on the measured mass flow rate of the pure fuel ($\dot{m}_{fuel}$) and estimated mass flow rate of nitrogen ($\dot{m}_{N2}$), the 'bulk' fuel velocity, U_{fuel}, is the average velocity over the circular flow area defined by the inner injector tube wall, d_{IN}, at the temperature of T_{fuel} and measured ambient pressure:

$$\begin{aligned} U_{fuel} &= \frac{\dot{m}_{fuel+N2}}{\rho_{fuel+N2}} \frac{4}{\pi d_{IN}^2} \\ \rho_{fuel+N2} &= X_{fuel}\rho_{fuel} + X_{N2}\rho_{N2} \\ &= X_{fuel}\rho_{fuel} + (1 - X_{fuel})\rho_{N2} \\ X_{fuel} &= \frac{\dot{Q}_{fuel}}{\dot{Q}_{fuel} + \dot{Q}_{N2}} \\ \dot{m}_{fuel+N2} &= \dot{m}_{fuel} + \dot{m}_{N2} \end{aligned} \tag{2.9}$$

The error in U_{fuel} is:

$$\frac{\delta U_{fuel}}{U_{fuel}} = \sqrt{\left(\frac{\delta \dot{m}_{fuel+N2}}{\dot{m}_{fuel+N2}}\right)^2 + \left(\frac{\delta \rho_{fuel+N2}}{\rho_{fuel+N2}}\right)^2 + 4\left(\frac{\delta d_{IN}}{d_{IN}}\right)^2} \tag{2.10}$$

The final term concerning the injector geometry, $\frac{\delta d_{IN}}{d_{IN}}$, is simply 1.3% and 0.4% for the 3 mm and small injectors respectively.

With respect to the rest of the terms in **Equation 2.10**, three classes of measurements exist:

1. Those corresponding to experiments with the 3 mm injector and the gaseous fuels (i.e. hydrogen, acetylene and ethylene), for which the FUEL-MFC was used for the fuels and rotameters were used for the nitrogen.

2. Those corresponding to experiments with n-heptane, for which the mass flow rate of n-heptane was measured directly with the peristaltic pump and the nitrogen flow rate was measured with the FUEL-MFC.

3. Those corresponding to experiments with the small injector and acetylene, in which the FUEL-VFM was used instead of the FUEL-MFC.

Consider the error in the mass flow rate, the first term of **Equation 2.10**:

$$\left(\frac{\delta\dot{m}_{fuel+N2}}{\dot{m}_{fuel+N2}}\right)^2 \approx \left(\frac{\dot{m}_{fuel}}{\dot{m}_{fuel+N2}}\right)^2\left(\frac{\delta\dot{m}_{fuel}}{\dot{m}_{fuel}}\right)^2 + \left(\frac{\dot{m}_{N2}}{\dot{m}_{fuel+N2}}\right)^2\left(\frac{\delta\dot{m}_{N2}}{\dot{m}_{N2}}\right)^2$$

Table 2.7 summarizes the error of each term in **Equation 2.10** for each of these cases and gives the final, total error in U_{fuel}.

Error Term $\frac{\delta U_{fuel}}{U_{fuel}}$ ***(± %)***				
Experiment Injector	*'3 mm'*			*'Small'*
Fuel & N_2 Measurement Instrument	*FUEL-MFC & Rotameter*		*Pump & FUEL-MFC*	*FUEL-VFM & Rotameter*
	H_2/N_2	C_2H_2 or C_2H_4/N_2	n-C_7H_{16}/N_2	C_2H_2/N_2
$\frac{\delta\dot{m}_{fuel+N2}}{\dot{m}_{fuel+N2}}$	2 – 7 (4)	2 – 7 (3)	4 – 6 (5)	3 – 9 (5)
$\frac{\delta\rho_{fuel+N2}}{\rho_{fuel+N2}}$	2 – 7 (6)	1	1 – 3 (2)	1 – 2 (1)
$\frac{\delta d_{IN}}{d_{IN}}$	1.3	1.3	1.3	0.4
TOTAL	8	4	6	5

Table 2.7: Errors in the calculation of fuel velocities for all types of experimental configuration and all fuels. All error rounded to the nearest single significant figure. The ranges show extreme low – high limits of the errors recorded over all experiments presented in this thesis. Overall error figures (defined so that 95% of all data fall within their bounds), are shown in parentheses.

In compiling this table the values of the errors in $\dot{m}_{fuel}$ were taken as mentioned for the case of the FUEL-MFC with the gaseous fuels, the FUEL-VFM with acetylene, and the peristaltic pump with n-heptane. As for the error in $\dot{m}_{N2}$, this was either from the rotameter set-up for all gaseous fuel experiments, or from the FUEL-MFC set-up of the n-heptane ones. The error is reported on a $\pm min - max(overall)\%$ basis, with the 'overall' error calculated based on a 95% probability of the actual U_{fuel} data falling within the bounds of the reported: $U_{fuel} \pm \delta U_{fuel}$. It is emphasized that total uncertainties, including systematic and random components, were used everywhere in this treatment.

Nitrogen-Diluted Fuel Mass Fraction – Y_{fuel}:

The nitrogen-diluted fuel mass fraction is related to the pure fuel mass flow rate ($\dot{m}_{fuel}$) and the mass flow rate of dilution nitrogen ($\dot{m}_{N2}$) through:

$$Y_{fuel} = \frac{\dot{m}_{fuel}}{\dot{m}_{fuel} + \dot{m}_{N2}} \tag{2.11}$$

The relative error in this variable is given by:

$$\begin{aligned} \frac{\delta Y_{fuel}}{Y_{fuel}} &= \left(\frac{\dot{m}_{N2}}{\dot{m}_{fuel} + \dot{m}_{N2}}\right)\sqrt{\left(\frac{\delta \dot{m}_{fuel}}{\dot{m}_{fuel}}\right)^2 + \left(\frac{\delta \dot{m}_{N2}}{\dot{m}_{N2}}\right)^2} \\ \Rightarrow \frac{\delta Y_{fuel}}{Y_{fuel}} &= (1 - Y_{fuel})\sqrt{\left(\frac{\delta \dot{m}_{fuel}}{\dot{m}_{fuel}}\right)^2 + \left(\frac{\delta \dot{m}_{N2}}{\dot{m}_{N2}}\right)^2} \end{aligned} \tag{2.12}$$

and in total can be up to 5 – 7% for acetylene, ethylene and hydrogen with the 3 mm injector. For n-heptane the error drops to 3% mostly thanks to the FUEL-MFC that was used to measure the nitrogen flow rate. In the small injector experiments, in which the fuel (acetylene) was measured with the FUEL-VFM, the error in the reported value of Y_{fuel} is again 7%.

Burner Condition Overview:

The range of air and fuel velocities and temperatures used in the CTHC and CHTAJ experiments described in this thesis are shown in **Table 2.8**. Also included are other variables of significance, such as macroscale and turbulent Reynolds numbers ($\mathcal{R}e_{air}$ and $\mathcal{R}e_{turb}$) for the air and the normalized fuel injection velocity (υ_{fuel}).

CTHC			
Air Quantity		Low Range	High Range
Temperature	T_{air} (K)	900	1200
Mass Flow Rate	$\dot{m}_{air}$ (kg/s)	1.5x10^{-3}	6.5x10^{-3}
Velocity	U_{air} (m/s)	10	35
Macroscale $\mathcal{R}e$	$\mathcal{R}e_{air}$ (-)	2000	8000
Turbulent $\mathcal{R}e$	$\mathcal{R}e_{turb}$ (-)	40	200
Fuel Quantity		Low Range	High Range
Temperature	T_{fuel} (K)	600	1100
H_2 Flow Rate	$\dot{m}_{H2}$ (kg/s)	1x10^{-6}	12x10^{-6}
C_2H_2 '3 mm' Flow Rate	$\dot{m}_{C2H2}$ (kg/s)	0.5x10^{-5}	5x10^{-5}
C_2H_2 'Small' Flow Rate	$\dot{m}_{C2H2}$ (kg/s)	3x10^{-6}	10x10^{-6}
C_2H_4 Flow Rate	$\dot{m}_{C2H4}$ (kg/s)	1x10^{-5}	3x10^{-5}
n-C_7H_{16} Flow Rate	$\dot{m}_{n-C7H16}$ (kg/s)	1x10^{-5}	9x10^{-5}
Normalized Velocity	$\upsilon_{fuel} = \frac{U_{fuel}}{U_{air}}$ (-)	0.4	7.1
CHTAJ			
Air Quantity		Low Range	High Range
Temperature	T_{air} (K)	1000	1100
Mass Flow Rate	$\dot{m}_{air}$ (kg/s)	1.5x10^{-3}	4.5x10^{-3}
Velocity	U_{air} (m/s)	10	35
Reynolds Number	$\mathcal{R}e_{air}$ (-)	1400	3600
Fuel Quantity		Low Range	High Range
Temperature	T_{fuel} (K)	700	900
C_2H_4 Flow Rate	$\dot{m}_{air}$ (kg/s)	2x10^{-5}	11x10^{-5}
Normalized Velocity	$\upsilon_{fuel} = \frac{U_{fuel}}{U_{air}}$ (-)	1.2	4.6

Table 2.8: Range of experimental conditions in the CTHC and CTHAJ experiments. Including range of macroscale and turbulent Reynolds numbers ($\mathcal{R}e_{air}$ and $\mathcal{R}e_{turb}$) for the air and normalized fuel injection velocity for the fuel (υ_{fuel}).

2.2.6 Data Acquisition System

A data acquisition (DAQ) system was put together in order to make the hot wire velocity measurements, the fine thermocouple measurements for the estimation of the air stream temperature fluctuations, but also chemiluminescence and acoustic (microphone) autoignition time-series measurements mentioned in **Section 2.4**.

Input devices could be connected to a 68-pin National Instruments connector block that had eight bi-polar, differential analogue channels. The block was secured in an earthed metal box and communicated via a standard 68-pin conductor ribbon cable provided by the manufacturer to a 6035E National Instruments Multifunction DAQ PCI board connected directly to the PCI bus of a conventional desktop Personal Computer (PC) running Windows® 2000. The PC had a 1.7 GHz Pentium 4 processor (CPU), 1 GB of Non-ECC Rambus RDRAM and 1 TB of total IDE hard drive space. The DAQ board is rated by the manufacturer as being capable of sampling at up to 200 kHz by digital triggering. The manufacturer specifies the following regarding the resolution and accuracy of the DAQ system[†]:

Total Uncertainty: In the specifications of the DAQ system no distinction is made between determinate or indeterminate errors and so, all errors are lumped together as a 'total' uncertainty. The uncertainty associated with any single data point arises from the DAQ board itself and a further rounding error incurred when a data point is saved by the software to disk down to a certain decimal point. The DAQ error includes: a basic random measurement error specified as being valid over the course of 1 year from calibration, a possible systematic measurement offset that depends on the input range, noise and quantization errors (due to random noise and depending on the number of points averaged for each measurement data point). Furthermore, temperature drifts must be noted when the instrument is used at an ambient temperature

[†]From *http://www.ni.com/pdf/products/us/4daqsc202-204_ETC_212-213.pdf*.

away from the calibration conditions of 25°C; in this case 15 – 35°C are extreme ambient variations during all data taking. **Table 2.9** summarizes:

Input Range	±0 – 10 V
Basic Error (% of Reading)	0.0688
Offset Error (μV)	1591.4
Noise and Quantization (μV)	885.0
Temperature Drift (%/°C)	0.0010
Rounding Save Error (μV)	50

Table 2.9: Breakdown of errors for the DAQ board. Reproduced from the manufacturer's data sheet.

At the range of velocities measured, the raw and bridge-amplified voltages from the hot wire ranged between 2 and 10 V. In the case of the fine thermocouple hardware amplification was performed prior to recording by the system, resulting in measured voltages of 5 – 10 V. Then for all these measurements, the total uncertainty of any single data point is between ±0.1 – 0.2%.

Final Sensitivity: The DAQ board has a 16-bit digitization resolution (i.e. 1 in 65536). The final sensitivity of the system is 1 mV, independent of calibration. This is a combined measure of system resolution and noise. For the raw fine thermocouple measurements this corresponds to a 2.5 – 5% of reading sensitivity, whereas for the hot wire this quantity is negligible ($<$ 0.05% of reading).

Other Dynamic Characteristics: Bandwidth of 413 kHz; settling time after full-scale step of 5 μs; system noise including quantization of 0.8 Least Significant Bytes (LSBs) rms and an adjacent channel crosstalk of -75dB.

The data acquisition process was controlled by a program written by the author and used with commercial software (LabView) supplied by the manufacturer of the DAQ system.

2.3 Flow and Mixing Characterization: Measurement Methodology

Flow (velocity and temperature) field measurements were desirable for three main reasons. Firstly, to check that the design for the 'air mixer' (including the grid) and injector produced an 'ordinary', well-developed, uniform flow leading into the quartz tube test section. The experiment was examined for possible leaks and regions of separated flow. Secondly, and in the absence of these, to characterize the inlet conditions, both for the correct reporting of experimental quantities *per se*, but also in order to facilitate any modelling efforts that will be undertaken, or have already been attempted of the autoignition phenomena reported in this work. Both the uniformity and turbulent character of the flow field were measured. As mentioned previously, these phenomena are extremely sensitive to initial conditions. Great emphasis was placed on the proper characterization of these conditions.

The third reason arises from the fact that the autoignition measurements were actually ones of autoignition length. Given the trend in the existing autoignition literature of reporting on autoignition delay times and in order to compare these findings with those in the literature, it was necessary to estimate corresponding residence times until autoignition, from the measured lengths. This required accurate knowledge of the velocity field. In the case of the CTHC 'equal velocity kinematic condition' experiments with $U_{fuel} = U_{air}$, or $\upsilon_{fuel} = 1$, a reasonable estimate can be made of an average time. On the other hand, for jets ($U_{fuel} > U_{air}$) and wakes ($U_{fuel} < U_{air}$) in the case of the CTHC burner and all CTHAJ results (that always involved the injection of a fuel jet), the stochastic nature of the turbulent velocity between injection and autoignition, together with the non-uniform conditions, introduce a difficulty in calculating a unique residence time, or delay time, based on the measured length. An attempt for a mean residence time is still made (**Section 2.4.3**), but this difficulty is mentioned here in order to make the point that, for the

following reasons:

1. The CTHAJ results are not considered in terms of the residence time, but only in terms of the autoignition length. Thus, there is no need to calculate the delay time from the velocity.

2. Chronologically, all CTHAJ experiments were performed after the CTHC flow field was characterized. Then, in the absence of the bluff-body (CTHC) the apparatus had already been tested for possible leaks and flow uniformity. Also, the inlet conditions had been characterized up to the location of the bluff-body so that this information can already serve as an input into a numerical domain beginning slightly upstream of the bluff-body.

3. It is not expected that the confined annular flows of the CTHAJ will be any different from those already investigated in depth by numerous researchers and outlined briefly in **Section 6.4**.

4. Hot wire measurements become inaccurate at the high turbulence intensities of bluff-body wake flows.

it was decided to perform all velocity and temperature field measurements in the CTHC burner.

2.3.1 Velocity Field

Given a particular setting on the AIR-MFC, the resulting velocity field inside the tube was measured with pitot tubes and hot wires. Because these measurements were intrusive in nature, the autoignition experiment quartz tube was removed and replaced by tubes of varying length but with the same inner diameter as the original tube. The exact tube inner diameters were measured with a digital Vernier caliper and found to be 24.85±0.05 mm, or, 0.2%. Radial profiles were taken at the exit

planes of these tubes. Axially, the velocity field was investigated by repeating the measurements at the exit planes of different tubes.

The ('*hot*') autoignition experiments involved a high temperature air co-flow and injection of fuel that had been heated by forced-convective heat transfer from the injector wall during its residence time inside the injector. In order to compare with the ('*cold*') velocity field characterization measurements made at ambient conditions, the mass flows used in the characterization measurements were set so that the Reynolds number was kept the same with that in the autoignition experiments. Because A_{air}, D_{TUBE} and M were the same in the autoignition experiments and the characterization measurements, this sets a single requirement from both the macroscale and turbulent $\mathcal{R}e$, that:

$$\begin{aligned} \frac{\dot{m}_{air}}{\mu_{air}}\Big|_{cold} &= \frac{\dot{m}_{air}}{\mu_{air}}\Big|_{hot} \\ \Rightarrow \dot{m}_{air}|_{cold} &= \Big(\frac{\mu_{air}|_{cold}}{\mu_{air}|_{hot}}\Big)\dot{m}_{air}|_{hot} \\ \Rightarrow U_{air}|_{cold} &= \Big(\frac{\rho_{air}|_{hot}}{\rho_{air}|_{cold}}\Big)\Big(\frac{\mu_{air}|_{cold}}{\mu_{air}|_{hot}}\Big)U_{air}|_{hot} \end{aligned} \tag{2.13}$$

The injection velocity (U_{fuel}) was then set so that the non-dimensional ratio $\upsilon_{fuel} = \frac{U_{fuel}}{U_{air}}$ was kept the same, resulting in:

$$\begin{aligned} \upsilon_{fuel}|_{cold} &= \upsilon_{fuel}|_{hot} \\ \Rightarrow \dot{m}_{fuel}|_{cold} &= \Big(\frac{\rho_{fuel}|_{cold}}{\rho_{fuel}|_{hot}}\Big)\Big(\frac{U_{air}|_{cold}}{U_{air}|_{hot}}\Big)\dot{m}_{fuel}|_{hot} \\ \Rightarrow U_{fuel}|_{cold} &= \Big(\frac{U_{air}|_{cold}}{U_{air}|_{hot}}\Big)U_{fuel}|_{hot} \end{aligned} \tag{2.14}$$

Equations 2.13 and **2.14** are always valid for comparison between flow field characterization and actual autoignition measurements of differing conditions. Note that the subscript '*fuel*' at cold conditions refers to the injected *air* flow.

Constant Temperature Anemometry (CTA):

The axial velocity, $u(t) = \overline{U} + u'(t)$, was measured at ambient conditions. From $u(t)$ it was possible to calculate mean axial velocities ($\overline{U}$), turbulence intensities ($\frac{\sqrt{\overline{u'^2}}}{\overline{U}}$), longitudinal integral (L_{turb}) and Kolmogorov lengthscales (η_k) and velocity power spectral densities. The integral (or outer) lengthscales were calculated from integrating the normalized velocity autocorrelation functions and by making the Taylor assumption of 'frozen' turbulence to convert the time to a lengthscale. Kolmogorov (or inner) lengthscales were calculated through the turbulent dissipation, i.e. from the variance of the spatial gradients of the velocity, $\epsilon = 15\nu\overline{(\frac{\partial u}{\partial x})^2} = 15\nu\overline{[(\frac{\partial u}{\partial t}) \cdot \frac{1}{\overline{U}}]^2}$ assuming isotropic turbulence. Power spectral densities were evaluated by averaging a number (n_{psd}) of finite Fast Fourier Transforms, suitably windowed (Hamming) to reduce spectral leakage and corrected for the loss in spectral magnitude after the windowing process. In this thesis, 'power spectra' and 'power spectral densities' are different, but related functions. The latter is equal to the former normalized by the 'bandwidth of analysis', so that it may be integrated to give the variance. The 'bandwidth of analysis' is the frequency resolution of the sampling method and is thus equal to the sampling rate divided by the number of samples generated, $\frac{f_s}{N}$.

A miniature, Dantec Dynamics model 55P16 hot wire was used in this work. The 55P16 is a built-in-one probe wire with a straight support and 1 m cable with BNC connector at the end. The probe sensor consists of a conventional platinum-plated tungsten, single cylindrical wire. It has a diameter of 5 μm and length of 1.25 mm. It is considered a general purpose probe, recommended by the manufacturer for most measurements in one-dimensional flows of low turbulence intensity and with all standard CTA anemometers. Dantec supply the following additional technical data for the wire sensor: an approximate resistance of 3.8 Ω at 20°C, a temperature coefficient of 0.36%/°C and a velocity range of 0.05 – 500 m/s, although natural convection is stated as influencing the measurement up to 0.2 m/s.

The hot wire was used in CTA mode with a Dantec 56C00 Multichannel System. The system consists of the 56C01 CTA, 56C17 CTA Bridge plug-in unit and 56N20 signal conditioner. The hot wire probe was connected to the anemometer with a 5 m (1 m from the 55P16 hot wire and a 4 m standard Dantec extension wire) BNC cable. The actual resistance of the wire, necessary to set the overheat, was measured independently with the 56C00 (accuracy for resistance measurements better than 5%; specified on the Dantec manuals) and a Fluke model 73III digital multimeter (resolution of 0.1 Ω and basic accuracy for resistance measurements 0.5%; specified by manufacturer) and found to be 3.5±0.2 Ω. As recommended by the manufacturer for measurements in air, the bridges were used to set the sensor to an overheating ratio of 0.8 (or overheat ratio of 1.8), giving an over-temperature of about 220°C. The actual bandwidth of the CTA system was calculated directly from square wave tests as $(1.3\tau_{CTA})^{-1}$ [Bruun, 1995, Jørgensen, 2002] where τ_{CTA} is the time between the start and first zero crossing of the response curve resulting from the test. This was done and found to be up to 15 μs at the measured velocities, resulting in a fastest response of at least 50 kHz.

The fastest scale measurable with a cartesian probe in the investigated flows was initially estimated as being around $\frac{U_{air}}{\eta_k} = 1 - 5\text{x}10^4$ s^{-1}, over the range of $U_{air} = 1 - 5$ m/s and based on a theoretical Kolmogorov lengthscale, η_k, of $[\frac{\nu^3 M}{(0.1U_{air})^3}]^{1/4} = 0.1 - 0.3$ mm. In this approximate expression for η_k the integral lengthscale was set equal to the grid hole diameter, M, and a value of 0.1 was used for the turbulence intensity. The Kolmogorov lengthscale was measured in subsequent experiments and results are presented in **Section 3.2**. It turns out that this estimate of η_k is reasonable for the purposes here. Then, based on the Nyquist–Shannon sampling criterion, the sampling frequency for spectral density and autocorrelation measurements was always set to twice the highest frequency in the flow, i.e. 100 kHz. Typically, $5\text{x}10^6$ samples were taken in these measurements, resulting in a sampling time ($T_s = \frac{N}{f_s}$) of the order of $10^4 - 10^5\tau_{turb}$; $\tau_{turb} = \frac{L_{turb}}{U_{air}} \approx \frac{M}{U_{air}}$

the turbulent longitudinal eddy turnover time. For moment measurements, such as mean velocities and turbulence intensities, the sampling rate was set so that the time delay between successive samples (or the 'sample period', $T_s = \frac{1}{f_s}$) was about twice the *measured* (from the autocorrelation measurements) integral timescale, so that: $T_s \approx 2\tau_{turb}$, or, $f_s \approx \frac{0.5}{\tau_{turb}}$, resulting in sampling rates of f_s = 200 – 800 Hz. This ensured uncorrelated samples in the calculation of the moments. Also, for these measurements the number of samples taken for each condition was in the range 1 – 4x10^4, so that the total sampling time was kept around 50 s.

All velocity time-series calculations were performed after the entire measured voltage data were converted to a velocity through the calibration curve. For this method and assuming isotropic turbulence Bruun [1995] specifies a worst-case error of up to 1% for the evaluation of the mean velocity and turbulence intensity, for turbulence intensities up to 15% as here. This error arises from the fact that velocity fluctuations in the normal plane to the flow measurement direction will also influence the wire voltage. The same source states that "the errors in these variables will be relatively small [<3%, CNM], provided that the turbulence intensity is $\lesssim$30%". Taking into account errors from probe positioning, ambient pressure and temperature variations, air humidity, the calibrator, the fit to the calibration curve and the DAQ system, the total relative uncertainty in any single velocity sample acquired and presented in this thesis was estimated according to the method of Jørgensen [2002] at 2%. Then for the calculation of the mean ($\overline{U}$) and variance ($\overline{u'^2}$) of the fluctuating velocity from a number of samples, N:

$$\frac{\epsilon_{\overline{U}}}{2} = \frac{std[\widehat{\overline{U}}]}{\overline{U}} \approx \frac{1}{\sqrt{N}} \frac{\sqrt{\overline{u'^2}}}{\overline{U}} \tag{2.15}$$

$$\frac{\epsilon_{\overline{u'^2}}}{2} = \frac{std[\widehat{\overline{u'^2}}]}{\overline{u'^2}} \approx \frac{1}{\sqrt{N}} \tag{2.16}$$

where $\frac{\sqrt{\overline{u'^2}}}{\overline{U}}$ is the local turbulence intensity. The uncertainty associated with these

variables, as defined in this thesis, will be twice the value obtained from the right-hand-side of **Equations 2.15** and **2.16**, i.e. 0.1 – 0.2% for the mean and 1 – 2% for the variance, or 0.5 – 1% for $\sqrt{\overline{u'^2}}$. Similarly, for the normalized autocorrelation $\varrho(\tau) = \frac{R(\tau)}{\overline{u'^2}}$ and spectral density measurements:

$$\begin{aligned} \frac{\epsilon_R}{2} &= \frac{std[\widehat{R}_U(\tau)]}{R_U(\tau)} \approx \frac{1}{\sqrt{2N}}\sqrt{1+\Big[\frac{\overline{u'^2}}{R_U(\tau)}\Big]^2} \\ \Rightarrow \frac{\epsilon_\varrho}{2} &= \frac{std[\widehat{\varrho}_U(\tau)]}{\varrho_U(\tau)} \approx \frac{1}{\sqrt{N}}\sqrt{\frac{1+[\varrho_U(\tau)]^{-2}}{2}} \qquad (2.17) \\ \frac{\epsilon_{psd}}{2} &= \frac{std}{psd_u(f)} \approx \frac{1}{\sqrt{n_{psd}}} \qquad (2.18) \end{aligned}$$

As expected, **Equation 2.17** reduces to **Equation 2.16** for $\tau = 0$ since by definition $\varrho_U(\tau = 0) = 1$. Then the maximum error in the autocorrelation function is equal to the error in the turbulence intensity, i.e. 1 – 2%, tending to 0.7 – 1% at large τ. Given n_{psd} between 128 and 512 the error associated with the compilation of the spectra alone from the velocity time-series is then 4 – 9%; above and beyond the error in the velocity values themselves.

Finally, the spatial resolution of these measurements is considered. The resolution of the measurement is affected both by mean velocity gradients, as in shear layers for example, that cause the mean velocity to vary along the length of the wire and by turbulent velocity gradients, when the length of the wire is not small compared to the small scales of the turbulent flow. For the former, Bruun [1995], Gessner and Moller [1971] report an underestimation of 1.3% and 1.4% in the measurement of $\overline{U}$ and $\sqrt{\overline{u'^2}}$ for wires of the same geometry as that used here, operated at the same overheat ratio and with the parameter $S = \frac{\Delta\overline{U}}{\overline{U}}$ having a value of 1.8 in flows down to 10 m/s. Ligrani and Bradshaw [1987a,b] investigated in detail the effects of the wire size on the measured turbulence intensity by using subminiature wires. From their experimental results they concluded that few eddies had a size

smaller than about $10\eta_k$ (note that the wire used here has $\frac{l}{\eta_k} \cong 4 - 12$). Based on this observation they concluded that as long as $\eta_k \gtrsim 0.1$ mm and for a wire geometry exactly as used in this work, the measured $\overline{u'^2}$ will underestimate the 'true' value by about 4%, or $\sqrt{\overline{u'^2}}$ will be underestimated by about 2%. In terms of frequency response, the finite spatial resolution will mostly affect the higher frequencies. Bruun [1995], Perry [1982], Wyngaard [1968] agree that for the geometry of the wire used here the worst case discrepancy in the power spectral densities will be around 10% at the highest frequency of interest, i.e. that corresponding to the Kolmogorov scale. This value drops monotonically at lower frequencies, crossing ∼1% at $1/10^{th}$ of the highest frequency. The finite spatial resolution, including its effect on $\overline{U}$ and $\sqrt{\overline{u'^2}}$ and the frequency response of the wire, was not accounted for through corrections to the results presented in this work, but the uncertainty is noted.

2.3.2 Temperature Field

The mean ($\overline{T}_{air}$) and fluctuations ($\sqrt{\overline{T'^2_{air}}}$) of the air stream temperature and the cross-correlations of the temperature and velocity fluctuations ($\overline{u'_{air}T'_{air}}$) were measured at the injection location with a fine (76 μm diameter) K-Type wire and a high-temperature hot wire. Again, these measurements were made in the CTHC only. It is not expected that the presence of the bluff-body will have any effect on these quantities at that location, so it is possible to use these results for all experiments.

Fine K-Type Thermocouple:

The fine K-Type thermocouple was used to measure $\overline{T}_{air}$ and $\sqrt{\overline{T'^2_{air}}}$. It was placed so that the thermocouple bead was at the axial location of the injector ($z = 0$) and at a radial distance of $\frac{r}{R_{TUBE}} = 0.5$ from the centreline. The thermocouple wires were aligned axially, along the direction of the flow, so as to minimize the mean

temperature gradient along their lengths [Heitor et al., 1985, Mastorakos, 1993]. The signal from the thermocouple extension wire was taken through a monolithic thermocouple amplifier with integral hardware cold junction compensation (Analog Devices model AD595C), before being recorded by the DAQ system described in **Section 2.2.6**. Corrections for radiation heat losses from the thermocouple were undertaken to provide the best possible measure of $\overline{T}_{air}$, while frequency domain compensation for the finite response time of the wire was performed in the manner described in **Appendix B** for the best possible measure of $\sqrt{\overline{T'^2_{air}}}$.

High-Temperature Hot Wire:

A high-temperature hot wire was used at a single hot condition ($T_{air} \cong 800$ K, $U_{air} \cong 21$ m/s) to obtain an estimate of $\sqrt{\overline{u'^2_{air}}}$, $\sqrt{\overline{T'^2_{air}}}$ and $\overline{u'_{air}T'_{air}}$. A Dantec Dynamics model 55A75 high-temperature hot wire probe was used, incorporating a 90%Pt – 10%Rh wire probe sensor with 10 μm diameter, 2.2 mm length and approximate resistance of 6 Ω at 20°C. The resistance was measured (as explained previously for the 55P16) and found to be 5.3±0.2 Ω. Platinum-rhodium is selected due to its relatively high temperature coefficient of resistance, specified as being 0.16%/°C in the product data sheet. The prongs are made of a nickel-chromium alloy with an almost zero temperature coefficient of resistance, so that temperature variations at the prongs will cause minimal resistance changes and hence minimum contamination of the wire signal due to the prongs. The probe was attached to a 55H21 long, straight probe support with a cylindrical body of outer diameter and length of 4 and 235 mm respectively, ending in a Teflon^{TM}-coated cable with a BNC connector that was in turn connected the probe to the 56C00 CTA system.

The probe assembly is suitable for making measurements in ambient temperatures of up to 1020 K and sensor temperatures of up to 1070 K. Its useful velocity range is 0.05 – 350 m/s, with natural convection influencing the measurement up to 0.2 m/s. Unlike the ambient velocity measurements, the measurements here were

made at various overheat ratios from 1.05 to 1.40, with a corresponding wire over-temperature of c. 30 to 250°C. The response cut-off frequency was found to vary with the overheat between 5 and 10 kHz, increasing approximately 1 kHz per 0.05 increase in the overheat ratio. The variation in the cut-off frequency estimate over many square wave responses was within ±1 kHz. In all other respects, the equipment and methods used for this measurements are similar to those already presented in **Section 2.3.1: Constant Temperature Anemometry (CTA)** above.

2.3.3 Mixture Fraction Field

To simulate and understand the axisymmetric mixing field in the autoignition experiments, formed by the continuous, concentric injection of 'fuel' into the turbulent hot air co-flows in the CTHC or annular jets in the CTHAJ, Planar Laser-Induced Fluorescence (PLIF) experiments were performed at low temperatures (200°C) by seeding the fuel stream with a fluorescent tracer (acetone vapour). Measurements of the local volumetric (or molar) concentration of acetone were suitably normalized to obtain the mixture fraction (ξ) field from the source (i.e. the injector nozzle) to a downstream distance of 60 – 70 mm, or about $20M$. The two-dimensional scalar dissipation rate (χ_{2D}) was calculated from the sum of the axial and radial gradients squared of the measured two-dimensional, planar ξ.

Dynamically, the condition of the co-flow can be described by the turbulent Reynolds number, $\mathcal{R}e_{turb}$. The dynamic state of the injection stream at the inlet can be expressed in terms of $\mathcal{R}e_{turb}$ in conjunction with a non-dimensional normalized injection to co-flow density ratio, $\varpi_{fuel} = \frac{\rho_{fuel}}{\rho_{air}}$. In addition, it is possible to describe the kinematic condition at the inlet by the non-dimensional normalized injection to co-flow velocity ratio, $\upsilon_{fuel} = \frac{U_{fuel}}{U_{air}}$. The effect of changes to the inlet dynamic and kinematic conditions on the mixing field are investigated. An attempt will be made in this thesis to extrapolate these results to the autoignition experiment conditions.

In the mixing experiments an optically polished synthetic silica tube was used in place of the autoignition quartz tubes in order to alleviate optical non-uniformities. The tube had an inner diameter (D_{TUBE}) of 33.96 mm. As with the autoignition experiments, the upstream end was open to atmosphere and the pressure everywhere in the tube was ambient and the same upstream turbulence grid was used with $M = 3$ m. Both the 3 mm and small injectors were used. By using injectors with different d_{IN} and thus changing the mixing geometry, but also different kinematic conditions at the inlet, with υ_{fuel} from near unity to values close to 6, it was possible to simulate mixing patterns both akin to diffusion downstream of a low-momentum release from a point source and those traditionally associated with the strong shear layers inherent to jets. Furthermore, the effect of the turbulence character on the mixing field was investigated by varying the co-flow velocities U_{air} (and hence $\mathcal{R}e_{turb}$).

Equal density flows with acetylene injected into air were examined, with $\varpi_{fuel} = 0.95$ – $1.01(\approx 1.0)$, as was the more buoyant hydrogen into air case, with $\varpi_{fuel} = 0.36$ – $0.42(\approx 0.4)$. In both cases the measured quantity is the concentration of acetone in the flow. Given the effect of differential diffusion in the latter results, extrapolation to the autoignition experiments must be made with caution. The mixture fraction has been defined in this work as the normalized local volumetric concentration of the acetone with respect to its concentration at the inlet (injection):

$$\xi(r,z) \quad = \quad \frac{n_{fuel}(r,z)}{n_{fuel}(r=0,z=0)} \tag{2.19}$$

where n are volumetric concentrations, and, r is the radial and z the axial direction. The absolute difference between this volumetric-based $\xi(r,z)$ and the more correct mass-based $\xi_m(r,z)$ is less than 0.045 for acetylene and 0.090 for hydrogen, with these values indicative at $\xi = 0.5$ and the discrepancy decreasing at higher and lower values of ξ, obtained via the relation $\xi_m(r,z) = [1-(1-\xi^{-1}(r,z))\varpi_{fuel}^{-1}]^{-1}$.

Fluorophore seeding, including Acetaldehyde (an Aldehyde), Acetone, Bi-acetyl, 3-Pentanone (all Ketones) and Toluene (an Aromatic), PLIF for concentration measurements is a relatively popular technique and has been used in a variety of applications over the past decade [Frank et al., 1994, Long et al., 1993, Lonzano et al., 1993, 1992, Seitzman et al., 1994, Tait and Greenhalgh, 1992]. Generally, acetone has been more widely employed outside internal combustion engine chambers, which together with its lower molecular weight have made it the preferred tracer for this application. Initial controversy over the use of acetone emission as a fluorescent marker came from reports of temperature dependence of its emission characteristics in reacting flow environments [Frank et al., 1994, Tait and Greenhalgh, 1992], although others had used acetone successfully in these flows, such as Seitzman et al. [1994] in hydrogen–air flames. More recently, understanding of acetone fluorescence has been extended [Ghandhi and Felton, 1996, Thurber, 1999, Thurber et al., 1997, 1998] and detailed accounts of the photo-physics of laser-exited acetone fluorescence can be found in these references. Briefly, for a given laser wavelength and in isobaric, non-reacting flows with small temperature variations in the measurement domain, such as here, the fluorescence signal is only a function of the local laser energy and tracer concentration. This study assumes constant temperature and pressure throughout the mixing field and a negligible drop of laser power in the laser sheet (cross-stream) direction. These assumptions were tested and found to be reasonable.

Operation and Seeding:

Figure 2.11(a) shows a schematic of the apparatus with the laser sheet in position. The co-flow had velocities, U_{air} = 3 – 8 m/s. The fuels, hydrogen or acetylene, were diluted with nitrogen and flowed continuously through a 'bubbler'-type seeder containing liquid acetone before being injected through the injector into the co-flow at ambient pressure and with velocities, U_{fuel} = 3 – 27 m/s. As with the autoignition experiments, the air, hydrogen and acetylene mass flow rates

were measured directly with the AIR-MFC and FUEL-MFC, whereas the nitrogen flow rates were measured with suitable rotameters. The hydrogen or acetylene and nitrogen flows were mixed before passing through the seeder, as in **Figure 2.11(b)**.

The acetone seeder was completely immersed in a well-stirred, isothermal bath of hot water, whose temperature was set to between 60 and 80°C depending on the flow rate of the fuel. The boiling point of acetone is 55 – 56°C. This temperature was monitored with a thermometer and found to vary by less than 1 – 2°C during any one series of measurement conditions. The purpose for this practice was three-fold:

1. To maximize the fluorescence signal by enhancing the entrainment of acetone vapour into the diluted fuel,

2. To make certain that the fuel stream was saturated with acetone, and,

3. Together with an accurate setting of the fuel flow rates, to ensure a steady concentration of acetone in the fuel, while avoiding the problems of a drop in temperature as the acetone evaporated.

Note that, in the definition of ϖ_{fuel}, ρ_{fuel} is the density of the fuel, not taking into account the presence of the acetone. As the fuel stream is virtually saturated with acetone, the actual density of the injected mixture is approximately 1.2 times larger than the value of ρ_{fuel}. The method was checked in a few cases by measuring the amount of acetone left in the seeder as a function of time and calculating the flow rate of escaping acetone for fuel flow rates in the range used in the experiments. Both the mean volumetric and mass flow (measured with a scale of rated error ± 1 g) rates were found to be constant, with a worst case deviation of 5% when the flow rates were high. The resulting acetone volumetric content in the fuel stream was of the order of 20 – 25%.

In order to avoid problems with the acetone condensing inside the injector, or after injection in the flow field itself in the form of droplets, both the co-flow air

and the seeded fuel flows were slightly preheated to a temperature of 200°C before entering the main test section of **Figure 2.11(a)**. The choice of the preheat temperature was arrived at as a compromise between the need to eliminate temperature gradients in the entire measurement domain and that of avoiding the condensation of acetone. Preheating was achieved with the same electrical heaters and controlled by the same PID controllers as in the high temperature autoignition experiments. The inlet air temperature (T_{air}) and fuel injection temperature (T_{fuel}) were also measured in the same way and could be set with a drift of less than ±1 K for all conditions. Both T_{air} and T_{fuel} were continuously monitored during each experiment. At the low temperatures used here the random (indeterminate) error associated with these measurements does not exceed 1 K, while the systematic (determinate) uncertainty is ±1% at most. Heat transfer to the walls of the injector assisted in minimizing any temperature differences between the two streams at the inlet. It was found that T_{fuel} was no more than 12 K lower than T_{air} across the whole condition envelope. Further downstream the temperature was measured everywhere in the domain with a finer (0.076 mm diameter) K-type thermocouple and the maximum temperature deviation was found to be 4 –6 K near the walls of the quartz tube. Along the centreline, the temperature dropped 10 K by 60 mm downstream. Thus, it may be concluded that the temperature in the domain was uniform to within 12 K, and that consequently the fluorescence variations due to temperature are less than 4 – 5% based on a ≈0.36%/K decay for 266 nm [Thurber, 1999, Thurber et al., 1998].

Optical Measurement Arrangement:

The laser beam was taken directly from a Continuum Surelite II Nd:Yag solid state laser at the fourth harmonic (266 nm) and 10 Hz, kept at constant ambient conditions in an air-conditioned environment. This imaging frequency is at least an order of magnitude lower than the frequency corresponding to twice the longest integral timescale measured in separate hot wire experiments in the examined flows.

The Nd:Yag is rated at ±7% shot-by-shot energy stability for 99.9% of pulses and a power drift of ±8% on average after an 8-hour operation. In order to remove any residual second harmonic (532 nm) component from the laser beam, a Schott UG5 filter was placed before the quartz tube and a Schott WG305 cut-off filter was placed in front of the camera lens. The UG5 has an 83% transmittance at 266 nm and 3% at 532 nm. The WG305 has a transmittance of less than 0.001% at 266 nm, while for wavelengths above 350 nm it transmits 92% of the power. Aiming to improve the fluorescence signal levels across the domain, the beam height was set slightly higher than the mean height of the imaging window in order to take advantage of the fact that the acetone concentrations were on average higher closer to the injector. The beam was checked before the optics, at the exit of the Nd:Yag, and was found to be near-spherical in the far field with a correlation coefficient of linear least squares fit to a Gaussian spatial beam profile of 0.92. At that location the beam power was measured at approximately 110 mJ/pulse. At the measurement location it was checked again and found to be 80 mJ/pulse. The diameter of the beam was also measured and found to be 6.0 – 6.5 mm. A cylindrical lens of focal length 40 mm and a spherical lens of focal length 500 mm were used to form a thin sheet of height approximately 60 – 70 mm. The sheet $\frac{1}{e^2}$ waist thickness (t) at the focusing point, in the centreline of the flow geometry, was measured by translating a razor blade with a micrometer, [Ni et al., 1995], and found to be 0.10±0.03 mm.

The LaVision NanoStar Intensified Charge Coupled Device (ICCD) camera is described in detail in **Section 2.4.2**. Briefly, it is a 12-bit camera and has a maximum resolution of 1280x1024 pixels. The lens was a Nikkor AF 50 mm focal length and f/1.4 maximum aperture lens, used at a measurement aperture of f/2.8. A 13 mm auto extension tube was placed between the lens and the camera body in order to further increase its effective aperture and decrease the employed focal length range. This allowed an increase in aperture to f/3.5 and further magnification by a factor of 26%. The final useful imaging area (interrogation window) after cropping

was 1280x480 pixels and the spatial pixel resolution (p) was 0.050 – 0.055 mm/pixel (18 – 20 pixels/mm). This value was arrived at by taking the average of 20 images of a brightly illuminated scale placed at the measurement location and is associated with a worst case uncertainty of ±0.2%.

As discussed in Muss et al. [1994], Stårner and Bilger [1996], the actual resolution (r) of the optical system will also depend on the orientation of the scalar gradients relative to the laser sheet. For this reason and taking into account the combined effects of the pixel resolution of the collection optics, p, and the effectiveness of the sheet making optics, t, the ultimate ensemble resolution $\langle r \rangle$ was estimated at 0.09 mm on the basis of $\langle r \rangle = \frac{t}{2} + \pi\frac{p}{4}$. In another approach, [Muss et al., 1994, Tsurikov and Clemens, 2002], the imaging system performance is described in terms the Modulation Transfer Function (MTF) that expresses the resolution as an ability of transferring contrast information. Tsurikov and Clemens [2002] measured the MTF of their camera/lens (Nikkor AF 105 mm and f/2.8; used fully open) system from the object to the image plane and describe an ability of resolving 90% of the spatial information of scales down to $3p$. The same lens, focused at infinity, was tested at: 0, 3, 6, 9, 12, 15, 18 and 21 mm from the image centre (along the axis), in two different directions (sagital and tangential) and at 10, 20 and 40 lines/mm with Hasselblads Ealing MTF equipment. It was found to have a weighted MTF of 0.75 at an effective aperture of f/2.8. In identical tests with the Nikkor AF 50 mm, f/1.4D lens used here, similar results were obtained, with a weighted MTF of 0.75 at the same effective aperture (f/2.8). These tests and results thereof are well-documented and were taken directly from the "Photodo AB" online database on MTF measurements[‡]. The MTF of the complete optical arrangement used in this work, from object to saved image file, has been quantified, based on the methods described on the Imatest^{TM} website[§]. Both the 'Koren 2003' and 'Slanted Edge' test charts were

[‡]Refer to *http://www.photodo.com/index.html*.

[§]Found at *http://www.imatest.com/*. For further details and more examples of test charts for imaging systems one can also consult *http://www.normankoren.com/Tutorials/MTF.html*.

used. It was found that (**Figure 2.12**) depending on the location in the image, 4 to 6p were enough to resolve 70 – 80% of the spatial detail, improving from the corners towards the centre of the image. Thus, the effective resolution at the useful regions (away from the corners) of the image will not be worse than about 0.25 mm, at which scale about 70 – 80% of the spatial information will be retained by the imaging system. With a measured η_k in these flows in the range 0.2 – 0.3 mm, this translates into an ability of resolving down the smallest physical scale.

Before each measurement condition an averaged (from 20 images) 'background' image was taken with the laser sheet in place but without the tracer in order to remove reflections from the tube. Following the injection of seeded fuel some time was allowed for the conditions to reach equilibrium both in terms of the flow rates and temperatures. As soon as the value of T_{fuel} (which was the slowest to equilibrate) settled to within 2 – 3 K of its final value, the laser was used to trigger the LaVision NanoStar ICCD camera, which recorded the two-dimensional planar fluorescence signal in 200 images with exposure times of 0.4 μs. This exposure time is at least an order of magnitude shorter than the fastest timescale in the flow. For certain conditions 2 or 3 batches of 200 images were taken.

Image Processing:

The raw instantaneous images were first corrected for the background reflections from the tube, by image subtraction of the 'background' image. Following this, the beam profile signals were used to correct for the profile non-uniformity in the axial direction. At this stage the image corrections were complete, since the beam profiles were also a means of taking into account the shot-by-shot variation in the laser power. In the next step a suitable intensity level was sought in order to normalize each image and obtain the mixture fraction. In order to lessen the normalization error the image was not divided by the (single value) global, absolute maximum in the whole image due to the noise associated with each raw image and

hence the consequential error in the value of the maximum. Instead, the mean intensity over a window directly adjacent to the injector was used. The size of the window was not preset, but allowed to adaptively resize according to the requirement that the window would contain regions with intensity higher than 90% of the maximum intensity in the image. The size, mean and rms intensity of this window was tracked across all images in a run in order to inspect whether: (i) the laser power correction was effective, and, (ii) the flow rate of acetone was varying significantly across the images corresponding to any particular condition.

After the attainment of instantaneous, corrected mixture fraction images, each image was processed in order to remove noise. This is critical for the correct evaluation of the scalar dissipation because a small noise power in the mixture fraction will be greatly amplified when the scalar dissipation is calculated as the square of the mixture fraction gradients. Great emphasis was placed on the lengths to which it was 'allowable' to go in order remove 'erroneous' signal from images that was deemed 'noise'. Specifically, any denoising was required to be capable of using local knowledge from the image itself, reducing processing were it is locally not required. The purpose here is one of quantitative image restoration, with attention to correct recovery of the signal intensity, based on a physical understanding of the processes being imaged and the characteristics of the noise as incurred by the imaging system. Image processing was not performed by allowing for arbitrary thresholds or tuning parameters. An approach was taken by which the denoising was performed without loss of generality and that can be easily extended.

For each run (i.e. set of conditions) a single parameter was pre-estimated and used to shape the entire processing procedure. This basic component for processing will be referred to as the 'mixing window', and is a square characterized by the largest length at which processing was allowed. It is the two-dimensional image equivalent of the Nyquist frequency for one-dimensional time-series. As will be shown, the 'mixing window' is not the same for both the scalar and the dissipation.

In the current section and in **Appendix C** reference is made to the 'mixing window'. According to Batchelor [1952] the smallest scalar structure occurs at the Batchelor lengthscale, $L_B = \eta_k \mathcal{S}c^{-1/2}$, where η_k is the Kolmogorov lengthscale corresponding to the smallest velocity lengthscale and $\mathcal{S}c$ the Schmidt number. In addition, Su and Clemens [2003] use scaling arguments and two assumptions to conclude that, $L_D \sim \eta_k \mathcal{S}c^{-1/2}$, with L_D the typical thickness of the dissipation structures. The two assumptions were that: (i) to a first order approximation the strain-diffusion mechanism should differ between the momentum and scalar fields only in the diffusivities, and, (ii) this is completely accounted for by $\mathcal{S}c$. Nevertheless, in the absence of these assumptions, the typical scalar dissipation scale has been described more generally by $L_D \approx (\frac{\Lambda}{1.9})\eta_k \mathcal{S}c^{-1/2}$ for axisymmetric (including co-flowing) jets [Su, 1998]. In an attempt to probe the universality of Λ many studies have measured this parameter in various conditions and mixing flow geometries. Typical values can be found in the literature: 7.8 [Tsurikov and Clemens, 2002], 11.2 [Buch and Dahm, 1998] and 14.5 [Su, 1998, Su and Clemens, 2003]. It should be noted that the larger values of Su [1998], Su and Clemens [2003] were obtained for planar jets, as opposed to the axisymmetric flows of Buch and Dahm [1998], Tsurikov and Clemens [2002], perhaps revealing a lack of universality for Λ, as pointed out by Su and Clemens [2003]. Then, the smallest scalar lengthscale should be of the order of, or even slightly larger than, η_k, while the typical dissipation lengthscale should be in the range $4 - 8\eta_k$. Final evidence that a consensus can be reached comes from the cold wire measurements of Antonia and Mi [1993], where the authors suggest that a resolution of $3\eta_k$ is sufficient to capture L_D. In our case, the 'mixing window' was a square, with sides conservatively set to the smallest lengthscale, i.e. η_k, based on the Nyquist–Shannon sampling criterion. The value of η_k was obtained from the hot wire velocity measurements for similar conditions. Note that the actual imaging resolution was smaller than these scales. About 18 – 20 pixels per mm were used, or typically 4 – 6 pixels per η_k.

Based on the characteristics of the imaging system and the nature of the images themselves, the processing procedure was completed in three stages and involved first the removal of system specific noise and at a latter stage image processing both in the frequency and wavelet domains and are described in **Appendix C**. The image obtained after the Wiener frequency domain filtering had incurred little processing and is termed the 'first mixture fraction image', ξ_1. Finally, following BLS-GSM denoising in the wavelet domain, at the end of the image post-processing, one obtains the 'second mixture fraction image', ξ_2.

Data Analysis:

The instantaneous two-dimensional scalar dissipation rate, χ_{2D}, was evaluated as the sum of the squares of the axial and radial spatial gradients (by second-order central finite differences) of ξ, with a constant of proportionality equal to $2\mathcal{D}$:

$$\chi_{2D} = 2\mathcal{D}\Big[\Big(\frac{\partial\xi}{\partial r}\Big)^2 + \Big(\frac{\partial\xi}{\partial z}\Big)^2\Big] \tag{2.20}$$

where $\mathcal{D}$ is the molecular diffusion coefficient of acetone into the multi-component air/fuel mixtures, calculated analytically for each run and at each point in the flow following Poling et al. [2001], with typical values in the range 2.3 – 3.3x10^{-5} m^2/s. Both the axial and radial components of χ_{2D} were kept throughout the processing in order to evaluate their respective contributions to χ_{2D}.

In general, the recovery of the full three-dimensional scalar dissipation rate, χ_{3D}, requires assumptions on the magnitude of the azimuthal gradient ($\frac{\partial\xi}{\partial\theta}$). However, along the centreline and on average, by symmetry, the azimuthal gradient must be equal to the radial one:

$$\langle\xi_{3D}\rangle = 2\mathcal{D}\Big[2\Big\langle\Big(\frac{\partial\xi}{\partial r}\Big)^2\Big\rangle + \Big\langle\Big(\frac{\partial\xi}{\partial z}\Big)^2\Big\rangle\Big] \tag{2.21}$$

Furthermore, it will also be shown that, along the centreline and on average, the axial ($\frac{\partial \xi}{\partial z}$) and radial ($\frac{\partial \xi}{\partial r}$) scalar gradients become approximately equal after a certain distance from the injector defined as L_{iso}. Here, it can be argued that the mixing field becomes asymptotically isotropic. For axial distances $z > L_{iso}$ along the centreline it can be said that $\langle \chi_{3D}(r = 0, z) \rangle$ can be approximated as being $\frac{3}{2}$ times the value of $\langle \chi_{2D}(r = 0, z) \rangle$. Also, for $z > L_{iso}$, the predictions from $\langle \chi_{2D} \rangle + 2\mathcal{D}(\frac{\partial \xi}{\partial r})^2$ and $\frac{3}{2}\langle \chi_{2D} \rangle$ match by definition. The extent of L_{iso} after which it is possible to write $\langle \chi_{3D} \rangle = \frac{3}{2}\langle \chi_{2D} \rangle$ is investigated. A radial extension of these arguments, by which the possibility of approximating $\langle \chi_{3D} \rangle = \frac{3}{2}\langle \chi_{2D} \rangle$ everywhere downstream of $z = L_{iso}$ and not only along the centreline (i.e. for all r) is also attempted.

To evaluate the effect of processing the instantaneous gradient was taken of both first and second versions of the mixture fraction, resulting in first and second versions of scalar dissipation χ_1 and χ_2, correspondingly. At a final stage and from the aforementioned results of Antonia and Mi [1993], Buch and Dahm [1998], Su [1998], Su and Clemens [2003], Tsurikov and Clemens [2002], all the instantaneous χ_2 images were further processed based on a wider 'mixing window', supported by the expectation of L_D being larger than η_k by at least a factor of 4 resulting in χ_3; effectively a filtered version of χ_2, 'cut-off' at a 'frequency' of $4\eta_k$.

The average and variance fields of ξ, $\langle \xi \rangle$ and $\langle \xi'^2 \rangle$, were compiled by calculating the first and second central moments at each point over all images for each run. This operation was performed both on all the ξ_1 and ξ_2 images. Likewise, for χ_1, χ_2 and χ_3 the mean and variance fields, $\langle \chi \rangle$ and $\langle \chi'^2 \rangle$, were obtained. In addition, for each condition, the axial and radial extent of the mean $\langle \xi \rangle = 0.1$ iso-contour was selected arbitrarily to define a certain extent of the plume, within which the intensity of the images was 'high'. Inside the region defined by this extent, point statistical descriptions of the local mixing were compiled over all images through the following variables: $\langle \chi|\xi \rangle$ and $\langle \chi''^2|\xi \rangle$, where the double prime $\chi''^2|\xi$ implies fluctuations around the conditional mean, $\langle \chi|\xi \rangle$, and, the probability density functions

(pdfs): pdf(ξ), pdf(χ) and pdf($\chi|\xi$). These results are presented in **Section 3.4**. As mentioned before, for most conditions the global statistics ($\langle\xi\rangle$, $\langle\chi\rangle$, $\langle\xi'^2\rangle$ and $\langle\chi'^2\rangle$) were complied from 200 images. For the point conditional ($\langle\chi|\xi\rangle$ and $\langle\chi''^2|\xi\rangle$) and all pdf statistics, square boxes of 1 and $2\eta_k$ length sides were defined on each image at particular locations. The 'point' statistical quantities at any location were then calculated over all images, but also for all points inside the box. Care was taken not to perform calculations in regions where the fluorescence signal was low (i.e. at locations of low ξ), while the conditional pdfs, pdf($\chi|\xi$), were only evaluated at windows of ξ containing at least 500 data points.

2.4 Autoignition Measurement Methodology

This section deals with the process of realizing and quantifying autoignition. It begins with an account of the methods used for preparation of the burners and subsequent achievement of the phenomenon. The types of autoignition measurement are classified into optical and acoustic. Optical measurements include global chemiluminescence time-series taken with a Photo-Multiplier Tube (PMT), global spectrometer measurements and two-dimensional imaging. In the sections that follow all equipment used for all types of autoignition measurements reported in this thesis are presented, as are all experimental methods with the exception of the two-dimensional optical techniques that are presented in **Section 4.4**.

2.4.1 Achieving Autoignition in a Duct

With no fuel flow, approximately 1 to 2 hours of heat-up time were allowed for the apparatus to reach the high temperatures necessary for autoignition. During this time and with the mass flow of air fixed to about $20 - 25\text{x}10^{-3}$ kg/s, the controller for T_{air} was set to progressively higher reference settings. Even through the temperature

was kept constant by active control, changes to the reference temperature where always done manually in a series of stages. The manual inputs were ramps of up to 50°C (decreasing to 2 – 3°C at higher temperatures and in between experiments) over a period of a up to 10 seconds after which the system was allowed time (minutes) to reach steady state. When the temperature of the apparatus reached about 500°C, a small amount of nitrogen was allowed to flow through the injector to keep it cooler. This flow was kept as the process of increasing T_{air} was resumed.

When the air temperature thermocouple indicated that T_{air} had reached the desired temperatures the heating up process was complete. Continued operation, lasting usually 1 hour, was allowed at this stage to bring the whole apparatus to thermal equilibrium, after which the apparatus would be deemed ready for autoignition measurements. Fuel flow would be allowed and the nitrogen flow rates adjusted in order to get the desired diluted fuel composition. With continuous injection of the correct diluted fuel autoignition would be detected in the tube. However, autoignition was allowed to continue for 1 – 2 minutes before any measurement was taken to ensure transients and drifts had been minimized. At this point T_{air}, T_{fuel} and the flow rates of the air, fuel and dilution nitrogen were recorded.

2.4.2 Optical Autoignition Measurements

The optical measurements can be classified into: global chemiluminescence time-series taken with a PMT, spectrometer measurements and two-dimensional imaging. The latter category includes images taken with a Charge Coupled Device (CCD) and an Intensified Charge Coupled Device (ICCD) camera, and, fast sequences taken with a Complementary Metal Oxide Semiconductor (CMOS) camera. The equipment and methods used for these measurements are described below.

Photo-Multiplier Tube:

Qualitative Photo-Multiplier Tube (PMT) data will be first encountered in **Chapter 4**, whereas quantitative results are presented in **Chapter 5**. The PMT was a Hamamatsu 28 mm (effective diameter is 25 mm) Head-on Type R374 model tube. The data sheets give a 185 – 850 nm spectral response, peaking at 420 nm with a cathode radiant sensitivity of 64 mA/W. The gain of the PMT is $5.3x10^5$ and it has a rated rise time of 15 ns. The full PMT assembly consisted of the following Hamamatsu components: the PMT itself, a 28 mm C7246 Head-on DA-Type Socket Assembly including integral voltage-divider and amplification circuitry and a C4900 Series High Voltage Power Supply Unit. The C7246 assembly is recommended for use with the R374 tube. The data sheet shows a bandwidth of 30 kHz and up to 10x amplification with an output voltage noise rms of 0.09 mV. The PMT measurements were made by connecting the output of the assembly directly to the same DAQ system used with the hot wires and fine thermocouples. The gain of the PMT amplifier was used to adjust the voltage so that it utilized the 0 – 10 V range of the DAQ card. Sampling of this measurement was done at 100 kHz and in some cases simultaneously with the microphone signal (see **Section 2.4.4**).

All PMT measurements were made with an 307±10 nm OH^* filter in place. The PMT was placed far enough (about 0.85 m relative to the focusing optics) from the apparatus so as to have the whole autoigniting volume in its field of view as demonstrated in **Figure 2.13**. In this way, any OH^* chemiluminescence from the three-dimensional space inside the quartz tube could be detected. Furthermore, this ensured that the signal intensity was insensitive to the location of the autoigniting region within the tube and mostly determined by the intensity of the emitted chemiluminescence at that region. The maximum error associated with the assumption that the voltage measurement from the PMT was solely proportional to the chemiluminescence intensity from autoignition, while neglecting the spatial location of this emission was 6%.

Spectroscopy System:

Spectral chemiluminescence measurements were made for all fuels and are presented in **Chapter 4**. Lower resolution (0.53 nm) measurements were made with a Princeton Instruments spectroscopy system borrowed from the EPSRC Engineering Instrument Pool (EIP). The Princeton Instruments system included an Intensified Charge Coupled Device (ICCD) camera, a PG-200 pulse generator, an ST-138 controller, a 320 PI spectrometer, an f/4 aperture optical fibre for making the measurements and a dedicated PC. The 320 PI spectrometer obtains light through a slit. The light is collected by collimating mirrors, strikes the grating and is then dispersed into individual wavelengths. The light is re-imaged in the ICCD camera, which is coupled to the exit port of the spectrometer. An optical fibre was connected to the opening slit of the spectrometer to allow more flexible positioning of the system. The camera was a spectroscopy kinetics ICCD with 1024x256 chip resolution, sensitive in the range 300 – 1000 nm. It is designed for fast spectroscopy and is suitable for low level emission measurements. Data acquisition to the PC is 16-bit.

Charge Coupled Device Camera:

CCD images can be found in **Chapters 4** and **6**. A Sony DCR-PC120E CCD Digital Video Camera Recorder was used with the hydrocarbon fuels and when the UV-sensitive CMOS and ICCD were not available. It was used with no automatic settings; focusing, exposure and white balance were all set manually. The DCR-PC120E is a 1.55 MPixel CCD and is equipped with an 4.2 – 42 mm focal length, f/1.8 – f/2.2 aperture Carl Zeiss Vario-Sonnar lens. During the recording of movies, such as here, a large number of 352x288 images are saved to a magnetic mini-DV tape in analogue format. Shutter speeds in the range 1/4 to 1/4000 in 24 steps, or exposure times of 0.25 to 250 ms, were possible with a mechanical shutter. The

CCD is only sensitive in the visible and near-IR from about 400 to 700 nm and so the use of this system was only possible in that case of the hydrocarbon fuels, as these gave illumination in the visible spectrum. In a few cases, images where taken with an additional CH^* filter placed in front of the lens.

After recording, the image sequences were downloaded to the PC hard disk with commercial software (MGI VideoWave). Chiao [2000] plots the RGB spectral response of a similar CCD chip from the same manufacturer with the components being: 'Red' (550 – 700 nm), 'Green' (475 – 600 nm) and 'Blue' (400 – 500 nm). After downloading the raw images to the PC, only the 'blue' intensity component was considered for calculations, so that all calculations based on CCD images presented in this thesis are actually based on light presence in the range 400 – 500 nm, which is largely from emissions of the CH^* radical, to a lesser extent C_2^* and not affected greatly by soot (see emission spectra of **Chapter 3**). The original raw images were kept and where CCD images are shown in this thesis they are with all three colour components.

Intensified Charge Coupled Device Camera:

As with the CCD images of autoignition phenomena, images taken with this camera can be found both in **Chapters 4** and **6**. A Nikkor UV-lens and two filters have been used in this work during autoignition measurements with the ICCD. The lens has a nominal focal length of 105 mm and maximum aperture of f/4.5. Mostly the lens was operated fully-open to capture the weak chemiluminescence signals. It is designed for the 190 – 1300 nm wavelength range. The filters were: a Melles Griot UG11 with 79% transmittance at 328 nm, falling to 76% at 310 nm (and <0.2% at 250 and 390 nm), and, an 'OH^*' filter supplied by LaVision with the camera, band-centred at 307±10 nm. For some measurements no filter was used. These images are referred to as 'UV-to-IR broadband', or 'broad' images.

The LaVision NanoStar Intensified Charge Coupled Device (ICCD) camera is a 12-bit camera (i.e. up to 4096 counts), with maximum resolution 1280x1024 pixels and pixel size 6.7 μm, or 14.5 μm effective size due to a 2.17:1 lens coupling. It has a built-in 25 mm Hamamatsu intensifier unit with a single Micro-Channel Plate (MCP) stage, S20 photocathode and P46 phosphor screen. All controllers are built into the camera head. The shutter can be operated (gated) down to 5 ns and framing rates vary from 8 Hz upwards as the number of pixels in the image is decreased, either by binning or by defining specific regions of interest (RoI). Readout takes places at a rate of up to 30 frames/s. With the intensifier the camera is sensitive down to single photons, with a maximum sensitivity of 90 counts per photon when the single-MCP is operating at its maximum luminous gain of $3x10^4$. Its spectral response ranges from the UV to near-IR and more specifically between 190 – 900 nm. Peak cathode sensitivity is ≈50 mA/W at 440 nm, dropping to 30 mA/W around 310 nm. Quantum efficiency is maximum (at 15%) around 440 nm. The CCD had a mean dark image intensity of 98 counts, but this was always removed by background subtraction before any measurement. These values are documented in the camera operation manual. The rms of the dark image after background subtraction was measured and found to be 2.0±0.3 counts (out of 2^{12}). The measured signal (in counts from 30 to about 3000) was calibrated before delivery and found to correlated as a power law with the input light signal to the camera with an exponent (known as 'Gamma') of 0.997 and little deviation from this linear behaviour up to 2000 counts. This camera was *always* used with much lower counts than 2^{11} and so the assumption of linear response is justified. It was controlled by commercial software (DaVis) supplied and installed by the manufacturer.

Complementary Metal Oxide Semiconductor Camera:

A custom high-speed, UV-sensitive intensified camera system has been assembled in-house from a separately purchased camera and intensifier, specifically for

the autoignition experiments (**Figure 2.14**). Detailed calculations concerning the performance of this system and relating to the coupling between the CMOS chip and intensifier were undertaken by the author.

Image sequences showing the process of the emergence of autoignition and of unsteady, post-ignition flame propagation from the autoignition sites were taken with this system and will be shown in **Chapters 4** and **5**, where these concepts will be introduced. The 512x512 pixel Phantom v.4.2 is a 10-bit CMOS camera that can take images at up to 100 kHz, with an on-chip shuttering capability of down to 0.01 ms. The CMOS sensor is only sensitive to visible and infra-red light in the range 350 – 1000 nm. The monochrome version of the v.4.2 was chosen due to its superior sensitivity (4800 ISO/ASA). The relative high sensitivity of the CMOS is assisted by a large 22 μm pixel size. Its peak response, both in terms of sensitivity (220 mA/W) and quantum efficiency (above 40%) is around 670 nm. The spectral sensitivity is broad, being above 150 mA/W in the range 520 – 720 nm. This is important for the spectral coupling with the intensifier screen (see next paragraph). As with most CMOS cameras the image size is linked to the potential framing rate. So, in order to achieve 90 kHz rates the image size must be reduced to 32x32. Up to 2.1 kHz rates are possible with the full 512x512 sensor array. In this work, up to 12 kHz frame rates were used with image sizes typically 500x100. Background subtraction was performed prior to all measurements.

In the UV and up to 30 kHz, images were made possible with a recent model C9546-04MP46 Hamamatsu intensifier, with a new-generation S20 Multialkali Photocathode, 18 mm Two-MCP Stages and P46 Phosphor Screen. This intensifier unit can be gated down to 3 ns. Light enters the intensifier through the photocathode, setting up an electrical charge that is amplified through the MCP stages before it hits the fluorescent screen. When connecting the CMOS camera to the intensifier the imaging sensor is coupled via relay optics to the phosphor screen. New-generation multialkali (S20) photocathodes have a spectral response from 190 to 900 nm, with a

maximum radiant sensitivity of ≈60 mA/W at 420 nm and ≈50 mA/W at 310 nm. Quantum efficiency is ∼15 – 20% in the range 200 – 420 nm. Two-MCP stage intensifiers have luminous gains of up to 8x10^6. A disadvantage of two-stage MCPs is a reduced (by a factor of 2) MTF relative to the single-stage models, but in this work imaging speed was more important than precise reproduction of spacial characteristics. The P46 screen can decay to 10% from a negative step in 0.2 – 0.4 μs. It has a peak emission at 530 nm falling to 10% at 670 nm. The complete system is of the order of at least 100 times more sensitive, in terms of radiant emittance gain, than an ICCD using a single MCP stage. The intensified camera system has been used with and without the same OH^* filters that were used with the ICCD. No processing was done to the CMOS images that are shown in this thesis. The camera was controlled by dedicated commercial software (Phantom).

2.4.3 Autoignition Delay Time Calculation

Let L_{IGN} be a general measure of the axial length from the injector to the location of autoignition. Mean residence times until the point of autoignition, based on any definition of L_{IGN} (see **Section 4.4.3**), could have been defined simply as $\frac{L_{IGN}}{U_{air}}$. However, this does not take into account the velocity of the diluted-fuel jet (or wake), which can be a factor of up to 5 times higher than U_{air}. In addition, there is an extended possibility of autoignition at relatively close distances to the injector nozzle, in which case the momentum of the jet cannot be ignored. An improved attempt at a suitable definition of a mean residence time can be made based on a mean velocity $\widehat{U}$ as in $\tau_{IGN} = \frac{L_{IGN}}{\widehat{U}}$, where L_{IGN} can be any measure of autoignition length. With $U(z)$ the mean centreline velocity in the jet:

$$\tau_{IGN} = \frac{L_{IGN}}{\widehat{U}} = \int_0^{L_{IGN}} \frac{dz}{U(z)} \tag{2.22}$$

For jets in turbulent co-flows with comparable velocities, the normalized axial centreline velocity can be described by:

$$\begin{aligned} \frac{U(z) - U_{air}}{U_{fuel} - U_{air}} &= \mathcal{F}\Big(\frac{z}{d_{eff}}\Big) \\ d_{eff} &= d_{IN}\sqrt{\frac{\rho_{fuel}}{\rho_{air}}} \end{aligned} \tag{2.23}$$

The functional relation $\mathcal{F}(\frac{z}{d_{eff}})$ was obtained by a fit to the data of Sakai et al. [2001]. It was checked in a limited number of cases, with pitot tube (in the case of a hydrogen jet at ambient temperature and a nitrogen jet at hot conditions) and hot wire measurements (in the case of an air jet at ambient conditions). **Figure 2.15** shows the normalized decay of the centreline velocity with axial distance from the injector in number of inner injector nozzle diameters, d_{IN}, as predicted by **Equation 2.23** for jets a various densities issuing into a co-flow of air and comparison with measurements. Good agreement was found. In the estimation of τ_{IGN} from L_{IGN} the densities of both streams were calculated from their known composition and the measured T_{air} and T_{fuel}.

'Equal velocity' experiments will be defined in **Section 6** as ones with $\frac{U_{fuel}}{U_{air}} = 1.0 \pm 0.2$. The difference between $\tau_{IGN} = \frac{L_{IGN}}{U_{air}}$ and τ_{IGN} from **Equation 2.22** for the lightest and heaviest fuels is shown in **Figure 2.16**. For these two fuels the difference between the diluted fuel jet momentum and the momentum of the air in the co-flow is the greatest. For the data points that are shown, properties of actual diluted fuel mixtures and conditions from the experiments have been used. L_{IGN} was allowed to span the full range of experiments and all measures of autoignition length for each fuel. The error is small, less than $\pm 15\%$ and so for 'equal velocity' calculations, τ_{IGN} was calculated directly from $\tau_{IGN} = \frac{L_{IGN}}{U_{air}}$.

2.4.4 Acoustic Autoignition Investigations

Two Brüel & Kjær (B&K) microphones and a dedicated B&K Type 2807 two-channel microphone power supply were employed, but only one microphone was used for the actual acoustic pressure measurements during the autoignition experiments. The second was only used to calibrate the autoignition microphone. The B&K microphone assemblies consisted of 1/4" Type 2633 preamplifiers and 1/4" Type 4135, free-field acoustic transducers. The 4135s are recommended by B&K for general, high-level, high-frequency measurements. Their sensitivities to ambient temperature and pressure are -0.01 dB/°C and -0.007 dB/kPa respectively. Since changes to ambient conditions were not corrected for, a possible 0.1 dB error can be expected. The 2807 power supply data sheet specifies a 2 – 200 kHz frequency range, an inherent noise of $<15\mu$V (an output voltage range of 0 – 5 V was used), a cross-talk between the two channels of less than -80 dB up to 20 kHz and -60 dB up to 200 kHz.

The autoignition microphone was placed at the end of an $L_{probe} = 0.5$ m stainless steel cooling probe tube that was in turn positioned at the inlet of the quartz tube (**Figure 2.13**). There were no obstacles between the tube's inlet and the flow. At the end of the cooling probe a long (25 m) close-ended tube was placed in order to approximate the acoustic semi-infinite boundary condition there. The signal was taken from the microphone to the power supply, after which it was amplified, hardware low-pass (Butterworth) filtered and recorded by the DAQ system in the same way as with the hot wires, fine thermocouples and PMT. A pistonphone was used to measure the pressure sensitivity of the microphone. A value of 3.556±0.001 mV.Pa^{-1} was obtained, 1% lower than the factory calibrated value. This quantity was used for the conversion of the voltage measurements to a pressure.

2.5 Methods Chapter Figures

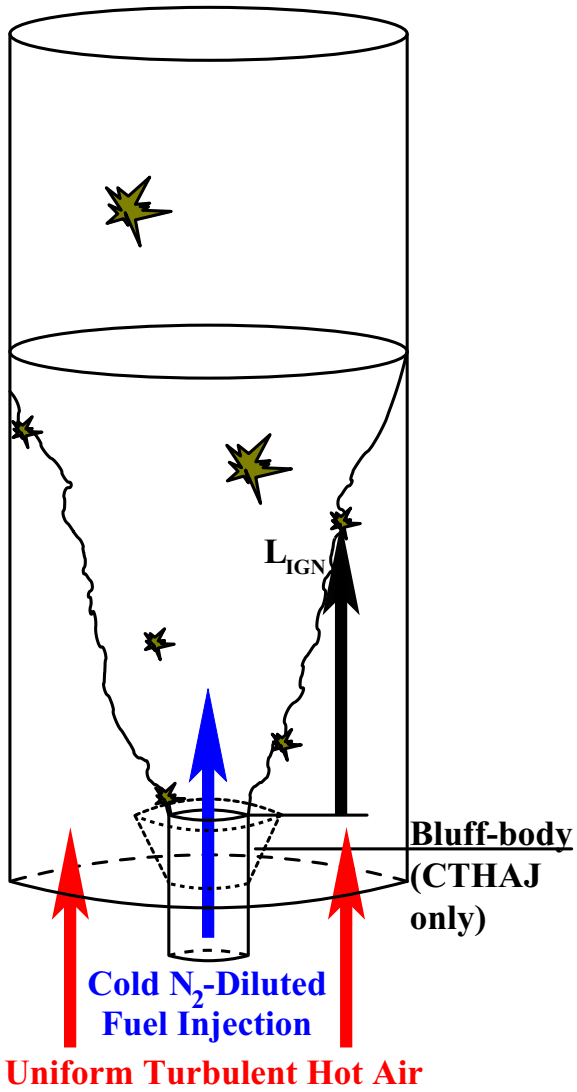

Figure 2.1: Experiment concept. Showing possible autoignition events and definition of instantaneous autoignition length L_{IGN}.

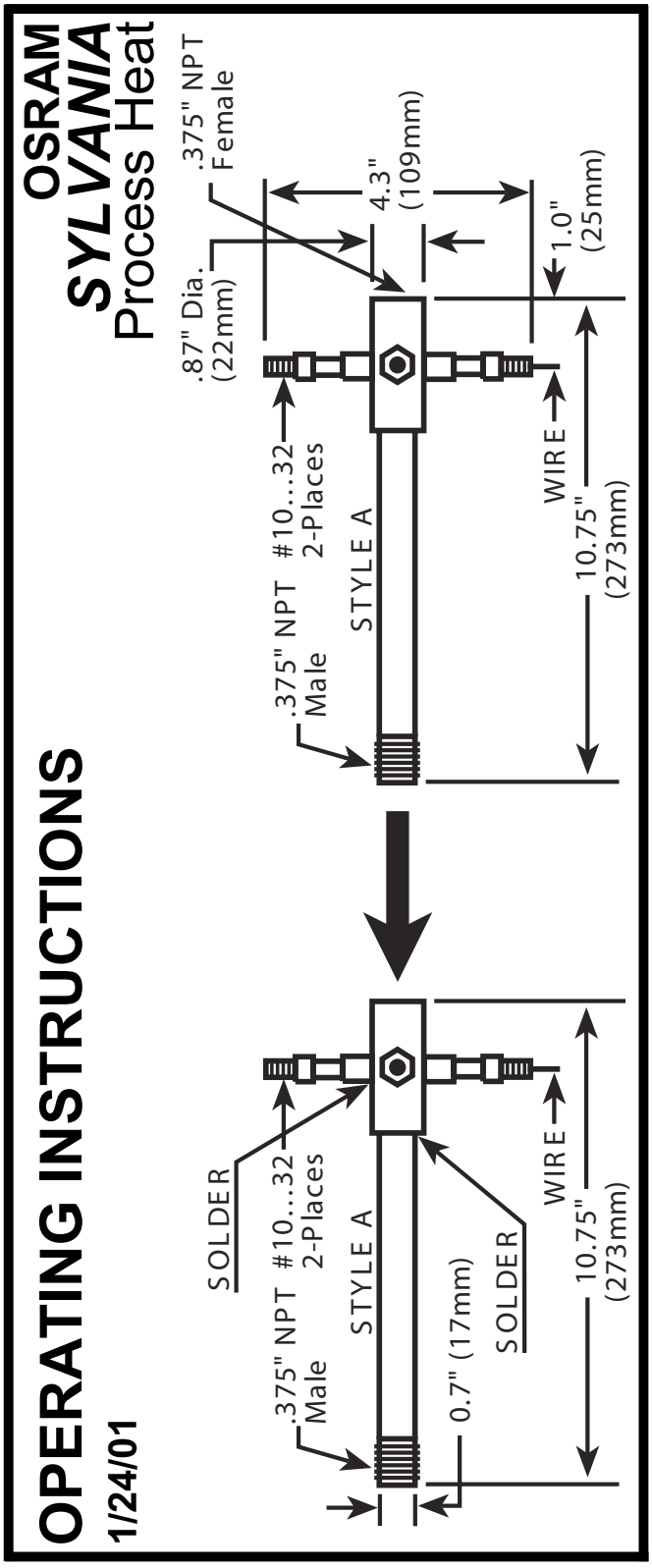

Figure 2.2: Original Osram Sylvania inline heaters. Manufacturer's specifications downloaded from *http://www.sylvania.com/BusinessProducts/MaterialsandComponents/AirHeaters.*

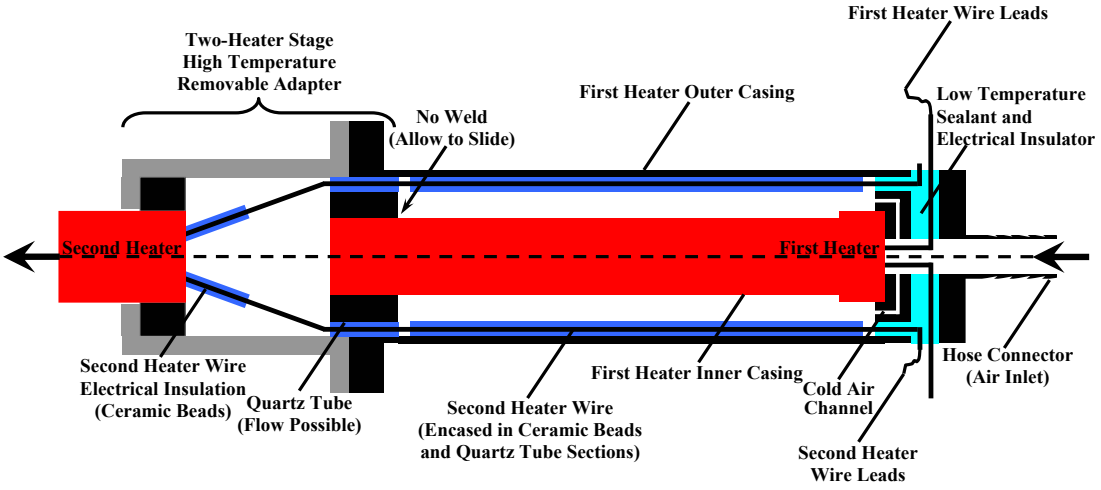

(a)

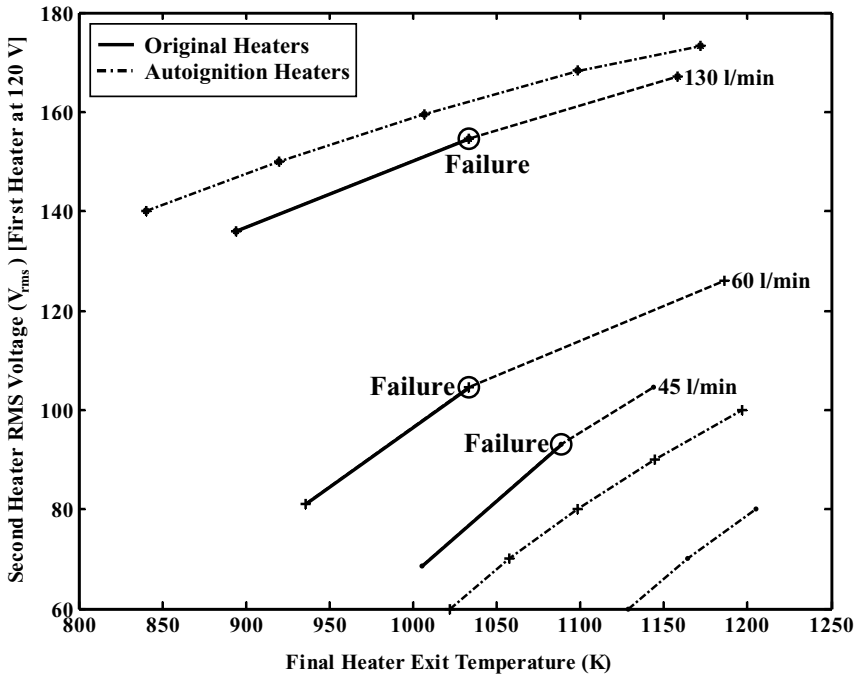

(b)

Figure 2.3: Revised autoignition heater design: drawing and performance. (a) Simplified annotated drawing of new heaters designed and manufactured for the autoignition experiments. To scale but no dimensions shown. (b) Performance chart and comparison with original commercial heaters. Showing voltage of the second heater necessary to achieve a certain final temperature of air exiting the second heater, with the rms voltage of the first heater fixed at 120 V_{rms} for various flow rates. Dashed lines indicating manufacturer's specifications not achieved in reality due to premature burn-out failure.

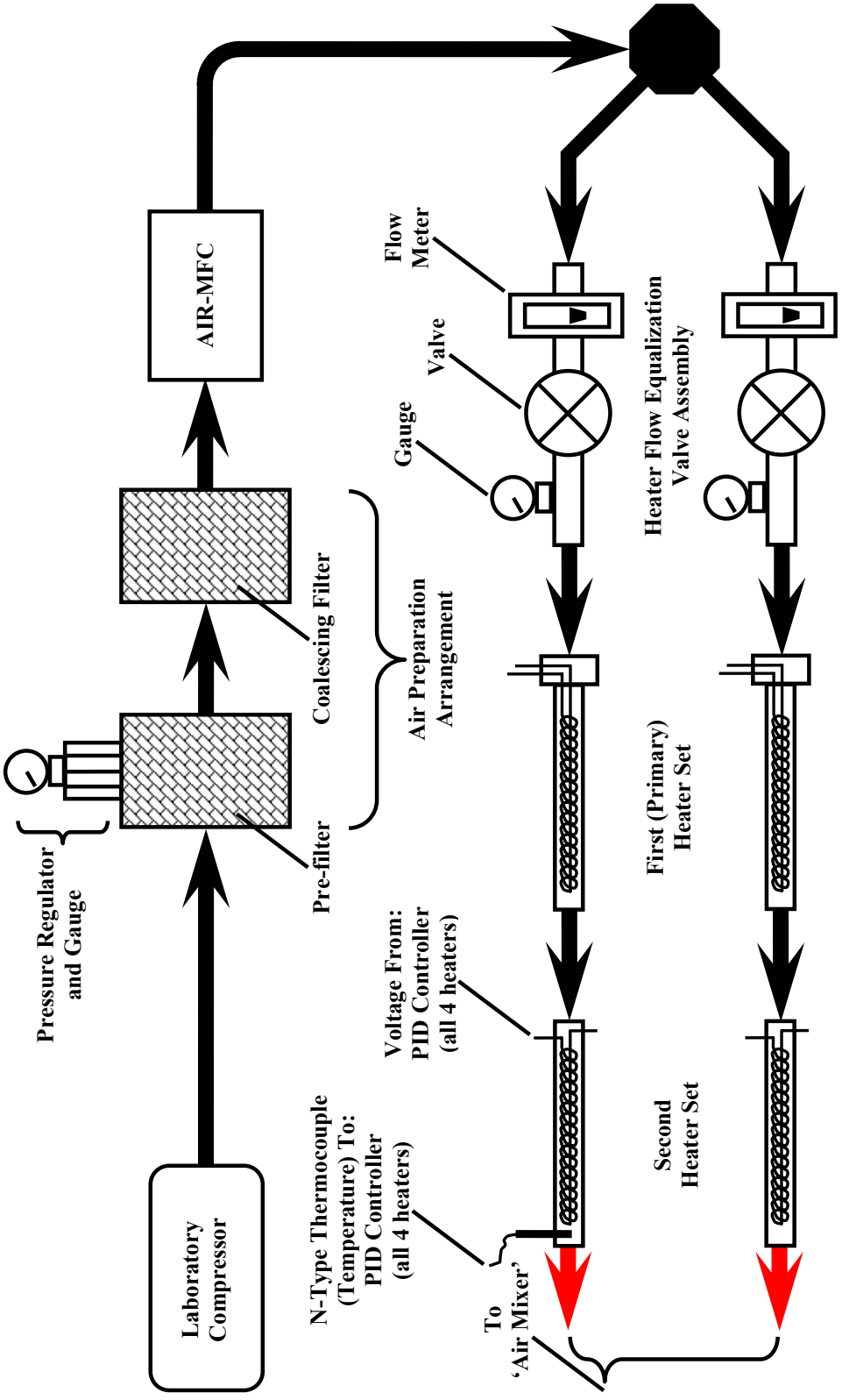

Figure 2.4: Apparatus schematic: Air preparation and heating (from compressor to 'air mixer').

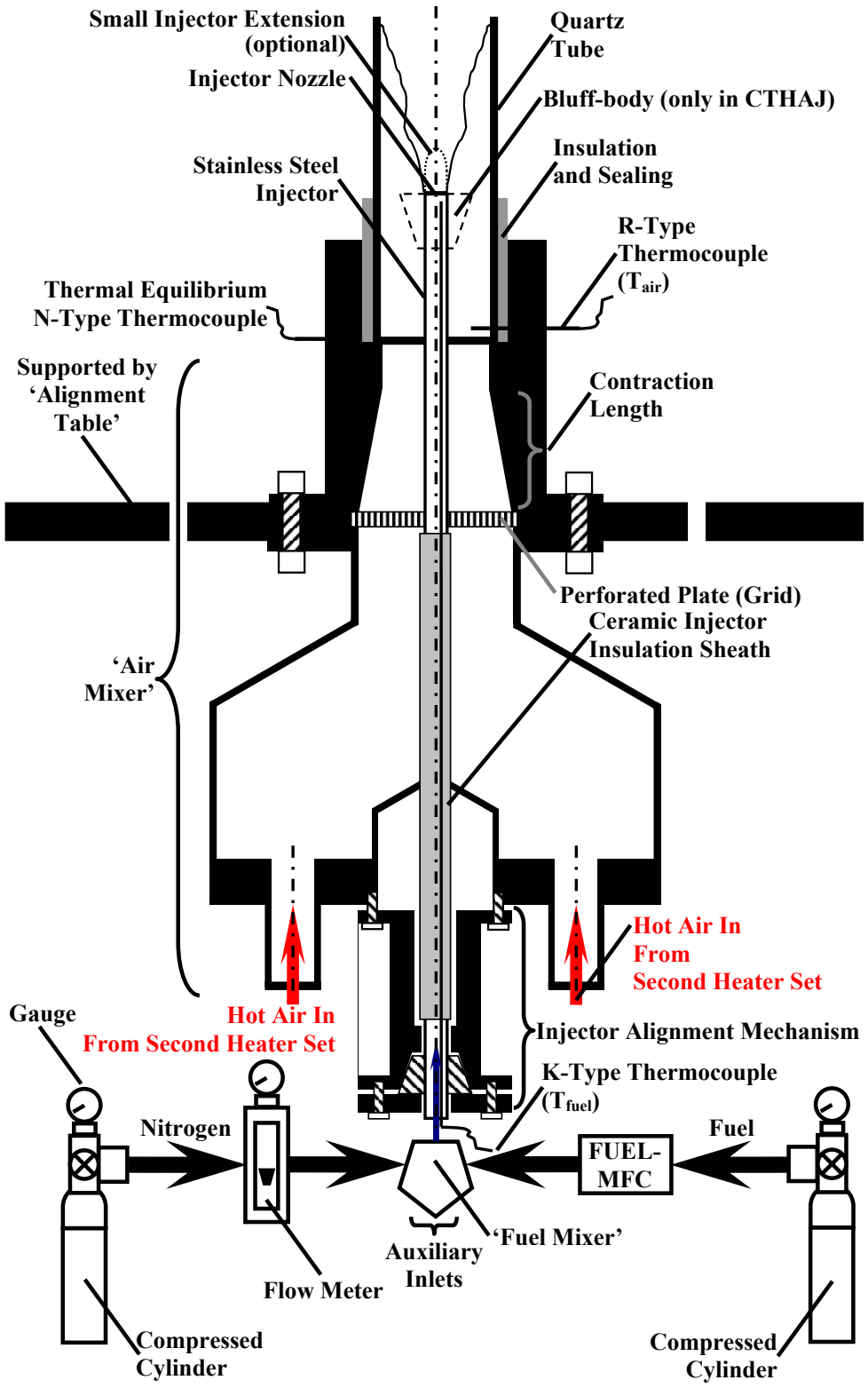

Figure 2.5: Apparatus schematic: Main apparatus (from 'air mixer' to quartz tube).

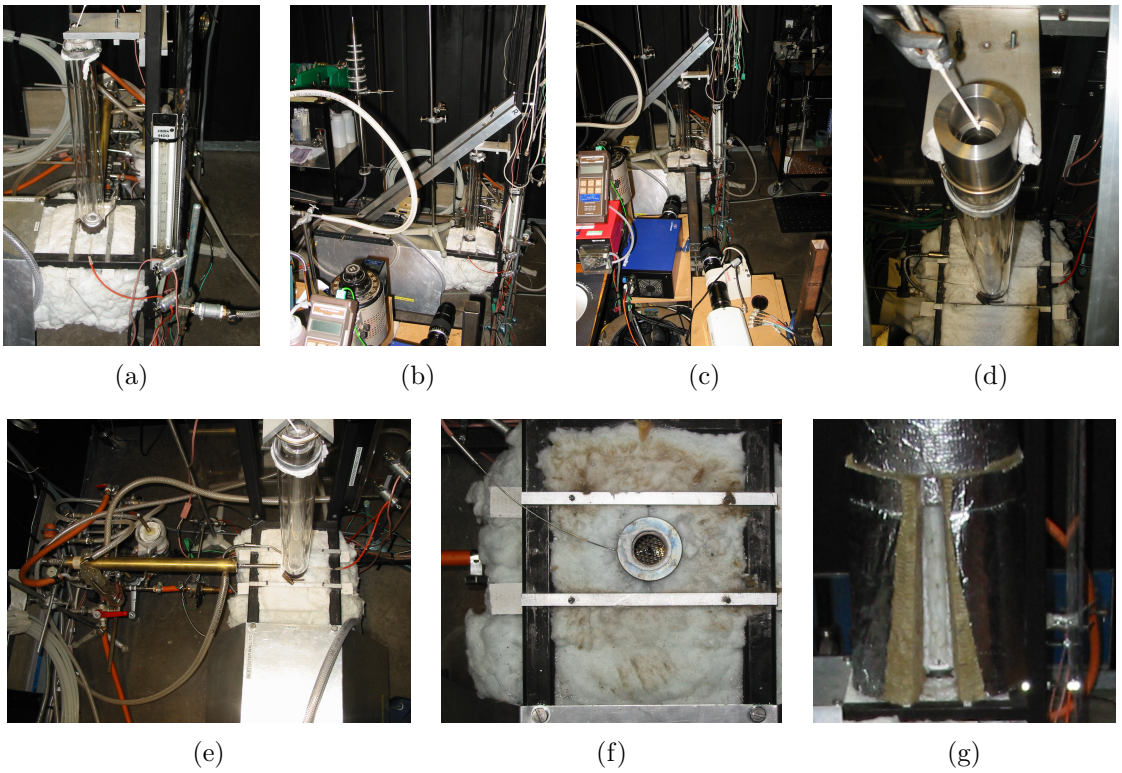

Figure 2.6: Photographs of the basic configuration for the Confined Turbulent Hot Co-flow (CTHC) burner. (a), (b), (c) Side-, and, (d) Front-views of the CTHC. Showing the vertical, 24.8 mm inner diameter 'jacketed' quartz tube. Flow direction upwards. The orange R-type thermocouple extension wire indicates the placement of the thermocouple for T_{air}. The 3 mm injector is positioned in the centreline of the tube at the upstream end (near the thermocouple). Also showing the black square section 'alignment table' and custom V-clamp for positioning and aligning the tube to vertical. Heavy insulation can be seen hiding the second stage heaters, 'air mixer' and 'injector alignment mechanism' below the tube. Tube exit thermocouple also visible. (e) Front-view of the same configuration. Showing in addition, the orange fuel supply lines on the left and liquid fuel brass vaporizer (last component attached to the short length of fuel line and going into the insulating blanket). Finally, the long brass microphone cooling probe used to make quantitative pressure measurements can be seen above the vaporizer. Various other components and equipment can be seen in all images, including for example thermocouples at tube inlet and cameras, but these are not critical to the design. (f) Top-view close-up with tube removed. Thermal equilibrium N-type thermocouple entering the 'air mixer' from left of image. Fuel line is connected to the (hidden) 'injector alignment mechanism' and disappears into the insulating blanket, again at the left of the image. Injector and grid are visible from this angle. (g) 'Blanket-insulated' tube as used in the CTHC with the 3 mm injector seen clearly in the centreline, at the height of the 'alignment table'. Insulation thickness shown here is around 0.15 m.

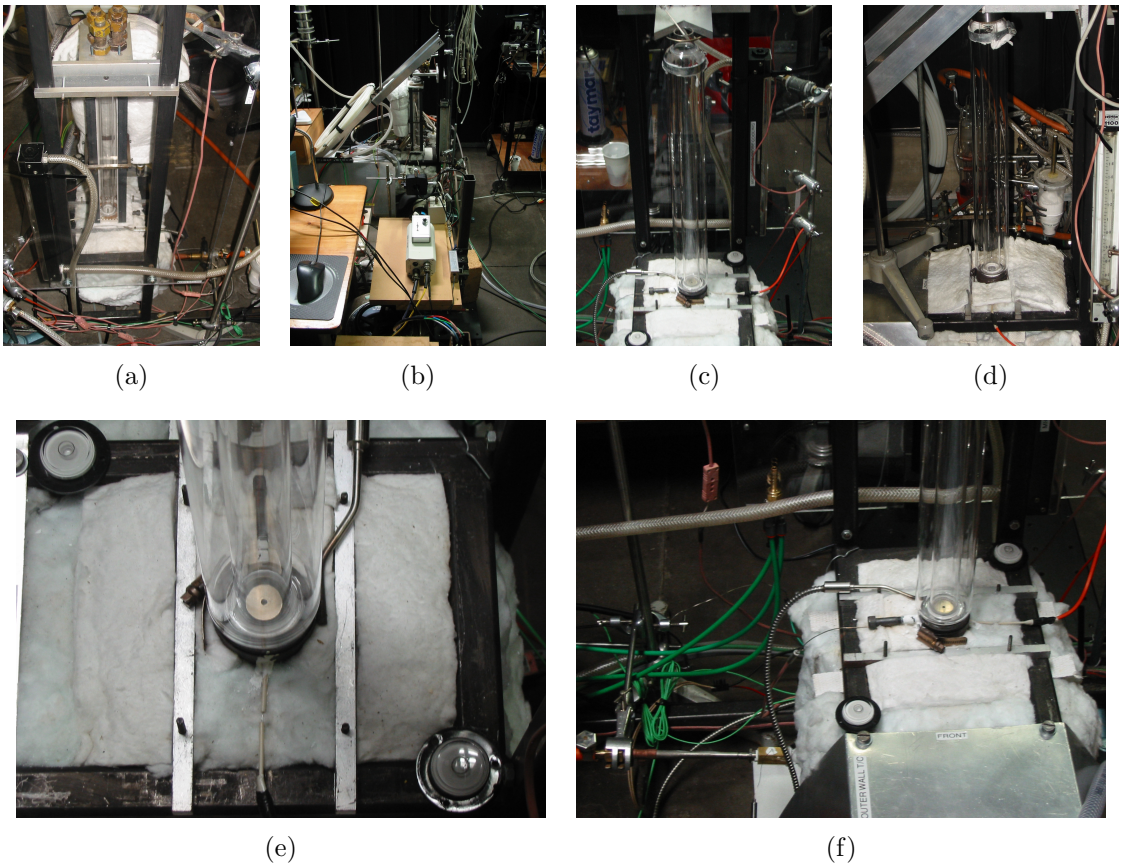

Figure 2.7: Photographs of modifications to the basic configuration. Includes the heat exchanger addition to the CTHC layout, fuel heater and Confined Turbulent Hot Annular Jet (CTHAJ) burner. (a) Back-, and, (b) Side-views of the heat exchanger placed over the 24.8 mm inner diameter 'jacketed' quartz tube in the CTHC. The vertical blankets hide the twin heaters of the heat exchanger. (c) Large (D_{BLUFF} = 17.8 mm), and, (d) Small (D_{BLUFF} = 10.0 mm) bluff-bodies in position over the 3 mm injector at the upstream end, inside the 'jacketed' tube. This is the CTHAJ configuration. (e) Close-up image of small (D_{BLUFF} = 10.0 mm) bluff-body in CTHAJ. (f) Showing in addition, on the left, the fuel heater (last component going into the insulating blanket in place of the vaporizer of **Figure 2.6(e)**). The K-type thermocouple inserted at the end of the fuel heater provides the T_{fuel} measurement. The long brass microphone cooling probe used for the quantitative acoustic measurements and seen in **Figure 2.6(e)** has been removed and replaced by a large Allen screw. Thermal equilibrium N-type thermocouple entering the 'air mixer' close to this point.

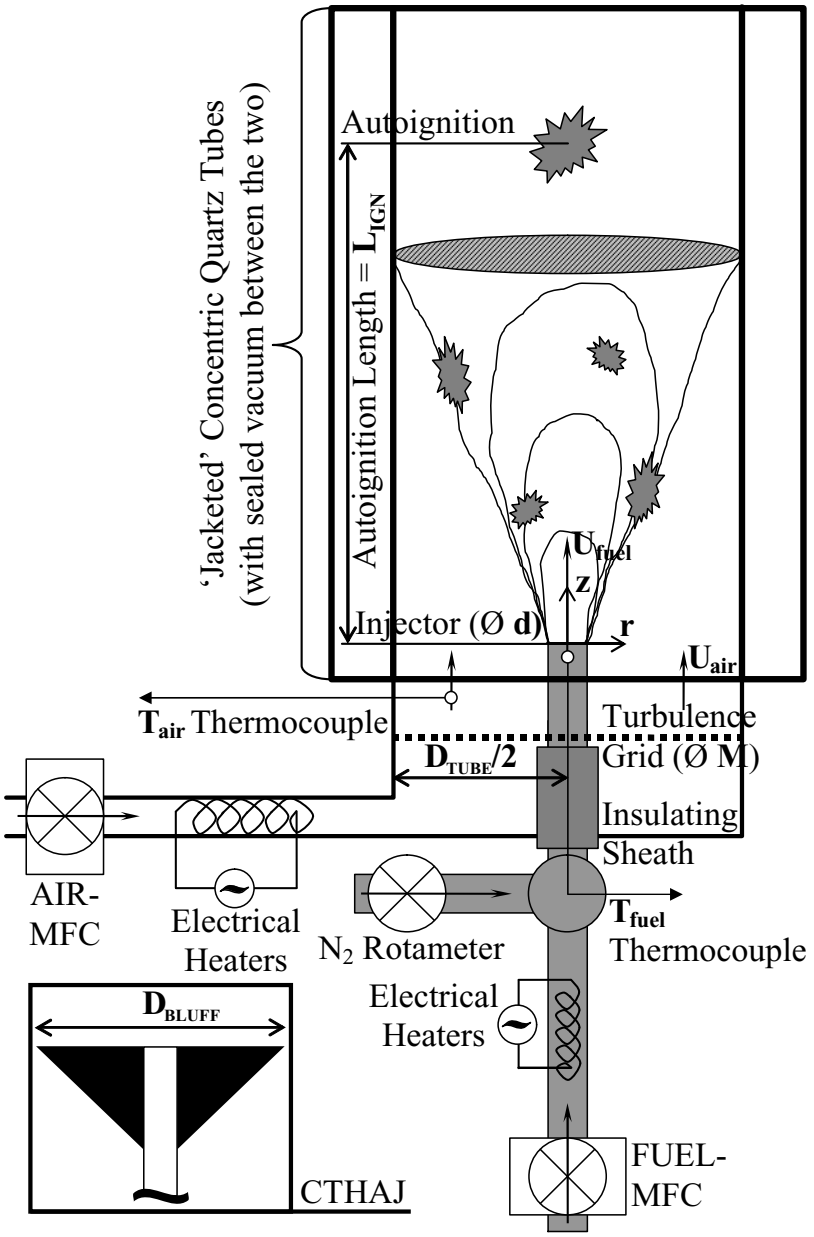

Figure 2.8: Concise apparatus schematic with dimensions and measured variables. Important geometrical and measurement variables including: the quartz tube diameter (D_{TUBE}), injector diameter (d), grid hole diameter (M), air and fuel injection temperatures (T_{air} and T_{fuel}) and air and fuel velocities (U_{air} and U_{fuel}) are shown in **bold**. Shown here is the tube radius R_{TUBE}.

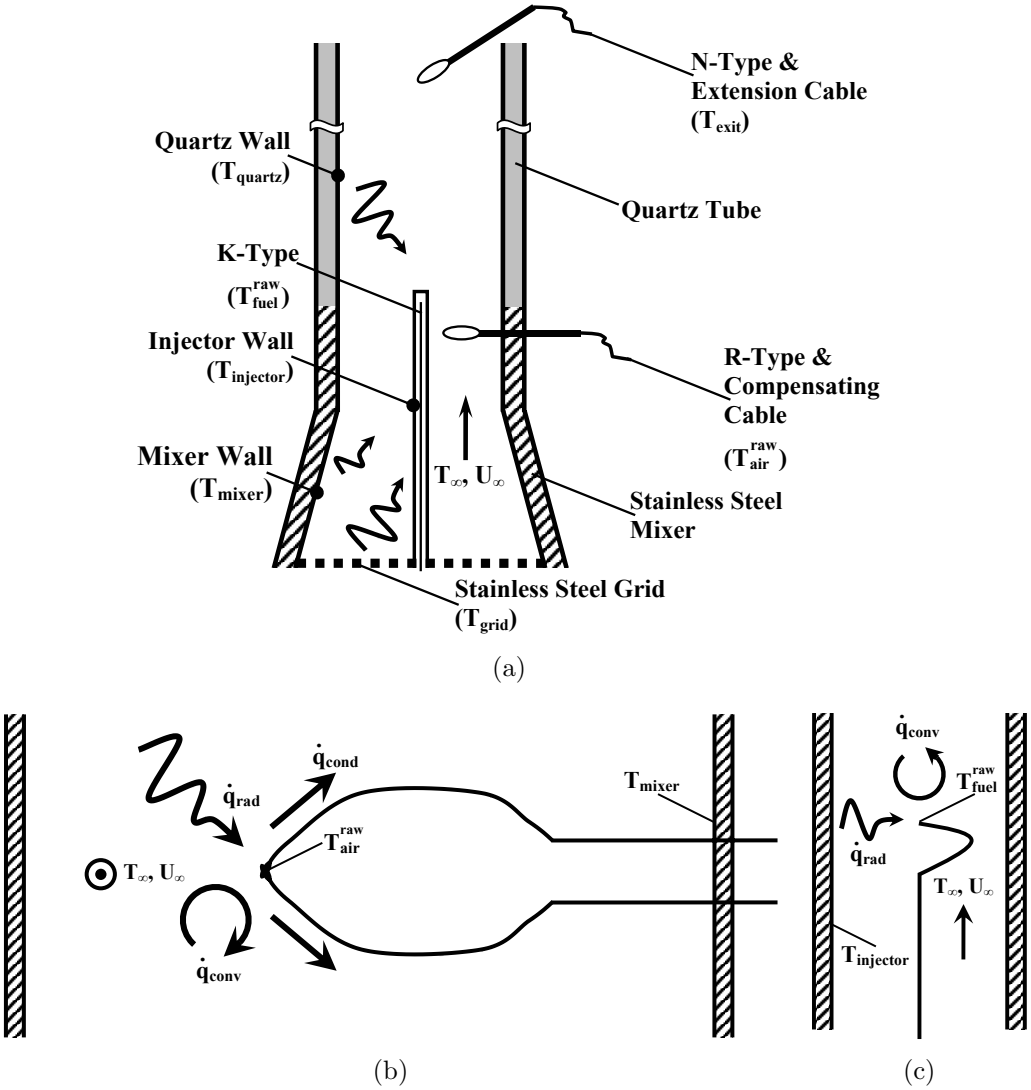

Figure 2.9: Thermocouple correction diagrams. (a) Side-view of the grid, mixer and quartz tube section of the burner. Idealized model of solid surfaces for radiative and conductive (air only) heat loss thermocouple corrections. (b) Top-view of the air thermocouple, embedded in the mixer wall. Heat transfer balance for the air thermocouple. (c) Side-view of the fuel thermocouple inside the injector. Heat transfer balance for the fuel thermocouple.

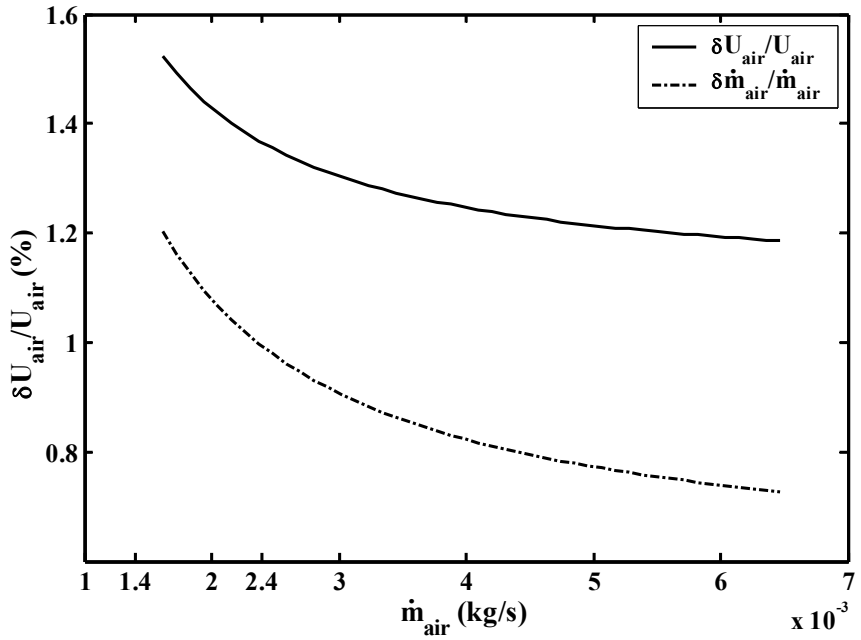

Figure 2.10: Errors in the calculation of the air velocity as a function of the AIR-MFC setting.

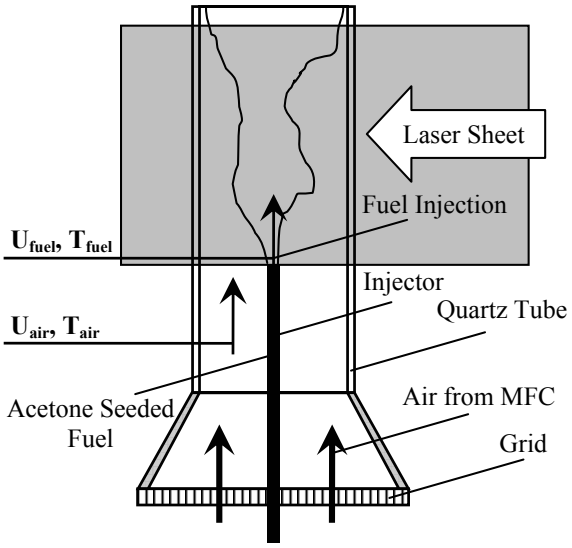

(a)

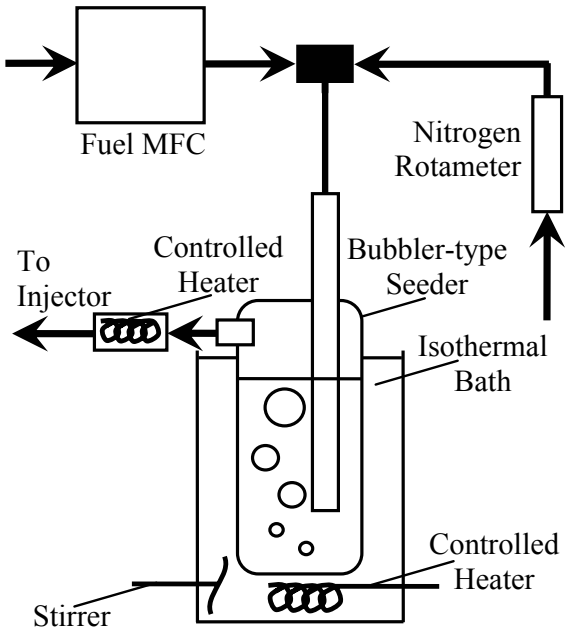

(b)

Figure 2.11: Laser sheet diagram and seeding apparatus for mixing experiments.

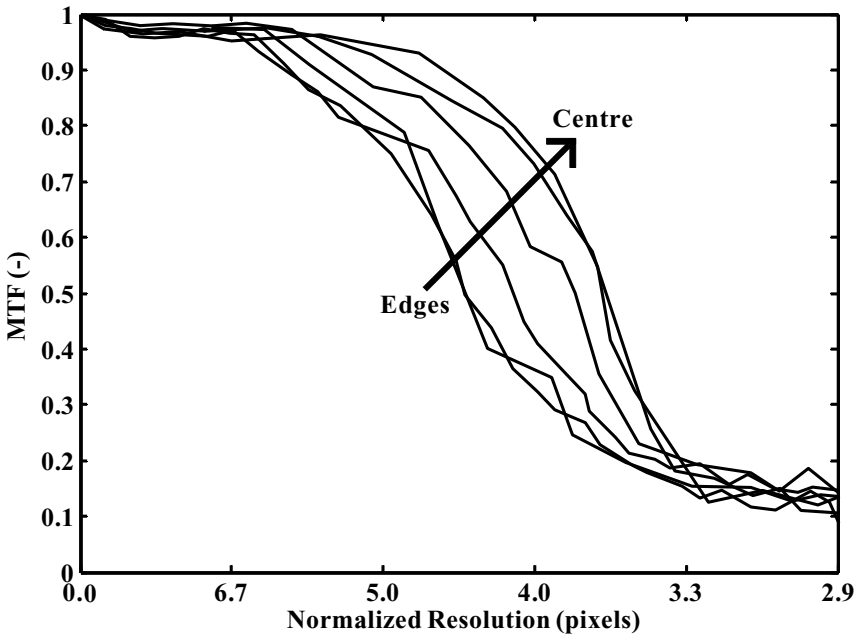

Figure 2.12: MTF spatial resolution determination of complete imaging system used for acetone PLIF measurements. MTF curves shown here are taken from results of 'slanted edge' tests of Imatest^{TM}. Showing variation of ability to resolve contrast information from the edges towards the centre of the frame for both sagital and tangential directions.

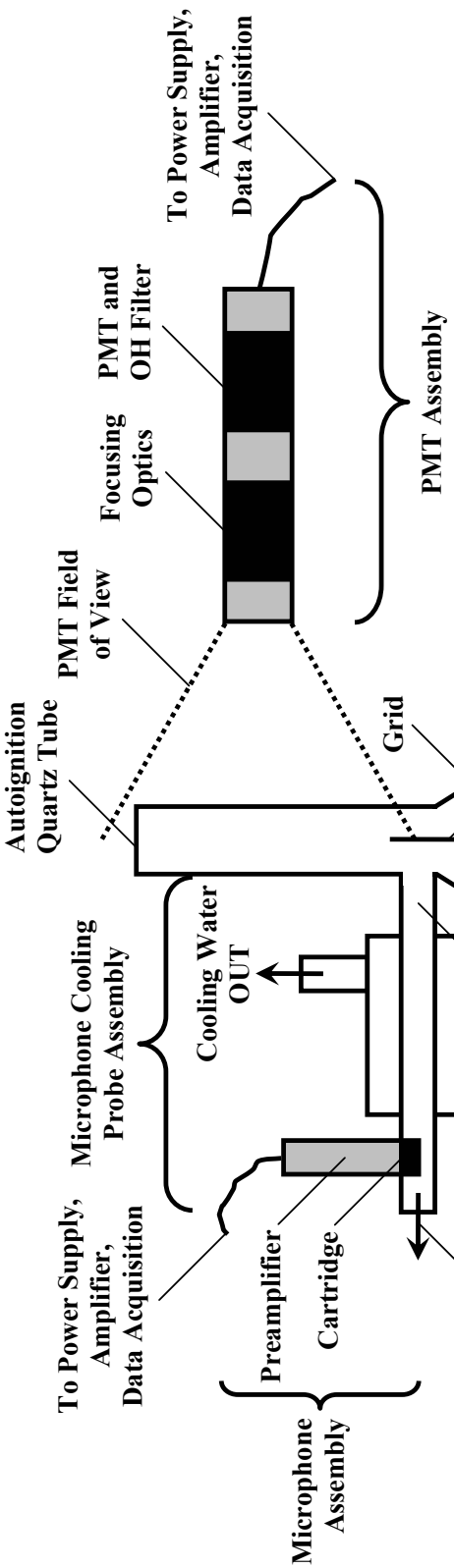

Figure 2.13: PMT and microphone measurement set-up.

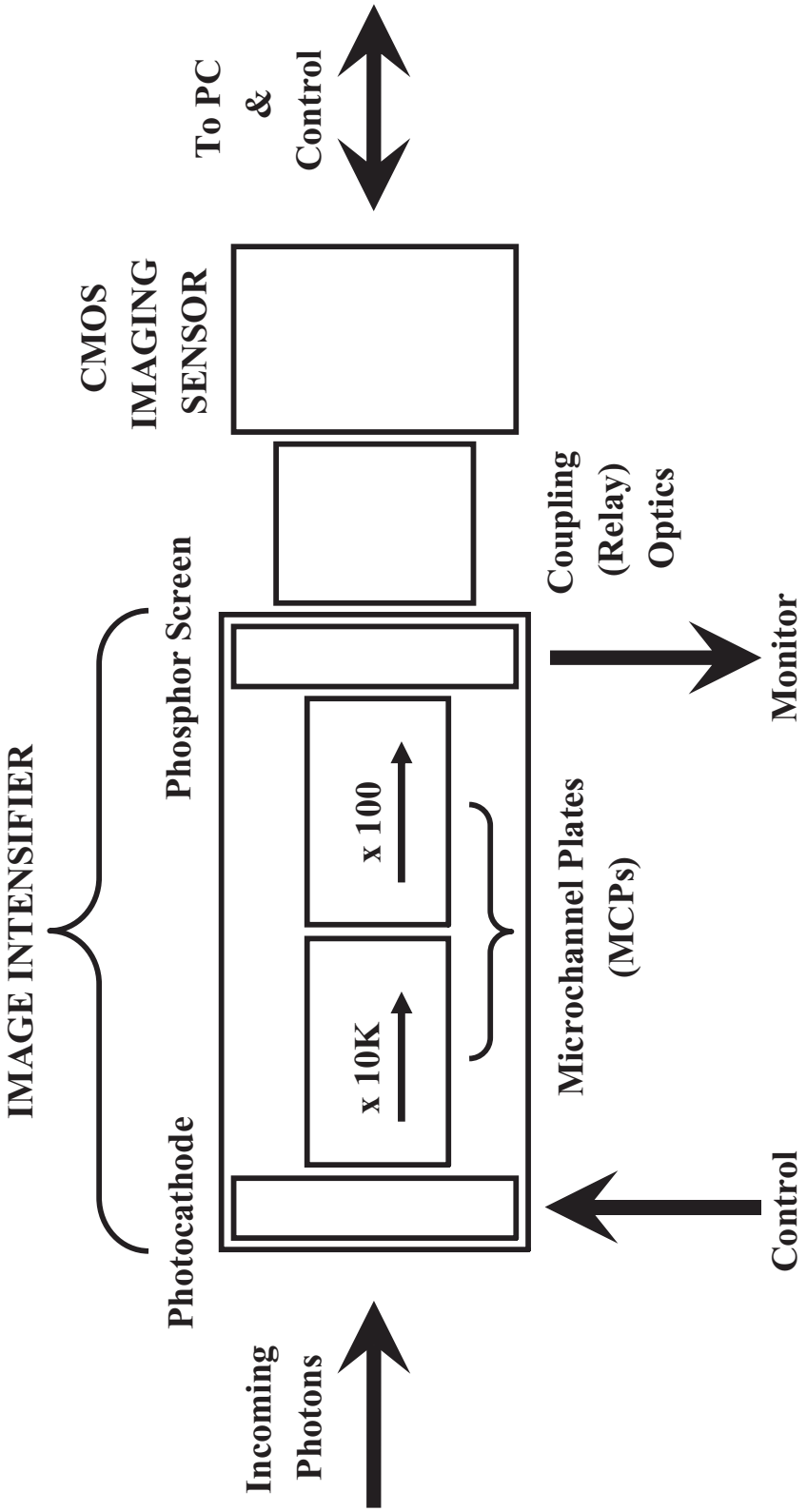

Figure 2.14: Design of a custom, digital high-speed imaging system with extended sensitivity in the UV.

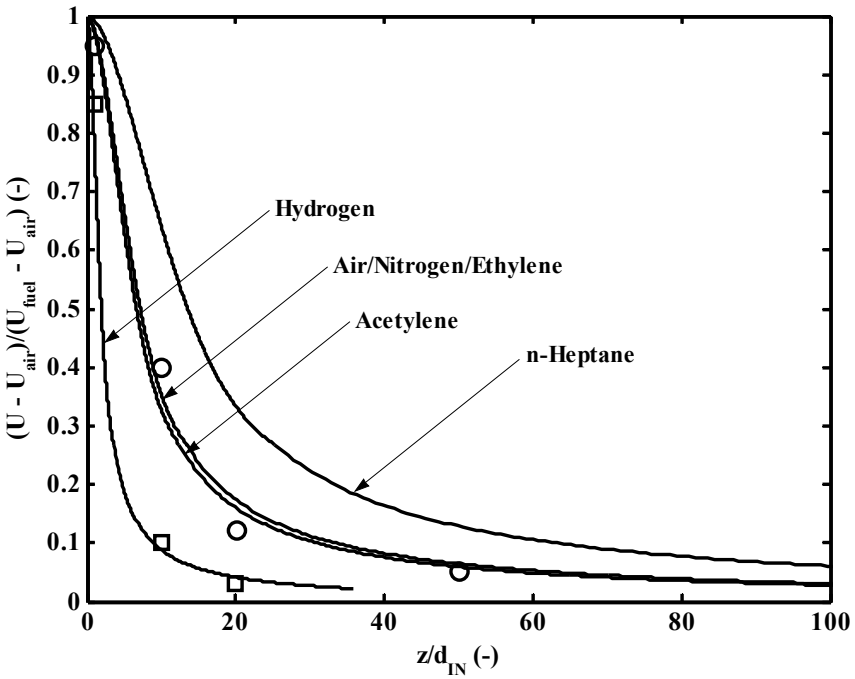

Figure 2.15: Prediction and measurement of jet in co-flow centreline velocity decay. Computed results from **Equation 2.23** and measurements for all fuels at cold conditions. Plots show normalized centreline velocity 'excess' from co-flow velocity, $U(z) - U_{air}$.

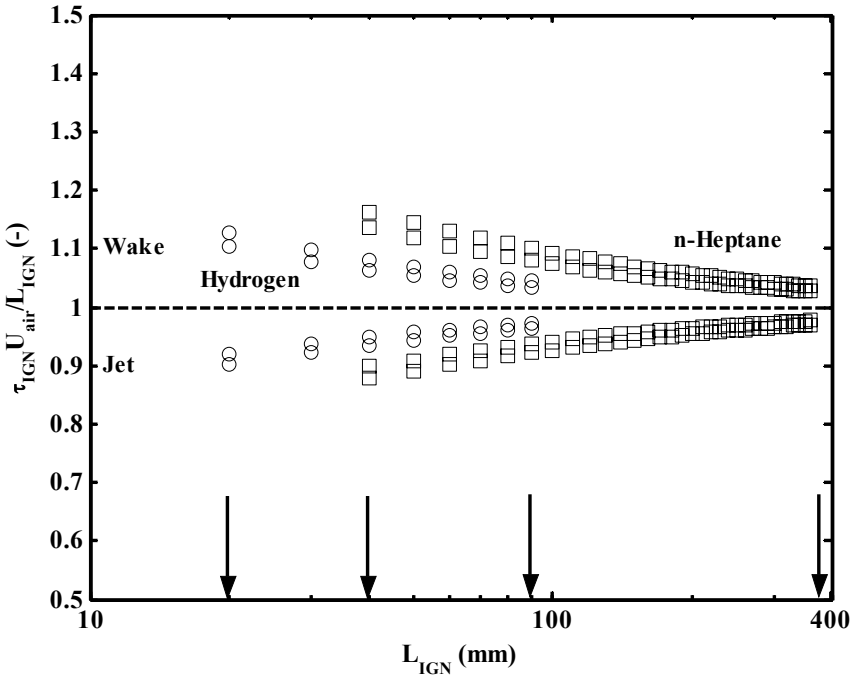

Figure 2.16: Effect of neglecting the diluted fuel jet momentum for 'equal velocity' experiments. Showing extreme cases: diluted hydrogen and n-heptane. Arrows denote minimum (at 20 and 40 mm) and maximum (at 90 and 380 mm) L_{IGN} for the two cases.

Chapter 3

Flow and Mixing Characterization

3.1 Characterization Chapter Objectives

In this chapter the conditions inside the tube are related to the inlet variables with the help of cold and hot flow characterization measurements. During a variety of experiments described collectively by the lack of autoignition, the complete conditions in the tube were measured together with the inlet variables. Where cold flow measurements were performed an attempt was made to better replicate the autoignition conditions by asserting dynamic similarity at the inlet. Thus, conditions were set so that $\mathcal{R}e$ was equal between the cold and hot flows. Results from these measurements for the velocity, temperature and mixture fraction (and scalar dissipation rate) can be found in **Sections 3.2**, **3.3** and **3.4** respectively.

Hence, the reported inlet conditions (**Section 2.2.5**) that will be used throughout the thesis, can be related to the conditions inside the tube during autoignition based on this information. The current chapter then, supplements the description of the apparatus in terms of accumulated knowledge concerning the velocity, temperature and mixing fields. But also from a broader point of view, it offers insight, through stand-alone data, into the flow and mixing of the axisymmetric, confined turbulent co-flows that are the subject of this thesis.

3.2 Velocity Field

This section includes measurements with a hot wire at cold conditions and with a pitot tube and thermocouple at hot conditions. Hot wire measurements were performed after ensuring that the cold flows exhibited dynamic similarity (equal $\mathcal{R}e_{turb}$) at the inlet with the autoignition experiments. The mean velocity and velocity fluctuations are considered first in **Section 3.2.1**. Following this, **Section 3.2.2** offers a typical pdf of velocity, autocorrelation functions and calculations of the longitudinal integral lengthscale, L_{turb}. **Section 3.2.3** looks at the characteristics of the turbulent flow in the frequency domain and provides estimated values for the smallest turbulent lengthscales, η_K. **Section 3.2.4** summarizes the main results.

3.2.1 Mean and Fluctuations of Axial Velocity

Figure 3.1 shows radial profiles of the mean axial velocity and rms of the fluctuations of the axial velocity at cold (ambient) conditions taken with a hot wire at various Reynolds numbers ($\mathcal{R}e_{turb}$), injection velocities ($\upsilon_{fuel} = \frac{U_{fuel}}{U_{air}}$) and axial locations ($z$). **Figure 3.2** shows radial profiles of the mean axial velocity at representative autoignition temperatures taken with a high-temperature pitot tube and thermocouple. The temperature measurements used to evaluate the local density are also shown. In the aforementioned plots the local mean velocity, $\langle U(r,z)\rangle$, is normalized by the bulk velocity, U_{air}. **Figure 3.1** shows that $\frac{\langle U\rangle}{U_{air}}$ amounts to 1.14 – 1.15 and is uniform, staying within 5 – 10% of the maximum over the range of at least $\frac{r}{R_{TUBE}} \cong 0.15 - 0.80$, away from the quartz tube and injector walls. At elevated temperatures (**Figure 3.2**) the presence of the temperature boundary layer and the finite heat losses to the wall cause the velocity boundary layer to thicken. In these conditions the region of uniformity reduces to $\frac{r}{R_{TUBE}} \cong 0.15 - 0.65$.

As can be seen, even with $\upsilon_{fuel} = 2.20$ at injection, the centerline velocity in the tube decays quickly, reaching levels less than 10% higher than the uniform

$\upsilon_{fuel} = 1.00$ profile by $18d_{IN}$ (40 mm) downstream. This point is of importance for the mixing results of this chapter (**Section 3.4**), but also for the delay time results of **Chapter 7**, because it implies that the mean residence time from injection to autoignition (based on a measure of L_{IGN}) will be mostly determined by U_{air} rather than U_{fuel}. Finally, it will be shown in the mixing results (**Section 3.4**) and from contour plots such as those in **Figures 3.11** and **3.14**, that the plume is relatively thin. The contour corresponding to $\langle\xi\rangle = 0.1$ occupies radial lengths of $\frac{r}{d_{IN}} < 1.5$, or $\frac{r}{R_{TUBE}} < 0.3$ in the first $8d_{IN}$ (18 mm). Hence, it is likely to expect that, initially, mixing will occur in regions of relatively uniform velocity.

For comparison, the rms plots show the rms of the axial velocity fluctuations normalized by both the local (blue lines) and the bulk (black lines) velocities. In general, values of normalized rms in this thesis will be stated based on the former. For a normalized rms of <15%, the error in this measurement is less than 1%. Values greater than about 30% are associated with errors larger than 3% (see **Section 2.3.1**). The normalized rms is between 0.11 and 0.14 in the region $\frac{r}{R_{TUBE}}$ of 0.4 – 0.7 and decays downstream to about 0.09 – 0.10.

For parabolic profiles the maximum velocity in the centreline is twice the bulk value. **Figures 3.1(a)** with $\upsilon_{fuel} = 1.15$, **3.1(b)** with $\upsilon_{fuel} = 0.60$ and **3.1(d)** with $\upsilon_{fuel} = 1.05$, reveal that the measured velocity close to the injector exit ($z =$ 2 mm), which is close to U_{fuel}, is about 1.7, 1.1 and $1.9U_{air}$ respectively. Hence, it is reasonable to assume a parabolic profile for the flow inside the injector, given also the fact that this flow is expected to be laminar. Yet, one must be cautious because the injector nozzle flow area ($d_{IN} = 2.24$ mm) is close to the hot wire length (1.25 mm), resulting in significant spatial averaging for this measure of velocity. The true profile is difficult to describe precisely from these measurements.

3.2.2 Pdfs and Autocorrelation Functions

In **Figure 3.3** a small deviation can be seen from the random process for the velocity data. The skewness of the pdf is -0.2 and the kurtosis 3.2. This is not due to measurement error, nor due to a lack of convergence of the pdf, which is made up of 5x10^6 independent points taken at twice the integral timescale for the conditions, i.e. 250 Hz. It is due to spatial averaging performed by the hot wire that causes a deviation from a true point measurement. Because of the finite measurement region, the measurement is influenced to a limited extent by the spatial gradients of $u' = \sqrt{\overline{u'^2(t)}}$. A slight deviation would have been expected in such a case even for wind tunnel turbulence, owing to the (strictly) non-Gaussian nature of u' that gives rise to the dynamics of turbulence [Davidson, 2004]. Nevertheless, it is clear that the turbulent signal here lacks the well-defined 'coherent structure' of shear flows, where velocity pdfs cannot be at all approximated as being Gaussian.

Figure 3.4 shows measurements of the longitudinal integral lengthscale, L_{turb}. This ranged between 3.0 and 3.5 mm at the inlet, or about 4.0 mm behind the air thermocouple (see **Figure 2.5**). The traverses were purposefully positioned so as to measure the flow in this region. This effect is not entirely absent from the rest of the data. For example, careful examination of **Figures 3.1(a)** and **3.1(c)**, reveals a slightly distorted mean profile and increased turbulent intensity at negative radii (these traverses were taken in the opposite direction). This scale increases by 0.5 mm downstream as expected and the effect of the thermocouple diminishes.

3.2.3 Energy Spectra, Scaling Laws and Lengthscales

The turbulent character of the air in the co-flow stream coming into the quartz tube can be assessed by considering the turbulent velocity and energy dissipation spectra of **Figure 3.5**. Consider first, **Figure 3.5(a)**. As the wavenumber (k) approaches zero all spectra collapse, forced by the choice of normalization, to values of about

4 – 5, exactly as with the sample data in Bogard and Thole [1998] and a value of 4 from Von Karman's Equation [Hinze, 1975] derived theoretically for isotropic turbulence and ignoring viscous dissipation:

$$\frac{2\pi E_{11}(k_1)}{\overline{u'^2}L_x} = \frac{4}{\left[1+(\frac{4}{3}L_x k_1)^2\right]^{5/6}} \tag{3.1}$$

where the '*11*' and '*1*' subscripts refer to the axial velocity component and L_x is the integral lengthscale from the autocorrelation function obtained from the axial component of the fluctuating velocity, as here.

As expected for canonical wall-bounded flows, [Bogard and Thole, 1998], three characteristic regimes can be identified in plots such as those in **Figure 3.5(a)**. At low k the energy is believed to scale with the outer length, here, L_{turb}. In such a case the flat behaviour would be expected at low k. At intermediate k the relevant scale should be the distance from the wall ($y = R_{TUBE} - r$). Finally, at the highest k where viscous dissipation is dominant, the flow should scale with η_K. **Figure 3.5(a)** shows -1 behaviour in the region $k \approx L_{turb}$. The significance of this scaling is that here the outer length, L_{turb}, is predicted to overlap with the scaling based on y and thus signifies an overlapping of the low and intermediate k regimes. Also shown is the $-5/3$ inertial subrange behaviour predicted for isotropic turbulence. **Figure 3.5(a)** is entirely consistent with the data of Bogard and Thole [1998] over the entire range and with Von Karman up to and including the -1 region, beyond which the effect of viscosity cannot be ignored.

The relative contribution to the total turbulent kinetic energy in the flow is apparent in the dissipation plots of **Figure 3.5(b)**. Eddies of the size of L_{turb} contribute the most to the energy. The maximum non-dimensional dissipation is around 0.3 – 0.4, compared to 0.3 of Bogard and Thole [1998]. The roll-off at higher k gives $kE(k)\frac{L_{turb}}{u'^2} \sim 1\text{x}10^{-3}$ at $kL_{turb} \cong 15$. In Bogard and Thole [1998]

$kE(k)\frac{L_{turb}}{u'^2} \sim 1\text{x}10^{-3}$ also occurs close to the value of $kL_{turb} \cong 15$ for measurements at a location of $\frac{y}{R_{TUBE}} = 0.8\frac{\delta}{R_{TUBE}}$ from the wall, where δ is the boundary layer thickness defined as the radial length from the wall to the point at which the mean velocity drops to $0.99U_\infty$. Note that here, $U_\infty = max\{U\} = U(r = 0)$. From the profiles of **Figure 3.1(a)** an estimate for $\frac{\delta}{R_{TUBE}}$ of 0.3 – 0.7 can be obtained for the experiments here and indeed the measurements were made at $\frac{y}{R_{TUBE}} \cong 0.3$ – 0.6.

The Kolmogorov lengthscale, η_K, was evaluated at each location where a spectrum was recorded. This scale was found to be as in **Table 3.1**.

η_k Co-flow Conditions	Local U (m/s)	Estimated $[\nu^3 \frac{L_{turb}}{u'^3}]^{1/4}$	Measured $[\frac{\nu^3}{\epsilon}]^{1/4}$	Error (%)
$\mathcal{R}e_{turb} = 55$, $U_{air} = 2.3$ m/s $L_{turb} = 4.8$ mm, $\frac{u'}{U} = 0.11$ $z = 1$ mm, $\frac{r}{R_{TUBE}} = 0.5$	2.6	0.165 mm	0.138 mm	+19%
$\mathcal{R}e_{turb} = 100$, $U_{air} = 4.4$ m/s $L_{turb} = 3.0$ mm, $\frac{u'}{U} = 0.13$ $z = 2$ mm, $\frac{r}{R_{TUBE}} = 0.3$	5.1	0.090 mm	0.090 mm	0%
$\mathcal{R}e_{turb} = 100$, $U_{air} = 4.4$ m/s $L_{turb} = 3.1$ mm, $\frac{u'}{U} = 0.14$ $z = 2$ mm, $\frac{r}{R_{TUBE}} = 0.4$	5.2	0.088 mm	0.092 mm	-4%
$\mathcal{R}e_{turb} = 100$, $U_{air} = 4.4$ m/s $L_{turb} = 4.2$ mm, $\frac{u'}{U} = 0.14$ $z = 2$ mm, $\frac{r}{R_{TUBE}} = 0.5$	5.1	0.094 mm	0.093 mm	+1%
$\mathcal{R}e_{turb} = 100$, $U_{air} = 4.4$ m/s $L_{turb} = 3.5$ mm, $\frac{u'}{U} = 0.13$ $z = 2$ mm, $\frac{r}{R_{TUBE}} = 0.6$	4.9	0.096 mm	0.094 mm	+2%
$\mathcal{R}e_{turb} = 100$, $U_{air} = 4.4$ m/s $L_{turb} = 3.1$ mm, $\frac{u'}{U} = 0.13$ $z = 2$ mm, $\frac{r}{R_{TUBE}} = 0.6$	4.9	0.092 mm	0.091 mm	+1%

Table 3.1: Experimental measurements of the Kolmogorov lengthscale. Here, U is the local measured mean velocity in the flow and U_{air} is the bulk velocity.

The estimation of this scale from L_{turb} is relatively accurate and this fact was used to predict η_K over a wider extent of the domain. **Figure 3.6** shows that η_K is

uniform and increases by not more than 30% in the first 42 mm, allowing a single value for η_K to be used for the whole domain in the image processing of the mixture fraction PLIF images of **Section 3.4**.

3.2.4 Velocity Field: Summary

From the preceding results it is possible to conclude that:

- The flow is uniform in terms of the mean and rms velocities and integral lengthscale, with the boundary layers confined to regions close to the injector and the tube walls. At elevated temperatures the region of uniformity reduces.
- The local mean velocity amounts to about $1.14 - 1.15U_{air}$. The longitudinal integral lengthscale, L_{turb}, ranged between 3.0 and 3.5 mm at the inlet (or 4.0 mm behind the air thermocouple), increasing by 0.5 mm downstream.
- The air flow at the inlet (and away from the wake or jet region downstream of the injector) is turbulent, in the manner expected from the current geometry, i.e. downstream of a grid but also confined in the tube. No evidence of organized shear flow such as vortex shedding or separated regions was found.
- It is possible to estimate η_K from knowledge of L_{turb}. The error associated with this practice has been found to be <20%. The smallest lengthscale is uniform and increases by not more than 30% in the first 42 mm from the injector.

3.3 Temperature Field

Results for the mean temperature are presented first in **Section 3.3.1**. Heat losses are quantified in terms of the drop of temperature within the tube along the axial direction and the extent of the thermal boundary layers. The degree of temperature

uniformity inside the section is also inspected. **Section 3.3.2** proceeds to the fluctuations of temperature, including results both from a compensated fine thermocouple and a high-temperature hot wire operated in CTA mode at various overheat ratios. The latter section also shows spectra and pdfs of temperature. **Section 3.3.3** is a brief summary of the main conclusions.

3.3.1 Mean Temperature

Radial profiles of mean temperature, $\langle T(r,z)\rangle$, can be found in **Figure 3.7(a)**. The thermal boundary layer on the quartz tube wall grows with increasing axial distance to about $0.6R_{TUBE}$ at 80 mm. At the inlet, the boundary layer on the injector extends to about $0.1 - 0.2R_{TUBE}$. Note that the definition of the boundary layer is based on a 99% drop from the centreline $T_\infty = max\{T\} = T(r=0)$, as with the velocity. The peak temperature at any given axial location drops downstream due to heat losses to the quartz tube walls. The heat losses are better quantified with the axial profiles in **Figure 3.7(b)**, taken at various T_{air} in the range 820 – 920 K and U_{air} between 11 m/s and 17 m/s. For all conditions tested the axial decay of temperature was found to be nearly linear, with an approximate 10 K drop measured per 100 mm in the 'jacketed' tube. At the higher U_{air} (17 m/s) the axial decay of the mean temperature per mm was found to be up to 15% smaller than the lower U_{air} (11 m/s) results at the same T_{air}. Also, at higher T_{air} (920 K) the decay per mm was 15% greater than in the low T_{air} (820 K) measurements.

The (on average) 10 K per 100 mm drop for the 'jacketed' tube was improved to about 5 K per 100 mm with the use of the heat exchanger. This is also shown by the data in **Figure 3.7(b)**, yet an improvement of down to 3 K was possible in cases with higher U_{air} and at relatively lower T_{air}. It is important to point out that the majority of phenomena that are the subject of this thesis are observed within the first 100 mm from the injector.

3.3.2 Temperature Fluctuations

Figure 3.8 shows the effect of compensation on the fine (76 μm) thermocouple temperature signal in the frequency and time domains. In particular, **Figure 3.8(a)** demonstrates that the cut-off that is necessarily introduced so that noise is not amplified by the compensation process removes very little energy from the signal, allowing for an accurate recovery of the true rms of the temperature fluctuations, $T' = \sqrt{\overline{T'^2(t)}}$. The cut-off was set to be close to the level at which the signal became indistinguishable from the background noise. Information on the background noise was extrapolated from higher frequencies. It was found that, in practice, a cut-off at 70 – 120 Hz was necessary, which was about 5 times the time constant of the wire. This conclusion is consistent with the findings of Heitor et al. [1985].

After compensation, the rms of the temperature fluctuation was found to be in the range 0.5 – 2.0 K for the condition envelope spanning T_{air} = 760 – 990 K and U_{air} = 10 – 25 m/s. This value is considered low. From **Figure 3.8(b)** it becomes apparent that the fastest temperature timescale was much slower than the (expected) 2 – 8 kHz fastest velocity scale based on eddies of size η_K. This reflects the fact that the main energy generating mechanism for the turbulent velocity is very different to that responsible for the heating of the flow. **Figure 3.9** inspects the pdf of T'_{air} for a case in which the rms of T'_{air} is about 0.7 K. The Gaussian shape fits the data well and suggests that this process, unlike the case of the turbulent velocity that has been discussed above in **Section 3.2.2**, is a normal one.

Figure 3.10 contains spectra taken simultaneously with a fine thermocouple and a high-temperature hot wire. It is again evident that the temperature field has a narrower bandwidth, both directly from the compensated thermocouple and from the increasing bandwidth of the hot wire spectra as the overheat ratio is increased. The hot wire at low overheats is most sensitive to variations in temperature, here by a factor of about 200, whereas at the higher overheats this factor falls to about

30. From these measurements the rms of the velocity fluctuations was found to be 0.05 – 0.10 of the mean local velocity, the rms of the fluctuations of temperature was 0.08 – 0.10% of the mean absolute temperature and the cross-correlations $\overline{(\frac{u'}{U})(\frac{T'}{T})}$ were an order of magnitude lower at 5x10^{-6}. These measurements were made at T_{air} = 800 K and U_{air} = 20.6 m/s with the hot wire placed at $\frac{r}{R_{TUBE}} = 0.5$ and $z = 0$ and will be taken as representative values for the hot conditions.

3.3.3 Temperature Field: Summary

It is concluded that:

- The mean temperature into the section is uniform for radii greater than $\frac{r}{R_{TUBE}}$ = 0.1 – 0.2 from the injector. The thermal boundary layer on the quartz tube wall grows and decreases the uniform region to about $\frac{r}{R_{TUBE}} = 0.6$ by 80 mm after injection.
- Axially, a (linear) mean temperature drop due to heat losses of 10 K in the first 100 mm is typical. This can be reduced to up to 3 K per 100 mm with the use of the heat exchanger.
- Temperature fluctuations are small relative to the mean temperature with values ranging between 0.05% to a maximum of 0.25%, affirmed by both a compensated fine thermocouple and a high-temperature hot wire. This corresponds to about 0.5 – 2.5 K in the conditions of the autoignition experiments.
- The cross-correlations $\overline{(\frac{u'}{U})(\frac{T'}{T})}$ are small with an indicative value of 5x10^{-6} in the centre of the radius at the inlet of the tube.
- The temperature fluctuations can be well modelled by a normal process.
- At elevated temperatures the rms of the velocity fluctuations is about 0.05 – 0.10 of the mean velocity.

3.4 Mixture Fraction Field

In this section measurements are made available of the mixture fraction (ξ) field in the CTHC, from the source (injector nozzle,) to a downstream distance of $20M$. The two-dimensional scalar dissipation rate (χ_{2D}) was calculated from the sum of squares of the axial and radial gradients of the measured two-dimensional, planar ξ, but limited inferences concerning the full three-dimensional scalar dissipation rate (χ_{3D}) are also made. These results are grouped into those concerning the mean and variance of ξ (**Section 3.4.1**) and those concerning χ (**Section 3.4.2**). In addition, local/point statistics of these mixing quantities, i.e. ξ and χ_{2D}, were evaluated at various locations in the domain and are presented in **Section 3.4.3**. For χ this is done both in conventional unconditional terms and conditional on ξ. Certain results are discussed in the light of turbulent reacting flow modelling.

Two cases of mixing are considered, corresponding to the two strategies of injection in the autoignition experiments, distinguished by their inlet kinematic condition as described by the non-dimensional, normalized injection to co-flow velocity ratio ($\upsilon_{fuel} = \frac{U_{fuel}}{U_{air}}$): (i) 'equal velocity' with $\upsilon_{fuel} \cong 1$, and, (ii) 'jet in co-flow' with $\upsilon_{fuel} > 1$. For each case, the effect the inlet dynamic condition, through the co-flow turbulent Reynolds number ($\mathcal{R}e_{turb}$), on the global mixing patterns is investigated. In an attempt to closely simulate the autoignition mixing fields, dynamic similarity was achieved by requiring the investigated range of $\mathcal{R}e_{turb}$ in these experiments to be close to the values of $\mathcal{R}e_{turb}$ in the autoignition experiments. The non-dimensional, normalized injection to co-flow density ratio ($\varpi_{fuel} = \frac{\rho_{fuel}}{\rho_{air}}$) and molecular diffusion coefficient ($\mathcal{D}$) were also kept by using the actual diluted fuels (acetylene and hydrogen) used for the autoignition experiments, although it must be stated that the hydrogen results will be an influenced by differential diffusion and must be judged with more care. The current section ends with a brief summary, **Section 3.4.4**.

3.4.1 Mean and Variance

Figure 3.11 shows results for the mean ξ field, with $\langle\xi_1\rangle$ and $\langle\xi_2\rangle$ shown for comparison. The effect of image processing is insignificant. As expected from the analytical treatment of diffusion from a point source, the centreline extent of the plume is not affected by the change in $\mathcal{R}e_{turb}$, because the injection velocity and hence input mass flux of fuel is suitably adjusted to set $\upsilon_{fuel} \cong 1$. This is reiterated in **Figure 3.12**, where the decay of the axial profiles of $\langle\xi\rangle$ along the centreline is plotted for cases of $\mathcal{R}e_{turb} = 50 - 90$ and fixed $\upsilon_{fuel} = 0.95 - 1.00$, both with acetylene and hydrogen. Solid lines are for $\langle\xi_1\rangle$ and dashed lines for $\langle\xi_2\rangle$. Again, the effect of processing on the results is small, to the extent that no appreciable difference can be seen between these lines for any run.

Gaussian axisymmetric plumes are described by a decay behaviour:

$$\langle\xi(z, r = 0)\rangle \quad = \quad \frac{1}{8}\upsilon_{fuel} \cdot \frac{1}{(\frac{\sigma}{d_{IN}})^2} \tag{3.2}$$

where σ can be estimated at 'long lengths' from the injector (i.e. $\sigma \gg L_{turb}$) by $\sigma^2 \cong 2C_\mu z(\frac{u'}{U})L_{turb}$, or at 'short lengths' (i.e. $\sigma \ll L_{turb}$) by $\sigma \cong z(\frac{u'}{U})$ and C_μ is a constant of order 0.1. In these experiments L_{turb} has been measured with hot wires in similar conditions and was found to be about 3.0 mm at the inlet to the mixing domain under investigation, increasing downstream to values around 4.0 mm (from **Section 3.2.2**). At the same time, $\frac{u'}{U}$ varied between a maximum of 0.14 upstream and 0.10 downstream in the same domain (from **Section 3.2.1**). Thus, σ is expected to be in the range $\sigma \ll L_{turb}$, if $z \ll \frac{L_{turb}}{(\frac{u'}{U})} = 30$ mm, or $\frac{z}{d_{IN}} \ll 13$. Viewed in terms of eddy turnovers this corresponds to $\frac{z}{L_{turb}} \ll \frac{1}{(\frac{u'}{U})} \cong 8$. On the contrary, 'long length' behaviour would be achieved for $\frac{z}{L_{turb}} \gg \frac{1}{[2C_\mu(\frac{u'}{U})]} \cong 42$ eddy turnovers, or in terms of lengths, $z \gg 146$ mm or $\frac{z}{d_{IN}} \gg 65$. This condition is never met in the measurements, with the maximum height of the laser beam being around 60 – 70 mm. Thus, these

'short length' plumes are characterized by a:

$$\langle \xi(z, r=0) \rangle \quad = \quad \frac{1}{8} \upsilon_{fuel} \cdot \frac{1}{\left[(\frac{z}{d_{IN}})(\frac{u'}{U}) \right]^2} \tag{3.3}$$

decay for $\sigma \ll L_{turb}$.

The data in **Figure 3.12(c)** collapse onto a unique straight line for $\frac{z}{d_{IN}} \gtrapprox 5$ for all conditions. The choice of fuel (and hence different ϖ_{fuel} and molecular diffusion coefficients, $\mathcal{D}$) does not affect this conclusion. The Gaussian 'short length' decay is shown marked as "-2". This is interpreted as confirmation that the decay of the Gaussian axisymmetric plume is a good description of the mean behaviour in this case, for axial distances greater than $\frac{z}{d_{IN}} = 5$ and extending further than the limit of $\frac{z}{d_{IN}} \ll 13$ for which it was theoretically derived. It should be noted, in relation to the final point, that $\langle \xi \rangle$ for $\frac{z}{d_{IN}} > 10$ drops below 0.01 and is thus associated with greater uncertainty. As expected, changes in $\frac{u'}{U}$ throughout the domain do not significantly affect the decay of $\langle \xi \rangle$ as they are only marginal.

Having studied the axial profiles, **Figure 3.13** is concerned with the radial direction. Returning to the Gaussian plume, consider the radial profile of $\langle \xi \rangle$:

$$\langle \xi(z, r) \rangle \quad = \quad \frac{1}{8} \upsilon_{fuel} \cdot \frac{1}{(\frac{\sigma}{d_{IN}})^2} \cdot exp[-(\frac{r}{2\sigma})^2] \tag{3.4}$$

Dividing through by the value at the centreline:

$$\frac{\langle \xi \rangle}{\langle \xi(r=0) \rangle} \quad = \quad exp[-(\frac{r}{2\sigma})^2] \tag{3.5}$$

Away from the injector, but still restricted to regions in which the 'short length' plume equation applies (with $\frac{z}{d_{IN}} \ll 13$), σ is expected to be well described by the

'short length' spread, $\sigma \cong z(\frac{u'}{U})$. Substituting this expression results in the profile:

$$\frac{\langle \xi \rangle}{\langle \xi(r=0) \rangle} = exp\Big[-\frac{1}{4} \frac{(\frac{r}{d_{IN}})^2}{(\frac{z}{d_{IN}})^2 (\frac{u'}{U})^2} \Big] \tag{3.6}$$

Figure 3.13(a) shows plots of radial profiles at $\frac{z}{d_{IN}} = 1$, 4, 5 and 6 for the same conditions as those in **Figure 3.12**. **Figure 3.13(b)** is a reproduction of **Figure 3.13(a)** with the independent and dependent axes scaled so as to test whether the profiles show self-similar Gaussian shapes; that is plotting the logarithm* of $\langle \xi \rangle$ normalized by its centreline value at that axial location (i.e. $\langle \xi(r=0) \rangle$), against the square of the non-dimensional radial distance $(\frac{r}{d_{IN}})/(\frac{z}{d_{IN}})$. Straight line behaviour in **Figure 3.13(b)** corresponds to Gaussian profiles in the radial direction. Self-similarity is observed for axial distances not too close to the injector (as with the axial profile). It should be pointed out that this also implies that the turbulence intensity, $\frac{u'}{U}$, does not change significantly. The value of $\frac{u'}{U}$ that would give rise to a gradient of approximately $-\frac{1}{0.05}$ to $-\frac{1}{0.08}$ is 0.11 – 0.14, from **Equation 3.6**. This agrees very well with the direct measurements of $\frac{u'}{U}$. At close lengths to the injector the Gaussian description is still valid, but the choice of σ cannot follow the downstream reasoning. Here, the effect of the finite source size becomes important.

Results have also been obtained with hydrogen jets. **Figure 3.14(a)** shows a plume generated by injection of hydrogen into the same background co-flow $\mathcal{R}e_{turb}$ as that of **Figure 3.11(f)**, but with higher $\upsilon_{fuel} = 2.00$ and **Figure 3.14(b)** shows mixing in an $\mathcal{R}e_{turb} = 110$, $\upsilon_{fuel} = 3.90$ flow. Only $\langle \xi_2 \rangle$ is shown, since the discrepancy with $\langle \xi_1 \rangle$ is again negligible. In more detail, **Figures 3.15(a)** and **(c)** show the axial decay characteristics of the jets. The "-2" decay is denoted, but this is not obeyed as robustly as for the $\upsilon_{fuel} \cong 1$ case. Self-similarity is observed as $\mathcal{R}e_{turb}$ increases from 65 to 90 for the same υ_{fuel}, but the two flows with different

*Throughout this thesis where reference is made to the 'logarithm' it is implied that it is to the base-10.

υ_{fuel} exhibit a different decay. The latter observation leads one to conclude that the characteristic spread σ cannot be simply stated in terms of the conditions in the co-flow as was previous achieved through $\frac{u'}{U}$. These outcomes have been anticipated, since the 'diffusion from a point source' idealization becomes unable to account for the finite jet velocity and momentum for $\upsilon_{fuel} > 1$. **Figure 3.15(b)** is the equivalent of **Figure 3.13(b)** for the jet flows, for axial distances from $\frac{z}{d_{IN}}$ of 1 to 12 in unity steps. It is clear that the Gaussian shape remains an adequate representation, especially at longer distances from the injector.

Figures 3.16(a) to **3.16(d)** show plots of $\langle \xi_1'^2 \rangle$ (left) and $\langle \xi_2'^2 \rangle$ (right) for injection of hydrogen with two different υ_{fuel} into the same $\mathcal{R}e_{turb}$ co-flow. **Figure 3.17** considers the centreline decay of these variables for a variety of conditions, but this time for both acetylene and hydrogen. The results are not as converged as those of the mean field, as expected. The most notable feature is the enormous difference in the region from close to the injector to about $2d_{IN}$. As far as the processing is concerned, there is no significant alteration of the results. This outcome is important and suggests that the energy that was removed from the raw data by the denoising procedure is not significant. In terms of trends, the variance increases from the injector to a maximum and decays farther downstream. The profiles of $\langle \xi'^2 \rangle$ are shifted to longer lengths ($\frac{z}{d_{IN}}$) with increasing υ_{fuel}, but are not strongly influenced by $\mathcal{R}e_{turb}$. Yet, closer to the injector, including the region of the maxima, $\langle \xi'^2 \rangle$ increases with $\mathcal{R}e_{turb}$ for a given υ_{fuel}.

3.4.2 Scalar Dissipation

Figure 3.18 contains contour plots of $\langle \chi_{2D} \rangle$ at three different stages of processing for the same condition. These plots indicate that the effect of processing is more pronounced for this quantity, with the processing between $\langle \chi_1 \rangle$ and $\langle \chi_2 \rangle$ being the more severe. From the small difference between $\langle \chi_2 \rangle$ and $\langle \chi_3 \rangle$ one can conclude that

the effect of image processing has converged by $\langle\chi_2\rangle$. Recall that $\langle\chi_3\rangle$ was processed based on a $4\eta_K$ window, as opposed to the η_K 'mixing window' used to obtain $\langle\chi_1\rangle$ and $\langle\chi_2\rangle$. Axial profiles of $\langle\chi_2\rangle$ in **Figure 3.18** signify that $\mathcal{R}e_{turb}$ (or U_{air}) and v_{fuel} affect $\langle\chi_{2D}\rangle$ in the same way as they were found to affect $\langle\xi'^2\rangle$. Specifically, closer to the injector $\langle\chi\rangle$ increases with $\mathcal{R}e_{turb}$ for a given v_{fuel}, whereas downstream $\mathcal{R}e_{turb}$ does not change $\langle\chi\rangle$. The effect of v_{fuel} is to increase $\langle\chi\rangle$ for all $\frac{z}{d_{IN}}$. Overall, the profiles are qualitatively similar to those of $\langle\xi'^2\rangle$.

It is interesting to examine possible isotropic mixing behaviour *per se*, but also because this would allow $\langle\chi_{3D}\rangle$ to be accurately estimated by $\frac{3}{2}\langle\chi_{2D}\rangle$. In **Figures 3.20(a)** and **3.20(b)** the radial and axial contributions to $\langle\chi_2\rangle$ are plotted along the centreline against each other both linearly and logarithmically. Isotropic mixing would be the case for straight lines passing through the origin. For small values of dissipation and consequently at longer distances from the injector, it is possible to argue for this case. Hence, if necessary, one can attempt to recover the full $\langle\chi_{3D}\rangle$ as $\frac{3}{2}\langle\chi_{2D}\rangle$, for $\frac{z}{d_{IN}} > 2-3$ along the centreline. In **Figure 3.20(c)** this reasoning is successfully extended to all locations with $\frac{z}{d_{IN}} > 3$, including off the centreline, so that $\langle\chi_{3D}\rangle \approx \frac{3}{2}\langle\chi_{2D}\rangle$ for $\frac{z}{d_{IN}} > 2-3$, *at any radius*. Note that *along the centreline* $\langle\chi_{3D}\rangle$ can be always be recovered even for $\frac{r}{d_{IN}} < L_{iso}$ from **Equation 2.21** as mentioned before.

It has been suggested that $\langle\chi_{3D}\rangle$ is well modelled by the following expression: $\langle\chi\rangle = C_D\frac{\langle\xi'^2\rangle}{\tau_{turb}} = C_D\frac{\langle\xi'^2\rangle u'}{L_{turb}}$, where a value of 2.0 is usually employed for the timescale ratio, C_D. In **Figure 3.21(a)** C_D is plotted as evaluated from this expression against the axial distance from the injector, $\frac{z}{d_{IN}}$. The value of τ_{turb} has been calculated from the mean of the measured values of L_{turb} and u' in the domain. For L_{turb} a value of 4 mm was used for the whole domain, while u' was estimated from the knowledge of U and from a mean value of measured $\frac{u'}{U}$ everywhere in the domain of 0.1. Hot wire measurements of τ_{turb} at cold conditions are shown in **Figure 3.21(b)**, that confirm that τ_{turb} increases by about 40% in the first 42 mm from the injector. Thus, the

error in the evaluation of C_D from an averaged (constant) value in the domain of τ_{turb} is ±20%. The non-dimensional distance downstream of the injector for which $C_D \approx 2$ is defined as L_χ, so that the $\langle\chi\rangle = 2\frac{\langle\xi'^2\rangle}{\tau_{turb}}$ model is justified by the data *along the centreline*, at least for distances from the injector greater than L_χ. The asymptotic distance L_χ was found to depend on the conditions, coming closer to the injector at lower $\mathcal{R}e_{turb}$ and υ_{fuel}. In the regions conforming asymptotically to $C_D \to 2$, i.e. $\frac{z}{d_{in}} > L_\chi$ along the centreline, the model was also valid in off-axis locations, but only inside the edges of the jet.

3.4.3 Local Statistics

The results presented so far, being (unconditional) moments of ξ and χ, are useful for a general understanding of the turbulent mixing flows that exist in the tube. An attempt to explain the results of **Chapter 6** concerning the locations of autoignition in the tube could have been made in terms of this data, since it is known that the quantities ξ and χ play a deciding role in the emergence of those locations. In the absence of the existing DNS findings, such an attempt would have perhaps sufficed. Nevertheless, in order to be able to understand strictly the autoignition results, the DNS have indicated that more detail is required. Specifically, it is known that autoignition will eventually emerge at some location with $\xi = \xi_{MR}$, but also, that the history of $\chi|\xi = \xi_{MR}$ determines the exact location. For example, consider the case of $\upsilon_{fuel} = 1$. From the results so far it may be concluded that $\langle\xi\rangle$ remains approximately constant and $\langle\chi\rangle$ increases with U_{air} (or $\mathcal{R}e_{turb}$), at least early on along the centreline. This is *not* a necessary condition for $\chi|\xi = \xi_{MR}$ to increase as well (although it will be shown that this is indeed true). In this section, the local statistics of $\chi|\xi = \xi_{MR}$ are inspected in detail, together with pdfs of ξ at ξ_{MR} for completeness. For ξ_{MR} two 'reasonable values' for the fuels and conditions used in the autoignition experiments are chosen from 0-D CMC computations. These are mentioned again in **Section 6.2.2**.

For two different values of ξ (that are chosen as possible candidates for ξ_{MR}) and two different values of U_{air} with $\upsilon_{fuel} \cong 1$, **Figure 3.22** shows: in the top two figures the axial centreline profiles of pdf($\xi = \xi_{MR}$), and, in the bottom two figures the axial centreline profiles of $\langle\chi|\xi = \xi_{MR}\rangle$. The same data is plotted as a function of: in the left two figures the distance z from the injector, and, in the right two figures an estimate of an averaged lagrangian residence time, $(\frac{z}{U_{air}})$, defined similar to τ_{IGN} from **Section 2.4.3**. The pdfs rise from zero at the injector to a maximum value and decay downstream for all tested conditions. The maxima occur at relatively short lengths, i.e. between 10 – 30 mm at the tested conditions. The effect of increasing U_{air} is to decrease the values of the maxima, bring them closer to the injector and to decrease the values of pdf($\xi = \xi_{MR}$) downstream of the maxima. This is true, both in terms of physical distance z *and* residence time $\frac{z}{U_{air}}$. The effect of choosing a higher ξ_{MR} is to decrease the values of pdf($\xi = \xi_{MR}$) at all z and $\frac{z}{U_{air}}$ downstream of the maxima. The mean conditional χ at ξ_{MR} decays monotonically from short lengths, as expected, for all U_{air} and choices of ξ_{MR}. The effect of either increasing U_{air}, or choosing a richer ξ_{MR}, is to increase $\langle\chi|\xi = \xi_{MR}\rangle$ at all distances downstream. Most interestingly, the effect of U_{air} is *not* collapsed by $\frac{z}{U_{air}}$, or seen otherwise, after the same residence time from injection, $\langle\chi|\xi = \xi_{MR}\rangle$ is locally still higher for the higher U_{air} case.

Figure 3.23(a) shows the mean conditional χ at a location on the centreline and about 10 mm downstream of the injector for three values of U_{air} as υ_{fuel} is kept constant at $\cong$1. As expected, $\langle\chi|\xi = \xi_{MR}\rangle$ increases monotonically at all ξ with increasing U_{air}. Any model for the mean conditional χ, such as the Amplitude Mapping Closure (AMC) [Chen et al., 1989] or the presumed β-pdf model of Girimaji [Girimaji, 1992] can be checked against these plots. The plots peak towards the lean side, suggesting that perhaps the Girimaji model is a better candidate, but the deviation from the AMC is not expected to be great in this case. It is clear that the *mean* conditional χ at a typical ξ_{MR} increases with U_{air}. Going a step further,

consider the pdf of the conditional χ from **Figure 3.23(a)** at $\xi = \xi_{MR} = 0.1$. As U_{air} increases and $\langle\chi|\xi = \xi_{MR}\rangle$ increases, the pdf of $\chi|\xi = \xi_{MR}$ *decreases at low values and increases at higher values.* This last finding is extremely important, because it is completely opposite to the results obtained from the DNS. It will not be discussed further here, nor will the results from above, because the main conclusion remains unchanged from that reached by considering only the mean, unconditional χ: an increase in U_{air}, 'increases χ' at the same location and after the same residence time, increases $\langle\chi|\xi = \xi_{MR}\rangle$, decreases pdf$(\chi|\xi = \xi_{MR})$ at low values and increases pdf$(\chi|\xi = \xi_{MR})$ at higher values of $\chi|\xi = \xi_{MR}$, again at the same location and after the same residence time. The finer points regarding the local, conditional statistics of χ will be implied, when making such a statement. The effect of U_{air} on χ will be returned to in **Chapters 6** and **7** in the context of explaining the observed trends in autoignition location as U_{air} is changed (for experiments with $\upsilon_{fuel} \cong 1$).

3.4.4 Mixture Fraction Field: Summary

Acetone PLIF measurements were performed, at reduced temperatures, to understand the mixing field during the autoignition runs. In order to better simulate the autoignition runs the PLIF conditions were chosen to be dynamically similar (i.e. at the same Re_{turb}) to the autoignition ones. In this chapter it has been shown that, for the mixing field downstream of the injector nozzle in the CTHC burner:

- For the equal velocity case (with $\upsilon_{fuel} \cong 1$) and at lengths with $\frac{z}{d_{IN}} \gtrsim 4 - 5$, the mixing process can be well described, in the mean, by diffusion from a point source. Hence, as expected from this behaviour, the mean contours of ξ are not affected by the co-flow velocity (U_{air}) and consequently $\mathcal{R}e_{turb}$.
- Even for the highest υ_{fuel} of around 4 the mean mixture fraction decays quickly to less than 0.1 by $\frac{z}{d_{IN}} = 20$.

- The effect of increasing $\mathcal{R}e_{turb}$ (or U_{air}) is to increase $\langle \xi'^2 \rangle$ and $\langle \chi \rangle$ closer to the injector, whereas far downstream these quantities remain largely unchanged.
- The effect of increasing υ_{fuel} is to shift the contours of $\langle \xi \rangle$, $\langle \xi'^2 \rangle$ and $\langle \chi \rangle$ downstream.
- In the equal velocity flows the centerline profiles of pdf($\xi = \xi_{MR}$) rise from zero at the injector to a maximum value and decay downstream. The maxima occur at relatively short lengths from the injector, specifically 10 – 30 mm at the tested conditions. The effect of increasing U_{air} is to decrease the values of the maxima, bring them closer to the injector and to decrease the values of pdf($\xi = \xi_{MR}$) downstream of the maxima, both in terms of distance (z) and residence time ($\frac{z}{U_{air}}$). The effect of increasing ξ_{MR} is to decrease the pdfs at z and $\frac{z}{U_{air}}$ downstream of the maxima.
- In the equal velocity flows an increase in U_{air} increases $\langle \chi \rangle$ and $\langle \chi | \xi = \xi_{MR} \rangle$ at the same physical location, decreases pdf($\chi | \xi = \xi_{MR}$) at lower values of $\chi | \xi = \xi_{MR}$ and increases pdf($\chi | \xi = \xi_{MR}$) at higher values of $\chi | \xi = \xi_{MR}$.
- In the equal velocity flows $\langle \chi | \xi = \xi_{MR} \rangle$ decays monotonically from short distances to the injector. The increase in $\langle \chi | \xi = \xi_{MR} \rangle$ due to U_{air} is *not* collapsed by $\frac{z}{U_{air}}$, or, after the same residence time from injection $\langle \chi | \xi = \xi_{MR} \rangle$ is locally still higher for higher U_{air}.
- The timescale ratio value of "2" is indeed reached by $10 d_{IN}$ along the centerline from injection. This value is attained from this length to as far downstream as there is available data, i.e. $26 d_{IN}$ or about 60 mm.

This data, together with the knowledge of the velocity and temperature in the tube that has been gained from this chapter will be used in **Chapters 6** and **7** to try to explain the observed trends of autoignition that resulted from changes in the independent experimental parameters, such as T_{air}, U_{air} and υ_{fuel}.

3.5 Characterization Chapter Figures

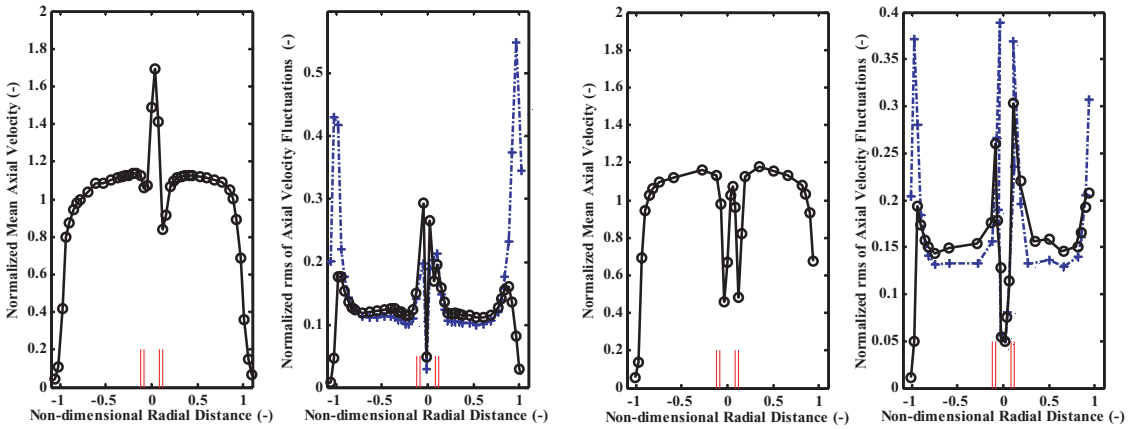

Figure 3.1: Mean and rms of axial velocity at cold conditions (cont. on next page). All data taken with a hot wire. Injector inner and outer diameters shown close to the centreline. Normalized mean velocities are relative to the bulk velocity U_{air}. Normalized rms velocities are relative to both the local mean (blue dash-dot lines) and the bulk (black solid lines). For all data the corresponding measured integral lengthscales can be found in **Figure 3.4**. (a) $z = 2$ mm: $U_{air} = 2.50$ m/s, $\upsilon_{fuel} = 1.15$, $\rho_{air} = 1.192$ kg.m^{-3}, $\mathcal{R}e_{turb} = 60$. From 21,000 samples taken at 410 Hz. (b) $z = 2$ mm: $U_{air} = 4.37$ m/s, $\upsilon_{fuel} = 0.60$, $\rho_{air} = 1.175$ kg.m^{-3}, $\mathcal{R}e_{turb} = 100$. From 36,000 samples taken at 480 Hz.

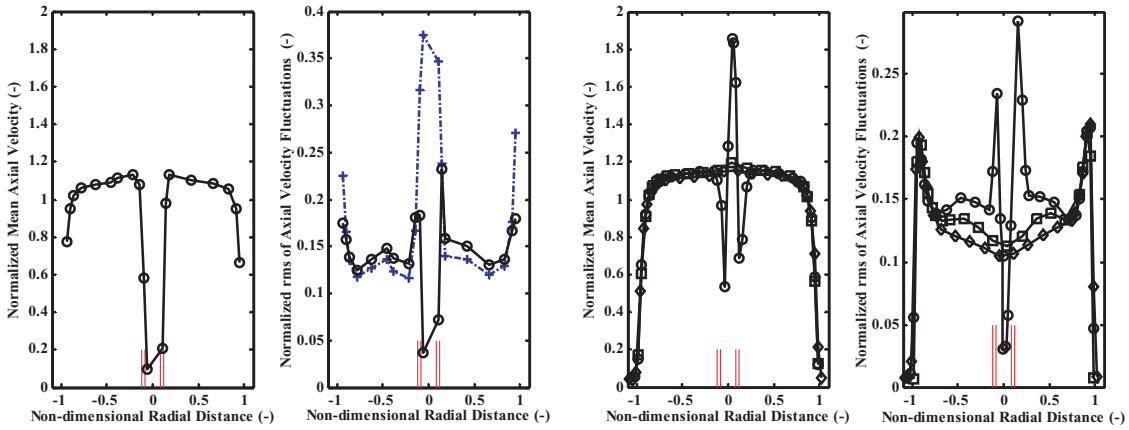

(c) (d)

Figure 3.1: Mean and rms of axial velocity at cold conditions (cont. from previous page). All data taken with a hot wire. Injector inner and outer diameters shown close to the centreline. Normalized rms velocities are relative to both the local mean (blue dash-dot lines) and the bulk (black solid lines). For all data the corresponding measured integral lengthscales can be found in **Figure 3.4**. (c) $z = 1$ mm: $U_{air} = 3.71$ m/s, $v_{fuel} = 0$, $\rho_{air} = 1.216$ kg.m^{-3}, $\mathcal{R}e_{turb} = 90$. From 29,000 samples taken at 410 Hz. (d) $z = 2$ mm (circles), 22 mm (squares) and 42 mm (diamonds): $U_{air} = 3.66$ m/s, $v_{fuel} = 1.05$, $\rho_{air} = 1.175$ kg.m^{-3}, $\mathcal{R}e_{turb} = 85$. From 29,000 samples taken at 410 Hz.

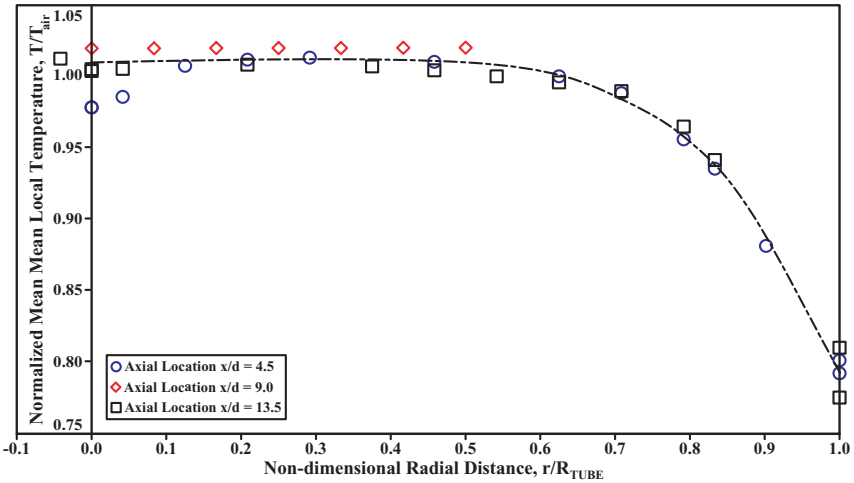

(a)

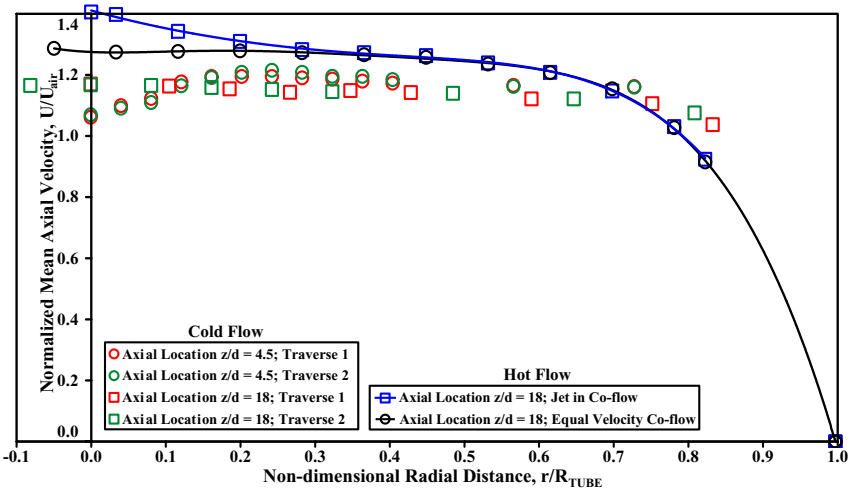

(b)

Figure 3.2: Mean temperature and axial velocity at hot conditions. Pitot tube velocity measurement corrected for local temperature, measured with a thermocouple in the vicinity of the pitot tube. For the cold flow profiles $U_{air} = 11.7$ m/s and $\upsilon_{fuel} = 0$. For the hot flow, the equal velocity profile has $T_{air} = 839$ K, $U_{air} = 10.2$ m/s and $\upsilon_{fuel} = 1.00$. For the jet $T_{air} = 822$ K, $U_{air} = 10.0$ m/s and $\upsilon_{fuel} = 2.20$. (a) Local corrected temperature used to calculate the local air density and consequently the local values of U provided in (b).

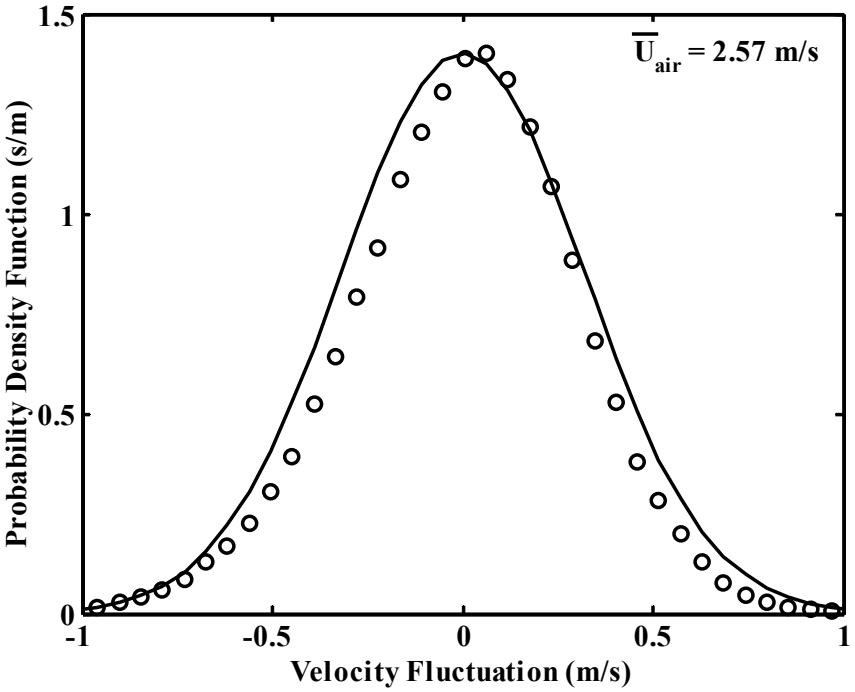

Figure 3.3: Pdf of velocity with best Gaussian fit. Data taken from measurement giving red solid lines in **Figure 3.5**. On the independent axis is the velocity fluctuation. Compare with the pdf of temperature and corresponding best Gaussian fit of **Figure 3.9**.

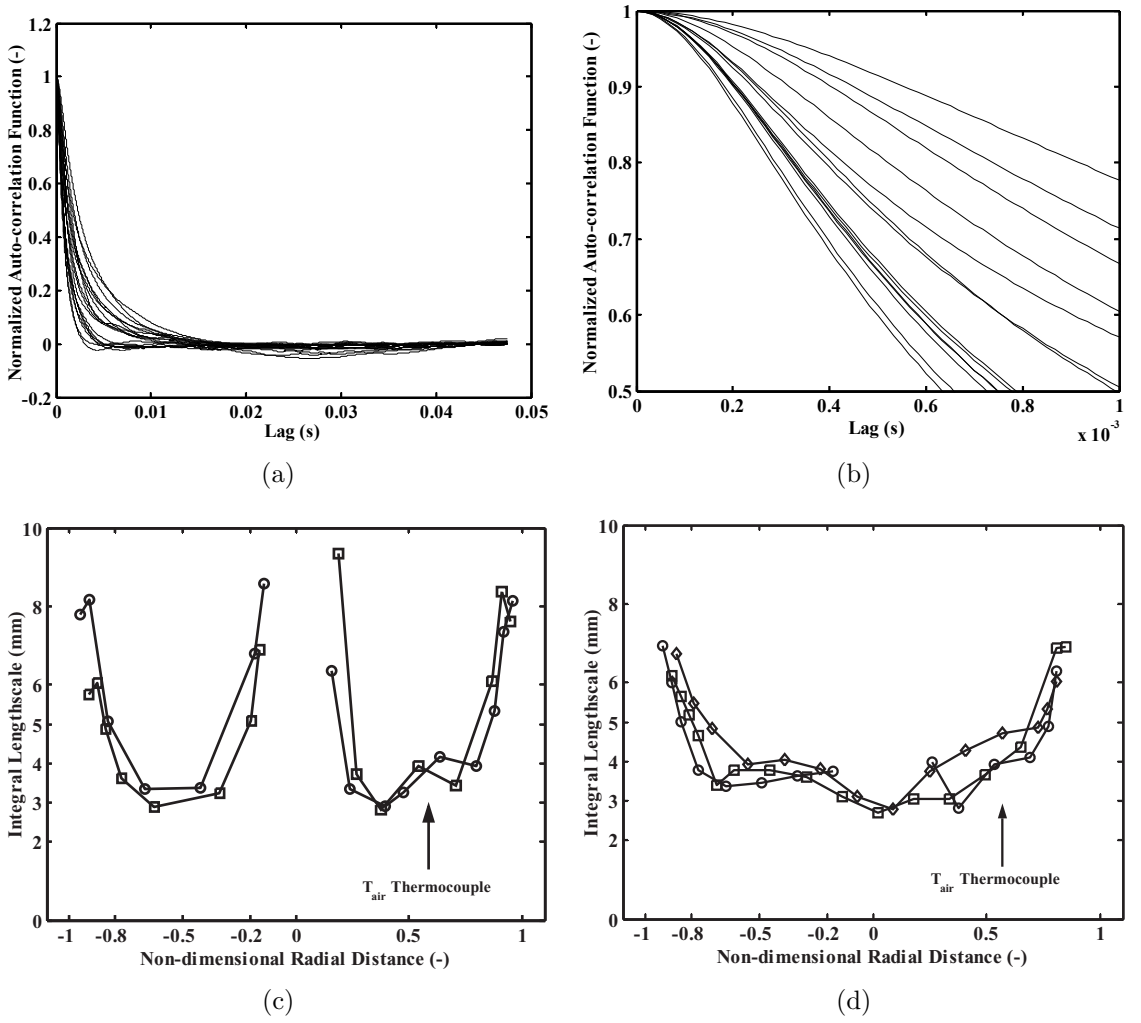

Figure 3.4: Longitudinal autocorrelation functions and integral lengthscales. From hot wire at cold conditions. (a) Typical autocorrelation functions normalized by the variance of the velocity in order to set the function to unity at zero lag. Extent of independent axis shows length of integration for the evaluation of the integral length. (b) Close-up of (a) near the zero-lag region to show the temporal resolution of the measurements. (c) Integral lengthscales corresponding to **Figure 3.1(b)**: $z =$ 2 mm; $U_{air} = 4.37$ m/s, $\upsilon_{fuel} = 0.60$, $\rho_{air} = 1.175$ kg.m^{-3}, $\mathcal{R}e_{turb} = 100$ (squares) and **Figure 3.1(c)**: $z = 1$ mm; $U_{air} = 3.71$ m/s, $\upsilon_{fuel} = 0$, $\rho_{air} = 1.216$ kg.m^{-3}, $\mathcal{R}e_{turb} = 90$ (circles). (d) Integral lengthscales corresponding to **Figure 3.1(d)**: $z = 2$ mm (circles), 24 mm (squares) and 44 mm (diamonds); $U_{air} = 3.66$ m/s, $\upsilon_{fuel} = 1.05$, $\rho_{air} = 1.175$ kg.m^{-3}, $\mathcal{R}e_{turb} = 85$. The Taylor hypothesis used to estimate the integral length breaks down in regions lacking isotropy, such as closer to the walls and in the injected flow. The wall regions can be located in the plots of **Figure 3.1**, where the normalized rms is becomes high.

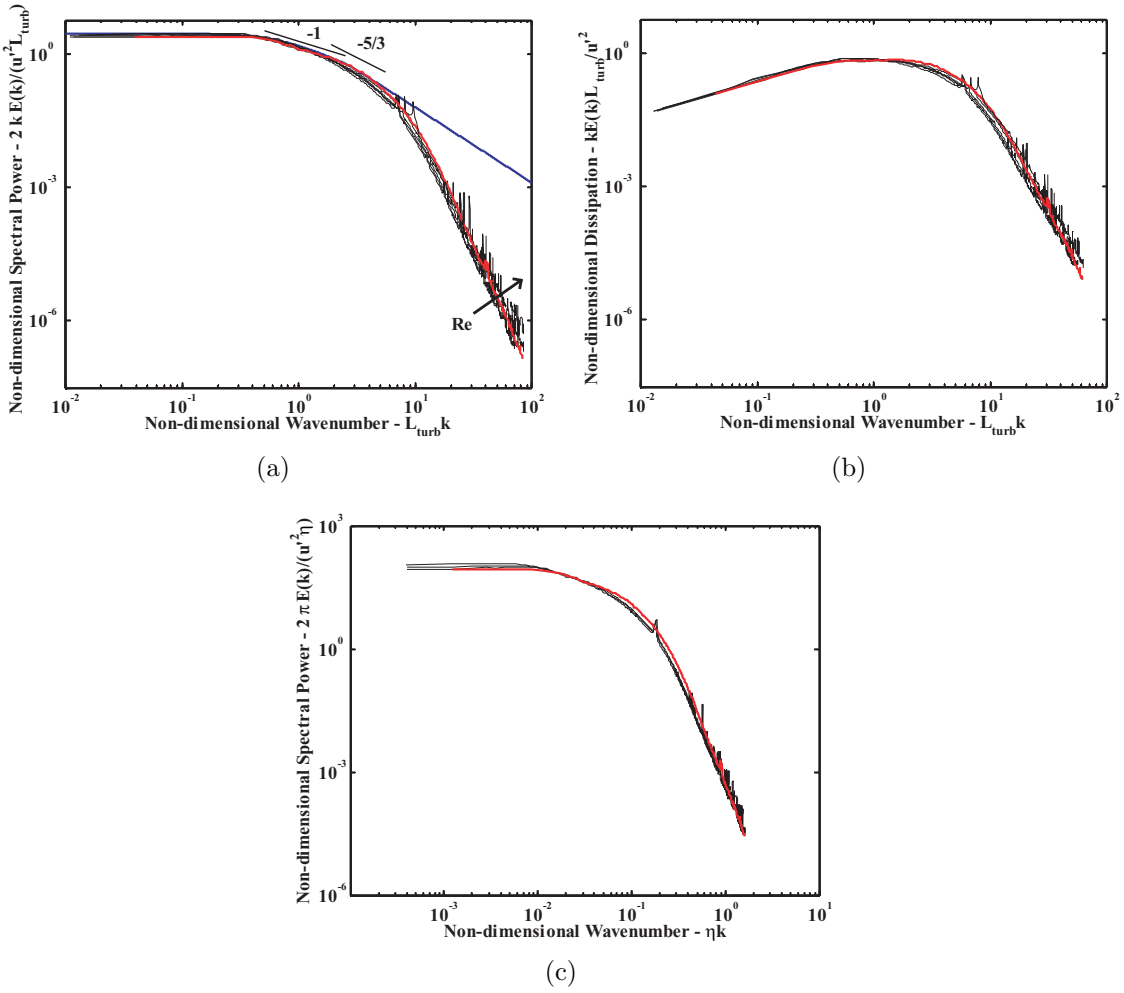

Figure 3.5: Normalized spectral power of turbulent velocity and dissipation. From hot wire at cold conditions. Thin, black lines are for $\mathcal{R}e_{turb} = 100$, $U_{air} = 4.4$ m/s (see **Table 3.1**). Red line is for $\mathcal{R}e_{turb} = 55$, $U_{air} = 2.3$ m/s (see **Table 3.1**), with local $U = 2.6$ m/s, $L_{turb} = 4.8$ mm and $\frac{u'}{U} = 0.13$ at $z = 1$ mm and $\frac{r}{R_{TUBE}} = 0.5$. (a) Velocity as a function of non-dimensional wavenumber (k) based on the measured integral length (L_{turb}). Local U varies in the range 4.9 – 5.2 m/s, L_{turb} in the range 3.0 – 4.2 mm and $\frac{u'}{U} = 0.15$ – 0.16 at $z = 2$ mm and $\frac{r}{R_{TUBE}} = 0.3$ – 0.6. Blue solid line is the Von Karman relation (**Equation 3.1**) for isotropic turbulence and no dissipation. (b) Dissipation as a function of wavenumber based on the measured L_{turb}. Theoretically expected to peak to a value of unity at $k = \frac{1}{L_{turb}}$. (c) Velocity as a function of wavenumber based on the measured Kolmogorov length (η_k).

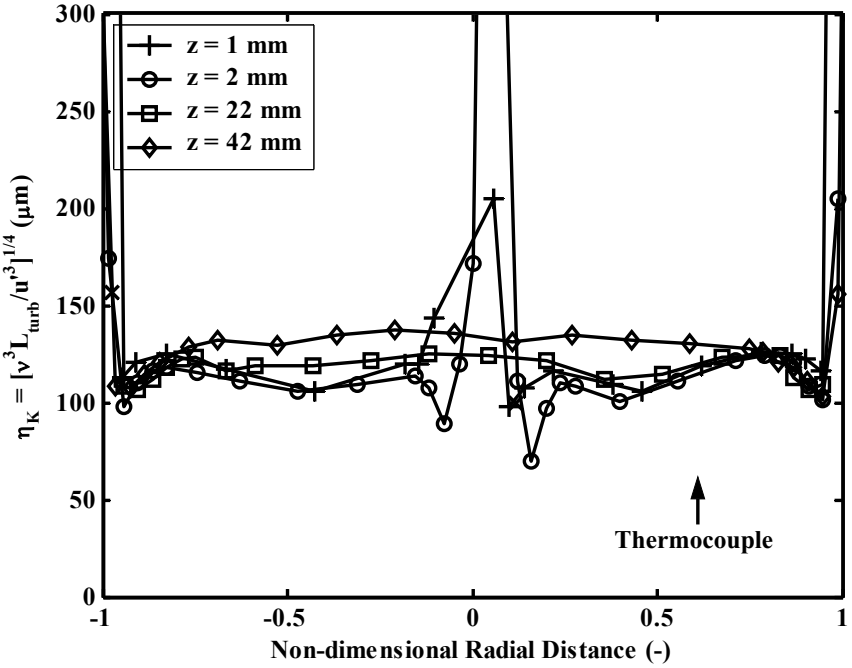

Figure 3.6: Estimated evolution of Kolmogorov lengthscale in the domain. Radial profiles at z = 1, 2, 22 and 42 mm from the injector, for $Re_{turb} = 85$. In this plot η_K is estimated from L_{turb} as indicated.

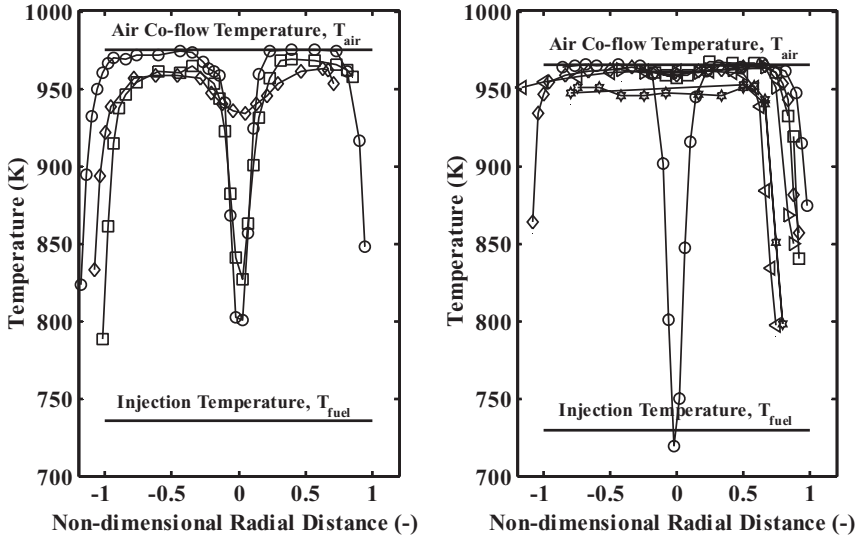

(a)

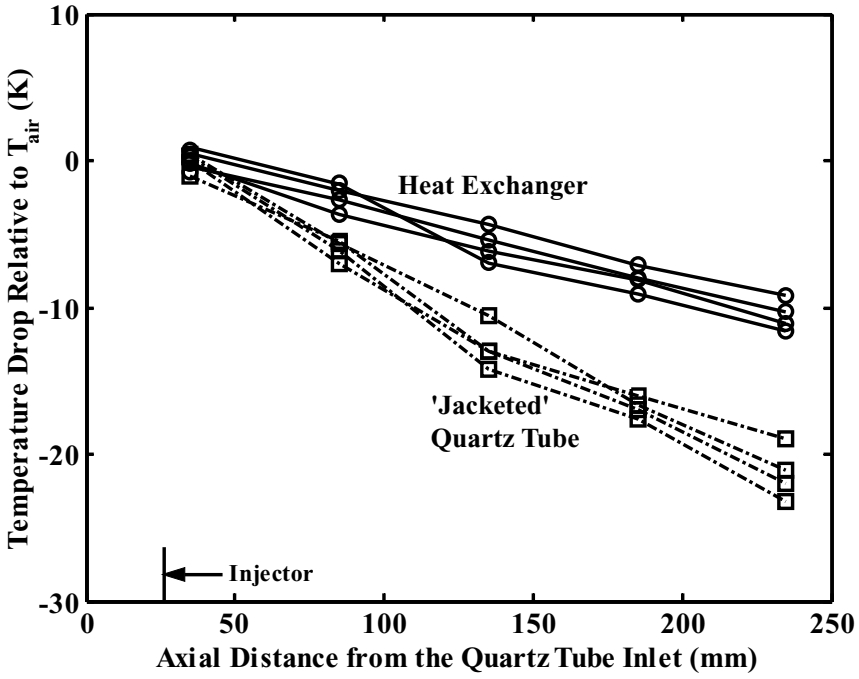

(b)

Figure 3.7: Radial and axial mean temperature profiles. (a) Mean radial profiles at various axial distances and for two (left and right) settings of T_{air} and T_{fuel}. Data with thin quartz tubes, not well-insulated 'jacketed' or 'blanket-insulated' tubes. Left: Figure extends from 0 to 40 mm downstream of the injector in steps of 20 mm. Right: Figure extends from 0 to 80 mm downstream of the injector in steps of 10, 20, 30, 40 and 80 mm. (b) Mean axial profiles for T_{air} spanning the range 820 – 920 K and U_{air} between 11 m/s and 17 m/s. Axial heat loss comparison between 'jacketed' tube and same tube with additional heat exchanger.

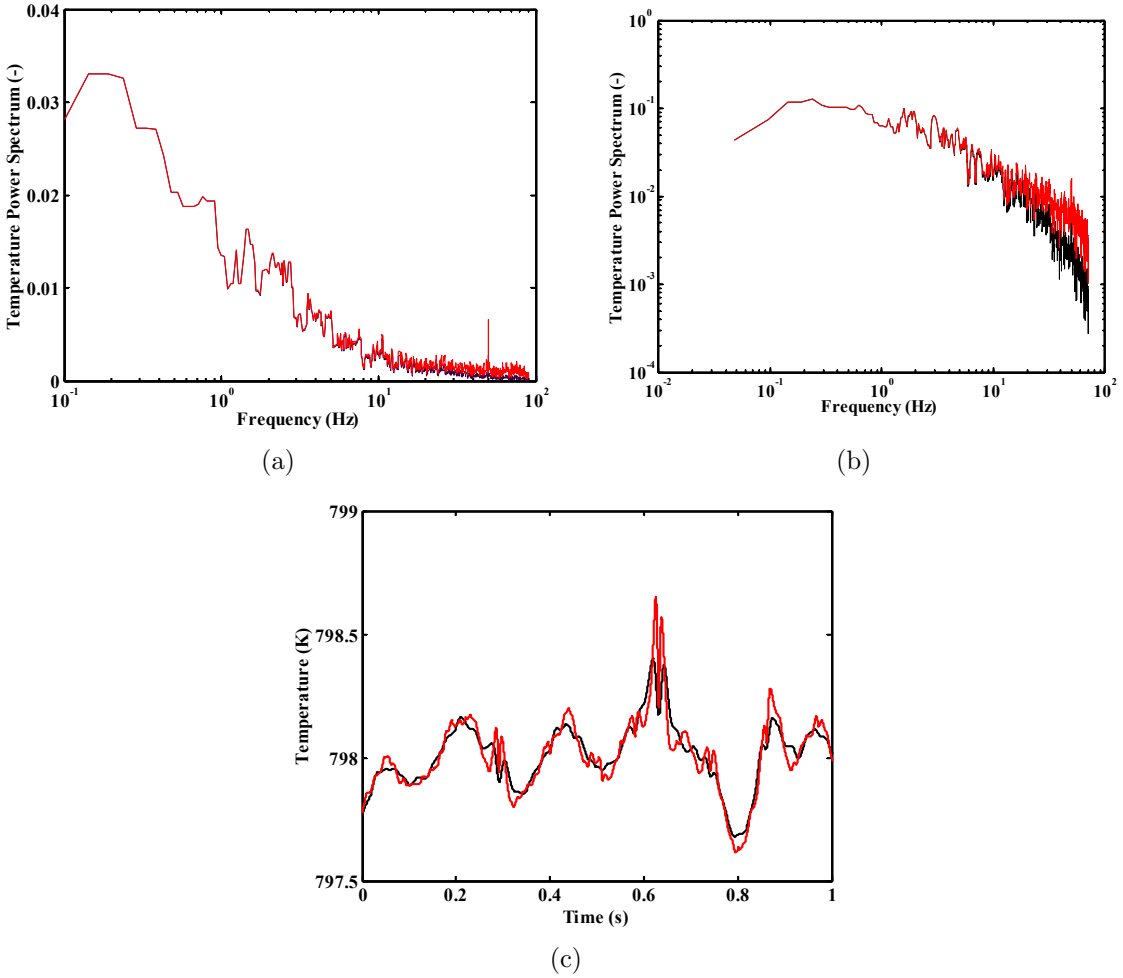

Figure 3.8: Temperature compensation for correct estimation of temperature fluctuations. (a) Semi-log, and, (b) log-log power spectra of two different temperature signals. Raw in black solid lines and compensated in red. (c) Raw and corresponding compensated temperature time-series.

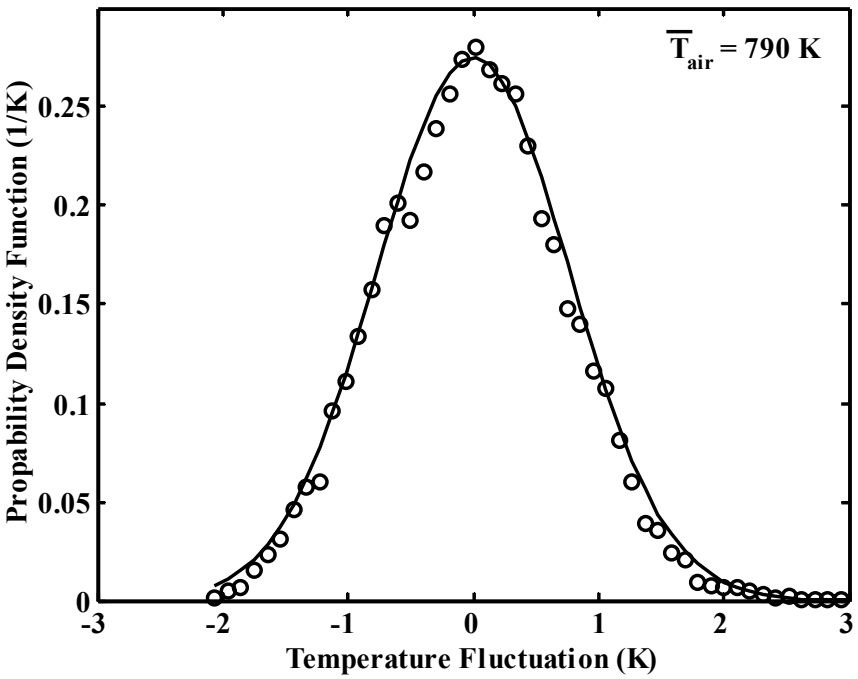

Figure 3.9: Pdf of temperature with best Gaussian fit. On the independent axis is the temperature fluctuation, i.e. the random variable minus the mean. T'_{air} here is about 0.7 K. Compare with the pdf of velocity and corresponding best Gaussian fit of **Figure 3.3**.

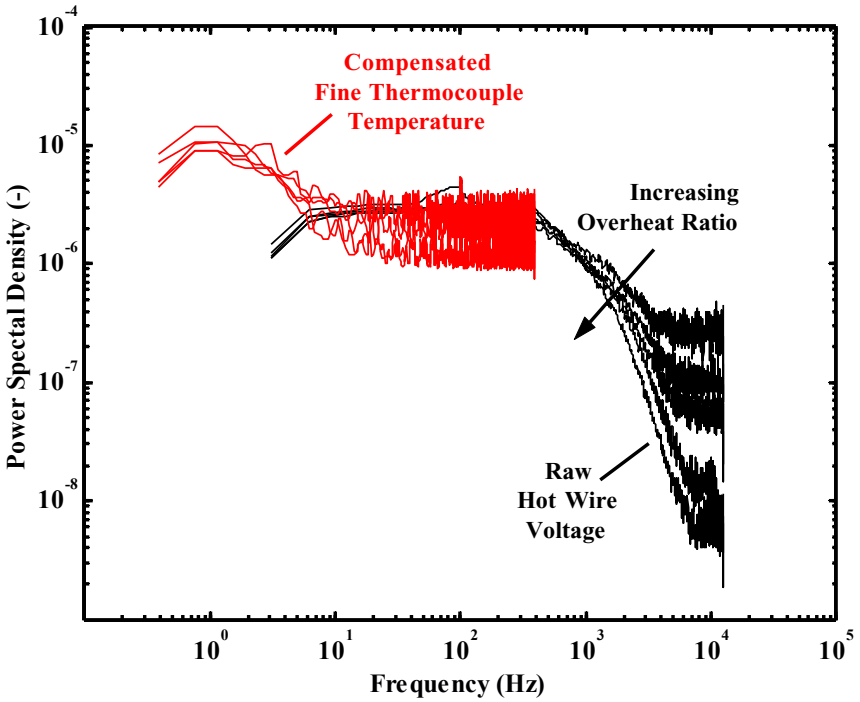

Figure 3.10: Simultaneous raw hot wire voltage and compensated temperature spectra.

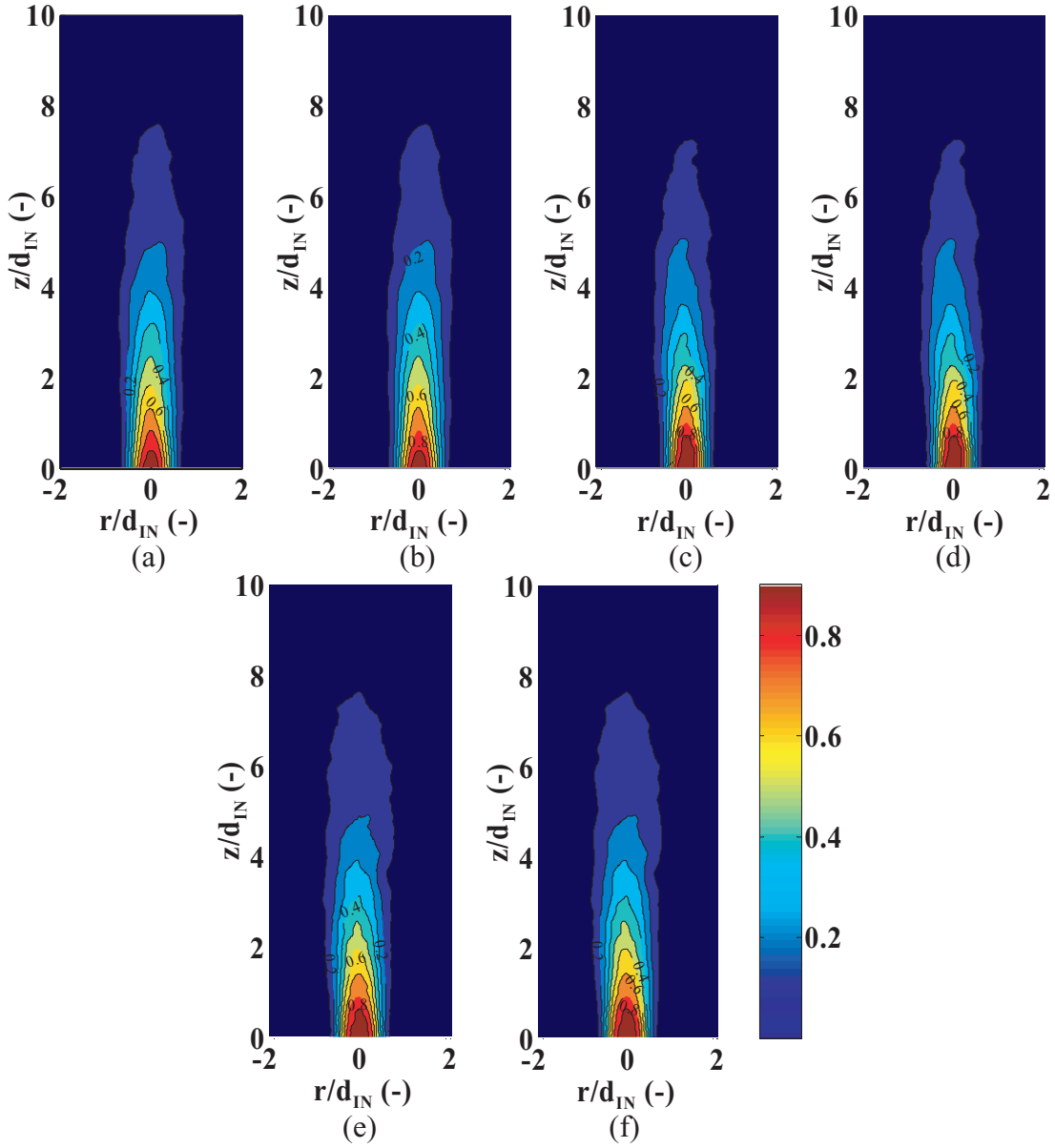

Figure 3.11: Mean mixture fraction contours for equal velocity. (a) $\langle \xi_1 \rangle$, and, (b) $\langle \xi_2 \rangle$ at $\mathcal{R}e_{turb} = 50$, $\upsilon_{fuel} = 0.95$, $\varpi_{fuel} = 1.00$, $Y_{C2H2} = 0.73$. (c) $\langle \xi_1 \rangle$, and, (d) $\langle \xi_2 \rangle$ at $\mathcal{R}e_{turb} = 65$, $\upsilon_{fuel} = 0.95$, $\varpi_{fuel} = 1.00$, $Y_{C2H2} = 0.73$. (e) $\langle \xi_1 \rangle$, and, (f) $\langle \xi_2 \rangle$ at $\mathcal{R}e_{turb} = 90$, $\upsilon_{fuel} = 1.00$, $\varpi_{fuel} = 0.35$, $Y_{H2} = 0.15$. Colour key for all plots.

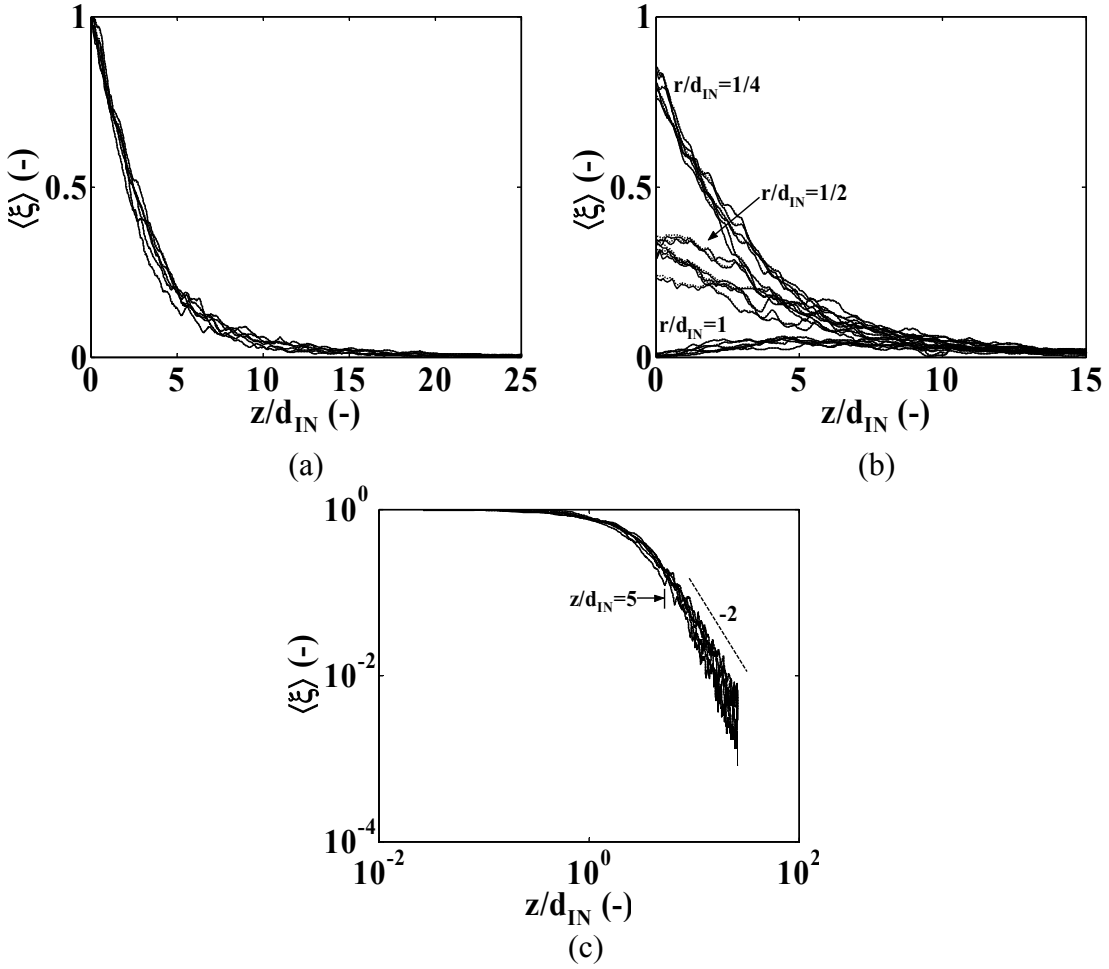

Figure 3.12: Axial profiles of the mean mixture fraction for equal velocity. (a) Centreline decay ($r = 0$) of $\langle \xi_1 \rangle$ (solid lines) and $\langle \xi_2 \rangle$ (dashed lines) for various $\mathcal{R}e_{turb} = 50$ – 90, $\upsilon_{fuel} = 0.95$ – 1.00 and for both acetylene (with $\varpi_{fuel} = 1.00$ and $Y_{C2H2} = 0.73$) and hydrogen (with $\varpi_{fuel} = 0.35$ and $Y_{H2} = 0.15$). (b) Centreline decay for off-axis radial locations with $\frac{r}{d_{IN}} = 0.25$, 0.50 and 1.00 as indicated. Conditions as in (a). (c) Logarithmic (to the base-10) plots of centreline decay ($r = 0$) data presented in (a).

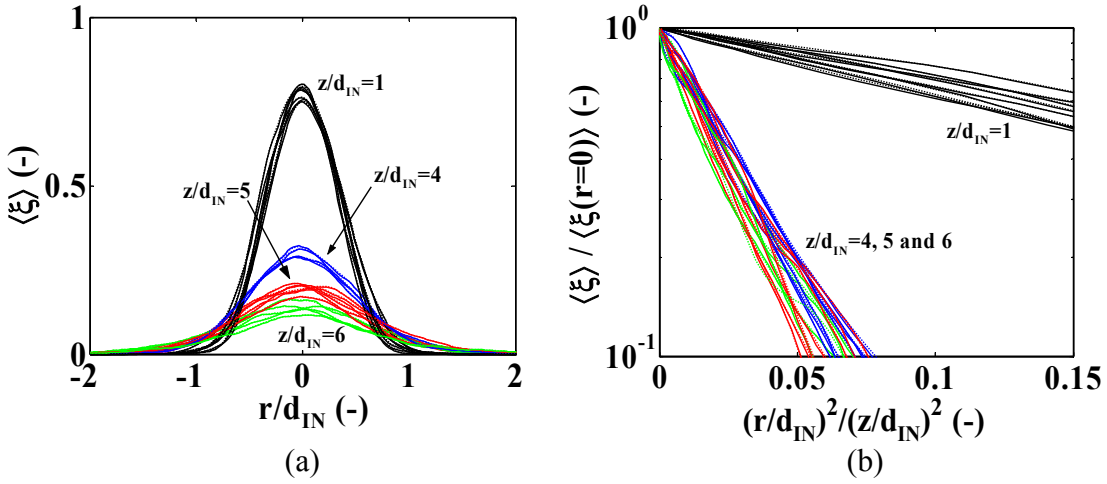

Figure 3.13: Radial profiles of the mean mixture fraction for equal velocity. (a) Standard, and, (b) Normalized, semi-logarithmic plots of radial profiles of $\langle \xi_1 \rangle$ (solid lines) and $\langle \xi_2 \rangle$ (dashed lines) for various $\mathcal{R}e_{turb} = 50 - 90$, $\upsilon_{fuel} = 0.95 - 1.00$ and for both acetylene (with $\varpi_{fuel} = 1.00$ and $Y_{C2H2} = 0.73$) and hydrogen (with $\varpi_{fuel} = 0.35$ and $Y_{H2} = 0.15$). Profiles taken at axial locations with $\frac{z}{d_{IN}} = 1$, 4, 5 and 6 as indicated.

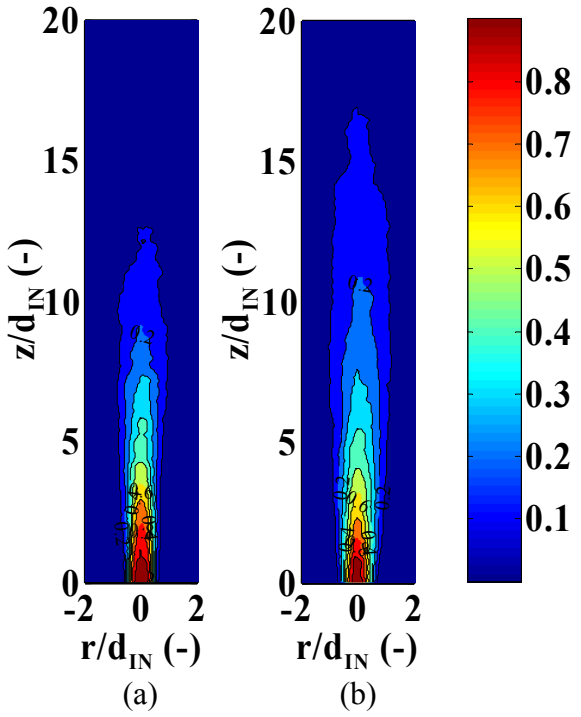

Figure 3.14: Mean mixture fraction contours for jet in co-flow. (a) $\langle \xi_2 \rangle$ at $\mathcal{R}e_{turb} = 90$, $\upsilon_{fuel} = 2.00$, $\varpi_{fuel} = 0.35$, $Y_{H2} = 0.15$. Can be directly compared to **Figure 3.11(f)** (same conditions as here but with $\upsilon_{fuel} = 1.00$). (b) $\langle \xi_2 \rangle$ at $\mathcal{R}e_{turb} = 110$, $\upsilon_{fuel} = 3.90$, $\varpi_{fuel} = 0.40$, $Y_{H2} = 0.12$. Colour key for both plots.

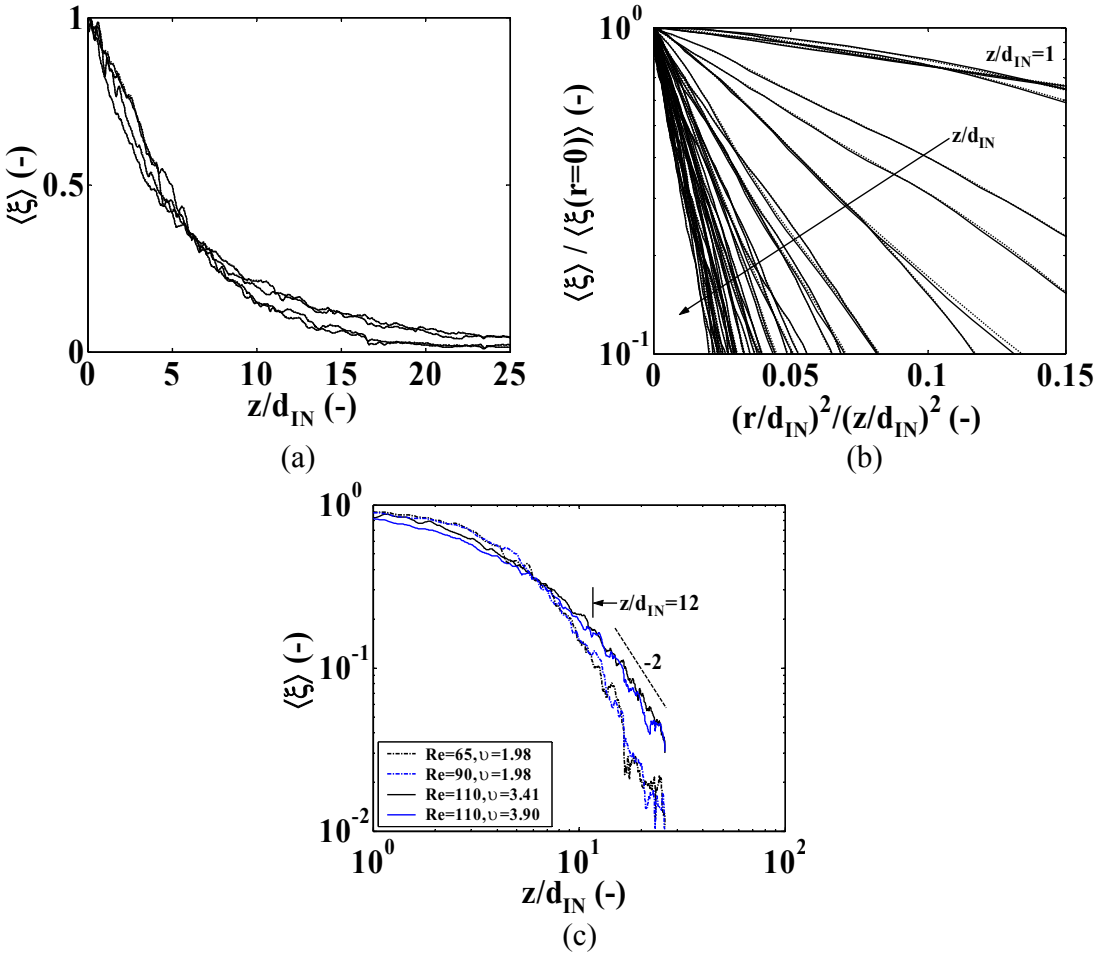

Figure 3.15: Axial and radial profiles of the mean mixture fraction for jet in co-flow. (a) Centreline decay ($r = 0$) of $\langle \xi_1 \rangle$ (solid lines) and $\langle \xi_2 \rangle$ (dashed lines) for the cases of: (i) $\mathcal{R}e_{turb} = 65$ and 90, $\upsilon_{fuel} = 2.00$, and, (ii) $\mathcal{R}e_{turb} = 110$, $\upsilon_{fuel} = 3.40$ and 3.90 for hydrogen. Across all conditions $\varpi_{fuel} = 0.35$ – 0.40 and $Y_{H2} = 0.12$ – 0.15. (b) Normalized, semi-logarithmic plots of radial profiles of $\langle \xi_1 \rangle$ (solid lines) and $\langle \xi_2 \rangle$ (dashed lines) for the same conditions as in (a). Profiles taken at axial locations with $\frac{z}{d_{IN}} = 1$ – 12 in unity steps, as indicated. (c) Logarithmic plots of $\langle \xi_2 \rangle$ centreline decay data presented in (a).

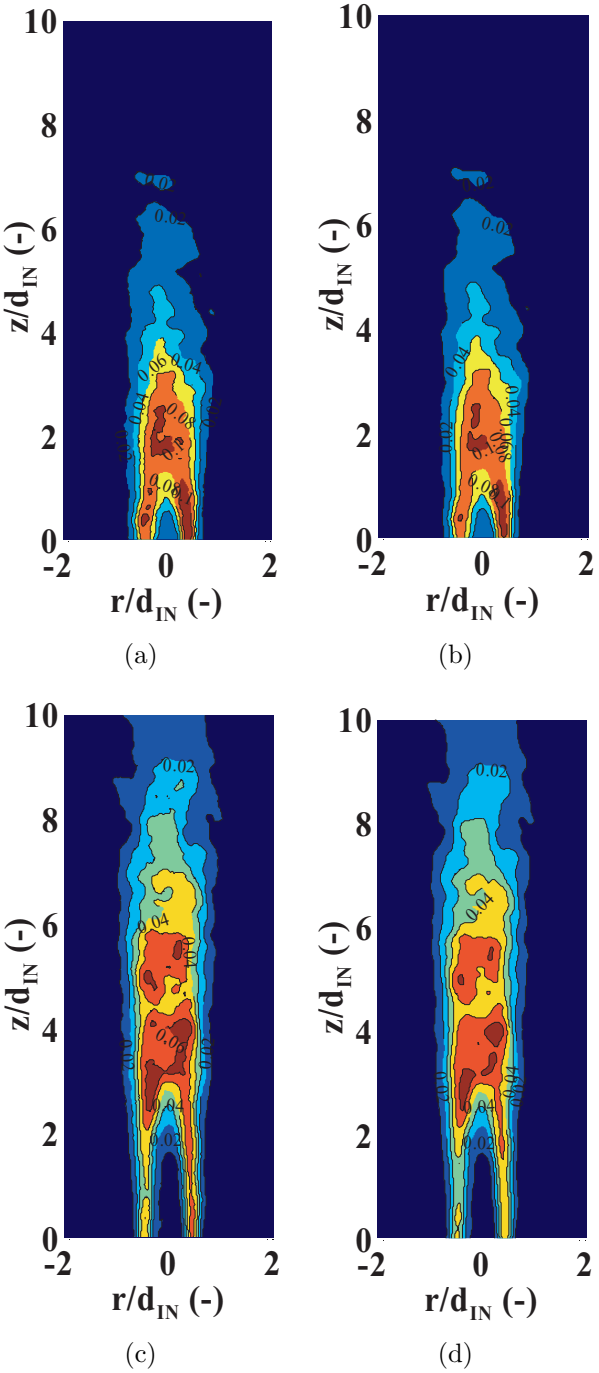

Figure 3.16: Contours of the variance of the fluctuations of the mixture fraction. (a) $\langle \xi_1'^2 \rangle$, and, (b) $\langle \xi_2'^2 \rangle$ at $\mathcal{R}e_{turb} = 65$, $\upsilon_{fuel} = 0.95$, $\varpi_{fuel} = 0.35$, $Y_{H2} = 0.14$. (c) $\langle \xi_1'^2 \rangle$, and, (d) $\langle \xi_2'^2 \rangle$ at $\mathcal{R}e_{turb} = 65$, $\upsilon_{fuel} = 1.85$, $\varpi_{fuel} = 0.40$, $Y_{H2} = 0.14$.

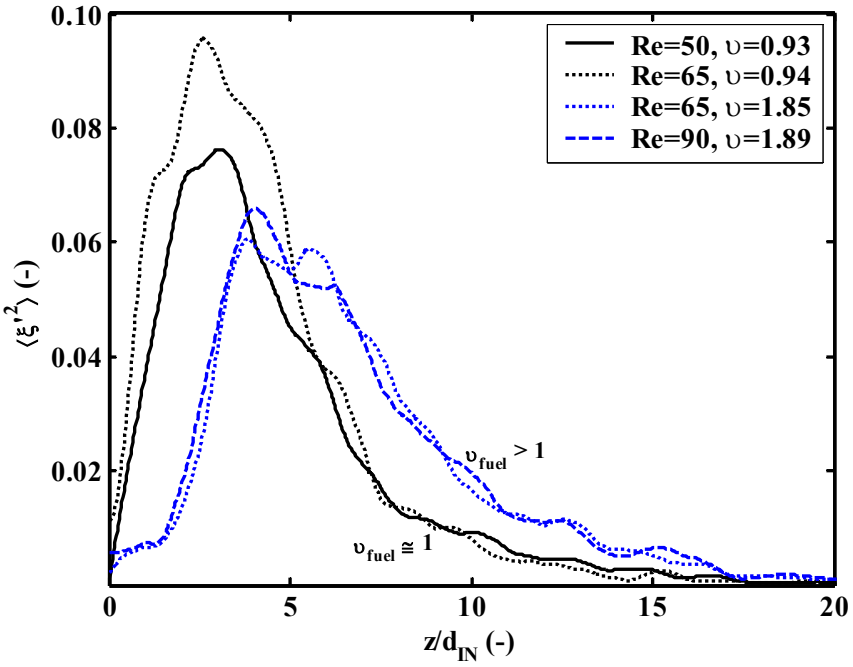

(a)

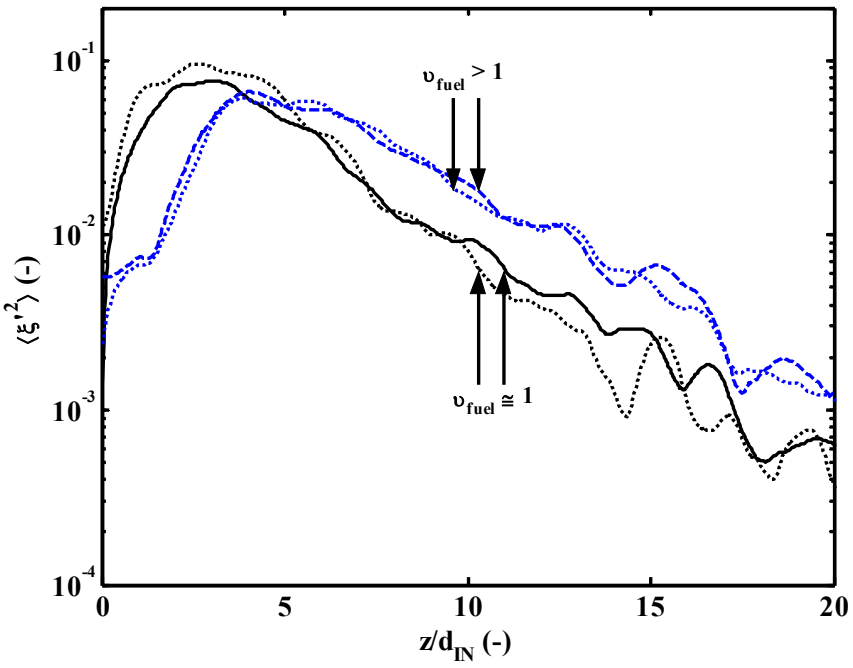

(b)

Figure 3.17: Axial Profiles of the variance of the fluctuations of the mixture fraction. Centreline decay ($r = 0$) of $\langle \xi_2'^2 \rangle$ for cases: $\mathcal{R}e_{turb} = 50$, 65 and 90 with $\upsilon_{fuel} = 0.95$, 0.95, 1.85 and 1.90 respectively as indicated in the legend. For the first 2 conditions $\varpi_{fuel} = 1.00$ and $Y_{C2H2} = 0.73$. For the last 2, $\varpi_{fuel} = 0.35 - 0.40$ and $Y_{H2} = 0.14 - 0.15$. (a) Linear, and, (b) Semi-logarithmic plots.

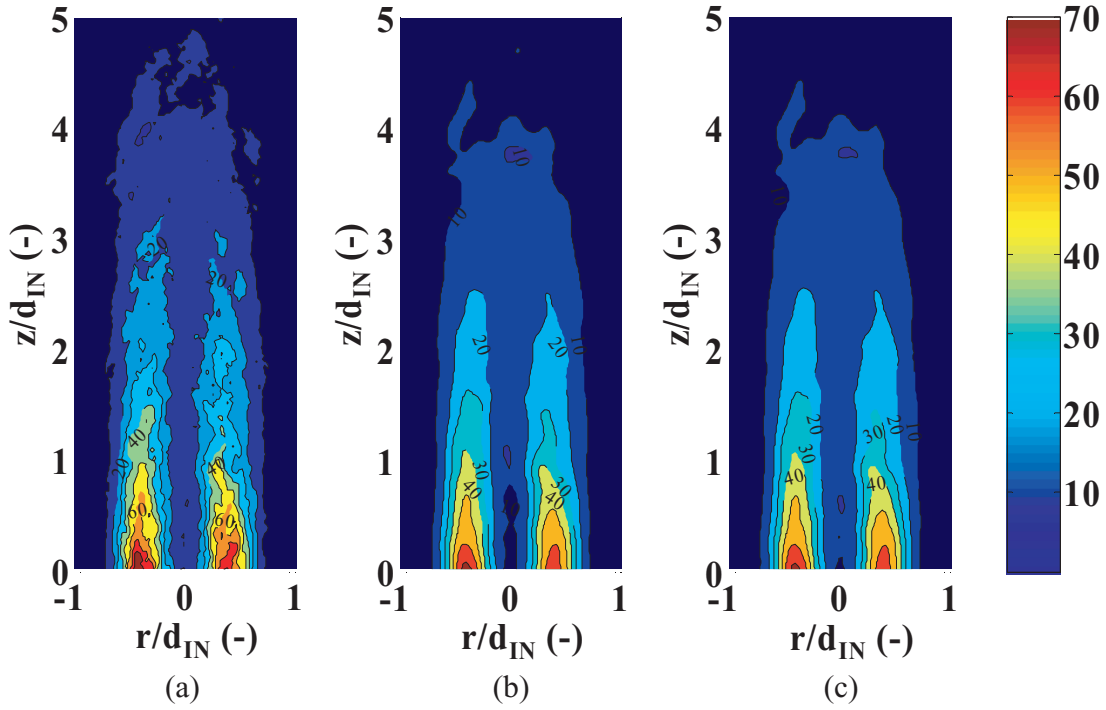

Figure 3.18: Contours of the mean two-dimensional scalar dissipation rate. (a) $\langle \chi_1 \rangle$, (b) $\langle \chi_2 \rangle$, and, (c) $\langle \chi_3 \rangle$ at the same conditions as **Figure 3.11(a)**. $\mathcal{R}e_{turb} = 50$, $\upsilon_{fuel} = 0.95$, $\varpi_{fuel} = 1.00$ with $Y_{C2H2} = 0.73$. Colour key for all plots.

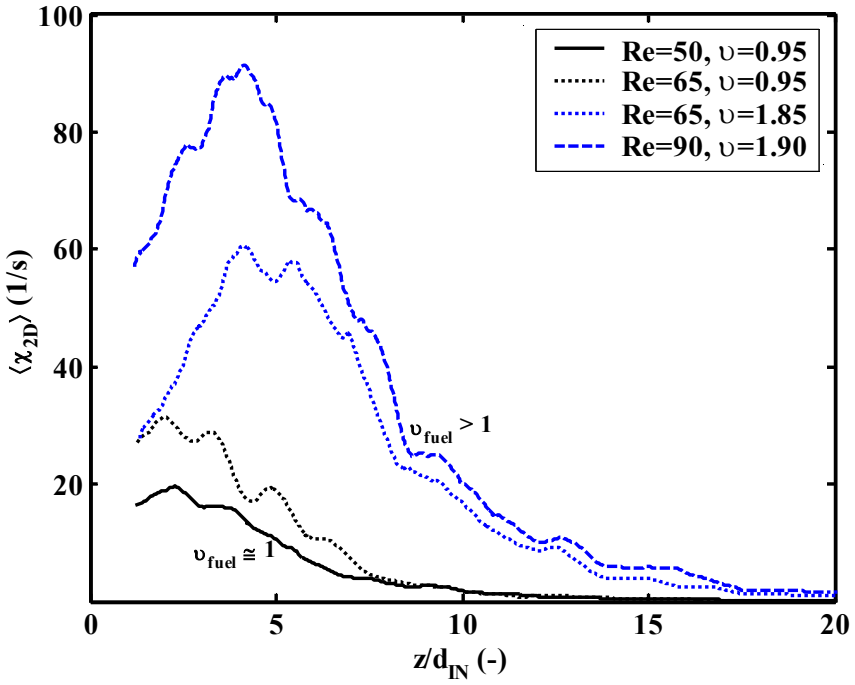

(a)

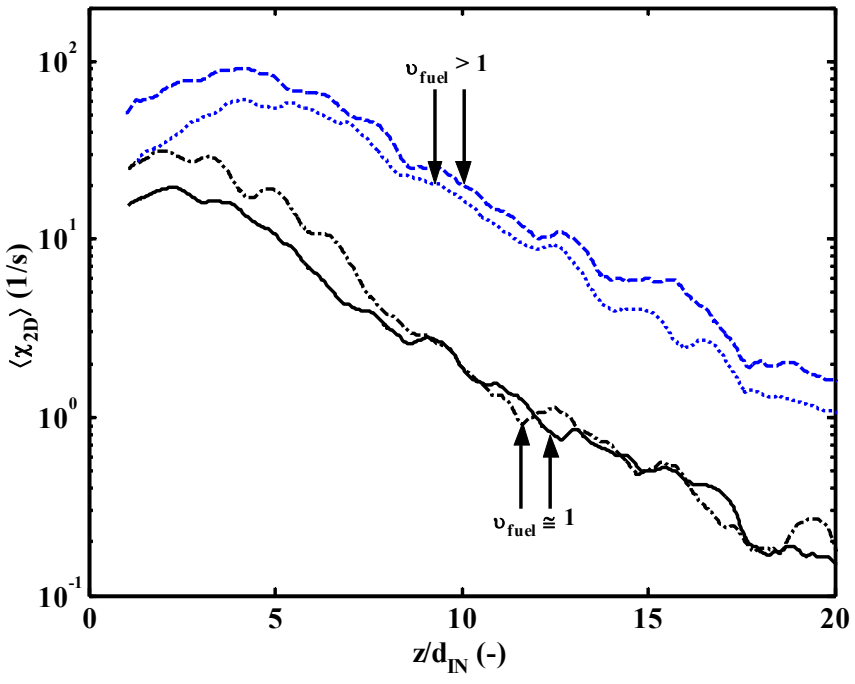

(b)

Figure 3.19: Axial profiles of the mean two-dimensional scalar dissipation rate. Centreline decay ($r = 0$) of $\langle \chi_2 \rangle$ at the same conditions as **Figure 3.17**. (a) Linear, and, (b) Semi-logarithmic plots.

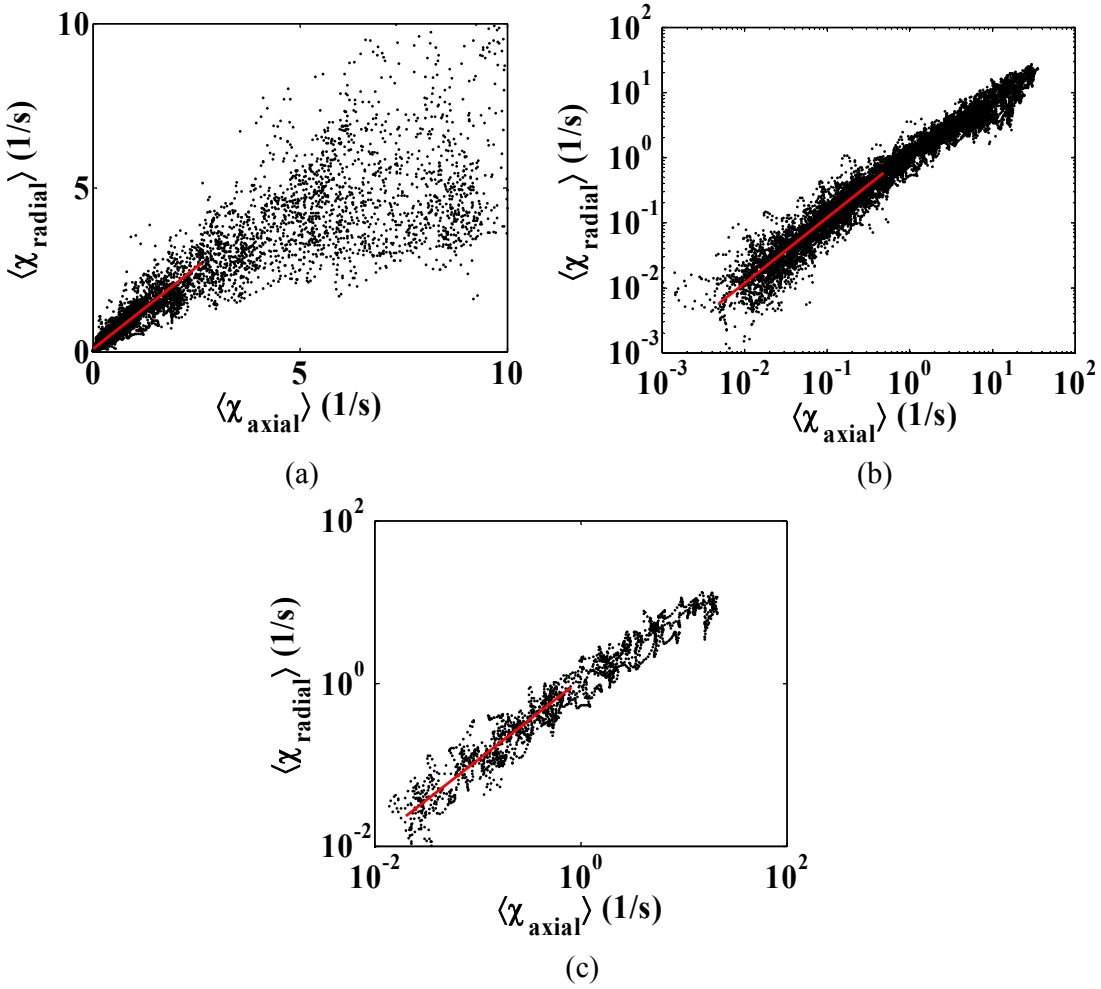

Figure 3.20: Mean axial and radial contributions to two-dimensional scalar dissipation. Isotropic mixing indicated by red lines. (a) Linear, and, (b) Logarithmic plots of axial and radial components of centreline $\langle \chi_2 \rangle$ at the same conditions as **Figure 3.16(e)**. (c) Logarithmic plot of axial and radial components of $\langle \chi_2 \rangle$ at the same conditions as **Figure 3.16(e)**, but for the complete downstream region ($0 \leq r < d_{IN}$) described by $\frac{z}{d_{IN}} > 3$.

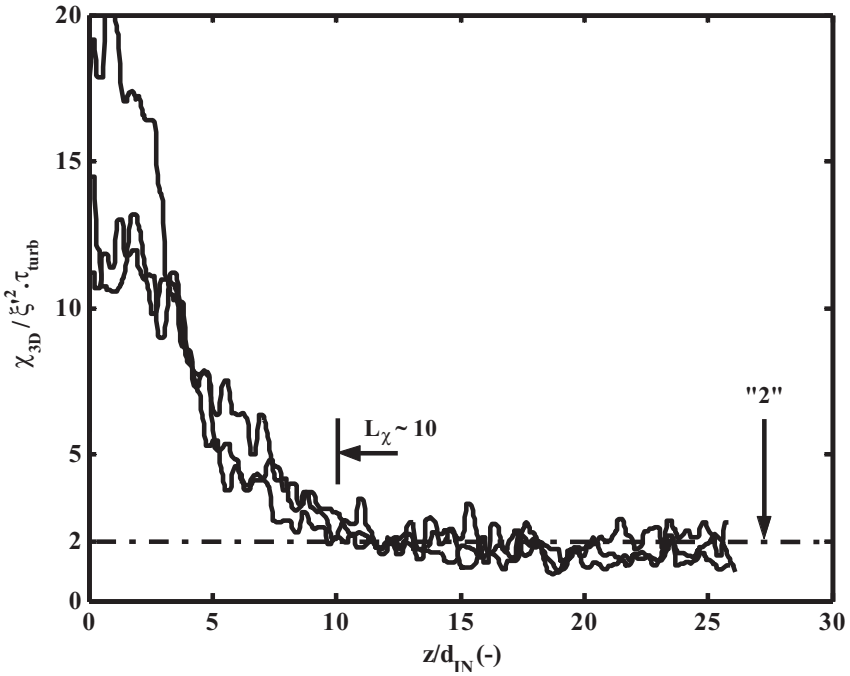

(a)

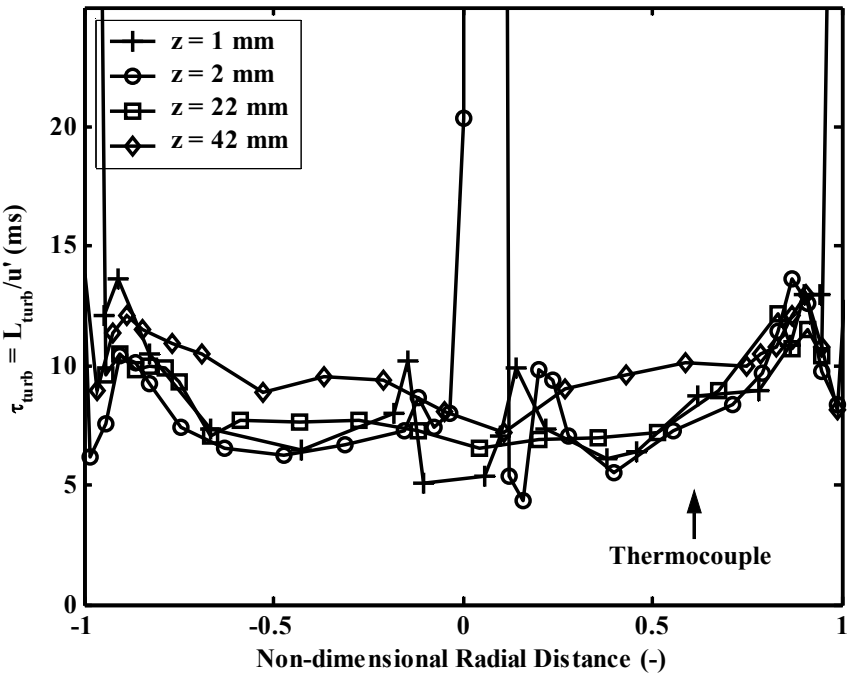

(b)

Figure 3.21: Measurements of timescale ratio. (a) Axial profiles of C_D at the same conditions as **Figure 3.17**. Centreline decay approximately reaches a value of "2" at L_χ as indicated. (b) Evolution of $\tau_{turb} = \frac{L_{turb}}{u'}$ in the domain. Radial profiles at $z = 1$, 2, 22 and 42 mm from the injector, for $Re_{turb} = 85$.

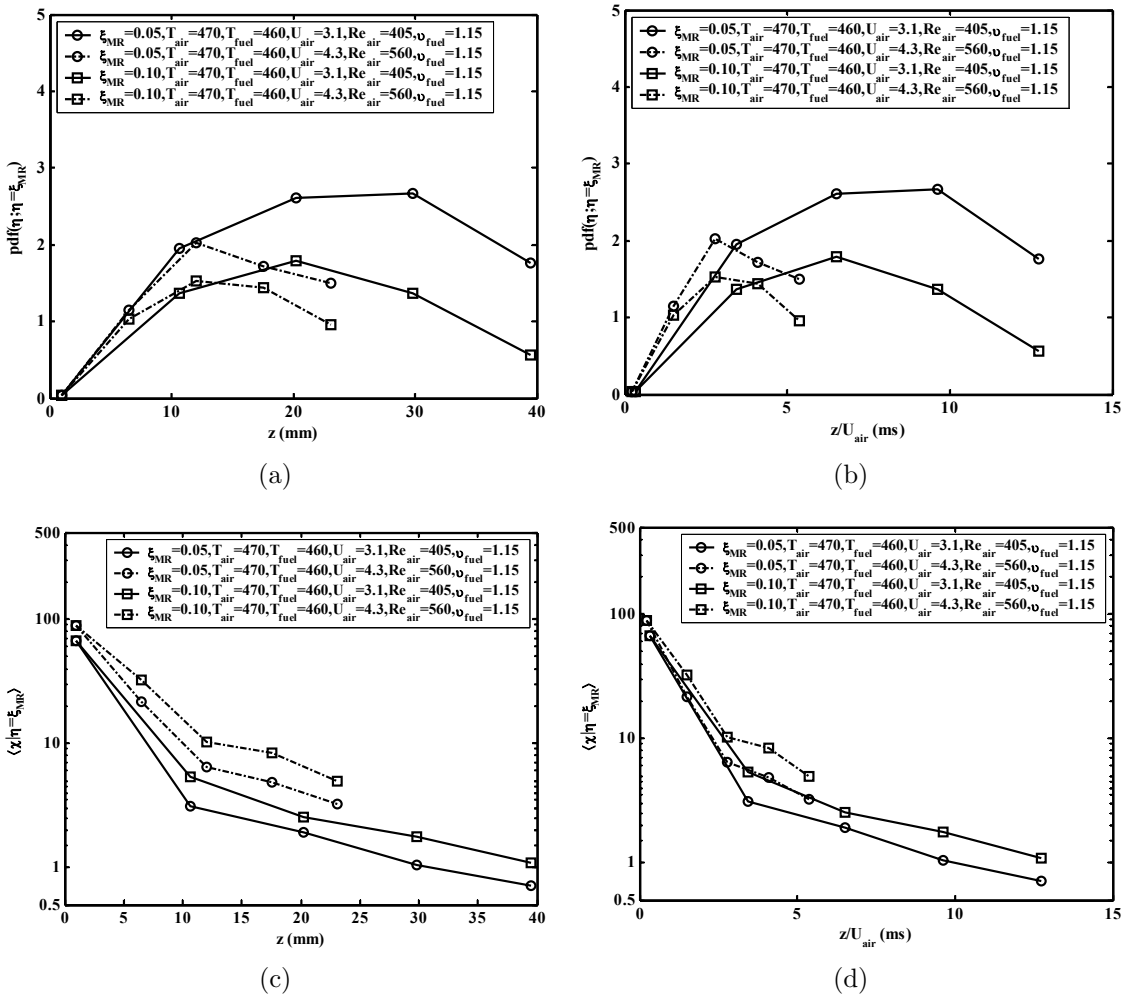

Figure 3.22: Effect of flow on spatial variations of point statistics for two hypothetical values of the 'most reactive mixture fraction' (ξ_{MR}). Chosen values of $\xi_{MR} = 0.05$ and 0.10. Equal velocity data shown, with $\upsilon_{fuel} \cong 1$. Axial variations of the pdf(ξ) at ξ_{MR}, along the centreline ($r = 0$), in terms of: (a) a physical distance from the injector, z (mm), and, (b) a mean 'lagrangian' residence time $\frac{z}{U_{air}}$ (ms). Axial variations of the mean conditional χ at ξ_{MR}, along the centreline ($r = 0$), in terms of: (a) a physical distance from the injector, z (mm), and, (b) a mean 'lagrangian' residence time, $\frac{z}{U_{air}}$ (ms).

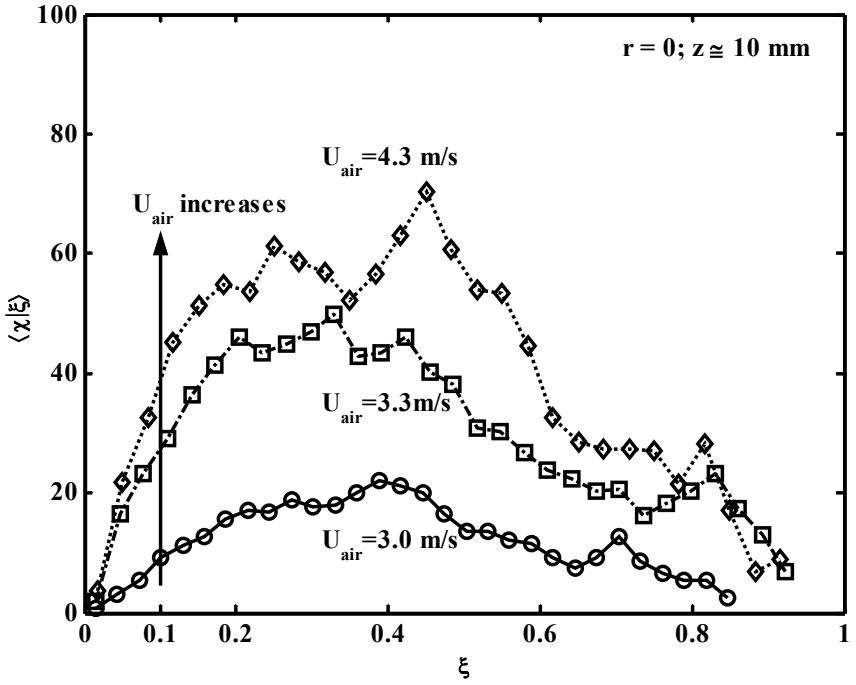

(a)

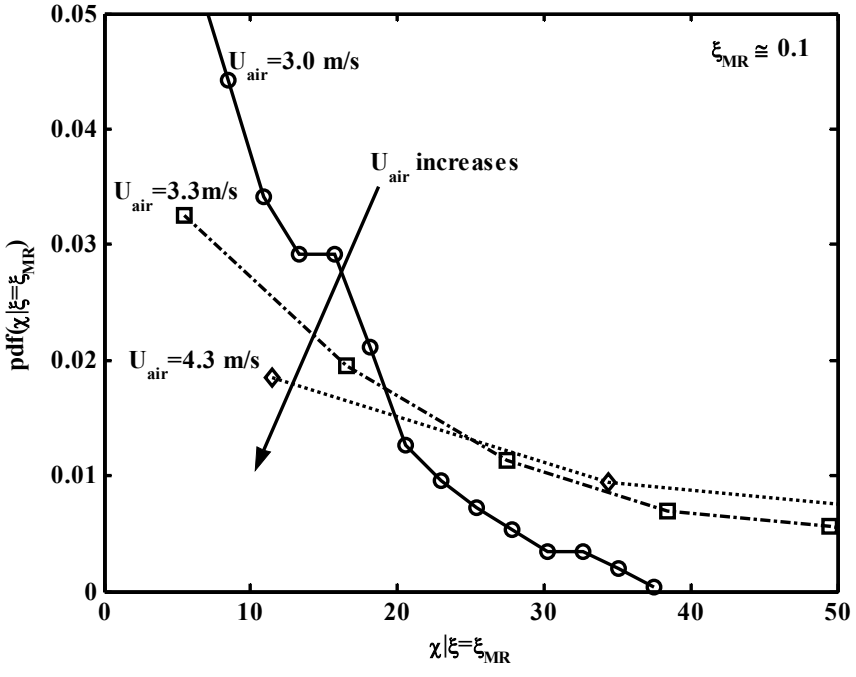

(b)

Figure 3.23: Effect of flow on point conditional statistics. (a) Mean conditional scalar dissipation rate, at ($r = 0$, $z \cong 10$ mm), and, (b) pdf of conditional scalar dissipation rate, at ($r = 0$, $z \cong 10$ mm) *and* a hypothetical value of $\xi_{MR} = 0.1$, with $\upsilon_{fuel} \cong 1$ and as U_{air} increases from 3.0 – 4.3 m/s.

Chapter 4

Observations of Autoignition: Main Features and Bulk Behaviour

4.1 Objectives of Chapter 4

This chapter is the outcome of an attempt to assist the understanding and interpretation of the results for the frequency, location and delay time of autoignition in **Chapters 5** to **7**. This aim is addressed in two ways. **Sections 4.2** and **4.3** offer a first look at characteristic autoignition phenomena. Following this and in the light of images such as those contained in these sections, **Section 4.4** addresses issues relating to the two-dimensional imaging measurements of autoignition.

The first two parts of this chapter are intended as a compilation of visual and audible observations of phenomena achieved across the full experimental operating condition envelope for the two cases of:

- Nitrogen diluted hydrogen, acetylene, ethylene and n-heptane fuels injected into a Confined Turbulent Co-Flow of Hot Air (CTHC), and,
- Nitrogen diluted ethylene injected into a Confined Turbulent Annular Jet of Hot Air (CTHAJ).

For each experimental configuration, depending on the inlet velocity and temperature of the air and fuel and the degree of dilution of the fuel stream with excess nitrogen, a variety of autoignition (and related) phenomena were possible. This 'bulk behaviour' is the subject of **Sections 4.2.1** and **4.3.1: Operating Regimes** for the CTHC and CTHAJ burners respectively. **Sections 4.2.2** and **4.3.2: Autoignition Kernels and Flamelet Propagation** focus on the main spatial and temporal features of autoignition in terms of:

- The characteristics of its localized explosive origins.
- The development from autoignition kernels to fully-fledged propagating flames.
- The fate of these unsteady post-ignition flames.

In some cases, post-ignition flamelets flashed-back and lead to diffusion flames on the injector. **Section 4.2.3** takes a close look at this process with high-speed images.

The purpose of **Section 4.4** is to give a detailed outline of the two-dimensional optical (cameras only) techniques employed, the methods of analysis and processing used and formal definitions of the autoignition length variables through which the phenomena will be quantified in the rest of this thesis. This section compliments **Section 2.4.2**, that offered only a description of the equipment used in the making of these measurements and **Section 2.4.3**, in which the method of estimating corresponding mean 'delay times' based on all measures of length was introduced.

Visual observations will be introduced, supported by images and PMT and spectrometer measurements. The images presented have been attained with a variety of equipment and techniques including UV sensitive ICCD cameras and high-speed sequencing. At the end of this chapter it is hoped that the reader will have been offered a first, albeit crude, glimpse of the phenomena, from which it will be evident that new phenomena, not previously reported, have been observed and an in-depth description of the optical methods used for their measurement and as such

will be in a better position to digest the results of the pursuing chapters, where the quantitative effects of various experimental parameters are examined.

4.2 Confined Turbulent Co-Flows of Hot Air

Attention is drawn initially onto the basic experimental layout, the Confined Turbulent Hot Co-Flow (CTHC) burner, as described in detail in **Chapter 2**. In the sections that follow, firstly the possible operating regimes will be described, followed by a detailed look at characteristic examples of autoignition in terms of kernel appearance and post-ignition flamelet propagation.

4.2.1 Operating Regimes

Generally, the phenomena that have been observed with the CTHC burner can be categorized into three behavioural groups, along with two transition regions. The paragraphs that follow describe phenomena that were observed during experiments with conditions varying in the sense indicated by the drawn arrow in **Figure 4.1**, in an attempt to illustrate the main features of this mapping. The observations mentioned were common to all fuels, except where specifically noted.

'No Ignition':

In the limit of either low T_{air} or Y_{fuel}, or high U_{air} or U_{fuel}, no autoignition was observed within the length of tube under investigation. Only a characteristic, muted background sound of the turbulent flow in the pipe could be heard. This sound, although affected by T_{air} and U_{air}, was only slightly changed by the conditions of the jet (or indeed its existence or absence). With the injection of the colder fuel the temperature at the exit of the quartz tube well downstream showed a drop (depending on the mixture flow rates of up to 10 K), which was the only indicator

of the continuous injection. This is the 'No Ignition' regime. It is important to stress that operation in this regime does not necessarily imply lack of autoignition, but rather, a lack of autoignition *in the finite length of tube available for the observation.*

'Nothing–to–Spots' or 'Pre-Ignition Reactions' Transition:

As T_{air}, Y_{fuel} were increased and/or U_{air}, U_{fuel} decreased, the temperature at the tube exit was initially raised by a few to tens of degrees relative to the frozen (non-reacting) conditions, a short time after fuel injection had been initiated. The low heat release is direct evidence of exothermic, pre-ignition reactions taking place inside the tube. The extent of this 'Nothing–to–Spots' transition increased with increasing temperature and velocities and decreasing dilution as illustrated in **Figure 4.1**. For hydrogen the boundary between 'No Ignition' and 'Random Spots' has been characterized. It is presented along with another boundary involving the 'Random Spots' behaviour in **Figure 4.12** and discussed in the 'Flashback and Lifted Flame' section below.

For ethylene and n-heptane the pre-ignition reactions were affirmed by weak chemiluminescence, visible by eye along long lengths of the tube, in the absence of any accompanying sound. Autoignition was first observed at the very exit (and even completely outside) of the tube. The appearance of autoignition differed from the pre-ignition transition chemiluminescence in that it arose in the form of well defined, although initially faint and infrequent (f_{IGN} of the order of a few seconds) localized, explosive events. These events had a 'spotty' appearance and were clearly audible. **Figure 4.2(a)** shows the raw, normalized global spectral signature recorded during transition conditions for ethylene and comparison with spectra taken immediately after the autoignition events had started to appear. Both spectra are long exposure (30 s) measurements. With the exception of the broad central crest occupying the region marked '$HCHO^*$ Bands' that is discussed below, the spectra are entirely consistent with the emission spectra of rich premixed hydrocarbon flames found in

Obertacke et al. [1996], Zizak [2000]. Referring to the 'Transition' spectrum, the most notable features are from left-to-right the bands of: NO^*, OH^*, HCO^*, NH^*, CN^*, CH^* and C_2^*.

The emission location of $HCHO^*$ (formaldehyde) is indicated and must be contributing to the wide content peaking around 430 – 440 nm. Although it is difficult to conclusively infer this from the current measurements, the presence of formaldehyde is well established in pre-ignition chemistry and would be expected here. Much work has been done, particularly in HCCI combustion, concerning autoignition proceeding through $HCHO^*$. See for example the $HCHO^*$ PLIF imaging of Brackmann et al. [2003], Graf et al. [2001], Koopmans et al. [2003]. In all these studies cool flame periods were found to be present in the overall combustion process. The LIF signals were detected from relatively early on in the cycle (10 Crank Angle Degrees, or, CAD) after fuel injection, increasing strongly as the Top Dead Centre (TDC) was approached. Most importantly, $HCHO^*$ disappeared to a large extent when combustion took place in the combustion chamber. It was found that at above a temperature threshold $HCHO^*$ was rapidly consumed, whereas at low temperatures the consuming reactions were quenched.

The current data is not sufficient to reveal the precise mechanism by which $HCHO^*$ is formed or consumed here and so in terms of chemical path ways, no comparison can be made with the aforementioned studies. Nevertheless, in the autoignition experiments here, strong $HCHO^*$ signals that could be separated out from the rest of the emissions were only possible near 'Pre-Ignition Reactions' conditions. During 'Random Spots' conditions any contribution from $HCHO^*$ was completely lost in the spectral signature in all but the faintest autoignition conditions. The initiation of autoignition and thus the introduction of the higher temperature flame chemistry lead to a decreased *normalized contribution* from $HCHO^*$, while the OH^* intensity was enhanced. **Figure 4.2(b)** shows the absolute intensity of the spectra in **Figure 4.2(a)**, illustrating how the overall chemiluminescence intensity increased

dramatically once autoignition had begun and thus making the whole process visible to the naked eye. As soon as autoignition is detected in the tube OH^* becomes the most serious candidate for the detection of the phenomenon.

Interestingly, in the case of hydrogen and acetylene it was impossible to arbitrarily shift autoignition downstream of the injector and along the whole length of the tube; even with the most careful adjustment of the upstream conditions within the transition regime. The first manifestation of autoignition was again in the form of low frequency autoignition events, but this time at relatively closer lengths (L_{IGN} of the order of 100 – 200 mm, or 4 – 8 D_{TUBE}) from the injector, in which case it was impossible to detect the weak pre-explosion chemiluminescence. This discontinuous behaviour is most exciting because it becomes impossible to explain in terms of a 'residence time' argument, as described in **Chapter 8**, and thus highlights the importance of the coupling between finite turbulent mixing effects and chemistry in cases where the turbulent mixing and chemical time scales are of the same order.

'Random Spots':

Moving further away from the temperature, velocity and dilution limits of the 'No Ignition' regime and for a certain range of higher T_{air} and/or Y_{fuel}, and/or lower U_{air} and/or U_{fuel}, the aforementioned transitional 'Nothing–to–Spots' situation gave way to the 'Random Spots' regime. For all fuels, operation in this mode resulted in continuous, recurring autoignition events inside the quartz tube, randomly realized in space and time. This activity was statistically-stable (steady in the mean). It should be mentioned that the range of conditions for which the 'Random Spots' behaviour was possible broadened at higher temperatures and velocities and lower dilutions (higher values of Y_{fuel}). The author is not aware of previous reporting of, or measurements made in, this regime. The existence of this behaviour becomes all the more important and interesting since a recent LES attempt based on these experiments has failed to reproduce the existence of this regime.

For the hydrocarbon fuels each autoignition event was clearly visible, with the flamelets originating from its immediate vicinity being blue in colour. Individual, instantaneous events manifested visually in the form of a spotty flashes, accompanied by a popping sound. **Figure 4.3** demonstrates acetylene autoignition examples observed to the 'Random Spots' regime. Autoignition of hydrogen was nearly invisible to the naked eye, especially in the low f_{IGN} limit. **Figure 4.4** affirms the absence of organic radicals during the autoignition of hydrogen with short exposure spectral measurements. Occasionally, for all degrees of nitrogen dilution (although shown only in one case here) sharp peaks appeared at visible wavelengths. The short term appearance of these peaks and their narrowness, lead to the conclusion that these were from excited atoms rather than molecules or radicals, perhaps originating from solid particles contained in the air, fuel and nitrogen supplies. For the hydrocarbons the emission intensity was enough to swamp these spurious signals. **Figure 4.5** shows images of the 'Random Spots' hydrogen autoignition taken with a UV-sensitive CCD camera and lens for various conditions and exposure times.

As the temperature was increased or dilution and velocities decreased, autoignition for all fuels moved upstream towards the injector and became increasingly frequent. Consequently, the radiated luminescence was intensified and the noise increased in pitch and loudness. At the high end of f_{IGN} some chemiluminescence could be visibly detected by eye even for hydrogen in the yellow to orange wavelengths. Away from the injector, and particularly for certain conditions with acetylene, yellow fronts were observed propagating axially downstream at higher velocities and across longer distances than the initiating autoignition sites farther upstream. Viewed for a sufficiently long exposure time these propagating flames resembled vertical 'streaks', much like rich, 'sooty' flames and examples can be seen in **Figures 4.3(d)** to **4.3(e)**. In general, for the hydrocarbon fuels, the displacement of the blue autoigniting regions towards closer L_{IGN} resulted in increasingly lengthened post-ignition flame 'streaks' and a decrease in the separation between these

two regions. Hence, operation at shorter L_{IGN} was associated with an overall appearance increasingly dominated by the downstream flames. The global appearance shifted from blue to bright yellow (almost white for very high f_{IGN}) for acetylene or more orange-yellow for the heavier hydrocarbons. On closer inspection of **Figures 4.3(d)** and **4.3(e)** it is evident that the global colour shift was mostly caused by the downstream post-ignition flames, with the autoigniting regions closest to the injector retaining their blue appearance.

It is especially apparent in images such as those of acetylene autoignition in **Figures 4.3** that there are common features in the spatial structure of autoignition. There exist propagating flame fronts, both immediately originating at the location of the initial explosion and farther downstream. The exact characteristics of this structure and its evolution from the instance of autoignition are the objects of an investigation presented in **Sections 4.2.2** and **4.3.2** for the CTHC and CTHAJ respectively. It will be established, with the aid of sensitive, high temporal and spatial resolution imaging, that the autoignition events such as those pictured in **Figures 4.3** and **4.5**, were short-lived autoignition kernels that propagated and died out (extinguished), or resulted in flashback depending on the conditions. The localized nature of initiation of autoignition and the immediate flamelet propagation away from these sites are not new. They have been demonstrated previously in the 2-D DNS of Mastorakos et al. [1997a] with simple chemistry and Echekki and Chen [2003] with detailed kinetics. The latter even mention and examine scenarios of autoignition kernels that failed to ignite due to chemistry effects at the heart of the radical pool. However, the eventual extinction of these flamelets and inability of establishing fully fledged combustion *a posteriori* of successful autoignition, in relative closeness to the original autoignition sites in the manner that has been observed experimentally, even in the case of the larger scale axial 'streaks', is a finding that has not been investigated before. As stated previously, a recent LES attempt based on the experiments here has failed to reproduce this behaviour.

The spatial separation between the autoignition events and the propagating flames can be further examined with the spectrometer measurements for acetylene. This fuel was chosen because it was easy to visually discriminate between the two regions by eye. **Figure 4.3(e)** indicates the placement of the fibre-optic cable at different view-heights with respect to the tube, for downstream (D) and upstream (U) measurements. 'Global' measurements were taken with the probe placed farther back so as to view the full span of phenomena. **Figure 4.6(a)** shows normalized spectra taken during the 'Random Spots' autoignition of acetylene for different probe heights, but same conditions. These spectra are time averaged over 100 s and can be considered long exposure measurements. The most striking feature is the contribution from the black-body radiation of soot particles that directly affects the spectrum for wavelengths upwards of c. 425 nm. This explains the more 'sooty' appearance of acetylene autoignition compared with the other hydrocarbon fuels. For example, ethylene autoignition only shows similar behaviour for conditions close to 'Flashback' (see **Figure 4.11** and the discussion in the 'Flashback and Lifted Flame' section below). **Figure 4.6(b)** shows normalized spectra taken during the 'Random Spots' autoignition of n-heptane and has been placed here for comparison with the acetylene results of **Figure 4.6(a)**. The n-heptane spectra are shorter exposure measurements taken over 2 s exposures, and like ethylene do not show significant soot radiation; although it can be seen from the absolute intensity in **Figure 4.7(a)** that this effect begins to appear above 550 nm for the lowest L_{IGN} conditions. The high frequency component in the n-heptane signals is not noise, but rather due to unsteady contributions from a large variety of species and molecules. To reinforce this point, it should be pointed out that **Figure 4.7** shows autoignition of n-heptane across a wide range of L_{IGN} (and hence f_{IGN}). Note that even for the high intensity spectra the high frequency component of the signal remains significant, even though the number of events recorded during this exposure is 1 – 2 orders of magnitude higher than the low intensity spectra.

More evidence to support the findings concerning the spatial separation between the autoignition and flame regions for acetylene can be found in **Figure 4.8** that shows 'Global', 'Upstream' and 'Downstream' *absolute* spectra for three different conditions and hence L_{IGN}. Because of the changing orientation of the probe relative to the emitted light, the absolute intensities cannot be directly compared between views. Nevertheless, it is still possible to compare the intensities between different values of L_{IGN} *at the same location.* The figure is organized as follows:

Figure 4.8(a) – Global Position: Spectra taken with the probe conventionally placed for a global view,

Figure 4.8(b) – Position U: Spectra taken with the probe at the height of the autoignition events upstream, and,

Figure 4.8(c) – Position D: Spectra taken with the probe downstream at the height of the propagating flames.

Continuous soot radiation is obvious in all plots. The intensities were very sensitive to L_{IGN}, as previously noted. As L_{MIN} decreased from 68 to 51 to 40 mm the intensities at all wavelengths increased; more so at the wavelengths attributed to CH^* and C_2^*. This can be most clearly seen in the downstream measurements in **Figure 4.8(c)**. At this location and at mid– to high–wavelengths the contributed chemiluminescence from CH^* and C_2^* was less than that of the same species at the upstream locations. On the contrary, at the lower wavelengths the levels of OH^* remained consistently high. The persistence of the OH^* radical into post-flame regions while CH^* was consumed is in agreement with the chemistry of CH^*, according to which OH^* is formed from the reactions involving the consumption of CH [Zizak, 2000]:

$$CH + O_2 \rightarrow OH^* + CO$$

The diminishing of peaks associated with C_2 downstream were either caused by reactions of the type [Zizak, 2000]:

$$C_2 + OH \rightarrow CH^* + CO$$

or by the loss of signal to the background soot radiation, or both. Together, **Figures 4.6**, **4.7** and **4.8** show clearly that the OH^* signal remains high in the 'Random Spots' regime, even for operation nearer the transition boundary towards 'No Ignition', while for the other major species (including CH^*) the emission levels are very much abated in certain cases and in others might contain contributions from soot. These findings were common for all hydrocarbon fuels. For hydrogen the choice of detection wavelength becomes trivial.

Previously, typical *normalized* hydrogen spectra were shown. Unfortunately, **Figure 4.4** fails to give an indication of how the absolute magnitude of the OH^* chemiluminescence signal for hydrogen compares with that for the hydrocarbon fuels. This is important to investigate because a weak OH^* emission for hydrogen would result in an arduous detection of autoignition for this fuel. An objective comparison between the spectrometer signals of different fuels, or even different conditions for the same fuel, can only be made if f_{IGN} between the two fuels is approximately the same, because the effective exposure time (as with any two-dimensional image) is not only related to the actual recording time but also the frequency of autoignition as discussed in **Chapter 2.4.2**. Reiterating briefly, the reason why it is difficult to make such comparisons between the two signal levels without knowledge of f_{IGN}, is because (as shown in **Figures 4.7** and **4.8**) the measured intensities vary strongly with changing L_{IGN} and (as will be shown in **Chapter 5**) L_{IGN} is itself exponentially correlated with the mean f_{IGN}. Thus, together the two situations imply that small changes in L_{IGN} are capable of causing large changes to f_{IGN} and the intensities in the measured spectra. In addition, it will be shown in **Chapter 5** that the

mean PMT OH^* signal is exponentially related to L_{IGN}. **Figure 4.9** shows that with the spectrometer intensifier sensitivity set to a value an order of magnitude higher than that used for acetylene and for similar exposure times, the typical OH^* levels recorded at the autoignition locations for hydrogen where a factor of about 1 – 6 lower than those for acetylene *across a range of* L_{IGN} *spanning the full extent of the condition envelope from 'No Ignition' to 'Flashback'.* Hence, the average intensity levels of hydrogen autoignition spectra were an order of magnitude lower than the weakest acetylene autoignition spectra, recorded at close to 'No Ignition' conditions. This development has serious implications on the capability to detect hydrogen autoignition with the spectrometer, cameras and PMT. In order to improve the accuracy of any measurement it is necessary to increase the exposure times and sacrifice the sampling or framing rates, or increase the gain and introduce the classic errors associated with high amplification.

In closing, there is an important distinction to be made between questions concerning the processes leading towards autoignition at a particular location and time, and those concerning the post-ignition propagation of flames originating from these autoignition sites. Since it is impossible to physically separate the two 'sub-phenomena', measurements will, in general, contain information of both aspects. Although in principle the main goal of this work rests with the former, interest and knowledge has not been restricted. Aiming to understand autoignition in the broadest of senses, this work concentrates on the 'Random Spots' regime. Here, autoignition occurs repeatedly and flamelets exist and propagate, but on a local scale only and in close proximity to the original autoignition events. Their short-lived nature due to extinction precludes the possibility of the fully-fledged combustion associated with large-scale flames and facilitates the proper characterization of both autoignition and propagation phenomena. For these reasons care has been taken in this work (and consequently this thesis) to point out the presence and explore the effects of both of these phenomena on the results where applicable.

'Flashback' and 'Lifted Flame':

At high T_{air}, Y_{fuel} and/or low U_{air}, U_{fuel}, as soon as the fuel mixture was injected, autoignition and subsequent flashback occurred, which resulted in a normal jet diffusion flame stabilized on the injector nozzle. The first appearance of an autoignition event was randomly located in space. The realization of the attached flame on the injector was associated with little or no noise. In terms then of sound levels, even with extreme fuel flow rates and flame lengths of the order of half the quartz tube, the flame was only faintly detectable by human ear. A quantitatively description of this statement will be presented in **Chapter 5**. This is the 'Flashback' regime. **Figures 4.10(a)** and **4.10(b)** show examples of autoignition events just before the onset of 'Flashback'. In each case the experimental run resulted in a diffusion flame attached on the injector, but not necessarily from the propagation of the indicated event. The exact process by which the emergence of an autoignition event can lead to flashback is examined closely in **Section 4.2.3**.

Spectra for ethylene at close to 'Flashback' conditions can be seen in **Figure 4.11** and can be directly compared with the normalized 'Random Spots' spectrograms of ethylene and acetylene in **Figures 4.2** and **4.6(a)** respectively. The characteristic soot radiation 'tail' at wavelengths above 425 nm becomes evident for this fuel. As the autoignition conditions move closer to 'Flashback', the contributions at the emission wavelengths of CH^* and C_2^* are enhanced, in agreement with both **Figures 4.8** and **4.9** for acetylene. Again, the chemiluminescence OH^* signal is mostly unaffected.

In an attempt to properly map the boundary between 'Random Spots' and 'Flashback', a further 'Lifted Flame' regime was observed with hydrogen and acetylene at even higher velocities and temperatures. In this case a stable lifted flame was achieved, which was associated with an intense noise. **Figure 4.10(c)** shows a lifted acetylene flame. This possibility, and the proximity to autoignition, has

been reported for hydrogen in this configuration in Mastorakos et al. [2003] and is consistent with similar observations concerning lifted hydrogen flames and related autoignition issues in configurations involving reactants supplied at elevated temperature. One such example is the 'Cabra' (or 'Dibble') burner [Cabra et al., 2002]. Here, a fuel jet is injected into a vitiated wide co-flow, originating from a large number (2200) of perforated plate-stabilized premixed flames upstream. In the detailed experiments of Dally et al. [2002] this involves turbulent jets of hydrogen/methane issuing into a stream of hot combustion products where the oxygen level can be varied. Various other experiments and numerical calculations have also been preformed on this configuration, such as those of Masri et al. [2004], Wu et al. [2003]*, which examined both issues of autoignition and lifted flame stabilization mechanisms in nitrogen-diluted hydrogen jets injected into a vitiated co-flow resulting from the premixed combustion of hydrogen-air flames. The experimental investigations of Wu et al. [2003] went as far as measuring the magnitude of the noise levels (only in mean with a sound level meter) and looking at the effects of various conditions, such as the co-flow velocity, on this variable to justify the fundamental difference in the two regimes they observed: 'lifted flame' and 'autoignition'.

One of the aims of the aforementioned experiments of Dally et al. [2002] was to test the accuracy of detailed methane mechanisms with regard to combustion in these reduced flame temperature conditions. Operation in such conditions is known as 'flameless oxidation' or MILD (Moderate and Intense Low Oxygen Dilution) combustion. MILD combustion is generally characterized by slower reaction rates and broadly distributed reaction zones associated with low luminosity, coupled with a capability of very low NO production. On account of the reduced pollutant production various MILD combustion concepts are under investigation for application

*The original presentation mentioned in this (second) reference had been downloaded from the web. It has since been replaced by a newer version available at: *http://www.aeromech.usyd.edu.au/showcase/AutoIgnition%20Poster-hugh.pdf*, but this version does not offer a detailed account of the operation of the burner. The original form of the presentation has been kept.

in high-efficiency, low-emission furnaces and have attracted considerable attention. The growing knowledge concerning configurations involving reactants supplied at elevated temperatures has in turn generated an increased interest in autoignition; particularly the boundary between fully-fledged, lifted flame combustion and autoignition, as in Masri et al. [2004]. In fact, these phenomena have been exactly reproduced here for conditions of operation in or close to the 'Lifted Flame' regime. Yet, the advantage of the current, confined hot air configuration is its improved simplicity and steady, well-defined conditions (especially of co-flow air stream) that are easier to model compared to, for example, the vitiated unconfined co-flow of the 'Cabra' burner. On the one hand, modelling the chemistry in the 'Cabra' burner is complicated by the difficulty of accurately measuring the concentrations of the combustion products in the vitiated co-flow (including unstable radicals). But also, due to the unconfined nature of the flow, entrainment of ambient air gives rise to both temperature and velocity field uncertainties. Furthermore, the 'Cabra' burner suffers from transient issues, such as an increasing co-flow temperature with experiment time due to the high flame temperatures upstream [Wu et al., 2003], controlled by varying the equivalence ratio in the nitrogen-diluted hydrogen co-flow. A solution such as this has the consequence of causing a drift in the content of the radical pool in the co-flow depending on the temperature, which in turn introduces uncertainty in the description of the inlet conditions.

'Spots–to–Flame' Transition:

Unlike the 'No Ignition' and 'Random Spots' transition, referred to as 'Nothing–to–Spots', the boundary between the 'Random Spots' and 'Flashback' regimes, termed 'Spots–to–Flame' is quite sharp. It was tested and found to stretch 1 - 2 K in temperature for given velocities and dilution with relatively high consistency. Generally, the temperature needed to cause flashback increased monotonically with both co-flow air and fuel mixture jet velocities.

A complete mapping of the regime boundaries requires a detailed, focused study of autoignition close to transitional behaviour, complicated by the need to explain the effects of a multitude of variables such as the air stream velocity and temperatures and injection velocity and perhaps temperature. Moreover, effects of possible changes to the geometry such as the use of different diameter injectors will have to be explained. Each of the above variables will have to be measured for each different fuel and for each fuel as a function of dilution with nitrogen. To the knowledge of the author, a quantitative description of the ability of an autoigniting flow to flashback, in any flow geometry and mixing arrangement and for any fuel has not been considered before. An effort has been made here to provide some data towards this direction. For the mapping of the regimes of hydrogen autoignition in the CTHC alone, 400 experimental runs were performed, out of which 100 data points appear in **Figure 4.12**. This figure shows results from this attempt as follows:

Figure 4.12(a): Here, a fixed dilution ($Y_{H2} = 0.15$) was used and the conditions for transition are plotted grouped per non-dimensional, normalized injection velocity ratio, υ_{fuel}. The value of υ_{fuel} varied from 3.2 to 5.6 across all experiments. Each data point then represents the T_{air} necessary at a given U_{air} to cause a shift from 'No Ignition' to 'Random Spots' (empty symbols), and from 'Random Spots' to 'Flashback' (filled symbols) for various injection to co-flow velocity ratios.

Figure 4.12(b): Beginning with pure hydrogen ($Y_{H2} = 1.00$), the range of T_{air} and U_{air} for which 'Random Spots' behaviour was possible is plotted with filled symbols. For a given value of U_{air} the envelope of this behaviour is marked by the black solid lines. Its extent was probed by changes to both T_{air} and υ_{fuel} (not directly shown in the figure). The values of υ_{fuel} examined varied from 0.35 – 12.6. Following this, the restriction on Y_{H2} was lifted and the experiments were repeated for values of Y_{H2} between to 0.05 – 0.40.

For $Y_{H2} = 0.15$ the 'Random Spots' regime extended about 15 – 35 K. The limiting T_{air} necessary for the first occurrence of autoignition showed a non-linearity, whereas that needed to cause the first instance of 'Flashback' increased monotonically with increasing U_{air}. The effect of v_{fuel} did not show a distinguishable trend as far as the 'Nothing–to–Spots' transition is concerned, but for the 'Spots–to–Flame' an effect is clear, with the higher velocities causing a higher T_{air} necessary for 'Flashback'. The $Y_{H2} = 1.00$ data confirm the non-linear behaviour of the 'Nothing–to–Spots' boundary. In addition, it is apparent that the 'Random Spots' regime extends to higher T_{air} and U_{air}. 'Flashback' is caused more easily at lower U_{air} and the effect of dilution is to shift the regime boundaries towards higher temperatures.

Generally, as already pointed out, the 'Nothing–to–Spots' transition is a very subtle affair, in complete contrast to that between 'Random Spots' and 'Flashback'. The non-linearity in the 'Nothing–to–Spots' transition is interesting and an attempt to explain this behaviour will be the subject of **Section 8.3**. With this exception, the main features outlined here have been observed under a wide range of conditions, for various injector sizes and fuels.

4.2.2 Autoignition Kernels and Flamelet Propagation

Images of the autoignition and subsequent post-ignition flame propagation of gaseous fuel plumes in any continuous flow apparatus are almost non-existent. Edwards et al. [1992] present high-speed photography of the autoignition and flame propagation of a transient diesel spray, but even here there is ample room, both for further visualization and measurements. Furthermore, before attempting to extract quantitative information from images such as those in **Figures 4.3**, **4.5** and **4.10**, it is useful to closely examine what so far have been referred to as 'autoignition events' and to investigate how they emerge. In the images that have been presented here, the exposure times varied from 200 μs upwards and the individual events and resulting

flames appeared as 'spots' and 'streaks'. This appearance is a direct consequence of the spatial evolution of propagating flame fronts that arise from the events, because of the spatial integration that necessarily occurs during the finite exposure time. The aim of the current section is to examine this outcome for the case of autoignition in the CTHC burner.

A typical high-speed sequence of acetylene autoignition taken at 4.5 kHz is shown in **Figure 4.13**. The bright front in the centre of the images corresponds to the yellow *vertical* 'streaks' of **Figures 4.3(d)** and **4.3(e)**, while the weaker, flat (almost counterflow in appearance) *horizontal* flame upstream is the blue autoignition region in the same images. Individual 'autoignition events' can be thought of as consisting of three component-processes:

1. They emerge in the form of a localized explosion. The images show that the explosive emergence of the 'spots' always occurs in a limited spatial region. Immediately before the explosion the camera records a dark background. The 'spot' appears at a point with very low signal.

2. From the point of emergence, flamelets propagate radially outwards in all directions and the size of the reacting region grows. **Figure 4.14** presents a closer look at the small scales of these processes for both acetylene and n-heptane. For the acetylene example here, the propagation velocity of the fronts away from the moving centre/explosion origin is estimated as being around 15 – 20 m/s. These velocities must be considered in terms of the state of the reactant mixture immediately surrounding the flamelets and into which they propagate (that is chemically close to autoignition) and the local mixture fraction and scalar dissipation. For example, one might expect the velocity to increase in accordance with an increased local scalar dissipation and decrease in the case of autoignition in regions of very lean mixtures (low ξ_{MR}). Despite the fact that a full enquiry into the effects of the aforementioned conditions on

the velocities is not considered central to the current work, an indirect attempt to inspect the role of the concentration gradients on the propagation velocities has been indirectly made based on PMT measurements and is presented in **Chapter 5**. The fast images have not been used extensively to measure post-ignition flame propagation velocities directly.

At the larger scales flamelet propagation has, in turn, its particular dynamics. Most commonly in 'Random Spots' conditions, away from 'Flashback', the flamelets are simply advected downstream by the flow in an 'advection driven' scenario, such as that depicted in **Figure 4.15(a)**. Note that the advection velocity in this example is about 10 m/s, close to the mean flow velocity and about half the estimated velocity for the propagation of the flame fronts relative to the centre of the spot (from pervious paragraph). In certain cases a short-term 'flame anchoring' was observed, referring once again to the upstream horizontal flame structures in **Figures 4.13** and **4.15**. 'Flashback', as presented previously, resulted in situations for which the upstream velocity of the post-ignition flames did in fact exceed the advection velocities of the flow.

3. Finally, there is the issue of the fate of the propagating flamelets. In 'Flashback' the propagation resulted in a diffusion flame on the injector nozzle. Otherwise, and depending on the conditions, the flamelets either extinguished, or induced secondary autoignition elsewhere. Evidence to support these claims can be found in all presented fast image sequences.

These findings have also been confirmed with fast PMT measurements, in which the time-series of the OH^* chemiluminescence collected from the entire domain shows a temporal signature that exactly matches the high-speed imaging observations and completely justifies the ideas above concerning the evolution of the autoignition and post-ignition propagation processes. The fast PMT measurements of OH^* are presented in detail and discussed in **Chapter 5**, but a typical profile is shown in

Figure 4.16. As expected, the instantaneous PMT measurement is the equivalent of the spatial average of a fast image taken at that time. The time signal clearly shows the explosive emergence of the autoignition event in the first 0.5 ms. The post-ignition propagation and gradual extinction are described by the decay of the long tail that takes about 3 ms to reach 10% and 6 ms to reach 3% of the peak value. The decay of the profile can be described by an exponential and the time constant is later used as an indicator of the propagation velocity of the flame.

4.2.3 Flashback

A characteristic flashback sequence is shown in **Figure 4.17**. In **Figures 4.10(a)** and **4.10(b)** the spots that were captured did not result in flashback as did that in **Figure 4.17** because the slow framing rate resulted in an inability to conclusively isolate the particular flamelet that 'flashed-back'. However, those images reveal that for conditions for which flashback is statistically highly likely the flamelets move *upstream* from the initial explosion locations before extinguishing. This is reflected in their inverted-V appearance, which is completely opposite to that in normal conditions such as in **Figure 4.3(a)**.

4.2.4 Confined Turbulent Hot Co-Flow: Summary

Key observations concerning the qualitative features of autoignition in this turbulent mixing flow were presented in this chapter. It has been demonstrated that a variety of phenomena are possible. The majority of work presented in this thesis focuses pre-dominantly on the 'Random Spots' behaviour. In this operating regime repeated autoignition spots appear in a statistically steady manner. From each spot a flame front begins to propagate and eventually extinguishes. The effect of conditions on the chemiluminescence spectra, autoignition locations and frequency and their randomness are discussed for various conditions in **Chapters 5**, **6** and **7**.

4.3 Confined Turbulent Annular Jets of Hot Air

The Confined Turbulent Hot Annular Jet (CTHAJ) burner has already been described in detail in **Chapter 2**. Recall that only one fuel has been used here, ethylene, and that two combinations of bluff-body/quartz tube have been used with diameters of the quartz tube and bluff-body being: (i) $D_{TUBE} = 24.78$ mm and $D_{BLUFF} = 10.00$ mm, and, (ii) $D_{TUBE} = 33.96$ mm and $D_{BLUFF} = 13.99$ mm respectively. Here, the operating regimes will be described for this burner configuration, along with an examination of autoignition in terms of kernel appearance and post-ignition flamelet propagation, similar to what has been done above for the CTHC. Some of the observations concerning the behaviour of autoignition in these flows are *similar* to those that have already been described and so emphasis will be given where major differences were observed between the two. The emphasis in the previous sentence was added to clarify the fact that, although certain phenomena might appear similar to what has been achieved in the CTHC, these are not completely identical. The differences will be highlighted in **Section 5.3**.

4.3.1 Operating Regimes

Autoignition was again detected by chemiluminescence radiated from the reacting regions. Not surprisingly the spectra were not dissimilar from those shown in **Figure 4.2(a)** for autoignition of ethylene in the CTHC burner. **Figure 4.18** shows averaged spectra (from 250 individual realizations of 100 ms exposure each) as a function of increasing temperature and all other conditions fixed. This resulted in L_{IGN} slowly moving closer to the injector. Time-series sampling at three wavelength bands, around 310, 430 and 510 nm for OH^*, CH^* and C_2^* respectively are also shown. **Figure 4.18(b)** corresponds to all 250 instantaneous spectra taken during the recording from which the average spectrum with the largest L_{IGN} was calculated in **Figure 4.18**. **Figure 4.18(c)** corresponds to the 250 spectra of small-

est L_{IGN} in **Figure 4.18**. The standard deviation of the time-series normalized by the mean signal for all spectra and over all frequencies ranges between 0.1 – 0.2, decreasing sharply from the 'Nothing–to–Spots' transition to operation within the 'Spots–to–Flame' regime. As before, the global C_2^* signal decreases strongly as L_{IGN} decreases in the stable spotting behaviour towards the 'Nothing–to–Spots' transition. Note also the relative strength of the OH^* bands and their insensitivity to the changing conditions. This assists chemiluminescence measurements for small L_{IGN} when the autoignition regions have this appearance. In conclusion, the spectral measurements show that chemiluminescence of the hydroxyl radical (OH^*) is an excellent marker for the detection of autoignition in both burner configurations and over a wide variety of conditions.

For very low T_{air} no autoignition was observed within the tube. This is the 'No Ignition' regime. As T_{air} was increased autoignition first appeared near the exit of the tube ($\sim 20 D_{TUBE}$). Qualitatively this is similar to the first appearance of autoignition with the same fuel in the absence of the bluff-body, even though the mixing field is different. Individual autoignition events manifested in the form of 'flashes' accompanied by a 'popping' sound in the same way as with the CTHC. In general, autoignition was again statistically steady for a significant range of T_{air}, U_{air} and υ_{fuel}. Random, consecutive autoignition events occurred continuously at a well-defined mean frequency and location, each with its own history of local explosion, flame propagation and extinction. This is the 'Random Spots' regime and typical images of operation in this regime can be seen in **Figure 4.19**.

As T_{air} increased further and/or U_{air} or υ_{fuel} decreased, the autoigniting region shifted closer to the injector. At a certain length, highly intermittent behaviour was observed. Steady autoignition was interrupted by bursts of loud, intense autoignition as much as $3 - 4 D_{BLUFF}$ closer to the injector before returning to the original situation, as shown in **Figure 4.20**. This behaviour was repeatable and belongs to the 'Spot-Wake Interactions' regime. The last two images in **Figure 4.19** are visual

examples of this interaction, which appears as a 'two-stage' or 'two-region' ignition. The rare excursions of the autoignition kernels to upstream locations may be related to rare large-scale, low velocity fluctuations induced by the wake of the bluff-body. High-speed imaging of the flame front propagation is presented in **Figures 4.21** and **4.22** and discussed further in the section that immediately follows.

Finally, for high T_{air}, autoignition occurred as soon as the nitrogen-diluted ethylene was injected and the post-ignition flamelets flashed-back to form a fully-fledged diffusion flame stabilized in the flow reversing wake region behind the bluff-body. This is the 'Flashback' regime. The propensity for flashback in the CTHAJ was higher than that observed in the CTHC. It was affected, as in the case of the CTHC, by the conditions including T_{air}, U_{air} and υ_{fuel}, but also was found to be strongly affected by the size of the injector (D_{BLUFF}) and tube (D_{TUBE}). For example, larger bluff bodies (e.g. $D_{BLUFF} = 17.8$ mm) showed acute propensity to flashback to the extent that the 'Random Spots' behaviour was nearly impossible to achieve (the 'Nothing–to-Spots' boundary was not strongly affected by D_{BLUFF}).

Figure 4.23 shows a map of the behaviour of autoignition in the CTHAJ burner in terms of T_{air} and U_{air}. It plots the T_{air} necessary at a given U_{air} to cause a shift from 'No Ignition' to 'Random Spots' and from 'Random Spots' to 'Flashback' for various injection to co-flow velocity ratios. The 'Random Spots' regime extends for about 15 – 20 K in T_{air}. The non-dimensional, normalized injection velocity ratio ($\frac{U_{jet}}{U_{air}}$) varies from 1.0 to 4.5 across all experiments. Both the limiting T_{air} necessary for the first occurrence of autoignition and that needed to cause the first instance of 'Flashback' increase monotonically with increasing U_{air}. The effect of $\frac{U_{jet}}{U_{air}}$ does not show a distinguishable trend, in opposition to the situation observed without the bluff-body. Moreover, this parameter proved to be less critical than T_{air} and U_{air}, a result that is also true for the autoignition location and 'delay time' results presented in **Chapters 6** and **7**.

4.3.2 Autoignition Kernels and Flamelet Propagation

High-speed imaging of the OH^* radical at 12 kHz revealed that each event composed once again of explosion, flame propagation and extinction on a local scale, but with three of distinct properties concerning the explosion and propagation phases:

1. Generally, the emergence of autoignition in the annular jet flow can be traced to a small localized event as before. Yet, the resulting post-ignition flames quickly spread over much larger distances. In **Figure 4.21** autoignition in the 34 mm diameter tube is captured at 7.3 kHz, giving a delay of 137 μs between successive frames. The condition here is relatively close to Flashback, but still in the 'Random Spots' regime. By the fifth or sixth frame the flames have reached the tube wall at the edges of the frame. The velocity of propagation during this flame spreading is of the order of 20 – 30 m/s.

2. A 'double reversal' tendency was possible in which after emerging from an autoignition kernel a flame would be advected downstream, upstream and then downstream again before eventually extinguishing. This tendency was made more persistent as L_{IGN} decreased. **Figure 4.22** offers a closer view of this phenomenon with images taken at 12 kHz, or 83 μs between successive frames.

3. Upstream flame propagation through the boundary layer is possible and does occur, while the first explosive appearance of autoignition might be itself frequently located close to the tube walls, as in for example **Figure 4.21(b)**. Note that the wall is at the edge of the frames. Although heat losses in these regions are not favourable for autoignition, this fact is not enough to completely avert autoignition.

4.4 Optical Autoignition Measurement Techniques and Data Processing

In **Section 2.4.2** the cameras used to make two-dimensional optical measurements of autoignition were presented. Purposefully, the techniques used for the making of these measurements were kept until the reader had been introduced to the possible phenomena. In this section the methods of autoignition length measurement by optical means are explained by discussing the raw imaging techniques, as well as the methods of analysis and processing used. Formal definitions of the autoignition length variables that will be used to quantify the various phenomena are also given.

Figures 2.1 and **2.8** demonstrated how axial measurements of autoignition length from the injection point to the onset of autoignition were made in order to quantitatively describe the phenomena. It is the aim of this thesis to examine this data, in the light of possible correlations with the measured conditions at the air inlet and fuel injection. The exact process of making the length measurements will be explained in **Section 4.4.1**. The autoignition length is generally denoted by L_{IGN}; the random length variable. There are also a number of more specific definitions. These are presented in **Section 4.4.3**, as are their statistics. Calculations were made on the raw and on processed (filtered, denoised) versions of the raw images. The processing method is briefly mentioned in **Section 4.4.1**.

4.4.1 Raw Imaging

For all fuels autoignition length measurements were made optically from images such as those already shown (e.g. **Figures 4.3**, **4.5**, **4.10** and **4.19**). Below, issues relating to the gain and exposure settings for the imaging are addressed. The discussions of this section are important for the correct interpretation of the results of **Chapter 6** from the raw images available.

Gain and Intensity:

Pixel intensity in all raw images was the result of on-chip, transverse line-of-sight integration. It has been shown that for the hydrocarbon fuels chemiluminescence of the CH^* radical, but also of C_2^*, in the visible spectrum made autoignition clearly visible to the naked eye. Hence, for the majority of experiments with these fuels a Sony DCR-PC120E CCD Digital Video Camera Recorder (**Section 2.4.2: Charge Coupled Device Camera**) was used. The resulting images will be referred to as 'CCD images'. Almost all CCD images presented in this thesis have been taken with no added optical filter. Instead, calculations based on CCD images were based on the 'blue' intensity component alone, which covers the range 400 – 500 nm and consequently contains mostly superposed emissions of the CH^* radical and to a lesser extent C_2^* (see emission spectra of **Chapter 3**). In a limited number of cases small quantities of methane were added to the diluted hydrogen in the fuel stream in order to examine the effect of mixing these two fuels on their autoignition behaviour (**Section 6.2.2**). The resulting phenomena were visible and so measurements in these experiments were also done with the CCD camera.

For hydrogen, but also for a number of hydrocarbon experiments, a UV-sensitive LaVision NanoStar ICCD camera together with a UV transmitting lens (**Section 2.4.2: Intensified Charge Coupled Device Camera**) was used instead to generate 'ICCD images'. During the autoignition of hydrogen no other species apart from OH^* emits light in the range 200 – 700 nm. However, in the IR range it is expected that other emission bands exist, such as H_20 (c. 1800 nm) and NO^* (c. 2600 nm), [Gaydon and Wolfhard, 1970]. In the case of the visualization of hydrocarbon autoignition with the ICCD, CO_2 is expected to appear around 2800 nm and CO at 2300 nm. The quartz tube will also radiate a high temperatures. According to Wien's displacement law for black-body radiation, spectral emissions at representative flame temperatures peak between 1000 and 2000 nm, [Gaydon and Wolfhard, 1970]. For these reasons a distinction will be made between images taken

with an OH^* filter (referred to as '*OH*' images) and those taken in the absence of any filter (referred to as 'broadband UV-to-IR', or '*broad*' images). The advantage of imaging without filters was a much better signal, which was a significant improvement in the case of hydrogen at lower f_{IGN}. The reasons behind this have already been discussed in **Section 4.2.1: Random Spots**, concerned with the low level spectral emission characteristics of hydrogen autoignition (see also **Figure 4.9**).

Frame Rates and Exposure Times:

There were two main requirements for measurements from the autoignition images:

1. To be able to locate the original autoignition sites, and,
2. To give an estimate of the propagation velocities of the post-ignition flamelets originating at the autoignition sites.

This section explains the attempts to measure these quantities.

It is generally considered advantageous to employ short exposure times, because the image is closer to the idealized instantaneous 'snapshot'. Unfortunately, this advantage is only true if the camera (but in general any optical instrument such as a PMT, spectral analyzer etc.) available for the measurement has the ability of making measurements capable of resolving the timescales in question. This must be done both in terms of a fast enough framing frequency (high f_{FR}) and in terms of a short enough exposure time (low t_{EXP}) per frame. Let t_{LIFE} be the time taken for the intensity of the chemiluminescent emission of a single event to fall to about 10% of its peak value. Consider the example of acetylene in **Figure 4.16**. The average spot life-time, t_{LIFE}, for acetylene was measured at around 2 ms. For 10 consecutive images per t_{LIFE} an f_{FR} of 5 kHz would have been adequate, whence the complete history of any motion picked up in the images (from the initial autoignition to the

post-ignition flame dynamics) could have been resolved over a number of consecutive images. The observer may concentrate/locate the moving object (flame) and trace its history backwards to find its origins (initial autoignition location).

In the same way these actions may be performed by an automated process. The high-speed, intensified CMOS camera was used along with a flame tracking script developed by the author to examine the axial propagation velocity of the flamelets originating at the autoignition sites for a limited number of experiments. Nevertheless, there is a very large number of images that must be analysed, especially at low f_{IGN}. Continuing the acetylene example from the previous paragraph, if f_{IGN} is of the order of 1 Hz (possible for 'slow spotting' conditions shown in **Figures 5.1** and **5.6**) and with an f_{FR} of 5 kHz, fast enough to capture the physical processes mentioned previously, an average of 150,000 images would have to be generated and later analyzed for a single run, if that run were to contain about 30 spots and last for approximately 30 s. Temporally the phenomena are random and it is impossible to trigger the camera and lock it to the events. In the measurements presented in this thesis, 10,000 images were recorded on average per run. For each of four fuels tested in this way about 20 conditions were tested, resulting in 1 million images that had to be processed for three distinct definitions of the flame front location. The tracking of flame fronts to find the original site and displacement of the reaction zones in order to evaluate a flame propagation velocity were both challenging attempts.

It is critical to emphasize that, in general, the autoignition events have an *absolute* velocity that is small and positive (in a downstream sense, away from the injector) in these experiments (see **Section 4.2.2**). Each post-ignition flame front travels downstream and cannot contaminate the information on the original autoignition site from where it initiated. The fast sequences presented in this chapter, such as in **Figures 4.14** and **4.15** for example, have shown that this is mostly the case. Nevertheless, the strongest evidence for this statement comes directly from the fast CMOS data in **Section 4.2.2**. Based on this knowledge, for most of the experi-

ments an alternative solution was found, instead of the fast CMOS sequencing, that allowed some information on the initial autoignition sites with the CCD and ICCD cameras, even though these cameras were limited by highest possible framing rates (f_{FR}) of 10 and 25 Hz respectively; an order of magnitude slower than the physical processes to be captured. **Equation 4.1** is a statement concerning the available exposure time, as set by the framing rate:

$$t_{EXP} \leqslant 1/f_{FR} \tag{4.1}$$

The resulting images were either the result of recorded superposition during t_{EXP}, of the full life-time of (possibly) more than one autoignition realizations, or, attempts at 'near-instantaneous snapshots' of the phenomena at certain locations along their trajectories. These possibilities are discussed in the following paragraphs.

In principle, depending on the conditions, the typical life-time of an autoignition event (t_{LIFE}) can be longer than the time between events as described by the frequency of autoignition (f_{IGN}). If $\overline{t}_{LIFE} > 1/\overline{f}_{IGN}$ and irrespective of the imaging method used, multiple events will exist simultaneously on any raw image, on average[†]. Consequently the conditions of an experiment through their effect on t_{LIFE} and f_{IGN} very much determine our ability to obtain information on the autoignition location, irrespective of the imaging capabilities. Only at relatively lower f_{IGN} when the time between events is longer than the life-time of the events themselves:

$$t_{LIFE} < 1/f_{IGN} \tag{4.2}$$

is it possible to completely resolve individual autoignition events. More importantly, if **Equation 4.2** is satisfied it is possible to argue for the independence between the

[†]All arguments made in the remainder of this section concern the imaging 'on average'. From this point the 'on average' will be dropped and implied as will all references to the mean of any random quantities used.

various events and claim that their initiation and propagation is unaffected by the presence of other events. This will be shown to be possible in **Section 5.2.2**, as will the finding that t_{LIFE} for all fuels is of the order of 1 ms and does not deviate greatly with the conditions. Specifically, for acetylene t_{LIFE} remains in the 2 ms range (**Figure 5.3**). On the other hand, f_{IGN} varies by 3 orders of magnitude with the conditions, but $1/f_{IGN}$ can be said to exist in the range of 1 – 1000 ms for the vast majority of cases spanning from the slowest to the fastest spotting. Hence, the experimental conditions are such that **Equation 4.2** is usually satisfied, with the exception of some very fast spotting conditions.

The average number of (not necessarily complete life-time) kernels contained per image (n_{IGN}) is proportional to t_{EXP} and f_{IGN}. Since **Equation 4.2** is usually satisfied, a single parameter primarily controls the information concerning autoignition events that can be retrieved from the raw images. This is t_{EXP}, and consequently, as the only parameter that can be controlled by the experimentalist, t_{EXP} is crucial in the optical investigation of the phenomenon. For a brief demonstration of the effect of t_{EXP} (due to the resulting n_{IGN}) on the possible information contained in the raw images consider the following examples. In **Figure 4.24(a)** t_{EXP} is long and the number of autoignition events is large enough (up to 300) that the resulting autoignition region appears continuous as one would expect for a lifted flame. **Figure 4.24(b)** shows approximately 20 distinct autoignition events with L_{IGN} spanning a significant region. In contrast, **Figure 4.24(c)** is a short exposure image in which a single event has been captured somewhere along its path.

If **Equation 4.2** is satisfied, then the value of t_{EXP} relative to f_{IGN} and t_{LIFE} can result in the following capabilities:

'Short Exposure' Strategy: If $t_{EXP} < t_{LIFE}$, then $n_{IGN} = 0$ and no *complete* events will be captured by a single raw image. Yet, with $t_{EXP} \ll t_{LIFE}$ the images can be made to approach 'instantaneous' snapshots with little conta-

mination by the effects of finite exposure time, albeit with the disadvantage of generating large amounts of images with no signal at all. Thus, the total reacting regions (including the original autoignition locations and the regions of post-ignition flame propagation that will be termed 'global' autoignition regions in **Section 4.4.3**) can be characterized, but without the ability of decoupling the two. The probability of having a non-empty image is given by $p_{NON-\emptyset} = \frac{t_{LIFE}}{(1/f_{IGN})}$, whereas the probability of any non-zero image containing the *whole* of the time history of a *single, complete* autoignition event (t_{LIFE}), including the location of the origin of the localized explosion initializing each featured event that is of direct interest along with the extinction of the post-ignition flamelets (p_{IGN}) is always zero. Finally, in order to ensure statistical independence between successive images, in that successive images will not contain the same autoignition events recorded at later times along their trajectories: $1/f_{FR} > t_{LIFE}$. This final requirement was satisfied by the f_{FR} limitations of the cameras.

'Long Exposure' Strategy: If $t_{EXP} > t_{LIFE}$ three possibilities exist:

- If $t_{EXP} > 1/f_{IGN}$, then the imaging strategy results in $n_{IGN} \geqslant 2$, ensuring that *more than* one event will be captured in each single raw image. In this scenario $p_{NON-\emptyset}$ is always unity and p_{IGN} is always zero. Here an additional requirement arises. It is necessary to keep the number of (not necessarily complete) events contained per image (n_{IGN}) close to unity in order to avoid losing information in each image regarding autoignition sites that appear at relatively longer lengths. If n_{IGN} is very high the location of autoignition kernels originating further downstream during t_{EXP} would otherwise be lost to the flamelets propagating from events that had already occurred upstream inside the t_{EXP} of the same image. This requirement takes the form $n_{IGN} \lesssim 1$, $t_{EXP} \lesssim 1/f_{IGN}$, where '$\lesssim$' is used in the form 'of the order of or less than'.

- If $1/f_{IGN} - t_{LIFE} < t_{EXP} < 1/f_{IGN}$, then the imaging strategy results in $1 \leqslant n_{IGN} < 2$, ensuring that *at least, but not more than* one event will be captured in each single raw image. In this scenario $p_{NON-\emptyset}$ is always unity, while the value of p_{IGN} is given by:

$$\begin{aligned} p_{IGN} &= \lim_{d \to \infty} \left\{ \frac{t_{EXP} - t_{LIFE} + 2^{1-d}}{1/f_{IGN}} \right\} \\ &\to \frac{t_{EXP} - t_{LIFE}}{1/f_{IGN}} \end{aligned} \tag{4.3}$$

- If $t_{EXP} < 1/f_{IGN} - t_{LIFE}$, then the imaging strategy results in $n_{IGN} \leqslant 1$, ensuring that at *most* one event will be captured by a single raw image. As t_{EXP} is shortened to approach t_{LIFE} the probability that a non-empty instantaneous image will contain information on the location of the initial explosion of each autoignition event captured (p_{IGN}) decreases. More rigorously, the probability of having a non-empty image and of having a non-zero image containing the full life-time of an autoignition event can be expressed mathematically by:

$$\begin{aligned} p_{NON-\emptyset} &= \lim_{d \to \infty} \left\{ \frac{t_{EXP} + t_{LIFE} - 2^{1-d}}{1/f_{IGN}} \right\} \\ &\to \frac{t_{EXP} + t_{LIFE}}{1/f_{IGN}} \end{aligned} \tag{4.4}$$

$$\begin{aligned} p_{IGN} &= \lim_{d \to \infty} \left\{ \frac{t_{EXP} - t_{LIFE} + 2^{1-d}}{t_{EXP} + t_{LIFE} - 2^{1-d}} \right\} \\ &\to \frac{t_{EXP} - t_{LIFE}}{t_{EXP} + t_{LIFE}} \end{aligned} \tag{4.5}$$

  Ideally the condition $t_{EXP} \cong 1/f_{IGN} - t_{LIFE}$ would be sought, but because f_{IGN} varies dramatically across the conditions it was difficult to adjust t_{EXP} accordingly. Instead, t_{EXP} is everywhere reported and the inferences from the results should be seen in terms of the discrepancy between t_{EXP}, $1/f_{IGN} - t_{LIFE}$ and $1/f_{IGN}$ as discussed and as outlined in the above expressions.

Summarizing, for short exposure imaging:

$$t_{EXP} \ll t_{LIFE} < 1/f_{FR} \quad \text{and} \quad t_{LIFE} < 1/f_{IGN} \tag{4.6}$$

with **Equation 4.1** automatically satisfied. For long exposure imaging, and keeping in mind the distinction based on the difference between t_{EXP} and $1/f_{IGN} - t_{LIFE}$:

$$t_{LIFE} < t_{EXP} \leqslant 1/f_{FR} \quad \text{and} \quad t_{LIFE} < 1/f_{IGN} \tag{4.7}$$

For all fuels t_{LIFE} was found to be of the order of a few ms. Hence, all short exposure imaging was performed with t_{EXP} less than about $1/10^{th}$ of a ms. During this exposure time and with typical flame propagation velocities in the range 20 – 30 m/s objects would have moved by 2 – 3 mm. This was considered sufficiently 'short' relative to the lengthscales involved (see for example **Figures 4.14** and **4.22** for autoignition and flame propagation in the 'jacketed' quartz tube with $D_{TUBE} =$ 24.78 mm and in the 'large-Ø' tube with $D_{TUBE} = 33.96$ mm for the CTHC and CTHAJ respectively). On the other hand, raw images taken with t_{EXP} greater than about 1 ms were considered long exposure and in general adequate for the recording of the initial autoignition locations with high probability.

The CCD camera was allowed to film for approximately 30 – 120 s for each run corresponding to a particular set of conditions. The overall methods involved:

- "Long Exposure": 50 – 400 still images at frame rates (f_{FR}) of 3 Hz and exposure times, $t_{EXP} = 250$ ms[‡], and,
- "Short Exposure": 1000 – 3000 still images at $f_{FR} = 25$ Hz, but with the shutter set to close faster, at $t_{EXP} = 0.25$ ms[‡].

[‡]Note that through this thesis the frame rate is always approximately equal to the inverse of t_{EXP}, except where specifically noted, as here.

The ICCD camera was used to take between 50 and 1200 images, but most often 200 images per operating condition, at a maximum of 10 Hz and over a wide range of exposure times in the range 0.1 – 80 ms. The exposure times were set *a priory* so as to approximately obey the requirements of either **Equations 4.6** or **4.7**.

4.4.2 Image Processing

In order to measure the autoignition length from the injector the raw images were first processed so as to remove background noise and improve the signal-to-noise ratio (SNR). Individual images were processed in stages by median smoothing, adaptive Wiener filtering and 4^{th} order low-pass filtering in the frequency domain. Aiming to examine the effect of the processing on the results and to ensure that it is not significant, all measurements of autoignition length were performed on both the raw and processed versions of all images. It was found that after processing the results were similar to the calculations based on the raw data and so throughout this thesis the processed results are used.

4.4.3 Image Calculations

The discussions of this section are important for the interpretation of the results of **Chapter 6**, which characterize the location of the autoignition regions. In **Sections 4.2.2** and **4.3.2** various scenarios were discussed concerning the propagation and extinction of flames originating at the autoignition sites. Here, a differentiation will be made between the 'earliest' autoignition locations and the 'global' autoignition region. The former are only those locations at which autoignition is first initiated by the localized explosive processes described in **Section 4.2.2** and pointed out in the caption of **Figure 4.16**. The latter is defined as the region inside which autoignition occurs and post-ignition flamelets exist and propagate. It spans the full extent described by L_{IGN} in **Figures 2.1** and **2.8**.

Short Exposure Images:

In **Section 4.4.1** it was explained how short exposure imaging strategies for which f_{FR} is slower than the physical timescales can only provide information on the 'global' autoignition regions, or in other words contaminated by the propagation of the post-ignition flamelets. Consider once again the short exposure image **Figure 4.24(c)**, with $t_{EXP} \ll t_{LIFE}$. For each experimental condition (run) a number (N) of such *non-zero* instantaneous images was generated. In any single, instantaneous image ('snapshot') a region of presence of light is defined as an 'autoignition spot' and the general distance of the spot extent from the injector is L_{IGN}. All images corresponding to the same run were used to compile three further 'averaged' images termed: average (AVG), standard-deviation (STD) and probability-function[§] (PF) images. The intensity, $I(r,z)$, at a radius r from the centreline and axial length z from the injector in these images is defined by:

$$I_{AVG}(r,z) = \frac{1}{N}\sum_{i=1}^{N} I_i(r,z) \tag{4.8}$$

$$I_{STD}(r,z) = \sqrt{\frac{1}{N-1}\sum_{i=1}^{N}\Big[I_i(r,z) - I_{AVG}(r,z)\Big]^2} \tag{4.9}$$

$$I_{PF}(r,z) = \frac{1}{N}\sum_{i=1}^{N}\lceil I_i(r,z) - I_{THRES}\rceil;\ I_{THRES} < 1 \tag{4.10}$$

[§]In this thesis a distinction *is* made between the (one dimensional in this explanation) number function of observations $n(x)$, the probability $p(x)$ and the probability density $pdf(x)$. The number function, $n(x)$, is the number of observations made at a particular value of the independent variable, x, in the range $x \pm \frac{\delta x}{2}$, or, $n(x) = n(x - \frac{\delta x}{2} < x \leq x + \frac{\delta x}{2})$. The probability $p(x)$ is the number function, $n(x)$, made at a particular value of the independent variable, x, divided by the total number of observations made at all x, $p(x) = \frac{n(x)}{\sum_{all\,x} n(x)} = \frac{n(x)}{N}$. The *total* probability is then the *sum* of all probabilities and is equal to unity, $\sum_{all\,x} p(x) \equiv 1$. On the other hand, the probability-density-function, $pdf(x)$, is the probability, $p(x)$, *normalized* by the discretization range, δx, of the independent variable, or $pdf(x) = \frac{p(x)}{\delta x}$, whose *integral* is unity, i.e. $\int_{all\,x} pdf(x)dx = \sum_{all\,x} pdf(x)\delta x = \sum_{all\,x} p(x) \equiv 1$.

Here, N is the number of instantaneous images and I_i the pixel intensity in the instantaneous images. For the I_{PF} normalization procedure I_{THRESH} is an appropriate threshold relative to the noisy background that sets the level above which chemiluminescence signal is considered to be present. The intensity was set to unity at the pixels whose intensity was higher than the threshold and zero elsewhere. Examples of AVG, STD and PF averaged images can be found in **Figures 4.25** and **4.26** taken in the CTHC and CTHAJ respectively.

From the generalized presence of chemiluminescence signal as described by L_{IGN} in the three 'averaged' images various measures of autoignition length have been defined and these are broadly split into:

1. For all images, the minimum autoignition length, $L_{MIN} \equiv min\{L_{IGN}\}$ that characterizes the axial distance from the injector to the most upstream point of the autoignition region occupied during the total exposure time of all images taken during a run, $N \cdot t_{EXP}$. This length was evaluated by finding the rise height from the background of a certain proportion (1, 3 and 5% have been used) of the peak value in the image. The precise level of the threshold was not critical because of the steep axial intensity profile in the regions facing the injector. This quantity is illustrated in **Figures 4.24** and **4.26** for the CTHC and CTHAJ burners respectively. Ideally, the measure of L_{MIN} from each of the AVG, STD and PF images should agree, but noise ensures that the results are not always similar. It was found that the STD images were generally better at detecting this length accurately, as demonstrated in **Figure 4.26(a)**.

2. In addition for the PF image it was possible to define lengths from the injector to the 'centre' of the autoignition region, including:

   (a) The mean of the autoignition length L_{IGN}, $L_{MEAN} \equiv \langle L_{IGN} \rangle$, that was calculated directly from the two-dimensional PF by double numerical integration: $L_{MEAN} = \sum_{i=1}^{n} \sum_{j=1}^{m} I_{PF}(i,j) L_{IGN}(i,j)$, and,

(b) The mode of the autoignition length L_{IGN}, $L_{MODE} \equiv mode\{I_{PF}; z\}$, which was located inside the two-dimensional PF: $L_{MODE} = L_{IGN}[I_{PF}(r,z) = max\{I_{PF}(r,z)\}]$.

Both mean and mode lengths have been calculated for all cases, with L_{MEAN} found to be usually within -5% to +25% of L_{MODE}. This is justified given the typical shape of the two-dimensional pdfs of L_{IGN} such as those shown in **Figure 4.25**, where it is noted that the pdfs are slightly skewed towards the injector. Based on this finding and to decrease the number of variables, L_{MODE} will be mostly used throughout this thesis as it is also easier to calculate.

Furthermore, two lengths defining the overall spread/size of the autoigniting region were calculated for all runs. These are L_{STD} and L_{SPREAD}. The former is the square root of the second central moment of L_{IGN}, calculated from the existing two-dimensional PF from: $L_{STD} = \sqrt{\sum_{i=1}^{n}\sum_{j=1}^{m} I_{PF}(i,j)[L_{IGN}(i,j) - L_{MEAN}]^2}$, whereas the latter is defined as the difference between the minimum length and either the mode: $L_{SPREAD} = L_{MODE} - L_{MIN}$, or mean of L_{IGN}: $L_{SPREAD} = L_{MEAN} - L_{MIN}$.

Long Exposure Images:

Contrary to short exposure imaging for which only the 'global' autoignition region can be characterized, for long exposure images it is possible to characterize both 'global' and 'earliest' regions. For the purposes of this thesis the later is of particular interest and so only the earliest lengths have been used from each image, examples of which can be found in **Figures 4.24(a)** and **4.24(b)**.

In the processing of each individual long exposure image the 'background' intensity was set to be equal to the mean plus 2 standard deviations of a zero-signal region sufficiently away from autoignition. In order to find the absolute closest reacting region from the injector, measurements of $\widehat{L_{MIN}}$ were made such that $\widehat{L_{MIN}}$

is the length from the injector to a rise height from the 'background' of only 1% *in each image*. A threshold method was developed to go through all images, detect $\widehat{L_{MIN}}$ in each non-empty image and use simple geometrical scaling in order to convert the measured length from pixels into mm. The scaling took account of any visual distortion introduced by the thickness of the curved tube.

From this it was possible to calculate, for each condition:

1. The absolute minimum recorded length during a run at those conditions, L_{MIN}, which is $min\{\widehat{L_{MIN}}\}$, and,
2. The average over all images of the minimum length in each image, $\langle L_{MIN} \rangle \equiv \langle \widehat{L_{MIN}} \rangle$.

Here, so as to discriminate between an instantaneous measurement of L_{MIN} from a single image/realization, the notation $\widehat{L_{MIN}}$ has been used. Otherwise, when referring to an 'averaged' image complied from many individual snapshots, as in the case of the short exposure images, or the overall minimum length from all images the notation L_{MIN} will be employed. There exists a subtle difference between L_{MIN} from the two methods. It is expected that L_{MIN} from a short exposure measurement, that is a measurement from an *averaged* image, will be slightly longer than that from a long exposure analysis at the same conditions, since the latter treats $\widehat{L_{MIN}}$ from *all individual/instantaneous* images. This small discrepancy is enhanced by the lower required level of rise height from the background in long exposure images. Recall that for short exposure measurements L_{MIN} was defined as the length from the injector to a rise height from the background of about 3% relative to the maximum intensity in each '*averaged*' (AVG, STD or PF) image, whereas in long exposure images the reacting region is tracked based on a rise of 1% from the background.

L_{MIN} can be compared directly across the various conditions and with values of the same variable obtained from either short or long exposure images. Only

its statistical convergence will vary, due to the total exposure time from all images associated with that run, $N \cdot t_{EXP}$. On the other hand, the interpretation of $\langle L_{MIN} \rangle$ depends on the exposure time *and* conditions (i.e. f_{IGN}). This has been the motivation behind the discussion in **Section 4.4.1**. Given a particular, long exposure t_{EXP} for all images and particular t_{LIFE}, $\langle L_{MIN} \rangle$ should approach L_{MIN} at conditions of high f_{IGN} when $t_{EXP} \gg 1/f_{IGN} + t_{LIFE}$ and n_{IGN} is large. Any difference between L_{MIN} and $\langle L_{MIN} \rangle$ when n_{IGN} is high (e.g. up to 600 for some faster spotting conditions when f_{IGN} is 2 kHz) can only be the result of the effects of low-frequency (relative to the imaging) temperature and velocity fluctuations on the phenomenon and hence the realizations of $\widehat{L_{MIN}}$. As the conditions are changed so that $t_{EXP} \to 1/f_{IGN} + t_{LIFE}$, then $\widehat{L_{MIN}} \to L_{TRUE}$. The statistical convergence of $\langle L_{MIN} \rangle$ towards L_{MIN} weakens and $\langle L_{MIN} \rangle$ approaches the mean axial length from the injector of the 'true' location of the first emergence of the autoignition kernels, $\langle L_{MIN} \rangle \to \langle L_{TRUE} \rangle$. The difference between $\langle L_{MIN} \rangle$ and $\langle L_{TRUE} \rangle$ is that the latter does not include any information related to the post-ignition flamelets. The reader is asked to keep in mind that strong evidence exists from high-speed image sequences that the original point of emergence of an autoignition kernel is close to the minimum distance from the injector that that autoignition event will ever get. Then, just as the pdfs of L_{IGN} from the short exposure images can be used to describe the global autoignition regions including the explosion and flame front propagation, pdfs of $\widehat{L_{MIN}}$ can be compiled for conditions resulting in images with n_{IGN} of the order of unity, to describe the true regions of autoignition. It is possible to recover the full pdf of L_{TRUE} by assuming, as before, that $L_{TRUE} \cong \widehat{L_{MIN}}$ and the spread in the true autoignition locations, σ_{TRUE}, can be calculated directly as the standard deviation of $\widehat{L_{MIN}}$, σ_{MIN}. Finally, the discrepancy between $\langle L_{MIN} \rangle$ and L_{MIN} *at* $n_{IGN} \cong 1$ is also expected to characterize the spread in L_{TRUE} and should be approximately equal to σ_{TRUE}.

4.5 Conclusions from Chapter 4

This chapter contained a preliminary presentation of visual and audible observations of autoignition and related phenomena achieved in the experimental apparatus. The observations were grouped into those made in the CTHC burner and those made in the CTHAJ. Depending on the inlet velocity and temperature of the air and fuel and the degree of dilution of the fuel stream with excess nitrogen, various regimes of operation were possible, but these were not identical in both burners. Four main regimes were found in the CTHC: 'No Ignition', 'Random Spots', 'Flashback' and 'Lifted Flame'. In the CTHAJ a further 'Spot-Wake Interactions' regime was observed. Autoignition has been described, mostly qualitatively, in terms of:

- The characteristics of its localized explosive origins.
- The development from autoignition kernels to fully-fledged propagating flames.
- The fate of these unsteady post-ignition flames.

In the 'Random Spots' regime, repeated autoignition spots appear in a statistically steady manner, both temporally and spatially, each associated with post-ignition flame propagation and extinction. In order to quantify these unsteady phenomena from optical measurements, various approaches were discussed, based on their lifetime and their mean frequency of occurrence.

4.6 Chapter 4 Figures

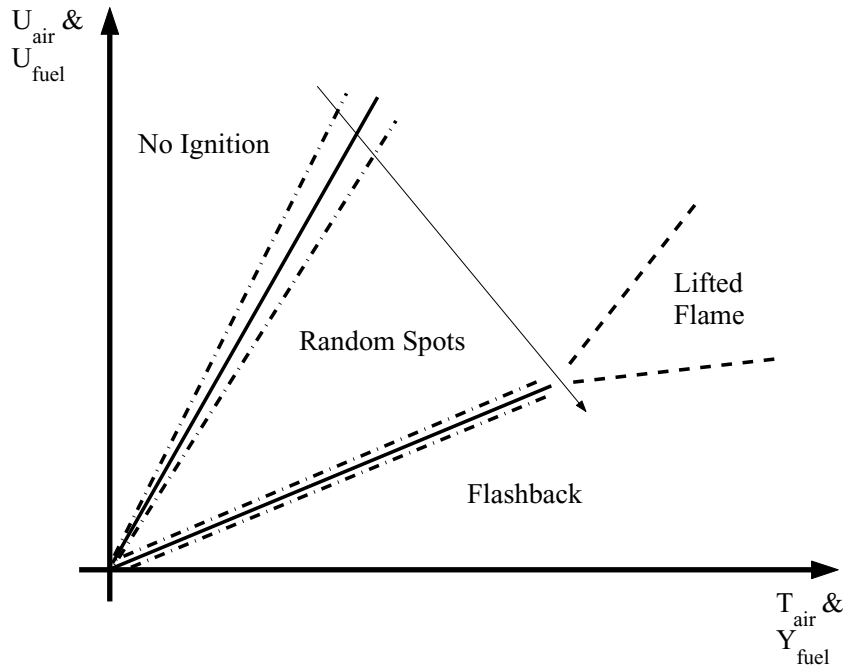

Figure 4.1: Operating regimes in terms of T_{air}, Y_{fuel} and U_{air}, U_{fuel}. Dashed lines denote the 'Lifted Flame' regime boundary. Dash-dot lines indicate the extent of regions of transitional behaviour. Arrow illustrates the order in which the various regimes will be explained in the current chapter, i.e. as the temperature and fuel dilution are gradually decreased and/or air and fuel velocities increased from conditions in which no autoignition is observed in the tube.

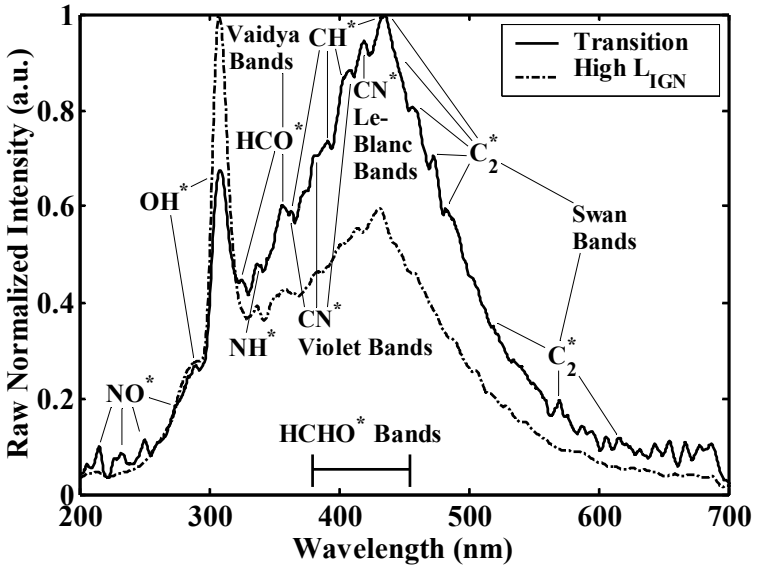

(a)

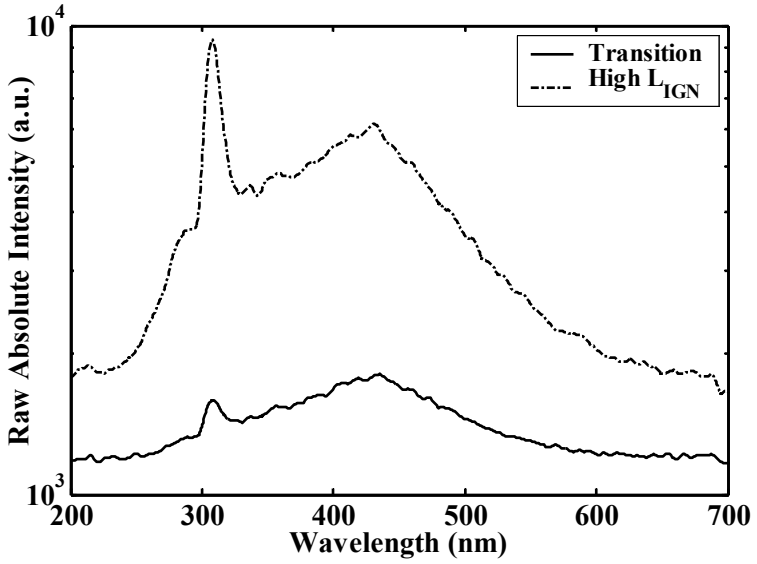

(b)

Figure 4.2: Raw normalized and absolute intensity emission spectra during 'Pre-Ignition Reactions' transition and 'Random Spots' regime for ethylene in CTHC. (a) Raw normalized intensity showing content at wavelengths attributed (left-to-right) to NO^*, OH^*, HCO^* ('Vaidya Bands'), NH^*, CN^* ('Violet' and 'Le-Blanc Bands'), CH^* and C_2^* ('Swan Bands'). Showing continuous region of expected formaldehyde ($HCHO^*$) emission. Certain bands cannot be resolved and appear merged. (b) Raw absolute spectra exactly corresponding to (a). Solid line at T_{air} = 1028 K, U_{air} = 13.3 m/s, υ_{fuel} = 2.45, Y_{C2H4} = 0.60. Dashed-dot line at T_{air} = 1036 K, U_{air} = 13.4 m/s, υ_{fuel} = 3.20, Y_{C2H4} = 0.75. Both spectra with 30 s exposure.

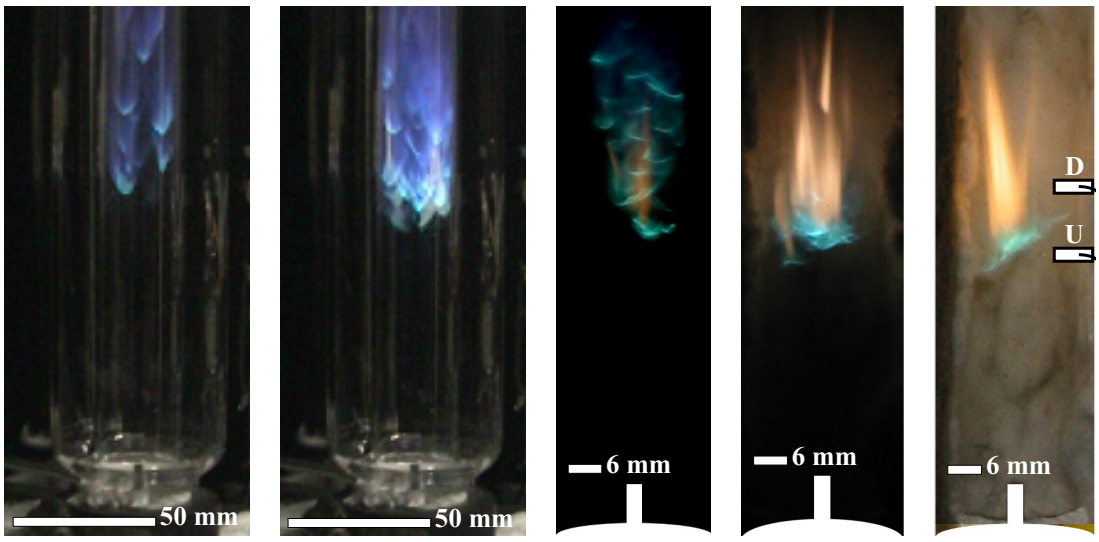

(a) (b) (c) (d) (e)

Figure 4.3: Digital RBG, direct-photography, visible images of acetylene 'Random Spots' autoignition in CTHC. (a) and (b) at $T_{air} = 877$ K, $U_{air} = U_{fuel} = 24.8$ m/s, $Y_{C2H2} = 0.65$ and with 160 ms exposure. (c) $T_{air} = 832$ K, $U_{air} = U_{fuel} = 10.9$ m/s, $Y_{C2H2} = 0.70$ and with 100 ms exposure. (d) $T_{air} = 846$ K, $U_{air} = U_{fuel} = 12.1$ m/s, $Y_{C2H2} = 0.70$ and with 100 ms exposure. (e) $T_{air} = 832$ K, $U_{air} = U_{fuel} = 10.9$ m/s, $Y_{C2H2} = 0.70$ and with 50 ms exposure. Also showing spectrometer probe locations/heights relative to the autoignition regions for 'Upstream' (U) and 'Downstream' (D) spectral measurements as explained in the 'Random Spots' section. Indication of scale given.

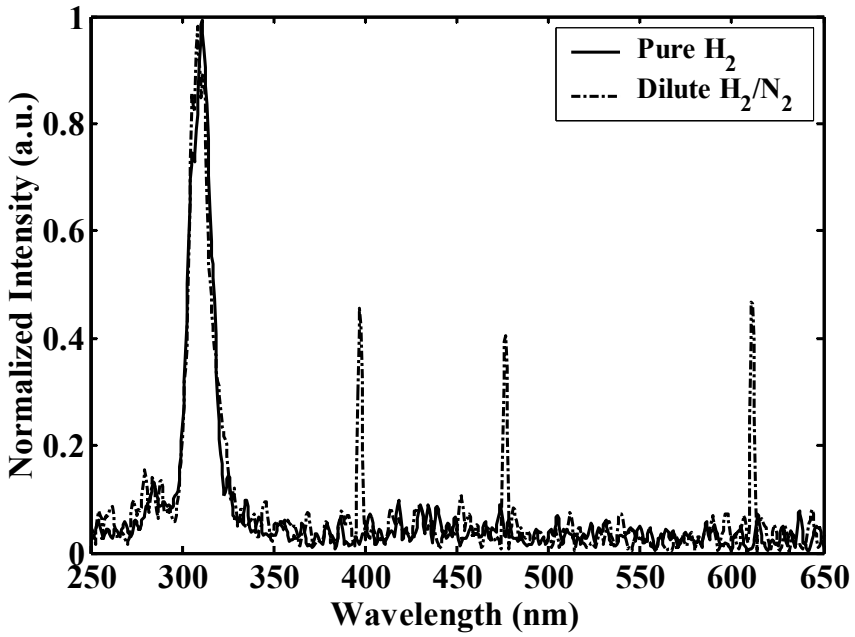

Figure 4.4: Normalized intensity emission spectra during 'Random Spots' regime for hydrogen in CTHC. Solid line at $Y_{H2} = 1.00$. Dashed-dot line at $Y_{H2} = 0.90$. Both spectra at $T_{air} = 947$ K, $U_{air} = U_{fuel} = 25.1$ m/s and with 1 s exposure.

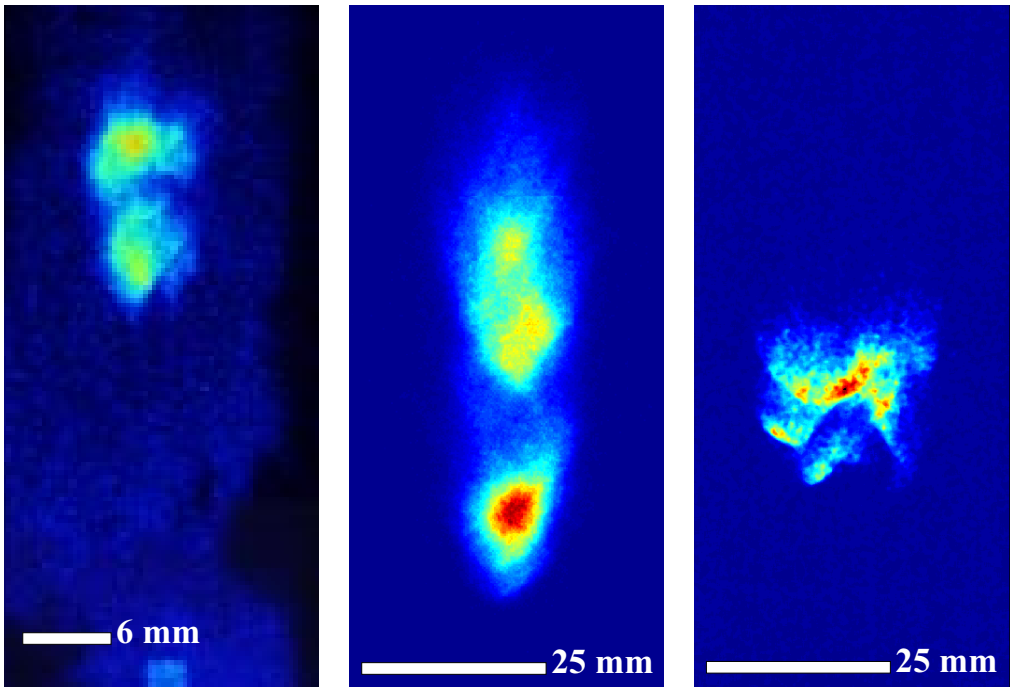

(a) (b) (c)

Figure 4.5: Hydrogen 'Random Spots' autoignition imaging in CTHC. (a) False-colour/intensity, UV-to-IR broadband image at T_{air} = 969 K, U_{air} = 14.0 m/s, $\upsilon_{fuel} = 5.52$, $Y_{H2} = 0.05$ and with 0.2 ms exposure. (b) False-colour/intensity, OH^* (307±10 nm) image at T_{air} = 949 K, U_{air} = 18.8 m/s, υ_{fuel} = 2.79, Y_{H2} = 0.15 and with 10 ms exposure. (c) False-colour/intensity, OH^* (307±10 nm) image at T_{air} = 947 K, $U_{air} = U_{fuel}$ = 25.1 m/s, Y_{H2} = 1.00 and with 5 ms exposure. Intensity has been re-scaled for each image to give maximum resolution. Indication of scale given.

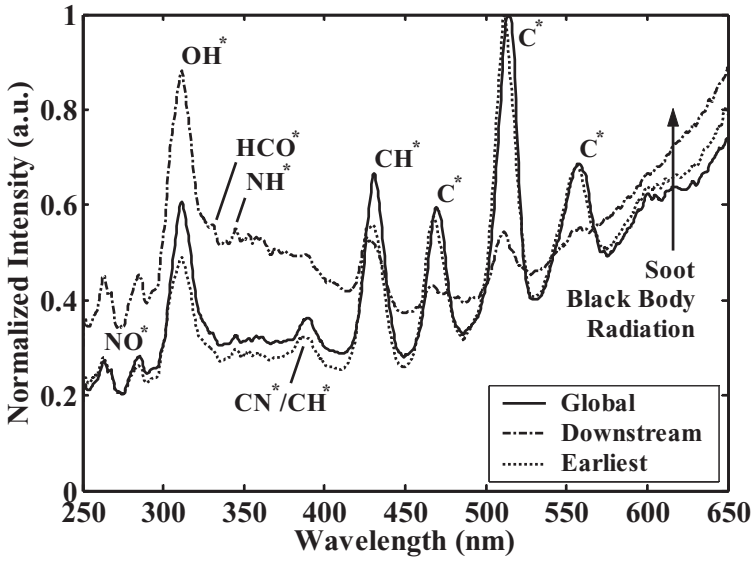

(a)

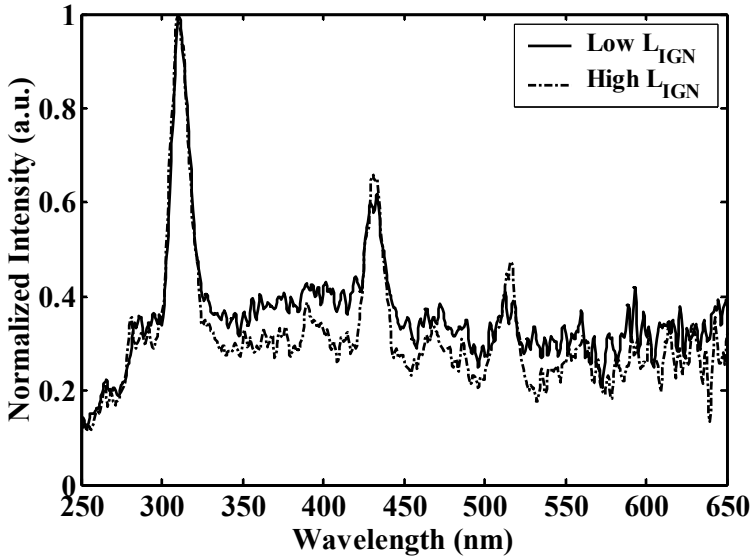

(b)

Figure 4.6: Normalized intensity emission spectra during 'Random Spots' regime for acetylene and n-heptane in CTHC. (a) Acetylene at various conditions and with 100 s exposure. (b) n-Heptane at various conditions and with 2 s exposure. L_{IGN} shown at 46 and 82 mm.

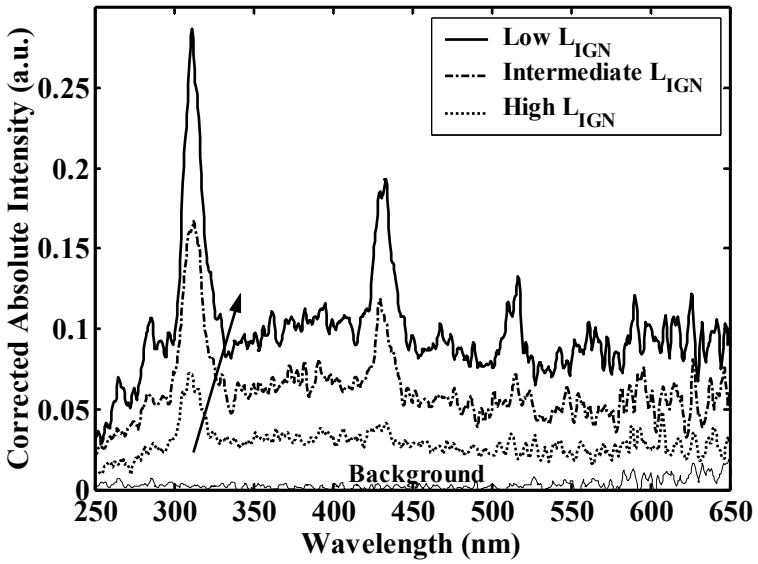

(a)

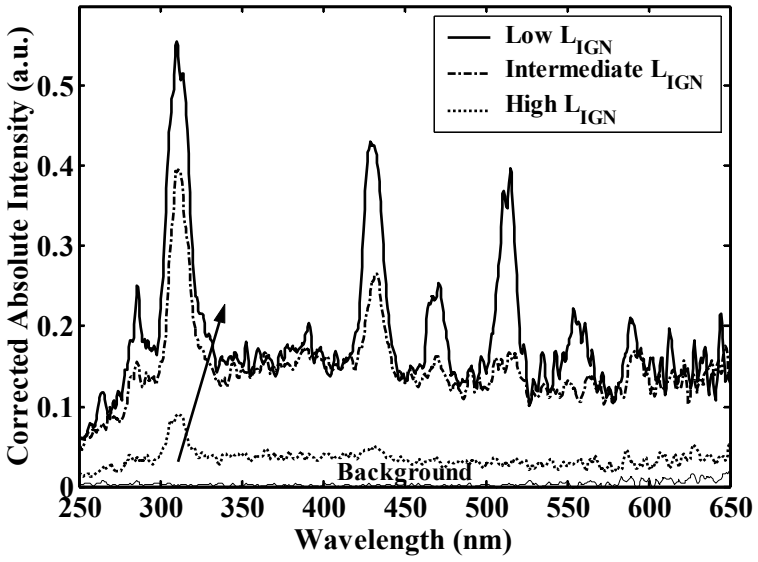

(b)

Figure 4.7: Corrected absolute intensity emission spectra for n-heptane as a function of L_{IGN} in CTHC. (a) At various conditions and with 2 s exposure. L_{IGN} shown decreasing from 66 to 55 to 51 mm. (b) At various conditions and with 2 s exposure. L_{IGN} shown decreasing from 97 to 65 to 46 mm. Background signal recorded with the spectrometer probe in place and at hot conditions but without fuel injection.

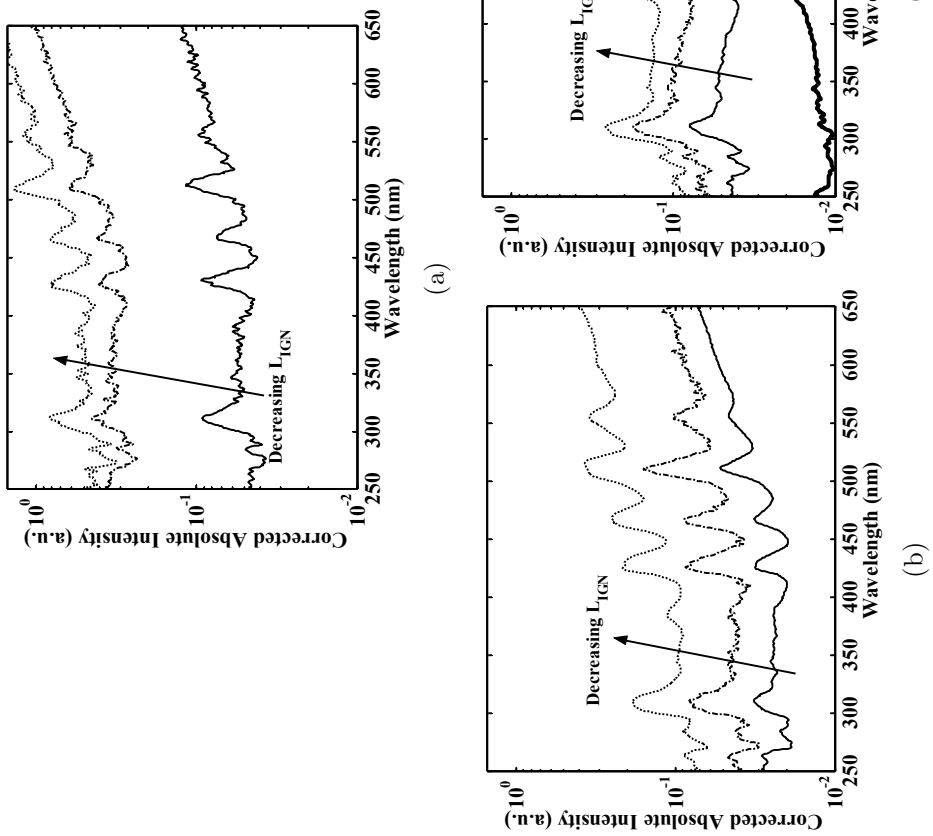

Figure 4.8: Corrected absolute intensity emission spectra for 'Global', 'Upstream' (U) and 'Downstream' (D) autoignition regions of acetylene as a function of L_{IGN} in CTHC. (a) 'Global' signal with 0.1 – 1 s exposures. (b) 'Upstream' autoignition region (U) with 1 – 100 s exposures. (c) 'Downstream' region with 1 – 100 s exposures (D) and comparison with attached diffusion flame with 100 s exposure (intensity divided by a factor of 20). L_{IGN} shown decreasing from 68 to 51 to 40 mm in all plots.

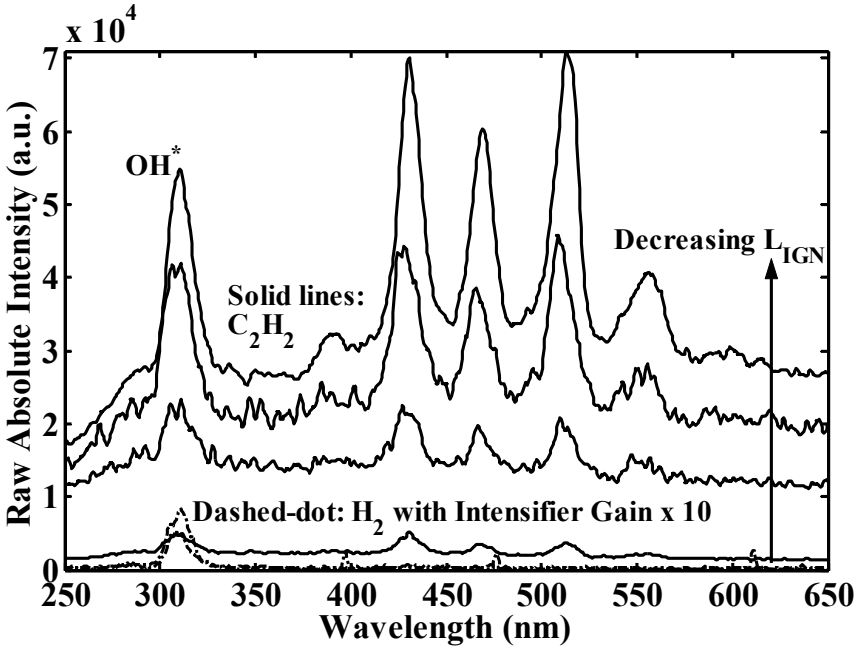

Figure 4.9: Global raw absolute intensity emission spectra comparison between hydrogen and acetylene in 'Random Spots' regime in CTHC. Dashed-dot line corresponds exactly to normalized hydrogen spectrum in **Figure 4.4**. Spectrometer ICCD gain used for this hydrogen measurement is 10x that used for acetylene. All solid lines are for acetylene at various L_{IGN} spanning from 'Nothing–to–Spots' to 'Spots–to–Flame' conditions as indicated by the arrow and with 1 s exposure.

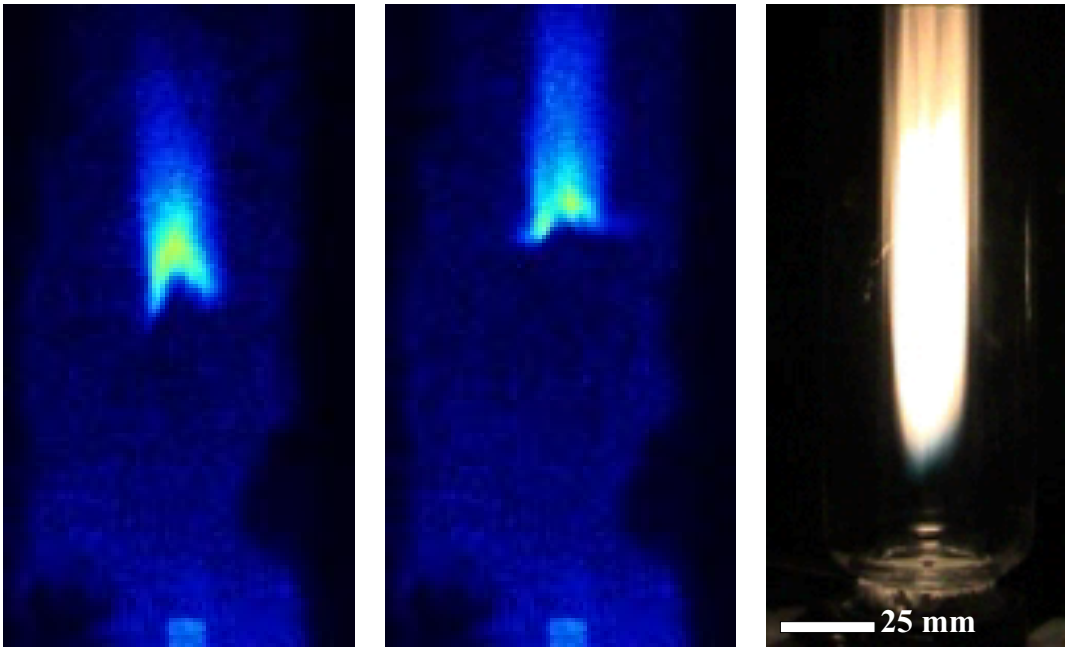

(a) (b) (c)

Figure 4.10: Autoignition examples of near-'Flashback' and 'Lifted Flame' operation in CTHC. (a) and (b) near-'Flashback' conditions with hydrogen. False-colour/intensity, UV-to-IR broadband images at T_{air} = 961 K, U_{air} = 13.5 m/s, υ_{fuel} = 4.70, Y_{H2} = 0.05 and with 0.2 ms exposure. Scale indicated by 3 mm injector. (c) 'Lifted Flame' conditions with acetylene. Digital RBG, direct-photography, visible images at T_{air} = 904 K, U_{air} = 25.5 m/s, υ_{fuel} = 0.84, Y_{C2H2} = 1.00 and with 160 ms exposure.

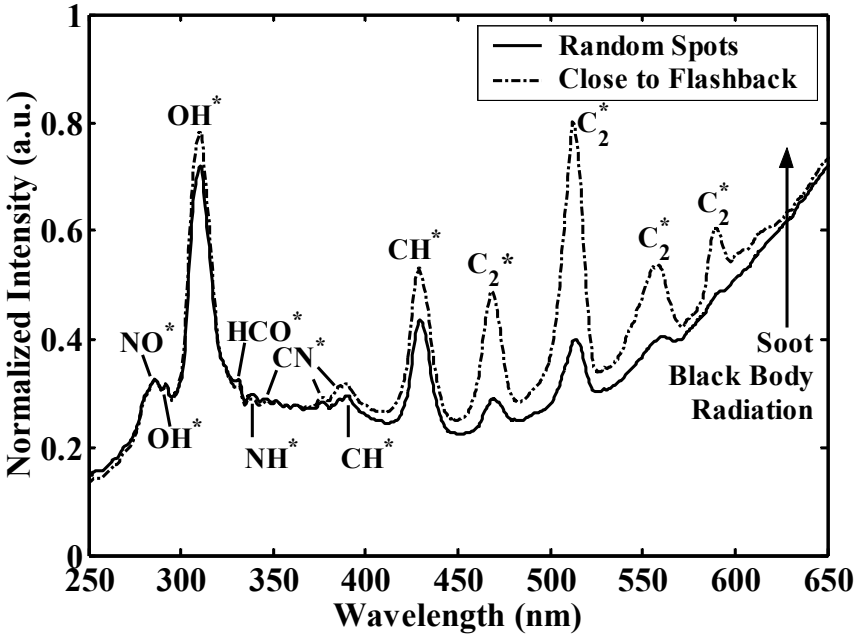

Figure 4.11: Global normalized intensity emission spectra in near–'Flashback' operation and comparison with 'Random Spots' regime for ethylene in CTHC. Solid line at T_{air} = 1074 K, U_{air} = 36.6 m/s, υ_{fuel} = 1.50, Y_{C2H4} = 0.75. Dashed-dot line at T_{air} = 1087 K, U_{air} = 38.2 m/s, υ_{fuel} = 1.45, Y_{C2H4} = 0.75. Both spectra with 0.1 s exposure. Showing from left-to-right content at wavelengths attributed to chemiluminescence from NO^*, OH^*, HCO^*, NH^*, CN^*, CH^* and C_2^*. Also showing continuous 'tail' at higher wavelengths (above c. 425 nm) caused by black-body radiation of soot. Certain bands cannot be resolved and appear merged. Can be directly compared to **Figure 4.2(a)**.

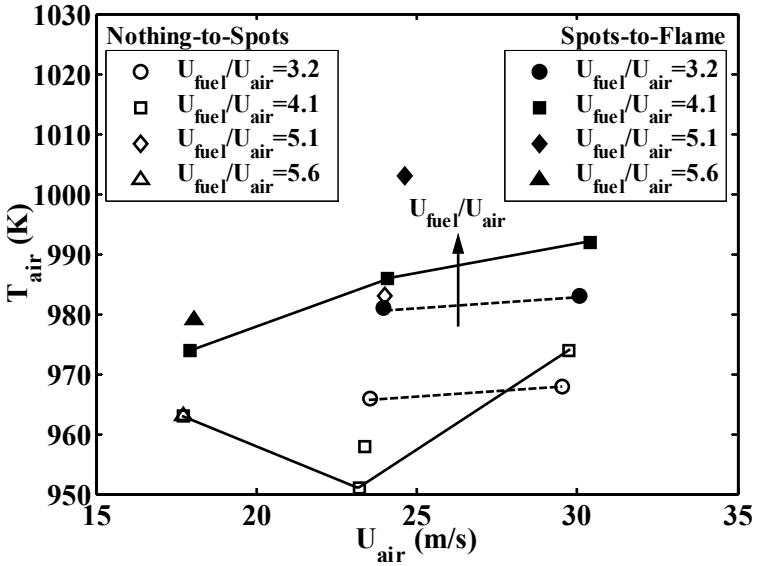

(a)

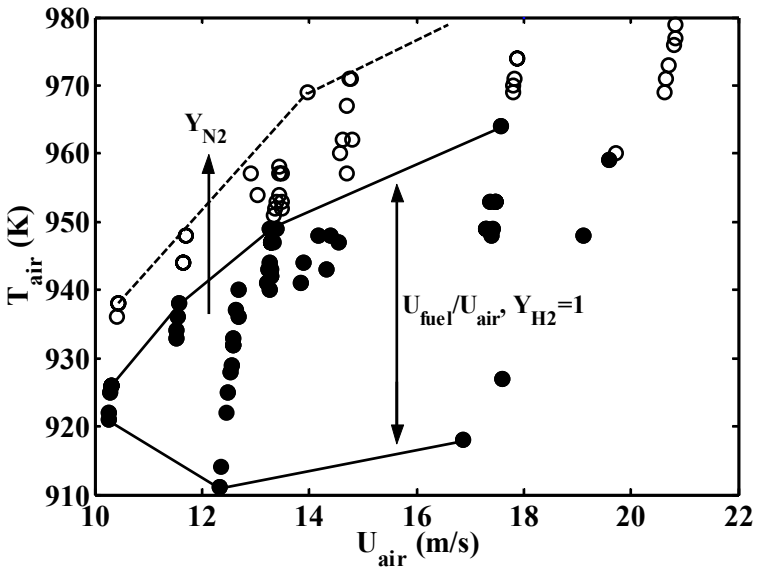

(b)

Figure 4.12: Temperature–Velocity operation envelope limits for hydrogen in CTHC. Showing 'Nothing–to–Spots' and 'Spots–to–Flame' transition boundaries. (a) Y_{H2} fixed to 0.15 for all data points. Solid lines mark boundaries of lowest T_{air} necessary at a particular U_{air} to cause the first instance of 'Random Spots' autoignition (lower bound) and the first instance of 'Flashback' (upper bound). Shown for 4 different values of υ_{fuel} as indicated in the legend. (b) All data points indicate the possibility of 'Random Spots' behaviour. Filled data points show $Y_{H2} = 1.00$ results, with υ_{fuel} varying from 3.2 to 5.6. Empty data points show results for Y_{H2} between 0.05 – 0.40, with υ_{fuel} varying from 0.35 to 12.6.

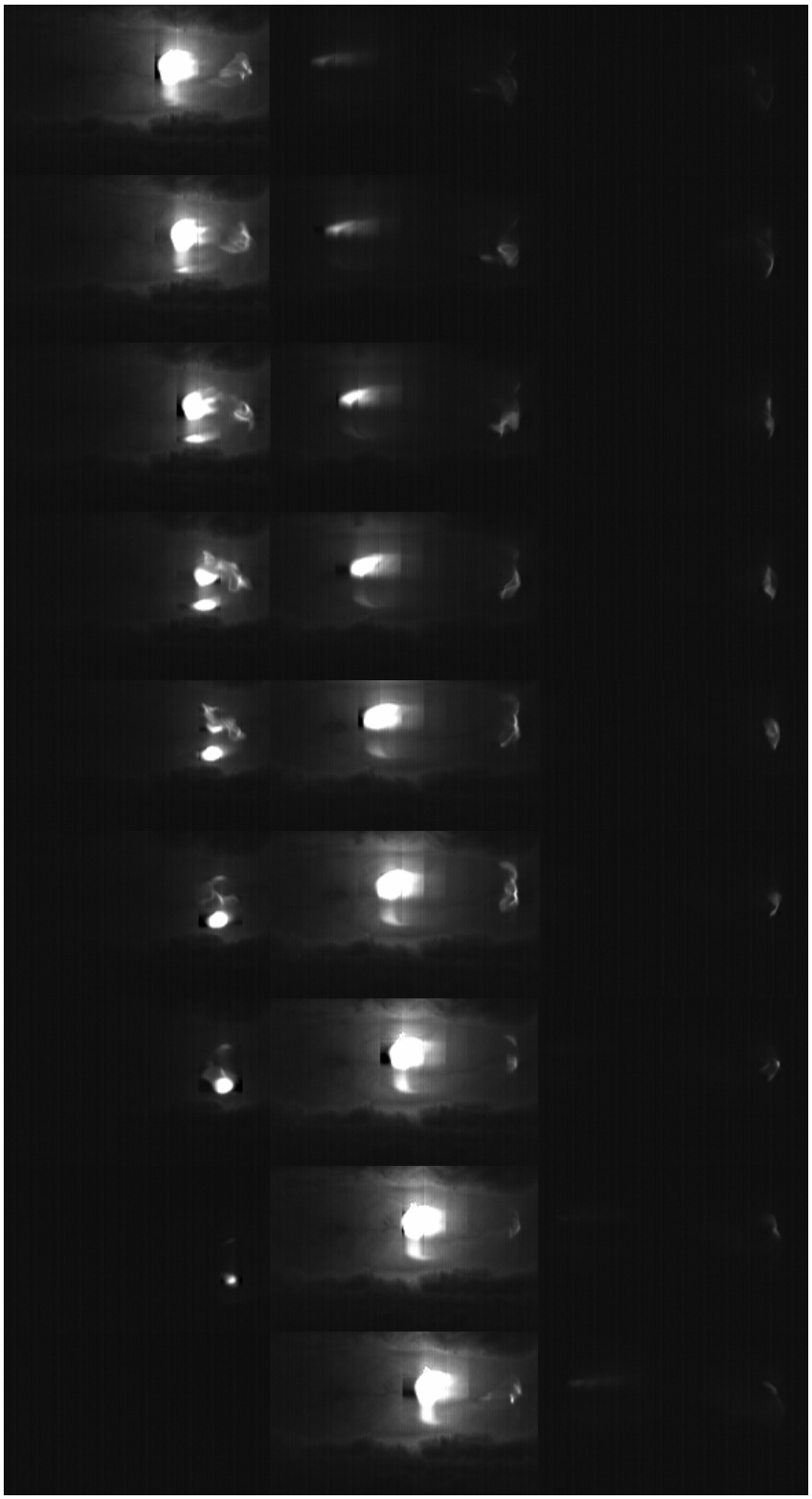

Figure 4.13: Fast sequence of acetylene autoignition in CTHC. Direct-photography, visible-to-IR broadband sequence kernel development and flame propagation at 4.5 kHz and conditions T_{air} = 832 K, U_{air} = 10.9 m/s, v_{fuel} = 1.04, $Y_{C2H2} = 0.70$.

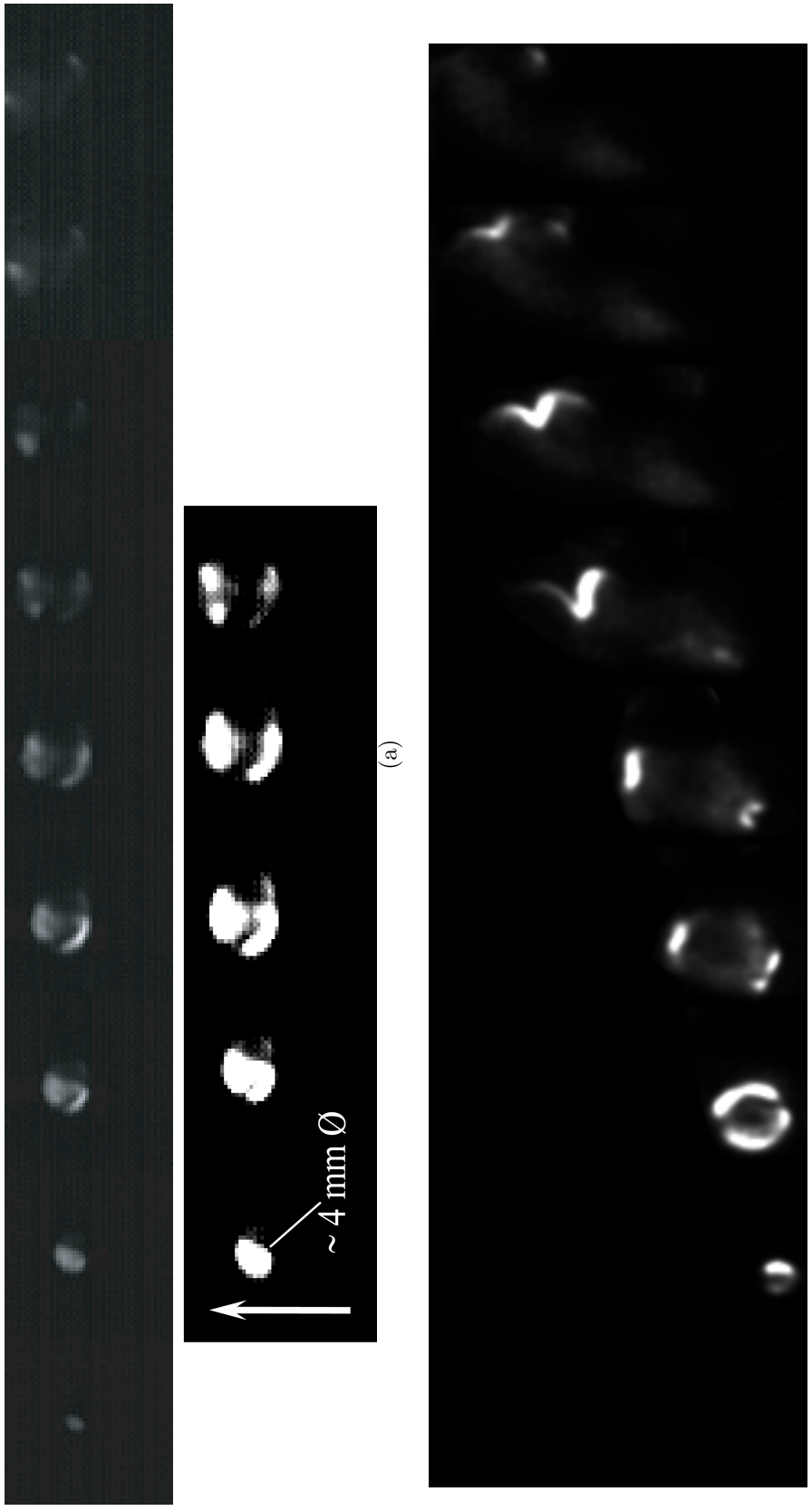

Figure 4.14: Close-up fast sequences of autoignition kernel development in 'Random Spots' regime in CTHC. (a) Direct-photography, visible-to-IR broadband sequence of acetylene at 13.5 kHz and conditions $T_{air} = 809$ K, $U_{air} = 10.4$ m/s, $v_{fuel} = 0.93$, $Y_{C2H2} = 0.75$. Flow direction upwards. Bottom row is high-contrast version of the top row of corresponding images. Indication of scale given. (b) OH^* (307±10 nm) sequence of n-heptane at 17 kHz and conditions $T_{air} = 1089$ K, $U_{air} = 15.8$ m/s, $v_{fuel} = 0.97$, $Y_{C7H16} = 0.95$. Flow direction upwards.

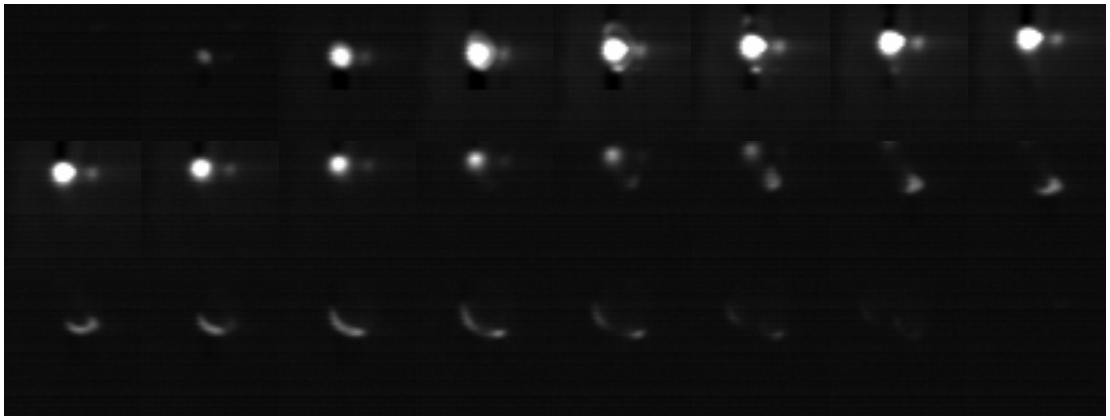

(a)

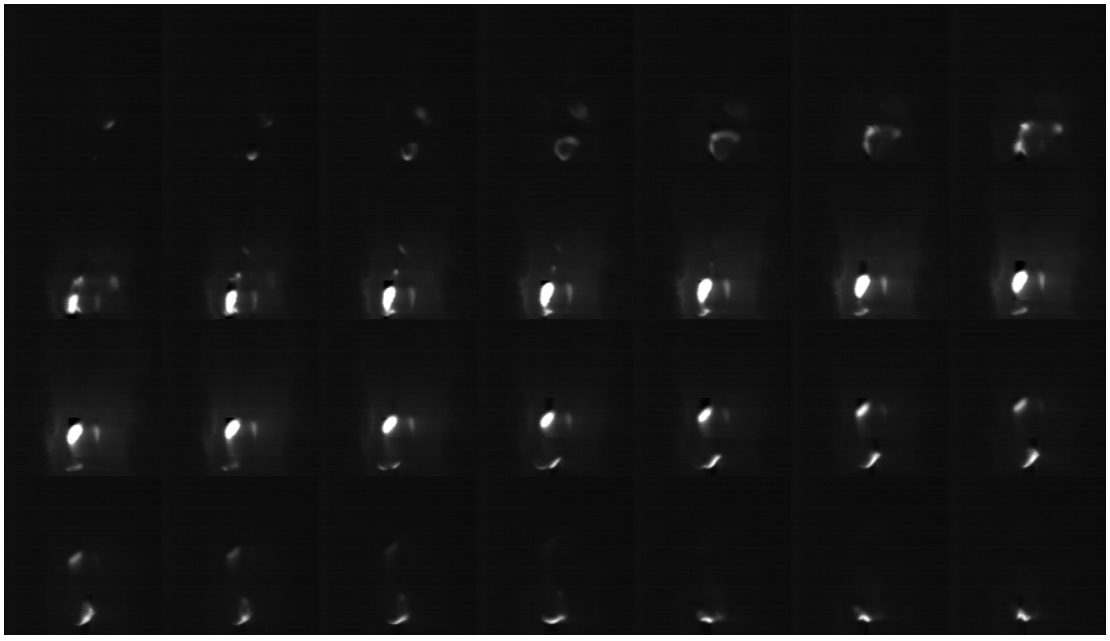

(b)

Figure 4.15: Fast sequences of acetylene post-ignition flamelet advection in 'Random Spots' regime in CTHC. (a) and (b) Direct-photography, visible-to-IR broadband sequences at 13.5 kHz and conditions $T_{air} = 809$ K, $U_{air} = 10.4$ m/s, $\upsilon_{fuel} = 0.93$, $Y_{C2H42} = 0.77$ (same as **Figure 4.14(a)**). Flow direction upwards.

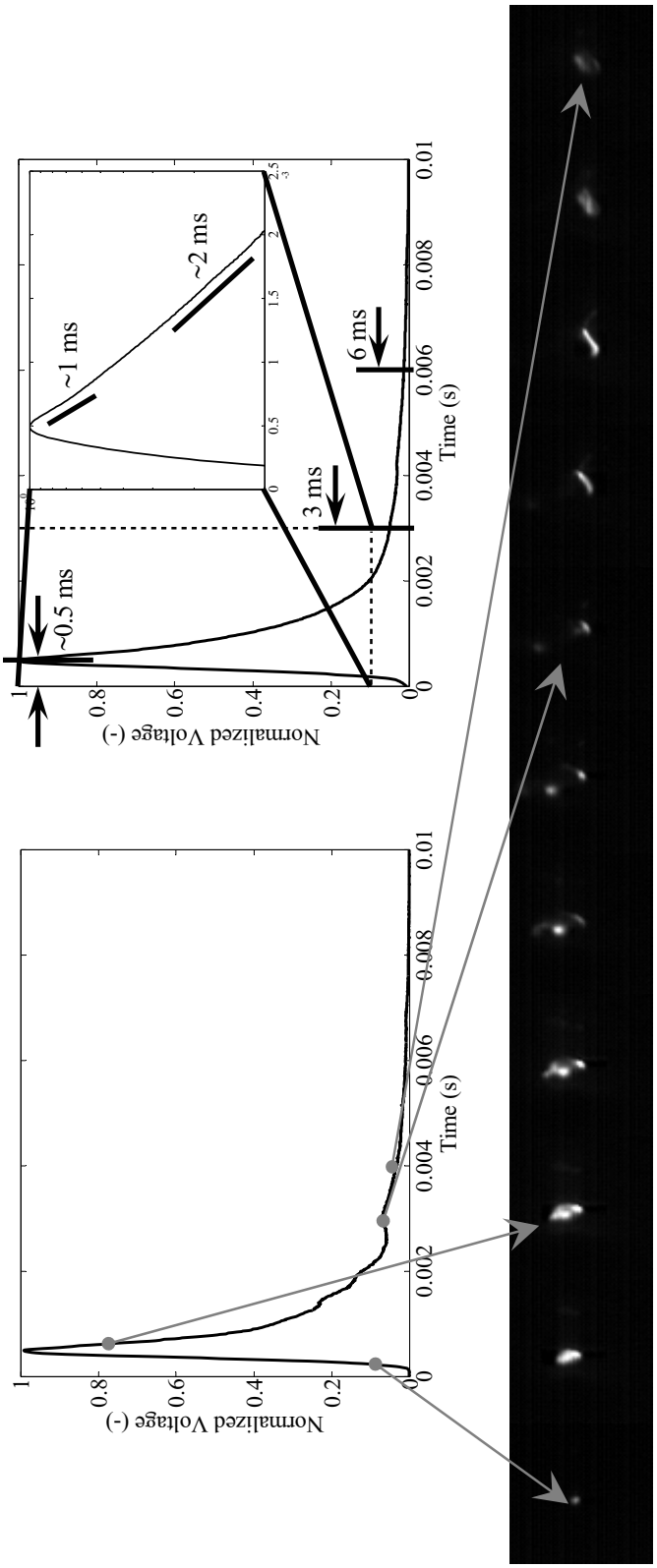

Figure 4.16: Typical PMT temporal profile of acetylene autoignition in 'Random Spots' regime in CTHC. Top-left: Instantaneous voltage profile recorded by PMT during a single autoignition event in low f_{IGN} conditions. Top-right: Average voltage profile (over many recorded profiles such as that shown on left) by PMT during low f_{IGN} autoignition events. Insert window focuses onto the post-ignition decay, plotting the logarithm of the voltage profile. The gradients show exponential decays of time constant 1 ms initially and 2 ms later on. Bottom: Fast OH^* sequence, taken simultaneously with PMT measurement shown on top-left. Taken at 10 kHz. Flow direction upwards. The first frame shows the location of the first instance of the explosive initiation of autoignition. The rest of the frames in the sequence show the post-ignition propagation of the flamelets that originated at the localized autoignition explosion of this first frame.

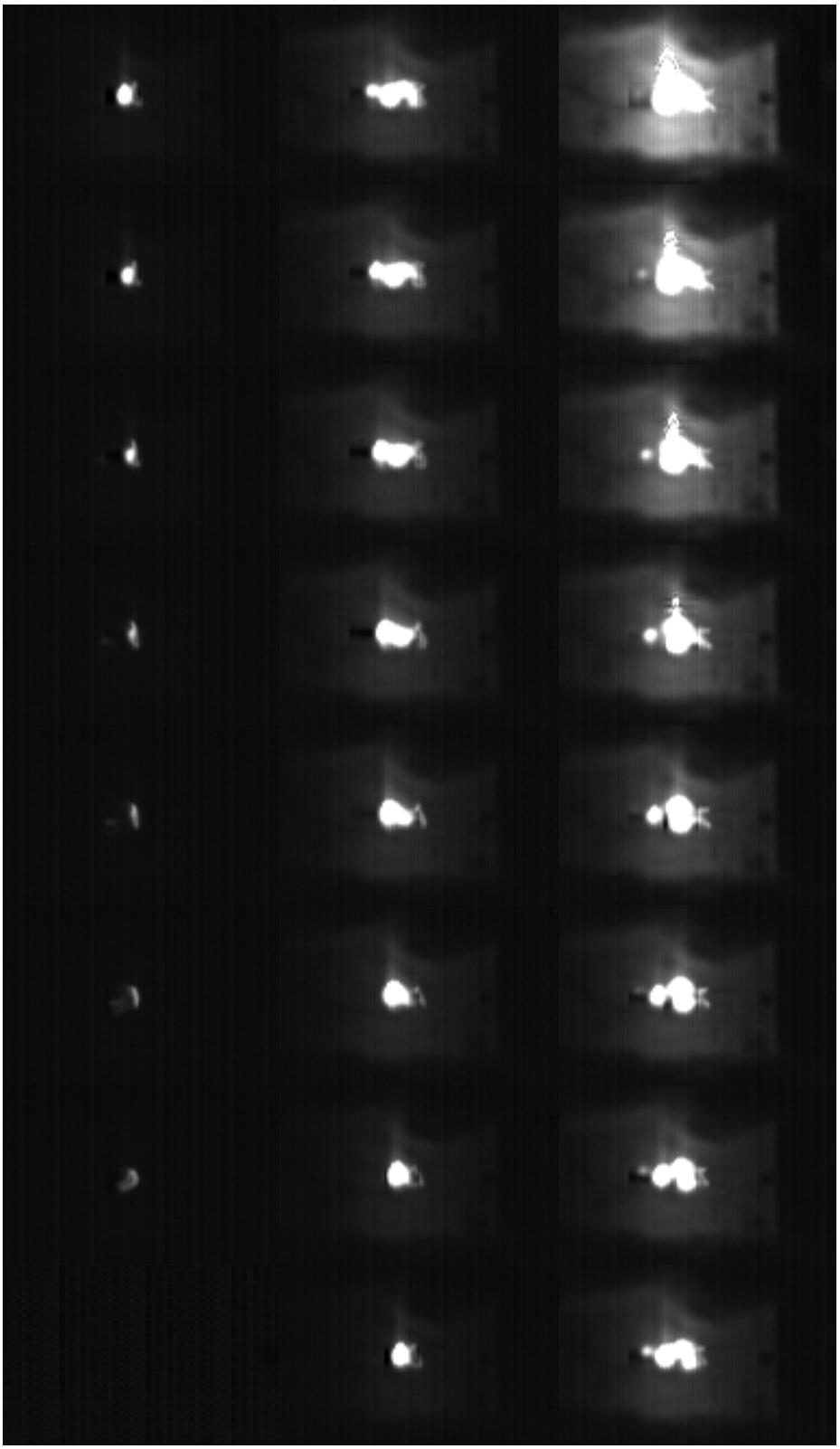

Figure 4.17: Fast sequence of acetylene flashback in CTHC. Direct-photography, visible-to-IR broadband sequences at 13.5 kHz and conditions $T_{air} = 809$ K, $U_{air} = 10.4$ m/s, $v_{fuel} = 0.93$, $Y_{C2H2} = 0.75$ (same as **Figure 4.14(a)**). Flow direction upwards.

(a) (b) (c)

Figure 4.18: Global normalized spectra and important radical chemiluminescence emissions for ethylene in CTHAJ. (a) Bold solid line for downstream region (D) in 'Pre-Ignition Reactions' regime at conditions $T_{air} = 1055$ K, $U_{air} = 17.7$ m/s, $T_{fuel} = 818$ K, $\upsilon_{fuel} = 2.5$, $Y_{C2H4} = 0.75$ and 1 s exposure. Thinner solid lines are in 'Random Spots' at conditions $T_{air} = 1049$ – 1062 K, $U_{air} = 17.7$ m/s, $T_{fuel} = 805$ K, $\upsilon_{fuel} = 2.7$, $Y_{C2H4} = 0.75$ and with 1 s exposure. (b) Temporal evolution of OH^* (at 310 nm), CH^* (at 430 nm) and C_2^* (at 510 nm) in long L_{IGN} 'Random Spots' regime at conditions, with $T_{air} = 1079$ K, $U_{air} = 37.3$ m/s, $T_{fuel} = 827$ K, $\upsilon_{fuel} = 1.5$, $Y_{C2H4} = 0.75$. Showing 250 intensities at specified frequencies in spectra taken with sampling time 0.1 s each. (c) Temporal evolution of OH^*, CH^* and C_2^* in short L_{IGN} 'Random Spots' regime, with $T_{air} = 1091$ K, $U_{air} = 38.2$ m/s, $T_{fuel} = 832$ K, $\upsilon_{fuel} = 1.5$, $Y_{C2H4} = 0.75$. Showing 250 intensities at specified frequencies in spectra taken with sampling time 0.1 s each.

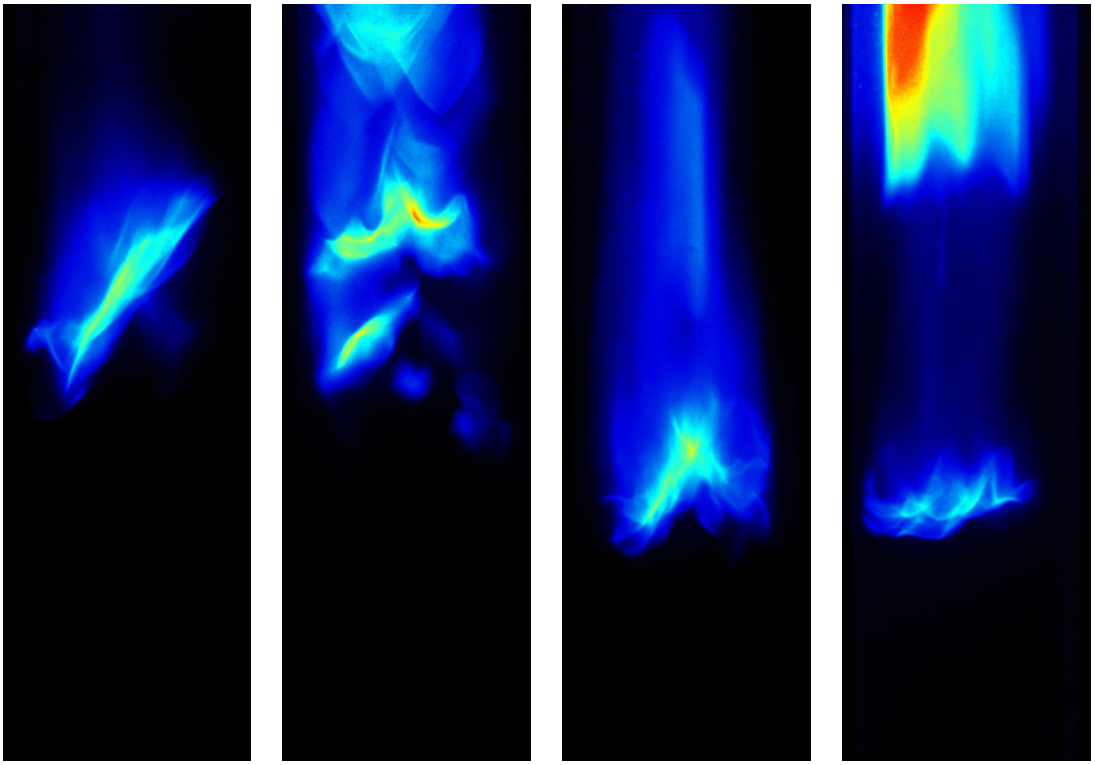

(a) (b) (c) (d)

Figure 4.19: False-colour/intensity, UV-to-IR broadband images of autoignition in CTHAJ burner. Showing results from the D_{TUBE} = 24.78 mm and D_{BLUFF} = 10.00 mm configuration. Instantaneous snapshots of autoignition for: (a) and (b) T_{air} = 1059 K, U_{air} = 17.8 m/s, υ_{fuel} = 2.5. (c) and (d) T_{air} = 1051 K, U_{air} = 13.2 m/s, υ_{fuel} = 3.1. All images taken with 1 ms exposure.

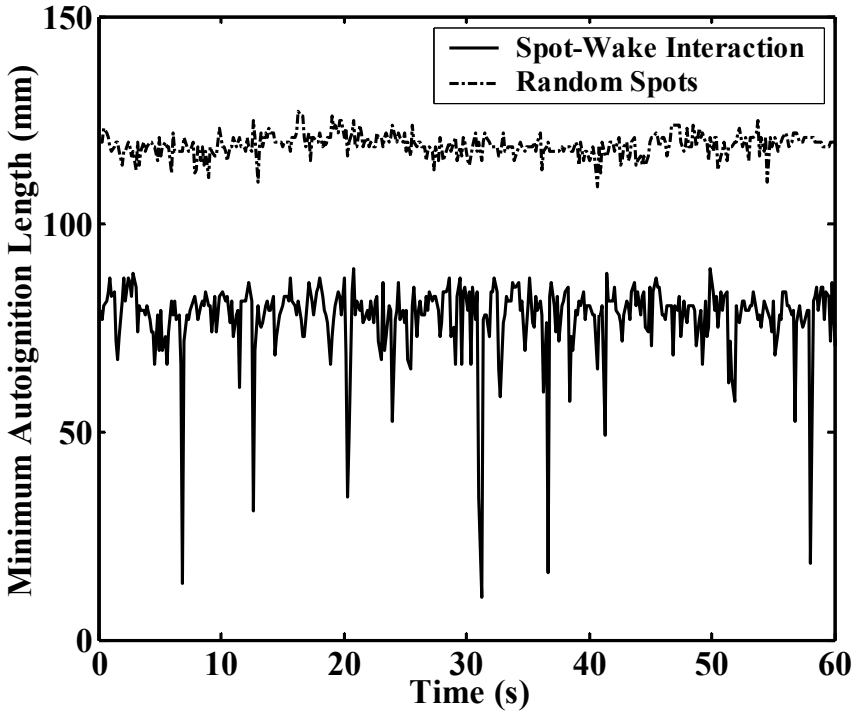

Figure 4.20: Ethylene/bluff-body L_{MIN} as a function of time in 'Spot-Wake Interactions' regime in CTHAJ. Conditions $T_{air} = 1068$ K, $U_{air} = 19.2$ m/s, $\upsilon_{fuel} = 3.17$, $Y_{C2H4} = 0.75$. Comparison with typical 'Random Spots' behaviour also shown at conditions $T_{air} = 1052$ K, $U_{air} = 18.4$ m/s, $\upsilon_{fuel} = 1.80$, $Y_{C2H4} = 0.75$. L_{MIN} calculated from images taken with exposure times of 40 ms. Sampling rate is thus 25 Hz.

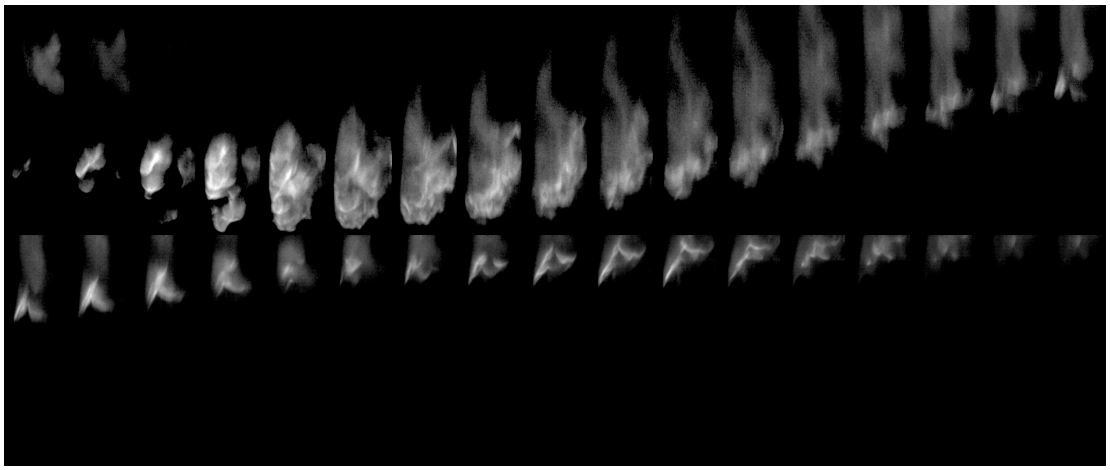

(a)

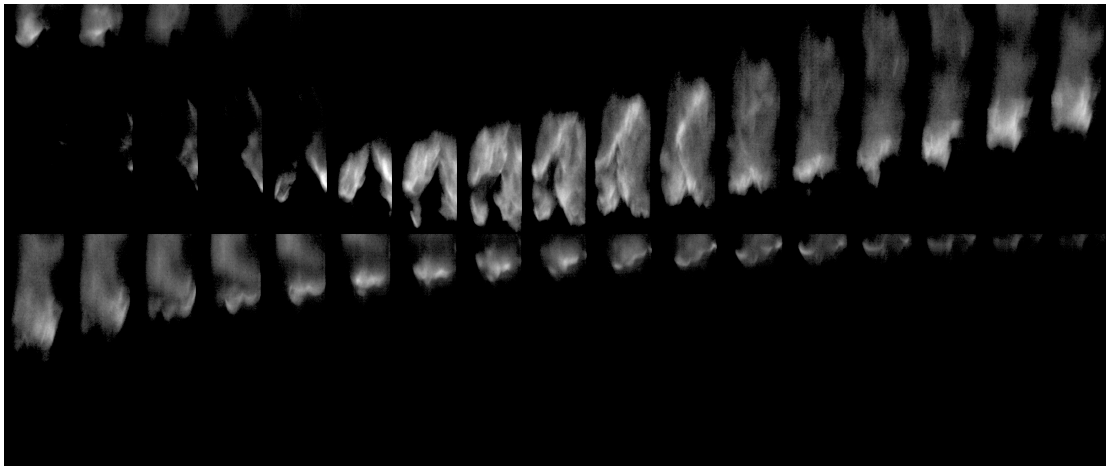

(b)

Figure 4.21: Fast sequences of ethylene autoignition and post-ignition flamelet propagation in 'Random Spots' autoignition regime in CTHAJ. (a) and (b) OH^* (307±10 nm) sequences at 7.3 kHz and conditions $T_{air} = 1088$ K, $U_{air} = 37.6$ m/s, $\upsilon_{fuel} = 1.47$, $Y_{C2H4} = 0.75$. Flow direction upwards. *NOTE: Tube wall at edge of frames.*

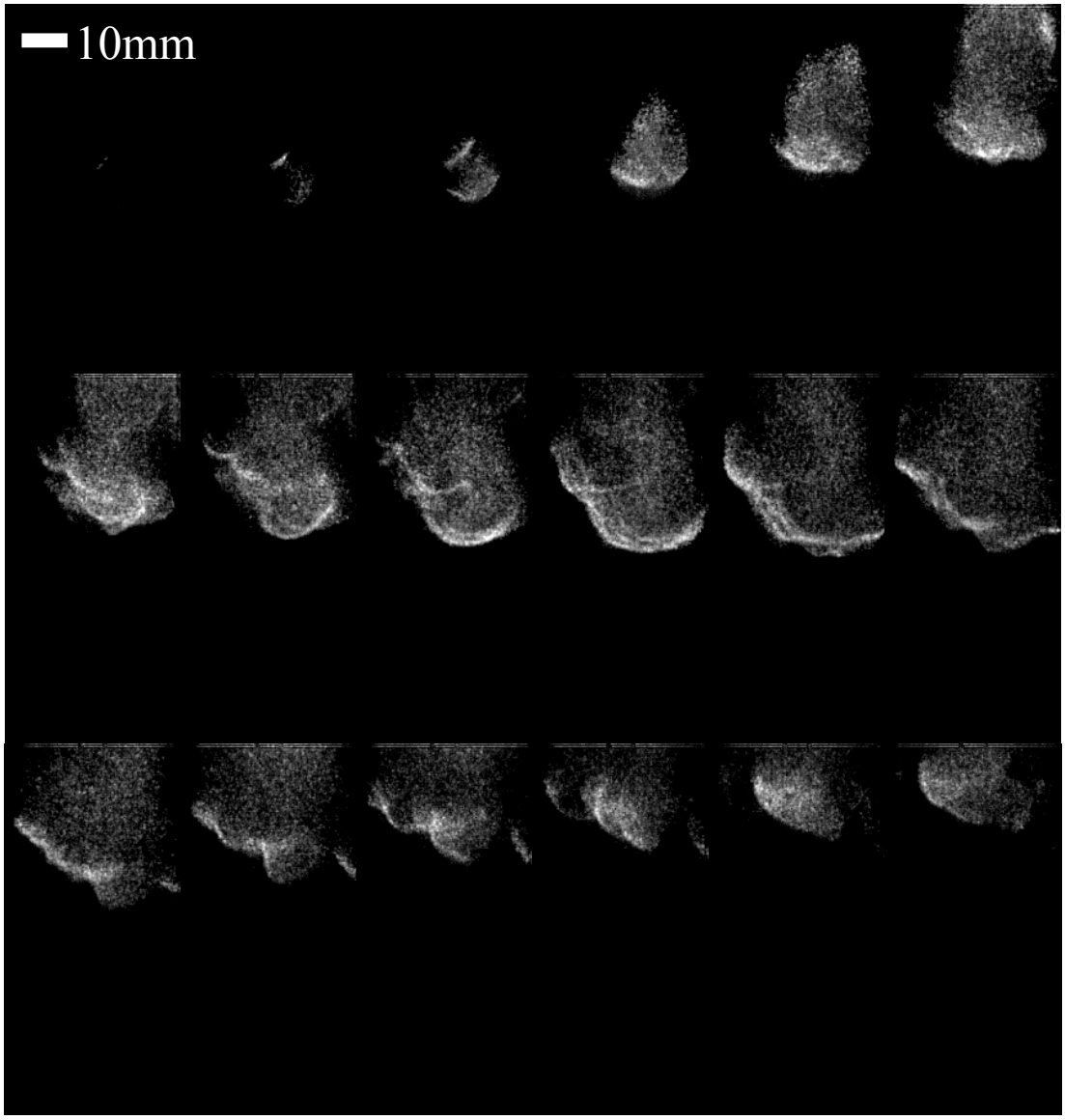

Figure 4.22: OH^* (307±10 nm) sequence at 12 kHz and conditions $T_{air} = 1091$ K, $U_{air} = 38.2$ m/s, $\upsilon_{fuel} = 1.50$, $Y_{C2H4} = 0.75$. Flow direction upwards. Indication of scale given.

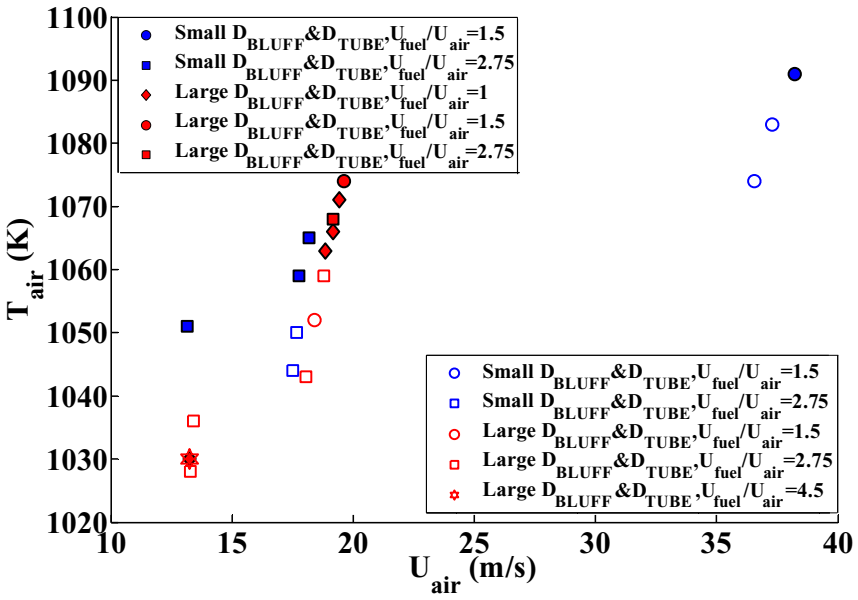

Figure 4.23: Temperature–Velocity limits of 'Nothing–to–Spots' and 'Spots–to–Flame' transition boundaries for ethylene in CTHAJ burner. Open symbols for 'Nothing–to–Spots' and filled for 'Spots–to–Flame' transitions. Various conditions shown as per legend.

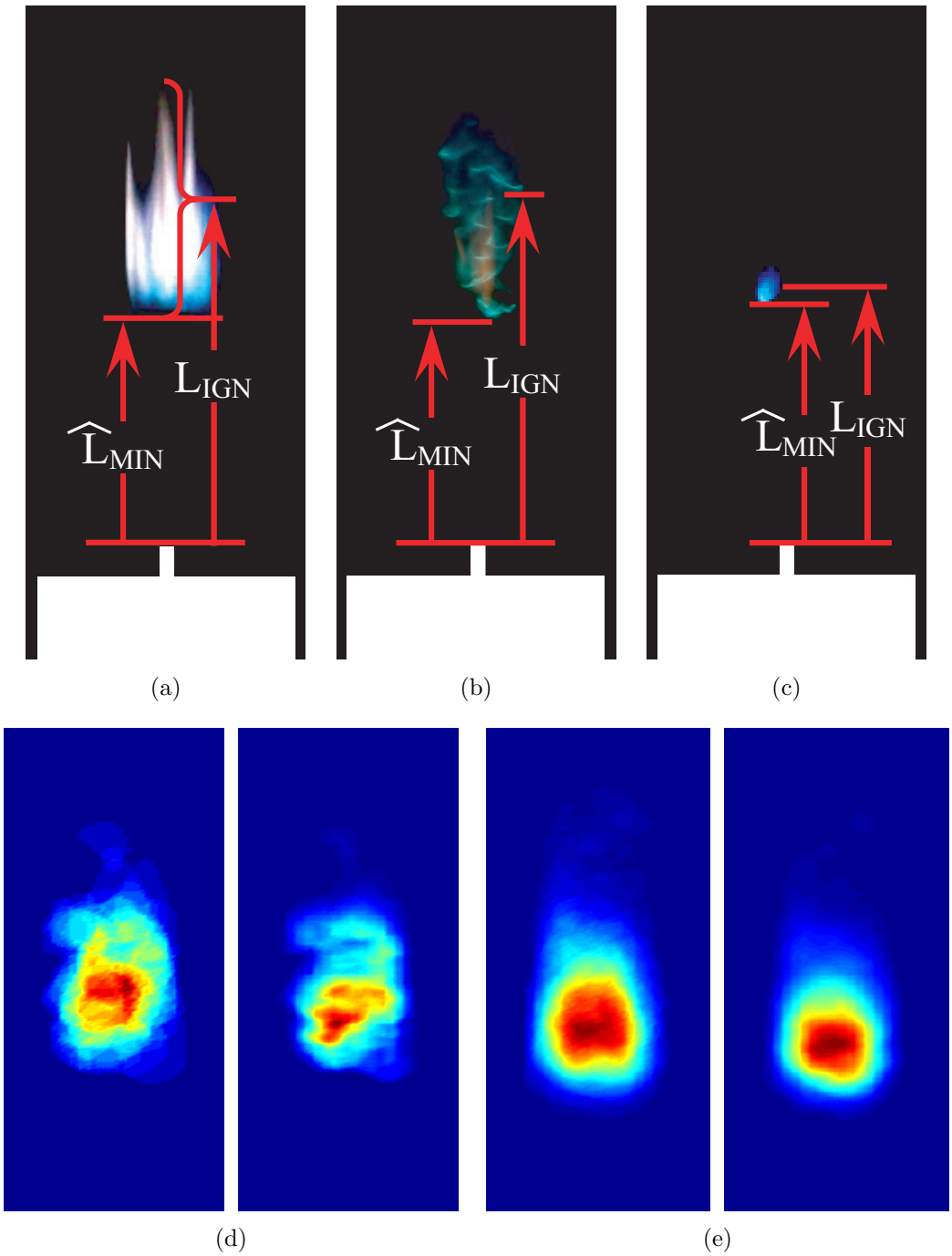

Figure 4.24: Typical raw and processed CTHC images. (a) Raw "Long Exposure" (250 ms) image; high f_{IGN}. (b) Raw image. Exposure time 80 ms; low f_{IGN}. (c) Raw "Short Exposure" (0.25 ms) image; low f_{IGN}. (d) (Left) PF and (Right) AVG processed image pairs corresponding to experimental runs with: lower T_{air} and/or higher U_{air}. (e) (Left) PF and (Right) Average processed image pairs corresponding to experimental runs with: higher T_{air} and/or lower U_{air}.

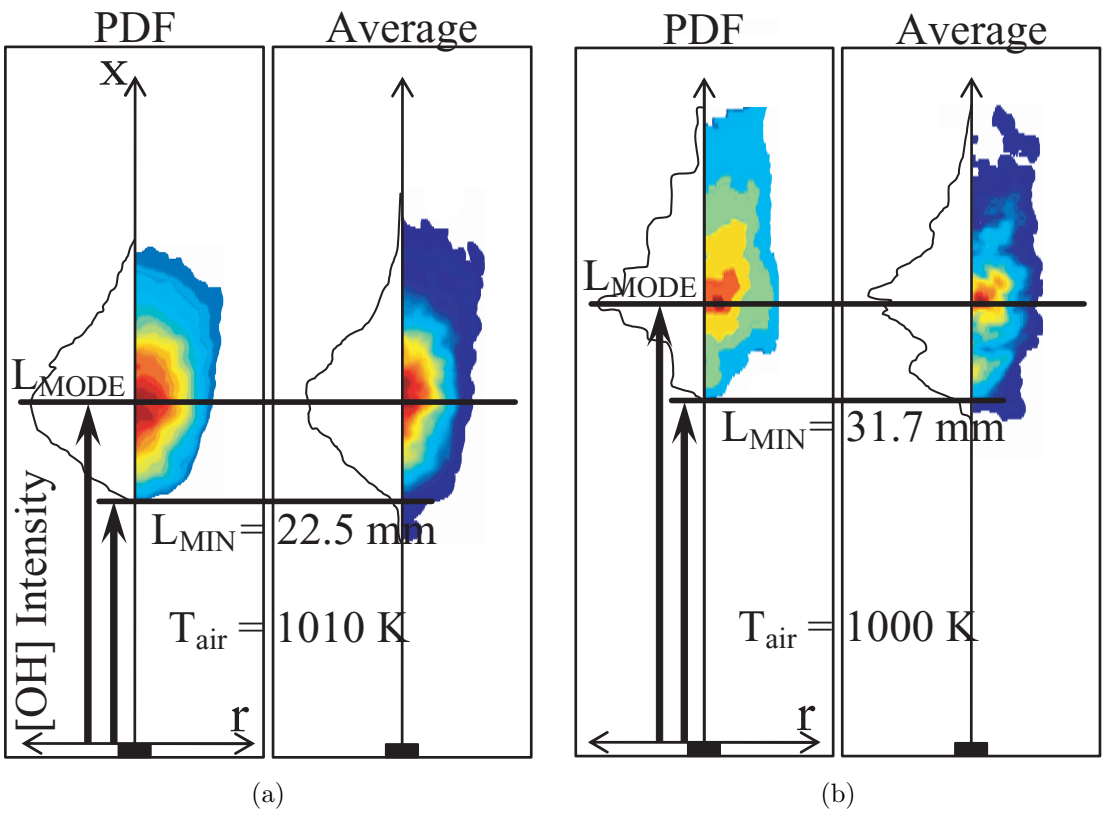

Figure 4.25: Comparison between AVG and PF averaged images obtained in the CTHC Burner. Autoignition of hydrogen at L_{MIN} = 22.5 and 31.7 mm due to a decrease in T_{air} from 1010 to 1000 K.

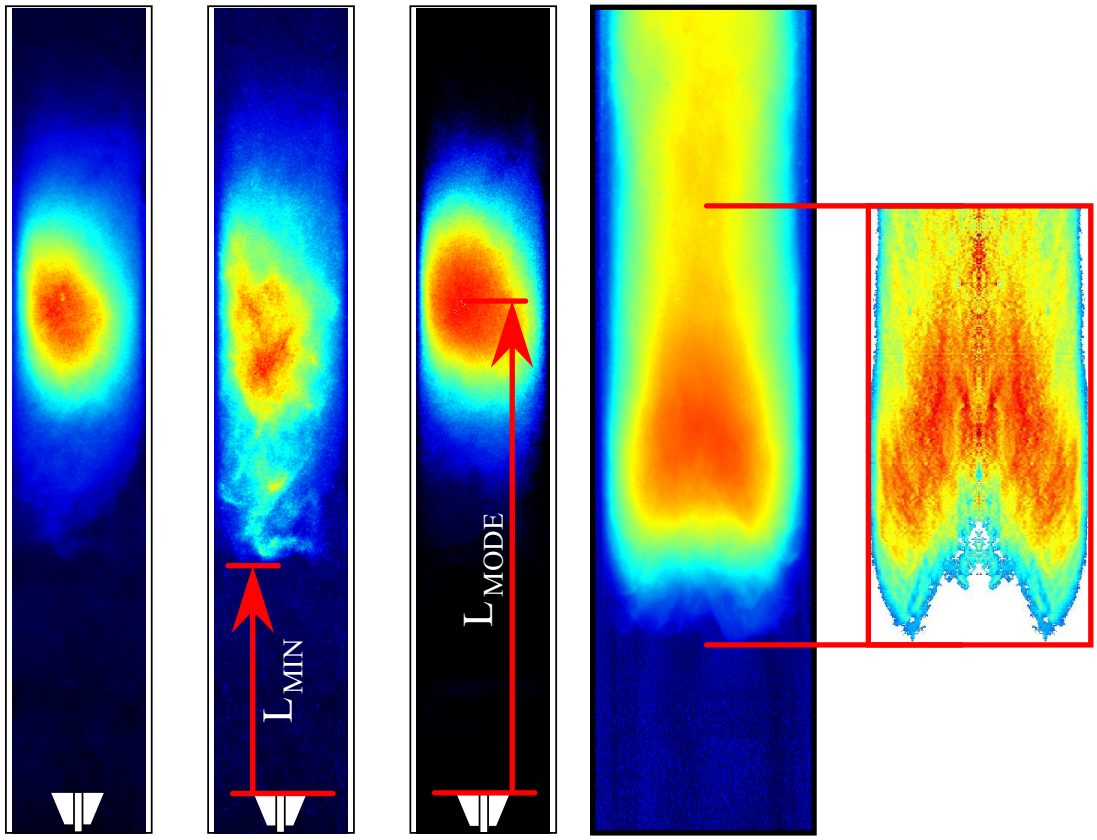

Figure 4.26: Typical processed CTHAJ images. (a) From left-to-right: AVG, STD, PF images compiled from 200 images taken during constant conditions of T_{air} = 1066 K, T_{fuel} = 745 K, U_{air} = 19.2 m/s, υ_{fuel} = 3.2. (b) Abel transform of STD image for conditions T_{air} = 1091 K, T_{fuel} = 832 K, U_{air} = 38.2 m/s, υ_{fuel} = 1.5.

Chapter 5

Results — I: Autoignition Frequency and Acoustics

5.1 Objectives of Chapter 5

In this chapter attention is drawn to the characteristic timescales of the processes taking place during the autoignition of:

Section 5.2: Nitrogen-diluted acetylene in the CTHC burner and with the '3 mm' injector, and,

Section 5.3: Nitrogen-diluted ethylene in the CTHAJ burner, with the 'jacketed' quartz tube and small bluff-body.

In both sections, results concerning the frequency of autoignition events and the acoustic signature recorded during autoigniting conditions are organized as follows. Firstly, the frequency of autoignition are presented. A link a made briefly to the temporal and spatial characteristics of autoignition mentioned in **Chapter 4**. This is followed by acoustic (microphone) measurements of the sound generated by the autoignition events.

5.2 CTHC Burner with '3 mm' Injector

5.2.1 Coupled, Simultaneous Measurements

Figure 5.1 shows typical time-series of global OH^* chemiluminescence intensity (top) and pressure fluctuations (bottom) for slow (left) and fast (right) spotting conditions. At lower temperatures and/or higher air velocities well-defined 'autoignition spots' appear with low frequency at relatively longer lengths from the injector. In terms of terminology, a number of 'explosive events', separated by an 'autoignition event period', Δt_{IGN}, are grouped together and make up each 'spot'. Each spot sequence consists of a 'spot leader event' (or primary event) and a number of 'secondary events'. The mean autoignition period is the inverse of the mean 'autoignition frequency', $\overline{f}_{IGN}$. Two autoignition spots are demonstrated in the plots on the left. The existence of a number of constituting autoignition events per spot is clearly evident in the PMT voltage signal, V, whereas the pressure signal shows decaying oscillations after each spot persisting after the initial explosion, possibly augmented by wave reflections within the tube. As the temperature increases and/or the velocity decreases, the mean frequency $\overline{f}_{IGN}$ increases, the spots begin to overlap and their separation becomes increasingly difficult.

Examination of the correlation between the two time signals reveals periodic, stationary cross-correlation coefficients that decay with increasing delay ($\Delta\tau$) as shown in **Figure 5.2**. The cross-correlation coefficients are normalized by the variance to give unity at zero lag. At long lags the coefficients damp out, indicating that the fluctuations are not due to external forcing. As expected, the pressure signal occurs consistently delayed from the detection of chemiluminescence. The delay associated with the first peak, as indicated in **Figure 5.2**, can be used to estimate the time necessary for pressure waves to propagate from the autoignition locations, through the quartz tube and the microphone probe to the position of the micro-

phone, based on the corresponding local sonic velocities and the velocity upstream of the autoignition events in the tube. For identical temperatures the sonic velocity is equal in acetylene and air so that there is no error introduced in considering that the pressure wave will propagate upstream in the quartz tube at the sonic velocity of air at the measured T_{air}. On the other hand, the temperature of the air in the microphone probe tube was not measured (see **Figure 2.13**). The assumption is made that this temperature was near-ambient that introduces an uncertainty in the calculation of the sonic velocity in the probe. As a consequence of the probe being long ($L_{probe} = 0.5$ m) relative to the propagation length in the quartz tube (L_{ING}), this uncertainty carries over into the calculation of the autoignition lengths based on the velocities and temperatures in the tube (U_{air}, T_{air}) and probe (U_{probe}, T_{amb}):

$$\begin{aligned} \Delta\tau &= \frac{L_{IGN}}{\sqrt{\gamma_{air}\frac{\overline{R}}{M_{air}}T_{air}} - U_{air}} + \frac{L_{probe}}{\sqrt{\gamma_{air}\frac{\overline{R}}{M_{air}}T_{amb}}} \\ \Leftrightarrow L_{IGN} &= (\sqrt{\gamma_{air}\frac{\overline{R}}{M_{air}}T_{air}} - U_{air})\Big(\Delta\tau - \frac{L_{probe}}{\sqrt{\gamma_{air}\frac{\overline{R}}{M_{air}}T_{amb}}}\Big) \end{aligned} \quad (5.1)$$

Despite the aforementioned, agreement is reasonable with the value of L_{IGN} obtained from planar images of visible light, with worst-case discrepancies in the two values around ±20%. The trends are also reproduced well. So, it can be concluded that the pressure rise is due to the occurrence of an explosive event, at a distance L_{IGN} from the nozzle. The 'relative silence' before and after the explosive events is consistent with the finding that (primary) autoignition events are independent of each other. This point will be returned to in more detail in **Section 5.2.2**.

The difference between the second and first delays in **Figure 5.2** can be converted into a further length. It is most likely that this describes the reflection of the waves at the open end of the quartz tube, the length of which is $L_{TUBE} = 0.5$ m (see **Table 2.1**). Propagation through the probe is no longer relevant, since one is

now dealing with a length *difference* from the microphone and this length is from the autoignition location to the open end of the tube downstream. Nevertheless, it remains difficult to obtain an exact value for L_{IGN}, this time because of the uncertainty in the estimation of the sonic velocity in the unknown mixture of combustion products, unburned fuel and excess co-flow air downstream of autoignition. Assuming values for the ratio of specific heat capacities of 1.3 and a gas constant of 240 J.Kg^{-1}.K^{-1}, gives values of 0.75 – 1.15 m for this length from a relation similar to that of **Equation 5.1**, approximately equal to $2L_{TUBE}$.

5.2.2 PMT OH^* Chemiluminescence

For a number of conditions that fall in the slow spotting regime and for which the autoignition spots were well separated, all autoignition events were located, averaged and normalized in order to obtain a characteristic profile of an autoignition spot. **Figure 5.3(a)** shows all normalized instantaneous profiles for conditions of T_{air} = 807 K, T_{fuel} = 761 K, $U_{air} = U_{fuel}$ = 11.1 m/s and Y_{fuel} = 0.63 recorded over 21 s at a sampling frequency of 100 kHz. The averaged profile is also shown. In **Figure 5.3(b)** averaged profiles corresponding to various flow conditions are plotted. The averaged profile corresponding to **Figure 5.1(a)** is represented by a single line (the solid line). In order to check the similarity in the time-series from which the profiles were taken, Kolmogorov-Smirnov comparison tests were performed and it was found, at the 95% confidence level, that the samples corresponded to populations with the same continuous pdfs.

The emergence and decay of the autoignition kernels is described by the shape of the profile. It features a very well-defined, strong initial peak due to the explosion, associated with a timescale of ∼0.5 ms, followed by a slow decay corresponding to flame propagation, during which secondary and induced events are possible. These are mostly evident in the instantaneous time signals as they are smoothed out by the

averaging associated with the profiles on the right. Looking more closely at the close-up logarithmic window in **Figure 5.3(b)** showing the initial decay, it may be said that the shape is well described by an exponential, with a gradient corresponding to a time constant (time to reach $\frac{1}{e}$) of about 1 – 2 ms. The chemiluminescence reaches a value of 5% of its peak value after 3 ms and falls to 1% after 6 ms, at which point the propagating flamelets are effectively extinguished.

Further evidence to support the above inferences concerning localized explosion and the emergence, propagation and eventual decay of flame fronts originating at those sites is possible from simultaneous high-speed images. The flame propagates in the form of a spherical shell, seen as two flame arcs by the line of sight of the camera. The arcs propagate in opposite directions and away from the site of the initial explosion. As demonstrated in **Figure 5.3** the flame fronts are advected by the background velocity field and are capable of inducing secondary events, although this is usually but not always so.

The voltage from the PMT is considered as being proportional to the global chemiluminescence and hence presence of OH^*. Based on conclusive experimental observations of the strong correlation and sensitivity of the autoignition frequency to the autoignition locations in the tube and hence relative to the injector, it was decided to present the frequency data as a function of the autoignition length, L_{IGN}. The temperatures, velocities and dilutions affecting the mixing patterns and chemistry, influence the results only in as much as they change L_{IGN}. **Figure 5.4** shows the mean (left) and standard deviation (right) of the OH^* time-series over the range of conditions spanning:

1. $U_{air} = U_{fuel} = 11.1$ m/s, $T_{air} = 807$ – 825 K, $T_{fuel} = 761$ – 780 K, $Y_{fuel} = 0.48$ – 0.63, and,

2. $U_{air} = U_{fuel} = 17.5$ m/s, $T_{air} = 851$ – 880 K, $T_{fuel} = 770$ – 792 K, $Y_{fuel} = 0.60$.

The mean OH^* increases exponentially as L_{IGN} decreases, reflecting the brighter and much more frequent autoignition at close lengths to the injector, as opposed to the rare and weaker occurrences when the fluid mechanical and thermal conditions inhibit the phenomenon and cause it to occur farther downstream in the tube. The rms also increases closer to the injector.

Following from the arguments presented previously concerning the in-the-mean similarity of normalized OH^* detected per autoignition event across a wide variety of conditions, the mean, global OH^* is expected to depend on the average intensity of the autoignition events during a run and on the frequency of the events. The intensity of the events did not change dramatically in these experiments. After comparing the maximum and minimum possible recorded voltages by the PMT corresponding to autoignition across all conditions, it was found that these were different by factor of 5. On the other hand, **Figure 5.4** shows that the mean OH^* voltage changes by 4 orders of magnitude. The frequency of autoignition must be responsible for this, in which case, its values will need to span about 3 orders of magnitude. Indeed, **Figure 5.6** concerning $\overline{f}_{IGN}$, supports this argument well.

In an attempt to look further into the temporal statistics of autoignition the pdf of autoignition frequency was recovered. For each condition, peak counting was done on a suitably processed version of the time-series. The PMT voltage signal was smoothed and a threshold method was used to detect peaks (mostly primary, but also secondary) according to crossings of the first and second derivative. **Figure 5.5** shows pdfs of the period (left) and frequency (right) of autoignition for the data presented in **Figure 5.4**. The inset in **Figure 5.5(a)** shows the pdfs plotted against the autoignition event period, Δt_{IGN}, normalized by the mean period for that run, $\overline{\Delta t}_{IGN}$, so that the independent axis represents $\frac{\Delta t_{IGN}}{\overline{\Delta t}_{IGN}}$.

The autoignition event period has strongly positive skewed (long-tailed) pdfs for all conditions, with modal (most probable) autoignition event periods being 1 – 3 orders of magnitude shorter than the mean period. The mean and mode of the

autoignition *frequency* is plotted as a function of L_{IGN} in **Figure 5.6**. The skewness and kurtosis associated with the pdfs shown in **Figure 5.5(a)** ranges between 2 – 7 and 10 – 80 respectively. Fast spotting conditions have pdfs that are smoother as they have been constructed by more measurements.

For at least 0.2 ms after the occurrence of any autoignition event there is no other event even at the very fast spotting conditions. At the temperatures of interest (∼850 K) the local sonic velocity is approximately 575 m/s. In 0.2 ms pressure waves from an event have travelled at least 115 mm from the location of the initial explosion, which is a large length when compared with L_{IGN}. This has significant implications, in that it points toward the fact that autoignition sites cannot be the result of pressure waves emanating from prior autoignition events elsewhere in the flow. Indeed, most evidence, backed by fast image sequences, supports the argument that (secondary) autoignition can be often induced by previous autoignition events, but this process is mostly through flame propagation (diffusion), rather than compression by pressure wave propagation.

The modal frequency falls around 2 – 3.5 kHz, which corresponds to a time between events of 0.3 – 0.5 ms. This time is of the order of the time necessary for the initial explosion of each event as shown in **Figure 5.3(b)**. It varies by a factor of 2 across the tested conditions. The mean frequency increases exponentially with increasing L_{IGN} and changes by 3 orders of magnitude. The ratio of the rms to the mean of the autoignition frequency, $\frac{f'_{IGN}}{\bar{f}_{IGN}}$, varies weakly with L_{IGN}, decreasing from 0.5 to 3 as autoignition moves closer to the injector for these conditions.

Thus, from the pdfs, the high-speed images, but also from the time-series themselves, there is significant evidence that the events appear in bursts, which have so far been termed 'spots'. Each autoignition spot is a superposition of a small number of explosions, some being independent events (such as the primary/spot leader), but most not (the secondary events). The important result that emerges is that secondary autoignition events are possible, do occur with high probability

and are mostly results of flame propagation from earlier autoignition events. These secondary events mostly occur after a time delay of the order of the timescale of the explosion. The time delay can be revealed by considerations of the mode of the frequency of autoignition and varies only slightly, as shown in **Figure 5.6(b)**. Further, examination of the mean frequency of the phenomenon reveals that the overall trends are much more strongly dependant on the varying flow conditions than the secondary events can explain. In contrast, they must be predominantly governed by the frequency with which the spots are initiated through the appearance of the spot leaders, more so than the processes that lead to the secondary events. As such, it is possible to consider the phenomenon in the mean as a collection of independent spots and it is not necessary to resolve for all the events.

As a final note, the frequency of occurrence of autoignition was found to increase with increasing temperature and/or decreasing air velocity, thus following exactly the same trends as those of autoignition length (and time). It is still not clear how rigorous the link is between the statistics of autoignition frequency, through f_{IGN}, and the manifestation of autoignition in physical space, through L_{IGN}. Nevertheless, the conditions at the locations of the autoignition kernels, through the local mixture fraction and scalar dissipation rate, are expected to be controlling the processes leading to autoignition, just as the same fields along the paths of the propagating flamelets must be controlling the flame propagation velocities and the possibilities of either eventual extinction or flashback.

Aiming to examine the existence of temporal dependencies in the OH^* time-series the autocorrelation functions of the fluctuations of the PMT voltages were considered for each condition and the integral and (an equivalent of the) Taylor time microscale were calculated. The autocorrelation functions decline steeply to values less than 0.1 after lags of 5 ms. In very fast spotting conditions, periodicity is apparent, as indicated by the dashed lines in **Figure 5.7(a)**. Careful examination of the original signals corresponding to these runs reveals that the PMT voltage

never falls to zero; compare for example **Figure 5.1(a)** and **Figure 5.1(b)**. Based high-speed sequences, two possible scenarios can be used to explain the PMT autocorrelations that have been observed when reaction is occurring at close lengths from the injector. In the first, turbulent 'Lifted Flame' phenomena were observed (see also **Figure 6.2(a)** and the relevant discussion in **Section 6.2.1**). In the second, autoignition occurred in the 'Random Spots' as before, but with high enough $\overline{f}_{IGN}$ that many spatially independent autoignition events occurred *simultaneously* at multiple locations in the tube. In the latter situation, even though there had been no qualitative change in the bulk behaviour, information of individual time histories becomes contaminated and decoupling of the characteristics of any single autoignition event in the measurement at any particular time is impossible.

In **Figure 5.7(b)** the solid square data points correspond to these conditions. In general, the Taylor times are of the order of 0.3 – 0.5 ms, describe the timescale of the initial explosions and are not strongly affected by the conditions. The integral scales vary between 1 – 3 ms, decreasing almost linearly with increasing autoignition location length, possibly because the shape of the long, post-explosion decay of each individual event is interrupted by superposition of other events, either occurring elsewhere in the tube or induced by the decaying flamelet. They are of the same order as the post-ignition decay associated with flamelet propagation and show a stronger dependence on the conditions. The three points associated with fast spotting fall off the trends observed for all other points. This could be explained by considering the scenario by which autoignition events occur *simultaneously* at multiple locations in the tube, thus corrupting the correlations. Nevertheless, this should not affect contributions to the global mean and rms of the signal and, indeed, the points fall back into the expected trends for these quantities.

For the turbulent velocity the ratio of Taylor microscale to integral timescale is given by $\mathcal{R}e_{turb}^{-1/2}$ and $\mathcal{R}e_{turb} = \frac{u' L_{turb}}{\nu}$. In these experiments: $\frac{u'}{U_{air}} \simeq 0.12$ – 0.15 and $L_{turb} \simeq 3.0$ – 4.5 mm. So, $\mathcal{R}e_{turb} \simeq 40$ – 80 and $\frac{\lambda_{micro}}{L_{turb}} \simeq 0.1$ – 0.2,

which is of the same order as the ratios in the timescales of the OH^* signals, i.e. 0.1 – 0.4. Also, the timescales of OH^* are themselves of the order of those of the turbulent velocity scales. Thus, the dominant eddy turnover time of the turbulent field is the same as the post-ignition flamelet extinction time and also the mean time between autoignition events, and furthermore, the timescale of the smallest eddies, as characterized by $\frac{\lambda_{micro}}{u'}$, is the same as the explosion time and the most probable (modal) delay time between successive events.

Finally, the OH^* signals are examined in the frequency domain for autoignition spanning an envelope of conditions of $T_{air} = 805$ – 880 K, $T_{fuel} = 751$ – 797 K, $U_{air} = 10.7$ – 17.8 m/s, $\upsilon_{fuel} = 0.80$ – 1.04 and $Y_{fuel} = 0.48$ – 0.73. The spectral power increases uniformly by 3 – 4 orders of magnitude across the full frequency range as $\overline{f}_{IGN}$ increases. **Figure 5.8(a)** shows the power density normalized by the variance for each condition, which collapses this trend. The spectra are also averaged so that the number of events per spectrum is constant across the conditions. As $\overline{f}_{IGN}$ increases significant features begin to appear up to 0.4 kHz, i.e. down to equivalent timescales of 2.5 ms. This value is close to the time constant associated with the decay of the typical event after the initial explosion and the time necessary for the decay. The frequency range of these features shifts to include higher and also lower frequencies as $\overline{f}_{IGN}$ increases. It is possible that this power increase at higher frequencies is a reflection of the faster decay of the post-ignition flamelets, either through an increased propagation velocity and/or a decreased distance before extinction caused by the mixing field in these conditions. The lower end content might be attributed to the interactions and event superposition that occurs inevitably as the three dimensional occurrence information is compressed into the one-dimensional time-series by the nature of the measurement. Thus, consistent features can be used to define a typical chemiluminescence spectral profile. The defining features of this profile do not significantly deviate across these conditions, but some deviations perhaps contain information on the autoignition and flame propagation processes.

5.2.3 Microphone Pressure

Following the examination of chemiluminescence in the frequency domain, it would be desirable to assess the frequency content in the microphone pressure signals. These signals are much more complex to analyse because they include broadband energy contribution from the background turbulent flow, but also because certain frequencies will be naturally amplified by resonance in the tube. In order to obtain a clearer picture concerning the pressure power spectra, tests were performed on autoigniting flows with fixed background velocities, so that the power contribution due to the flow would be constant. Results are shown in **Figure 5.8(b)** for the following condition envelope: $U_{air} = U_{fuel} = 10.8$ m/s, $T_{air} = 805$ – 825 K, $T_{fuel} = 755$ – 797 K, $Y_{fuel} = 0.48$ – 0.63 and $\overline{f}_{IGN} = 10$ – 715 Hz, along with a background spectrum of the turbulent pressure with no autoignition in the tube.

Note that, once again, the spectral densities are normalized by the variance of the pressure signals. The absolute value of the spectral power increases by 3 – 4 orders of magnitude as $\overline{f}_{IGN}$ increases, similar to the PMT results. In addition, significant frequency content appears at around 0.2, 0.5, 1, 1.5 and 2 kHz. These frequencies are even multiples of the fundamental resonant frequency of the tube, f_{TUBE}, which from the background spectrum is estimated at 0.2 kHz. A further notable frequency in the background turbulent flow, but also the autoigniting pressure measurements, is one around even multiples of 0.3 kHz, although the power at these frequencies is less than that at f_{TUBE}. The Strouhal Number corresponding to this is 0.1, based on a length of 3 mm, which represents the injector outside diameter and the grid hole diameter. Given the macroscale $\mathcal{R}e$ based on this length at the hot conditions to be around 300, it is possible that this frequency reflects vortex shedding in the tube, possibly from the injector *outer* rim, or the acoustics of the orifice/grid. At low frequencies, between 0.04 – 0.15 kHz, i.e. for timescales of 6 – 25 ms, which cannot be attributed to any aspect of the flow, the autoignition spectra show a small power increase from the background.

In general, the power density distribution scales well with the variance and so all these effects are collapsed in **Figure 5.8(b)**. Thus, it appears that there is significant broadband spectral content that can be attributed to autoignition. The resonant frequencies are preferentially amplified by the tube and thus the autoignition spectrum cannot be decoupled and recovered simply. Nevertheless, the resulting shapes are similar for all conditions and hence it must be that the spectrum associated with autoignition alone must also be similar across conditions.

The frequency content of the pressure signal was also inspected through wavelet analysis. This type of analysis represents the next logical step because wavelets are based on the treatment of variable-sized windowing, with long time intervals for more precise low-frequency information and shorter regions for high-frequency information and include information on the scale/frequency content as a function of time. A bi-orthogonal spline wavelet was used to detect high degree of correlation at various locations along the microphone time signal. The wavelet was chosen so as to closely represent the typical shape of the pressure decay associated with each autoignition spot, as demonstrated in **Figure 5.1(c)**. A typical result is shown in **Figure 5.9** for extreme conditions included in **Figure 5.8(b)**, with $\overline{f}_{IGN} = 10$ (left) and 715 Hz (right) and the time signals superimposed over the wavelet maps in the centre of the figures (in white).

Fractal behaviour can be seen from the different ranges of 'active' scales that exist at each instant in time. The independent axis is that of time and the dependent axis is of scale, which is in turn inversely proportional to 'pseudo-frequency'. The intensity in these figures is proportional to the local wavelet correlation coefficient between the signal and the wavelet at the appropriate scale. The resulting wavelet image for each condition was processed in order to recover the dominant scale and hence frequency. The dominant frequency, which is the fundamental frequency of the tube, f_{TUBE}, was calculated as being around 0.15 kHz for all conditions presented in **Figure 5.8(b)**. This agrees relatively well with the Fourier results, given the

approximate nature of the wavelet pseudo-frequency. Also, this result has been extended and holds true for the broader condition envelope examined in the previous section concerning the PMT, namely: T_{air} = 805 – 880 K, T_{fuel} = 751 – 797 K, U_{air} = 10.7 – 17.8 m/s, υ_{fuel} = 0.80 – 1.04 and Y_{fuel} = 0.48 – 0.73.

Examination of time-averaged intensity profiles, i.e. value of the wavelet coefficient as a function of frequency averaged at all autoignition times during each run as shown in the **Figure 5.9(c)**, reveals a power-law decay with increasing frequency away from the dominant frequency with exponent between -1.15 and -1.35 and is otherwise very similar to the Fourier spectrum, although no scaling has been done on the wavelet results. Finally, the low frequency content is again detected. It is then possible to conclude that, both Fourier and wavelet analyses show broadband content in the pressure signals that can be independently attributed to autoignition. More importantly, the shape of the spectral distribution of energy across the scales does not significantly change with the conditions and the absolute value of power spectral density scales well with the variance of the signal.

5.3 CTHAJ Burner with Jacketed Tube and Small Bluff-Body

Operation in the CTHAJ burner has already been shown to be qualitatively different from the brief discussion of **Section 4.3**. The raw time-series reveal that even at the lowest temperatures and highest velocities tested (and hence lowest $\overline{f}_{IGN}$) it was not possible to achieve signals of OH^* that fell instantaneously to zero, as those of **Figure 5.1(a)**. Instead, all time-series resembled **Figure 5.1(b)**.

Figure 5.10 shows the mean and standard deviation of the PMT voltage signal as a function of the location of autoignition in the tube and as a function of an autoignition delay time, based on U_{air}, $\tau_{IGN} = \frac{L_{IGN}}{U_{air}}$. The absolute magnitude of the voltage cannot be compared to that of corresponding CTHC experiments of

Figure 5.4, because of the different placement of the PMT relative to the quartz tube and different gain settings. The mean OH^* chemiluminescence decreases with L_{IGN}, as with the CTHC, but the standard deviation of this measure does not. If anything this increases, in direct opposition to the results from the CTHC.

In **Figure 5.11** the probability of f_{IGN} is shown for all conditions that were plotted in **Figure 5.10**. The shape of the functions resembles those of **Figure 5.5**, but one notices that the probability at higher frequencies does not increase as significantly with increasing mean $\overline{f}_{IGN}$. Also, the probabilities die away at 3 kHz and not 6 – 8 kHz as with the CTHC. $\overline{f}_{IGN}$ is not strongly affected by the conditions, being in the range 600 – 800 Hz.

The autocorrelation functions in **Figure 5.12** are the most obvious evidence of qualitatively different phenomena. **Figure 5.12(a)** shows autocorrelations at lower $\overline{f}_{IGN}$. The shapes are not exactly as before (**Figure 5.7**), with a longer delay required before successive samples are independent. Still, the functions fall towards zero. Typically, after 10 ms the functions drop below 0.1. **Figure 5.12(b)** shows autocorrelation functions at higher $\overline{f}_{IGN}$. Sustained oscillations are evident that persist for much longer than the shown 30 ms delays. The dash-dot line, re-plotted in both autocorrelation plots, indicates the transition towards this behaviour.

Evidence of the transition can also be found in **Figure 5.13**. The spectra show a shift from power content such as that in **Figure 5.13(a)**, to a content such as that in **Figure 5.13(b)**. The spectrum denoted by the dash-dot line in both graphs corresponds to the same conditions as those of the dash-dot lines in **Figure 5.12**. In **Figure 5.13(b)** strong peaks of emission occur at multiples of 120 Hz due to oscillations in the OH^* released from combustion. Hence, the fundamental frequency of combustion must be 120 Hz, changing minimally with the conditions. This frequency is not equal to the fundamental resonant frequency of the tube, $f_{TUBE} \cong 200$ Hz, suggesting that the phenomena are not completely controlled by acoustics, although a certain level of interaction perhaps exists.

In conclusion and by taking into account fast images (such as those already shown in **Chapter 4**) one cannot reject the possibility that, for conditions other than those with very low $\overline{f}_{IGN}$, unsteady lifted flames are set up within the tube that interact with the acoustics of the tube, and perhaps, the oncoming turbulent flow and the autoignition phenomenon itself, resulting in a form of pulsed combustor.

5.4 Conclusions from Chapter 5

In this chapter it was shown that the temporal scales of autoignition could be inspected with one-dimensional, global time-series of chemiluminescence and pressure. It was found that the so-defined 'primary' autoignition events were independent of each other and were not caused by pressure waves. Secondary autoignition events were also possible, caused by flame propagation and diffusive/advective processes from earlier events and (again) *not* pressure waves instigated by the other events. The most important conclusion from this chapter is that the randomness in the occurrence of autoignition is significant and cannot be completely explained in terms of the randomness in the initial temperature, T'_{air}, because this is known to be low. Also, if this had been the case, the spectra of T'_{air} would have correlated with the OH^* spectra. Another interesting outcome is the exponential decrease in the mean autoignition frequency with increasing L_{IGN} and the close relationships between the integral and Taylor OH^* timescales and L_{IGN}, but also between the same scales and the characteristic scales of the turbulent flow.

5.5 Chapter 5 Figures

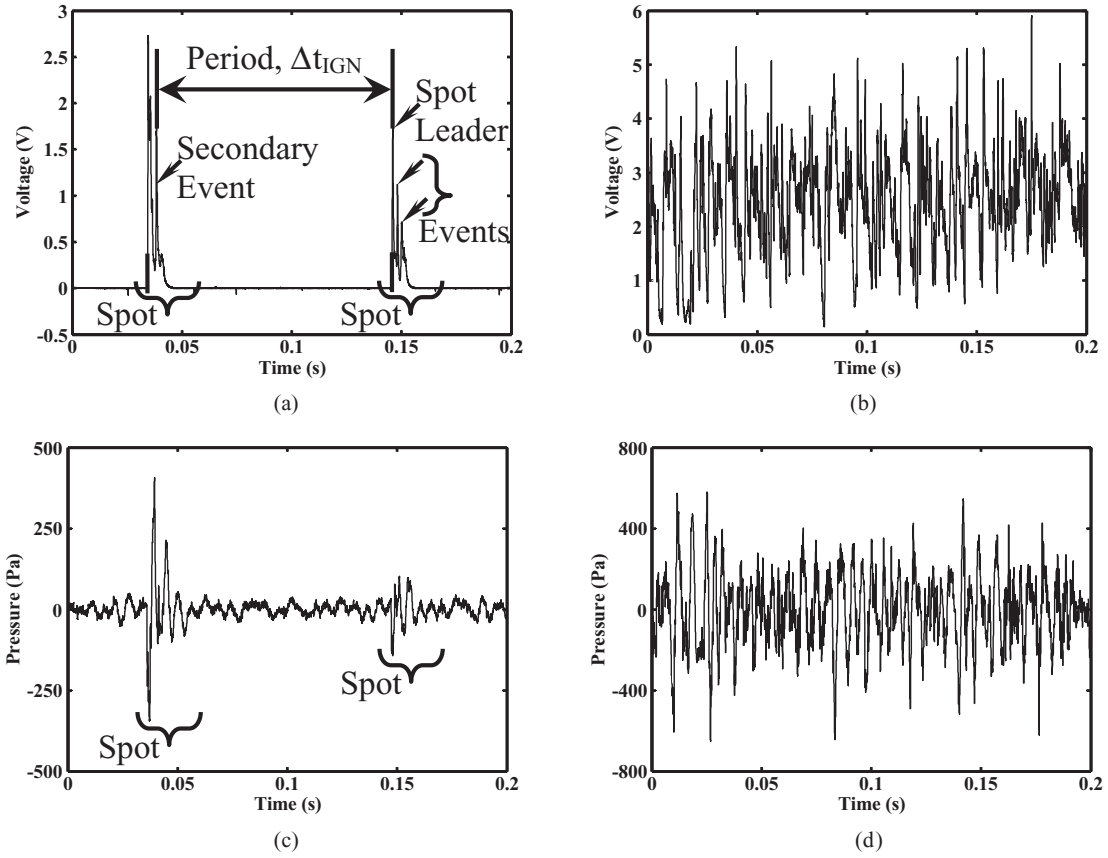

Figure 5.1: Simultaneous PMT and microphone signals. (a) Chemiluminescence – Slow Spotting Regime (T_{air} = 834 K, U_{air} = 16.1 m/s). (b) Chemiluminescence – Fast Spotting Regime (T_{air} = 843 K, U_{air} = 12.9 m/s). (c) Pressure – Slow Spotting Regime. (d) Pressure – Fast Spotting Regime.

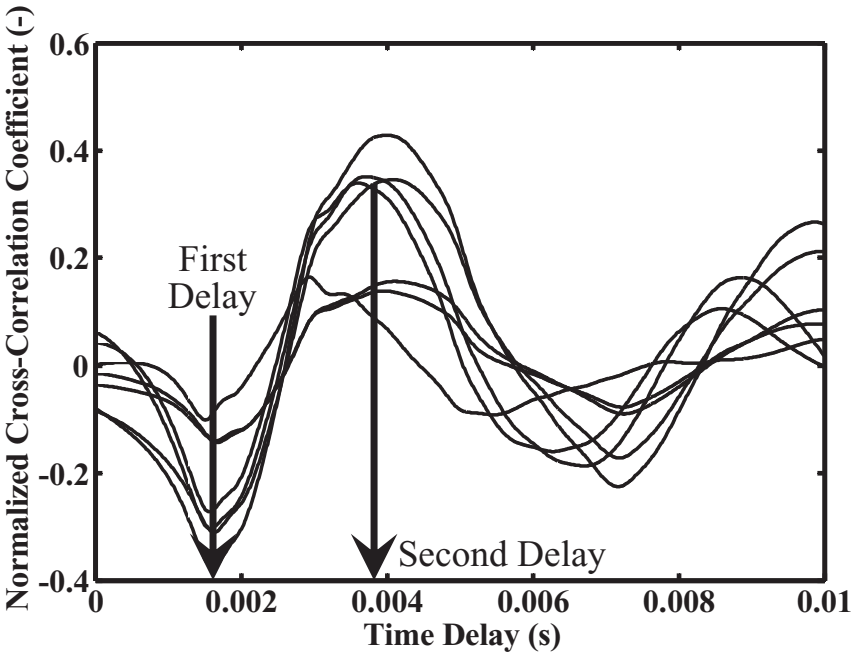

Figure 5.2: Chemiluminescence and pressure cross-correlation coefficients. Results shown for conditions in the range: U_{air} = 12.9 – 16.1 m/s and T_{air} = 834 – 843 K.

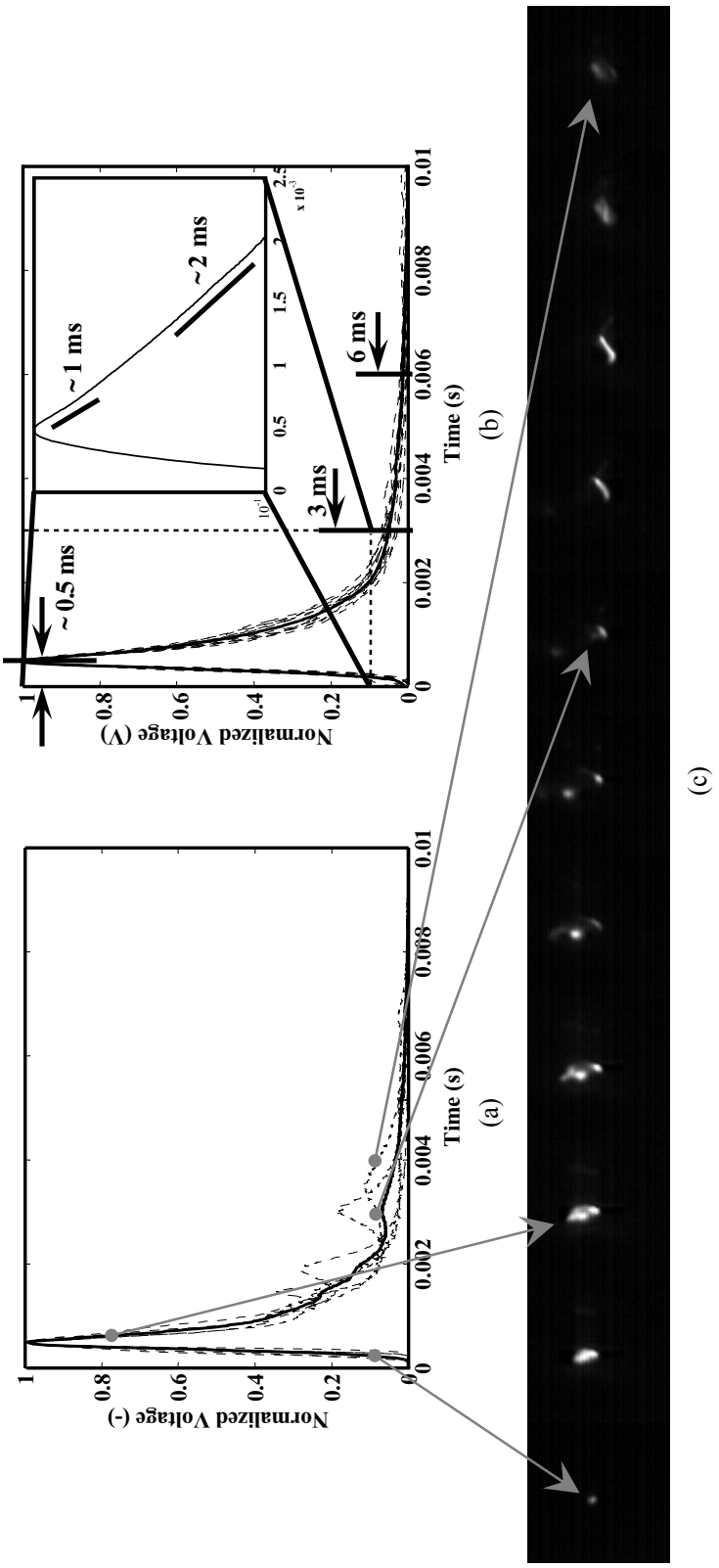

Figure 5.3: Typical autoignition chemiluminescence profiles and corresponding images. (a) Instantaneous normalized autoignition spots for: $T_{air} = 807$ K, $T_{fuel} = 761$ K, $U_{air} = U_{fuel} = 11.1$ m/s and $Y_{fuel} = 0.63$ recorded over 21 s at a sampling frequency of 100 kHz. (b) Averaged profiles for various conditions. (c) Selection of images from typical image sequence taken at 15 kHz.

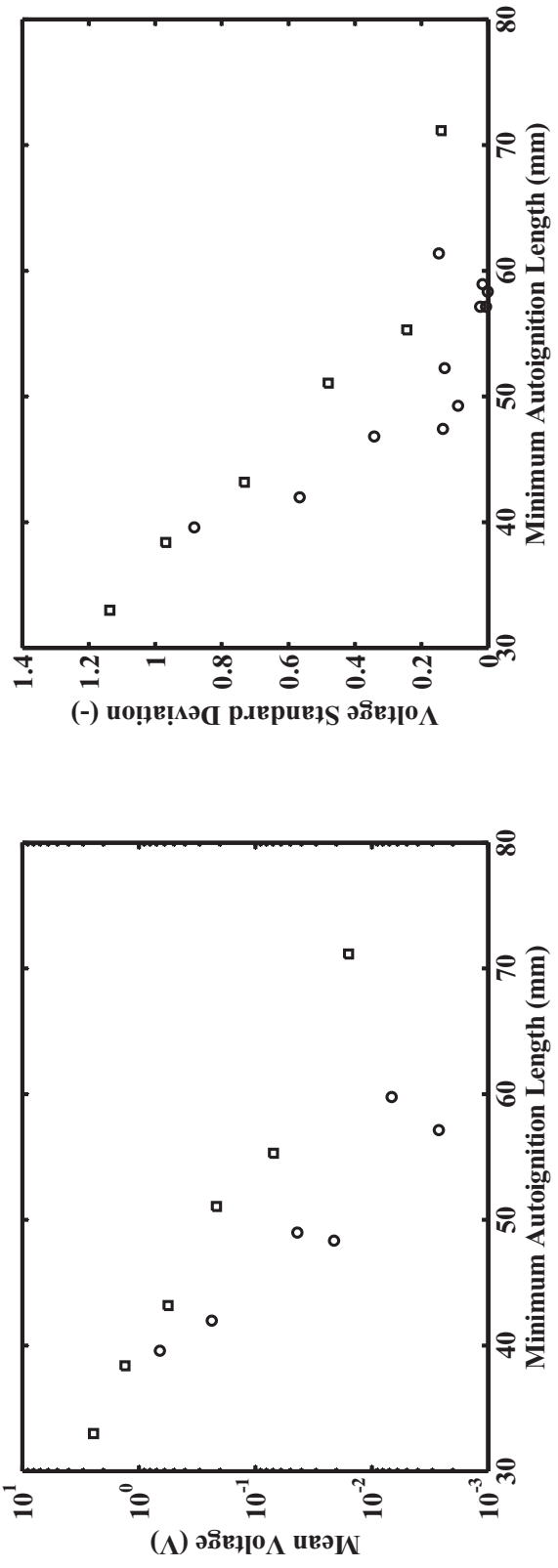

Figure 5.4: Mean and standard deviation of global autoignition chemiluminescence intensity as a function of autoignition length in the CTHC. (a) Mean, and, (b) Standard deviation of of global autoignition chemiluminescence intensity (OH^*) for conditions $U_{air} = U_{fuel} = 11.1$ m/s (circles) and $U_{air} = U_{fuel} = 17.5$ m/s (squares), with temperature T_{air} varying.

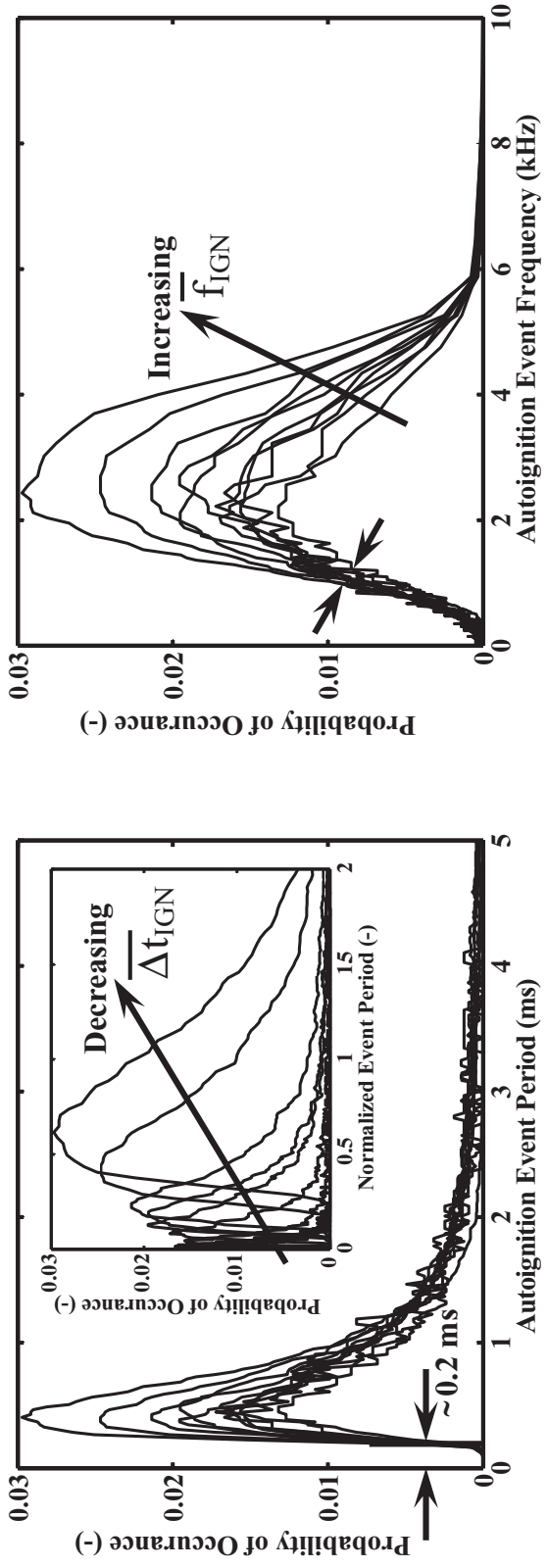

Figure 5.5: Autoignition period and frequency pdfs in the CTHC. Conditions same as those in **Figure 5.4**. (a) Pdfs of autoignition period, Δt_{IGN}, for conditions with various $\overline{\Delta t}_{IGN}$. (b) Pdfs of autoignition frequency, f_{IGN}, for conditions with various $\overline{f}_{IGN}$.

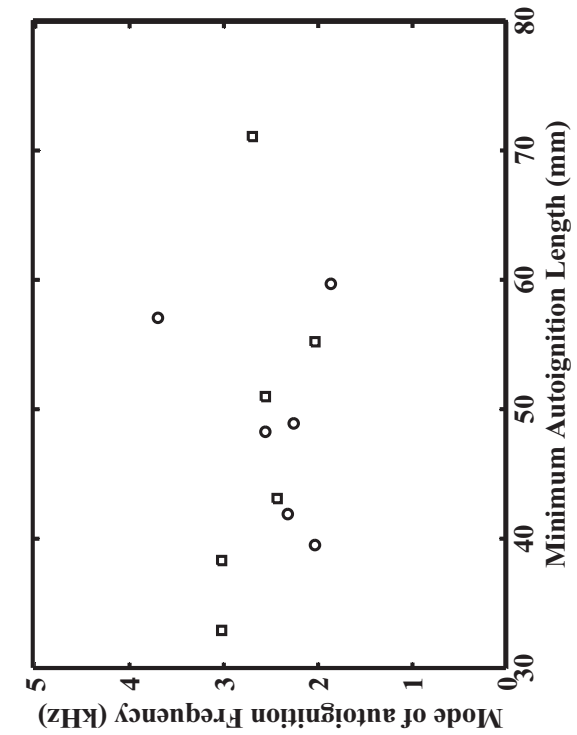

(b)

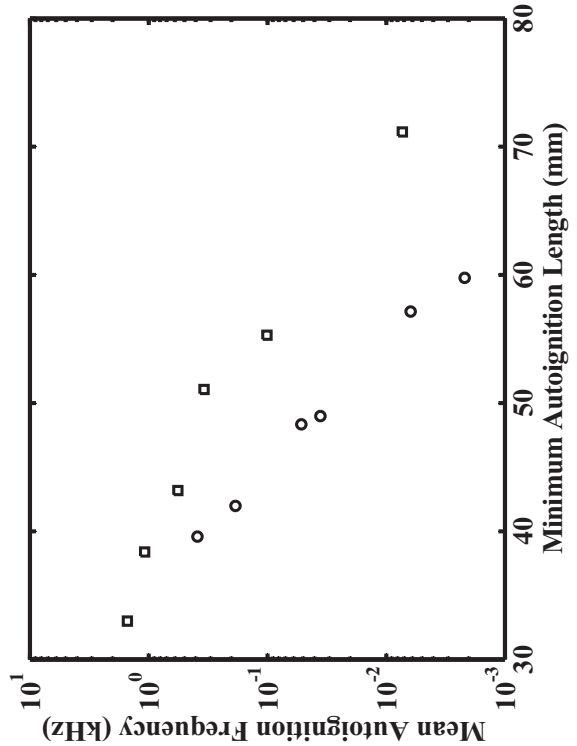

(a)

Figure 5.6: Mean and mode of autoignition frequency as a function of autoignition length in the CTHC. (a) Mean f_{IGN}, and, (b) Mode of f_{IGN} for conditions $U_{air} = U_{fuel} = 11.1$ m/s (circles) and $U_{air} = U_{fuel} = 17.5$ m/s (squares), with temperature T_{air} varying.

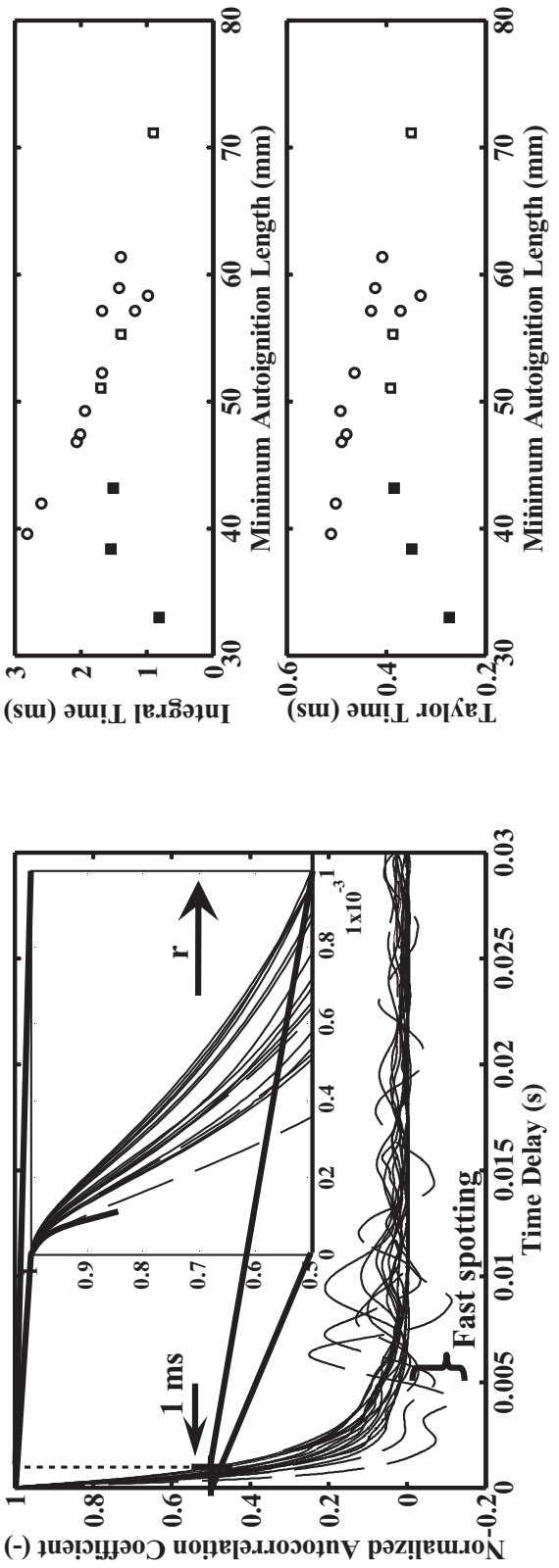

Figure 5.7: Autoignition integral and Taylor timescales in the CTHC. (a) Autocorrelation functions of OH^*, and, (b) Integral and Taylor timescales calculated from autocorrelations such as those in (a), for conditions $U_{air} = U_{fuel} = 11.1$ m/s (circles) and $U_{air} = U_{fuel} = 17.5$ m/s (squares).

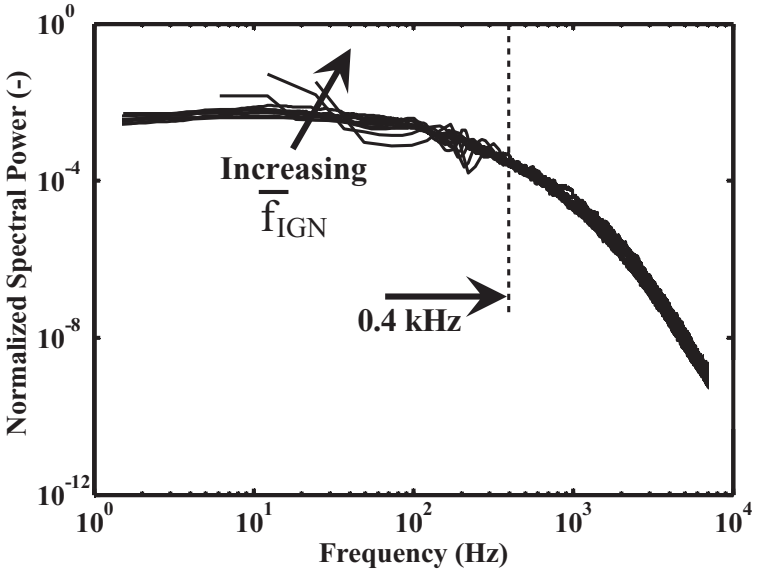

(a)

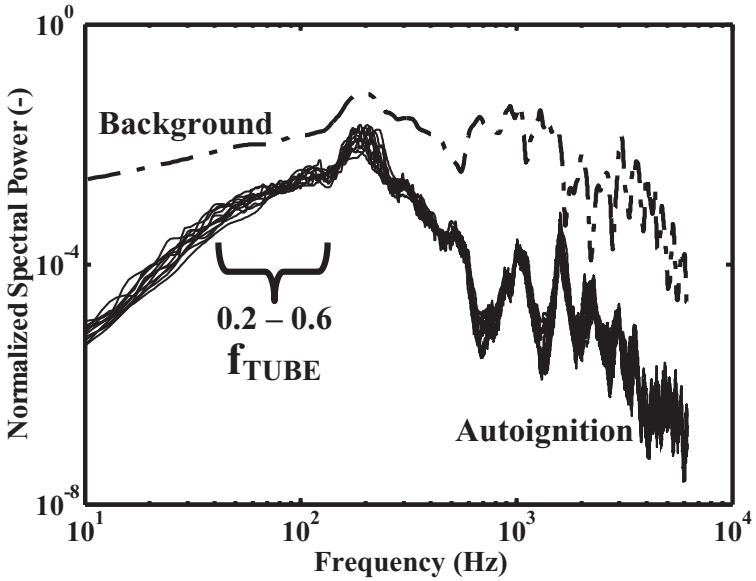

(b)

Figure 5.8: Normalized power spectra of chemiluminescence from PMT and microphone pressure in the CTHC. Normalized power spectra of: (a) Chemiluminescence, and, (b) Pressure, for conditions of fixed $U_{air} = 10.8$ m/s. Background noise spectrum appears higher because of normalization by its (low) variance. $f_{TUBE} \approx 0.2$ kHz.

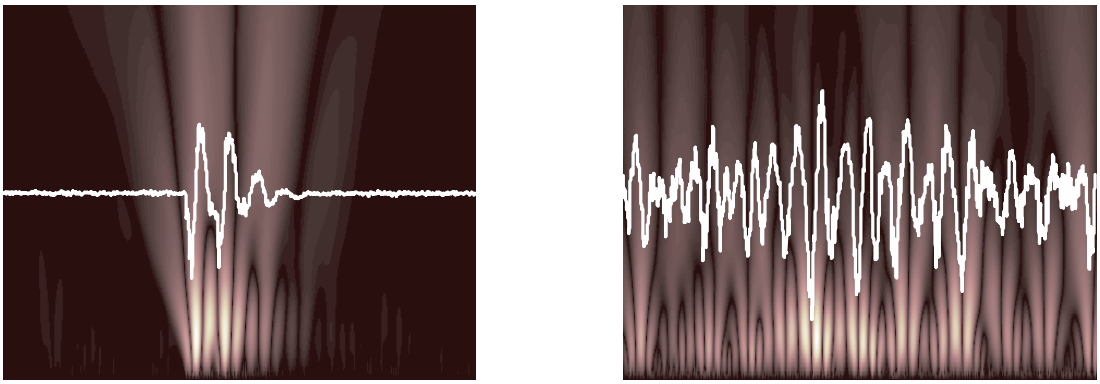

(a) (b)

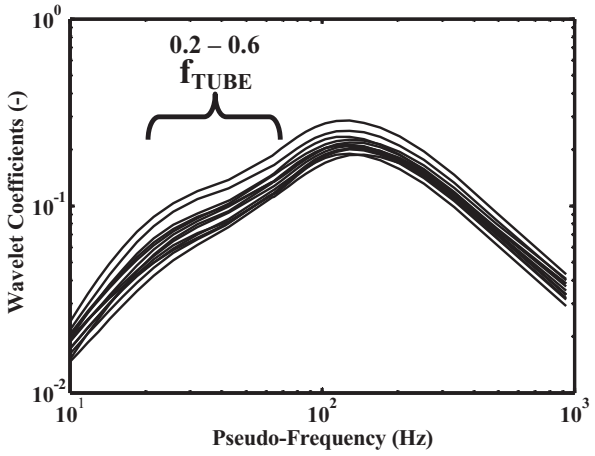

(c)

Figure 5.9: Wavelet analysis of pressure signals from the CTHC. (a) Example of pressure signal correlation coefficients at instant of autoignition in slow spotting regime. (b) Example in fast spotting regime. (c) Pressure signal correlation coefficients for all conditions as a function of wavelength frequency averaged over all autoignition events. $f_{TUBE} \approx 0.2$ kHz.

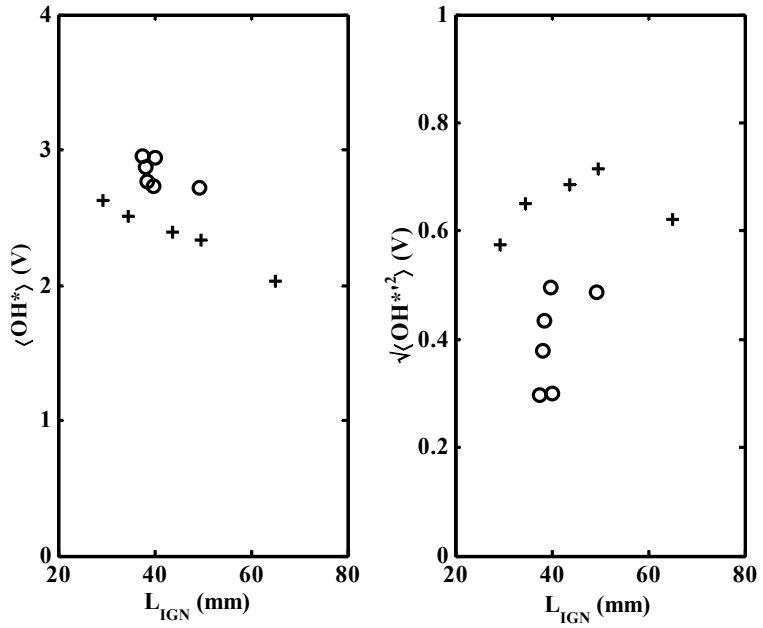

(a)

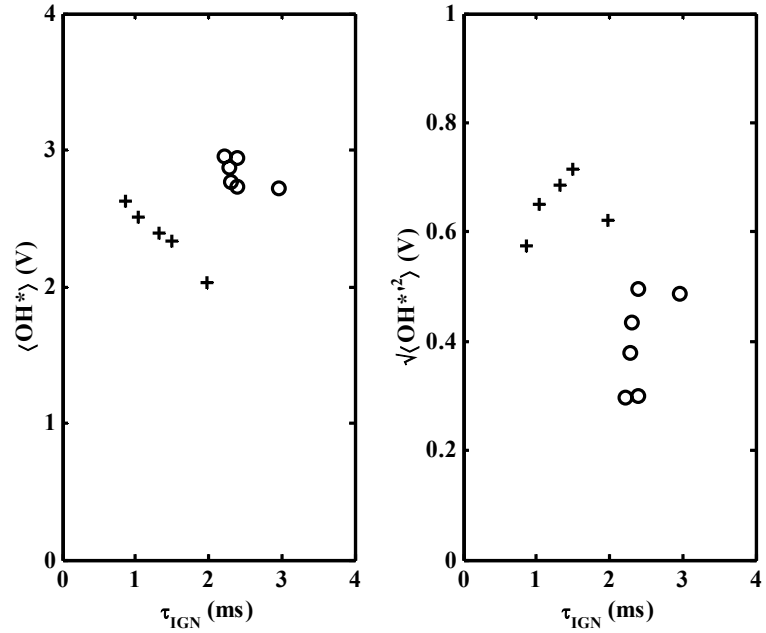

(b)

Figure 5.10: Mean and standard deviation of global autoignition chemiluminescence intensity (OH^*) as a function of autoignition length and delay time in the CTHAJ.

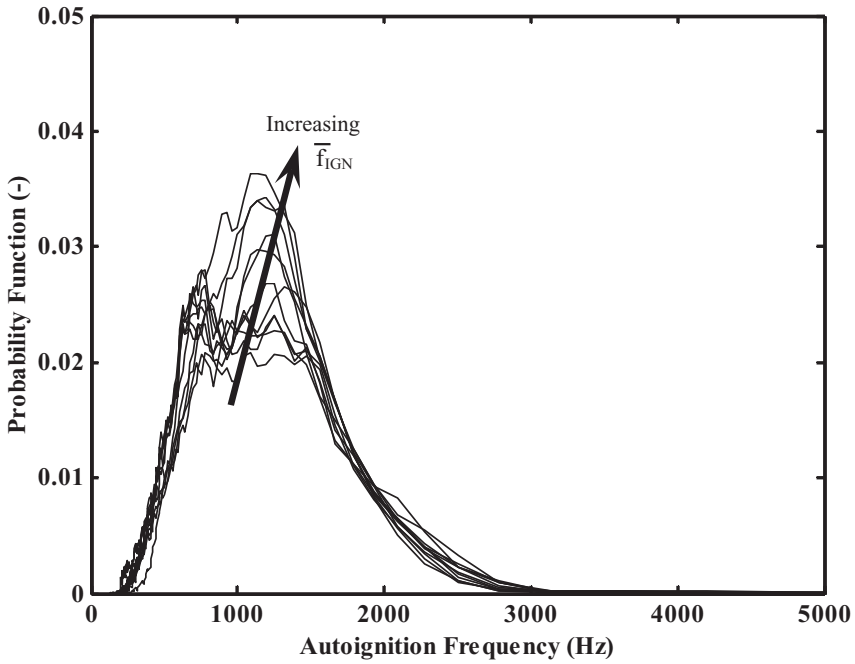

Figure 5.11: Autoignition frequency pdfs in the CTHAJ. Conditions with various $\overline{f}_{IGN}$.

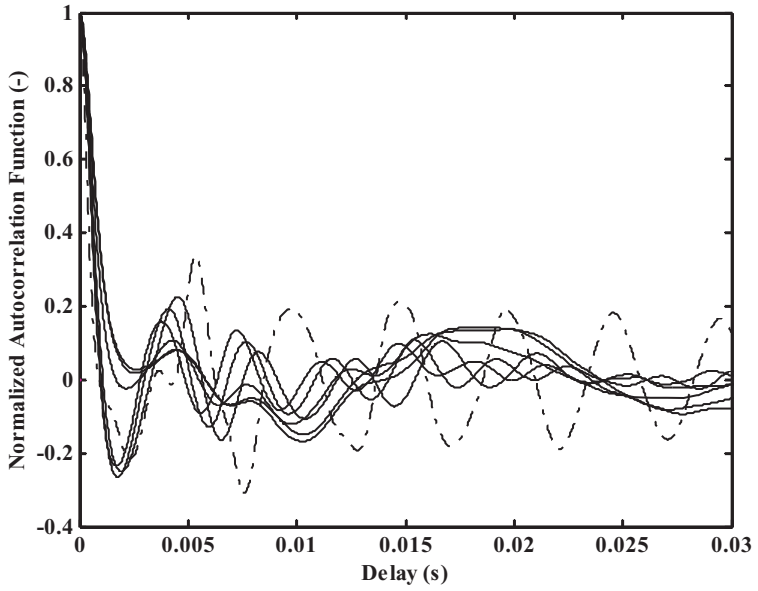

(a)

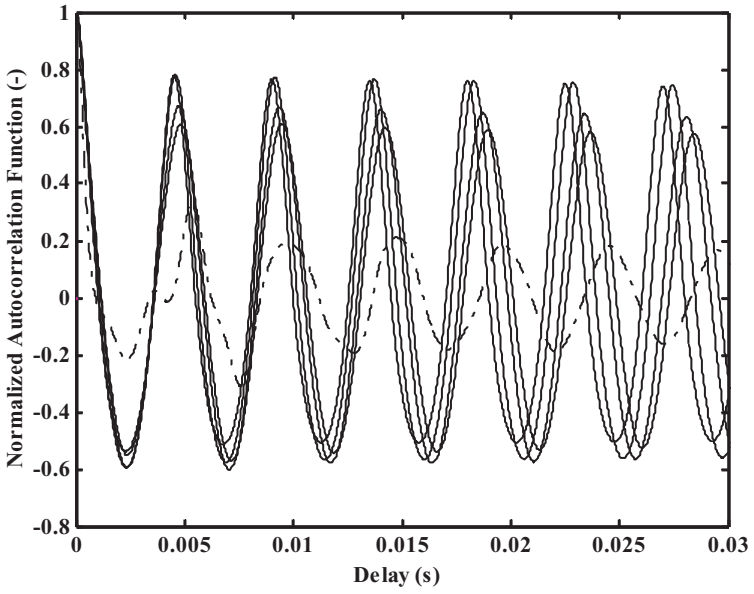

(b)

Figure 5.12: Autocorrelation functions of global autoignition chemiluminescence intensity in CTHAJ. (a) Autocorrelations of OH^* at lower $\overline{f}_{IGN}$. Plots correspond to spectra in **Figure 5.13(a)**. (b) Autocorrelations of OH^* at higher $\overline{f}_{IGN}$. Plots correspond to **Figure 5.13(b)**.

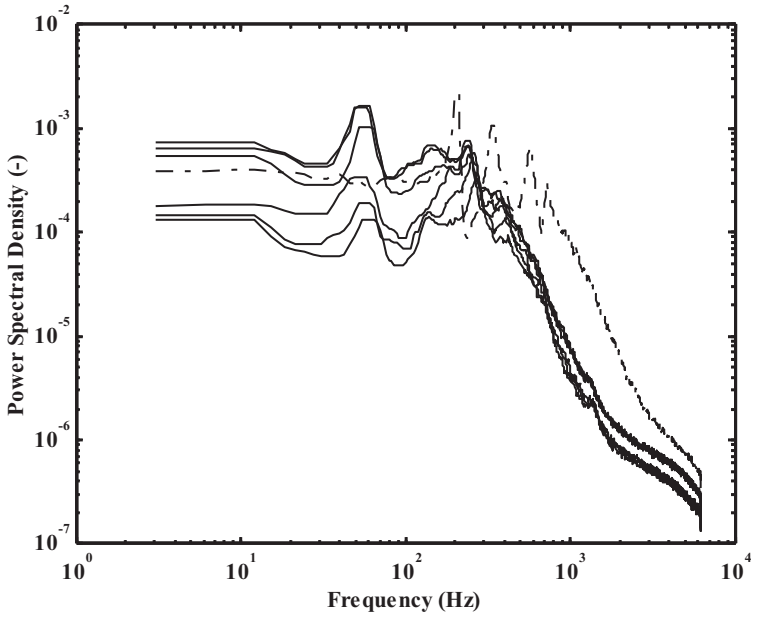

(a)

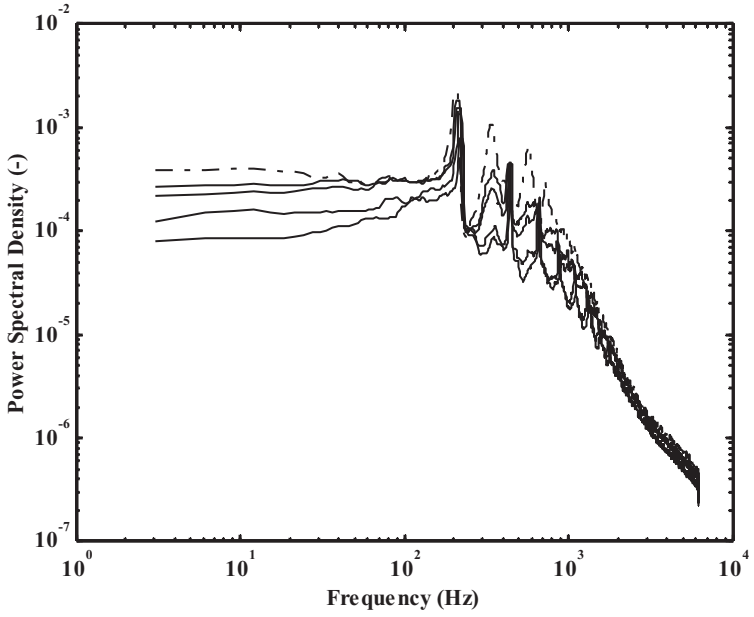

(b)

Figure 5.13: Normalized power spectra of chemiluminescence in CTHAJ. (a) Normalized power spectra of OH^* at lower $\overline{f}_{IGN}$. Plots correspond to autocorrelations in **Figure 5.12(a)**. (b) Normalized power spectra of OH^* at higher $\overline{f}_{IGN}$. Plots correspond to **Figure 5.12(b)**.

Chapter 6

Results — II: Autoignition Length

6.1 Objectives of Chapter 6

This chapter is concerned with measurements of autoignition location. Results for the CTHC are split into 'Equal Velocity' (**Section 6.2**) and 'Fuel Jet and Wake Flows' (**Section 6.3**). In each section the effect of various parameters is examined. Autoignition length measurements were not found in the literature, which is dominated by homogeneous experiments that report only on delay times. Hence, the data will be discussed in connection (where possible) with the work of others in the next chapter. Results from the CTHAJ burner are presented in **Section 6.4**. This data will not be considered in terms of mean residence time for reasons that have already been stated and so an effort will be made to view the results in terms of others in the literature here. A third class of temporally highly resolved measurements are presented in **Section 6.5**. High-speed OH^* images taken with the CMOS system were analysed, with particular attention to: (i) the true (earliest) autoignition location and its randomness, and, (ii) the spatial extent of post-ignition propagation. This insight is used to explain the differences between the various versions of L_{IGN} in **Sections 6.2** to **6.4**. The extent to which the various measures of L_{IGN} can be used to estimate L_{TRUE} and L_{STD} are discussed. The chapter closes with a brief summary of the main conclusions and a note on experimental errors.

6.2 Confined Turbulent Co-Flows of Hot Air: Equal Velocity Kinematic Condition

For all data points taken during 'equal velocity' experiments with the '3 mm' injector, the fuel velocity fell inside the range $\upsilon_{fuel} = 0.80 - 1.20$, with less than 1-in-10 of the measurements outside $\upsilon_{fuel} = 0.85 - 1.15$. In the small injector experiments the fuel velocity was harder to set accurately, but still the condition $\upsilon_{fuel} = 0.80 - 1.20$ has been satisfied for all 'equal velocity' data. So, for the purposes of this section all experiments with $0.80 < \upsilon_{fuel} < 1.20$ will be considered to have an 'equal velocity' condition at the inlet, i.e. $U_{fuel} \cong U_{air}$, or $\upsilon_{fuel} \cong 1$.

6.2.1 Effect of Fuel Dilution

The variations in the axial autoignition lengths for hydrogen, acetylene, ethylene and n-heptane due to changes in the fuel dilution with nitrogen, as described by Y_{fuel}, are shown in **Figures 6.1** to **6.3**. These figures show results for the most important measures of autoignition length taken during runs for which T_{air} (and T_{fuel}) and U_{air} ($\cong U_{fuel}$ throughout **Section 6.2**) were kept constant while Y_{fuel} was changed.

Figure 6.1 shows that hydrogen was only weakly affected by Y_{fuel} in the tested range of $Y_{fuel} > 0.2$, for constant $T_{air} = 948$ K, $U_{air} = 24.8$ m/s and $\upsilon_{fuel} = 1.00$, but also approximately constant T_{fuel}. This result is consistent with the inhomogeneous counterflow experiments of Blouch et al. [1998], Fotache et al. [1997b, 1995], where it was found that above concentrations of 15 – 20% hydrogen in nitrogen, or Y_{fuel} of about 0.18, the fuel concentration did not significantly affect the temperature of the air stream necessary for autoignition. In addition, this fuel exhibited an interesting behaviour, in that the OH^* images show almost no change for both L_{MIN} and L_{MODE} for Y_{fuel} above 0.3 – 0.4, whereas the '*broad*' images show a small decrease in both lengths as Y_{fuel} increased.

Measurements of acetylene autoignition lengths as Y_{fuel} was varied in the range 0.45 to unity (pure fuel), while all other variables were kept approximately constant, are shown in **Figure 6.2**. Three conditions were investigated: T_{air} = 816, 875 and 903 K, with corresponding U_{air} = 10.4, 24.6 and 25.2 m/s. **Figure 6.2(a)** shows plots of two measures of the earliest autoignition region, namely L_{MIN} and $\langle L_{MIN} \rangle$, against Y_{fuel}. The global autoignition region is characterized in **Figure 6.2(b)** with L_{MODE} and L_{MEAN} from averaged '*PF*' images for conditions corresponding to certain data in **Figure 6.2(a)**. Irrespective of the particular measure of L_{IGN} chosen, the effect of increasing Y_{fuel} was to move the autoignition regions monotonically closer to the injector. The sensitivity of the autoignition lengths to Y_{fuel} was greater than that of both hydrogen (**Figure 6.1**) and ethylene (**Figure 6.3(a)**). Generally, within the tested range of conditions, an increase in Y_{fuel} of 0.1 resulted in a decrease of L_{MIN} and $\langle L_{MIN} \rangle$ of about 9 – 20 mm on average. For L_{MODE} and L_{MEAN} the (modulus of the negative) slope falls to 2 – 10 mm per 10% increase in Y_{fuel} on average. It should be mentioned that the high temperature data in **Figure 6.2(a)** include phenomena that do not strictly belong to the 'Random Spots' regime. Especially at higher Y_{fuel}, when L_{IGN} was short, images show the existence of unsteady, lifted acetylene flames. This possibility has also been considered in the data contained in **Chapter 5**. Nevertheless, L_{MIN} and $\langle L_{MIN} \rangle$ (that characterize the lift-off height in this case) exhibit the same qualitative trend, but with a shallower gradient of about 4 – 5 mm per 0.1 increase in Y_{fuel}.

Figure 6.3(a) shows the effect of Y_{fuel} on L_{MIN} and $\langle L_{MIN} \rangle$ for ethylene autoignition. Experiments were performed at T_{air} of 1027 K and 1042 K, with U_{air} at 14.4 m/s and 17.5 m/s respectively, while Y_{fuel} spanned the range 0.65 to unity (pure fuel). The two measures of autoignition length show the same trend, which is for the autoigniting regions to move monotonically towards the injector with decreased dilution, or increased Y_{fuel}. Typically, for a 0.1 increase in Y_{fuel}, 1 – 6 mm shifts towards the injector in both L_{MIN} and $\langle L_{MIN} \rangle$ were observed.

Finally, **Figure 6.3(b)** shows n-heptane plots exactly similar to those in **Figure 6.3(a)** for ethylene, but at T_{air} of 1088 K and 1092 K, with U_{air} at 11.4 m/s and 13.4 m/s respectively. In these experiments Y_{fuel} spanned the range from 0.5 to unity. For n-heptane the effect of fuel dilution was more complex than for the other hydrocarbons. The results allow the possibility of a maximum autoignition length, but such a conclusion rests heavily on the single data point at $Y_{fuel} = 1$. Nevertheless, the trend for $Y_{fuel} < 0.76$ is for the autoignition length to *increase* with increasing Y_{fuel}; contrary to what was observed for acetylene and ethylene.

6.2.2 Effect of Temperature

Results concerning the effect of temperature on the phenomenon must take into account the following:

1. Autoignition is not solely a result of the local, instantaneous temperature at the autoignition site, but of the evolution (history) of the chemistry from injection to the point of eventual autoignition and is expected to be influenced by both T_{air} and T_{fuel}.

2. The air temperature into which the fuel is injected decreases almost linearly downstream of the injector, due to (inevitable) heat losses from the quartz tube walls. The mean temperature along the centreline is denoted by $\langle T(r = 0, z)\rangle$ and the reported air temperature, T_{air}, near the inlet of the quartz tube is: $T_{air} = \langle T(\frac{r}{R_{TUBE}} = 0.3, \frac{z}{M} = -8.7)\rangle$. The decay of the mean temperature relative to T_{air}, i.e. $T_{air} - \langle T(r = 0, z)\rangle$ at an axial distance z from the injector, was found to worsen (its modulus increased) by about 15% per 100 K increase in T_{air} (from **Section 3.3.1**).

3. Because of forced-convective heat transfer from the injector walls during the residence time of the fuel in the injector, T_{fuel} is generally not an independent

parameter, but a function of T_{air}, U_{air} and U_{fuel} (and various thermodynamic properties of the diluted-fuel mixture). With the exception of experiments with varying U_{fuel} (treated in **Section 6.2.3**), T_{fuel} is strongly correlated with T_{air} and negligibly affected by U_{air}, especially if the diluted-fuel (Y_{fuel}) is kept unchanged.

4. Autoignition is expected to occur at ξ_{MR} and (for simple chemistry) $\xi_{MR} < 0.5$ as long as $T_{air} > T_{fuel}$. In particular, hydrogen autoignition occurs at very low ξ_{MR}, typically around 0.006 – 0.06. The highest ξ_{MR} is expected for n-heptane with $\xi_{MR} = 0.08$ – 0.2. These calculations were obtained from 0-D CMC runs, mentioned previously in **Section 3.4.3**[*] over the complete range of actual values of T_{air}, T_{fuel} and Y_{fuel} used in the experiments. Acetylene and ethylene are expected to have intermediate values of $\xi_{MR} \approx 0.1$. For all fuels, the local temperature at any autoignition site is expected to be closer to T_{air} than T_{fuel}, with the leaner ξ_{MR} fuel showing the least dependence on T_{fuel}.

Hence, the effect of temperature is investigated by looking at the effect of T_{air} on the various measures of L_{IGN}.

Results for acetylene with $Y_{fuel} = 0.6$ and $\upsilon_{fuel} = 1.00$ constant as T_{air} (and consequently T_{fuel}) was increased are shown in **Figure 6.4**. **Figure 6.4(a)** shows L_{MIN} for data grouped together per constant: U_{air} = 10.9, 17.3 and 24.8 m/s. Certain trend lines were obtained with the heat exchanger placed over the quartz tube in order to reduce the heat losses to a minimum. There is a strong trend for the autoigniting regions to come monotonically closer to the injector with increasing temperature. A slight non-linearity can be deduced, but even so its degree is small. On average, L_{MIN} decreases by about 1 – 2 mm per K increase in T_{air}. **Figure 6.4(b)** shows that L_{MODE} obtained from two different techniques is also observed

[*]The ξ_{MR} results were not significantly affected by the particular value of $\langle\chi\rangle$ used in the calculations. A brief parametric study over two orders of magnitude variation in $\langle\chi\rangle$ centred on representative values obtained from the acetone PLIF measurements, showed that this was indeed the case, with worst case discrepancies of 0.015 in ξ_{MR}.

to decrease (closely with L_{MIN}) as T_{air} increases. The decrease amounts to about 2 mm per K. The trends are independent of U_{air} and also of the particular measure of L_{IGN} or optical measurement technique chosen.

Ethylene autoignition lengths were also tested against T_{air} in similar experiments (**Figure 6.5**) with conditions of constant: (i) $U_{air} = 10.1$ m/s, $Y_{fuel} = 0.70$, (ii) $U_{air} = 14.0$ m/s, $Y_{fuel} = 0.75$, and, (iii) $U_{air} = 15.5$ m/s, $Y_{fuel} = 0.75$. For all experiments υ_{fuel} was fixed at 0.95 and T_{air} spanned the range from 1025 to 1045 K. Both L_{MIN} and $\langle L_{MIN} \rangle$ decrease monotonically by 1 – 3 mm per K with increasing T_{air}, close to what was observed for acetylene.

N-heptane results for the effect of T_{air} on L_{IGN} are presented in **Figure 6.6** for: (i) $U_{air} = 13.8$ m/s, $Y_{fuel} = 0.95$, $\upsilon_{fuel} = 1.05$, (ii) $U_{air} = 17.8$ m/s, $Y_{fuel} = 0.95$, $\upsilon_{fuel} = 1.20$, and, (iii) $U_{air} = 13.3$ m/s, $Y_{fuel} = 0.50$, 0.60, 0.70 and 0.75, $\upsilon_{fuel} = 1.00$. It may be noted that for 'Random Spots' autoignition of this fuel[†]:

1. Far from the injector (relative to say 150 – 200 mm), autoignition moves monotonically closer to the injector with increasing T_{air} such that both L_{MIN} and $\langle L_{MIN} \rangle$ decrease by 5 – 8 mm per K. In **Figure 6.6** this includes all lower temperature results (below c. 1100 K).

2. Closer to the injector (relative to 150 – 200 mm), autoignition also moves monotonically closer to the injector with increasing T_{air}, but *at most* by 3 mm per K. In **Figure 6.6** this includes all higher temperatures (above c. 1100 K).

For both ethylene and n-heptane (but especially n-heptane) ξ_{MR} is expected to be a relatively rich mixture (n-heptane has $\xi_{MR} = 0.08 - 0.2$). At long distances from the injector the value of pdf(ξ) at ξ_{MR} is expected to be very low. If the probability of having the most reactive mixture is low enough, this 'lack' of most reactive mixture could lead to a situation in which autoignition cannot be achieved at ξ_{MR} and at the

[†]As with ethylene, although the ethylene measurements presented in this thesis do not show this behaviour because they are all associated with autoignition at relatively short lengths.

optimal reaction rate of this mixture. Instead, it is possible to reach an 'imperfectly premixed phase', in which the mixture is adequately mixed to a value of ξ_{PREMIX} (or an equivalence ratio, ϕ_{PREMIX}, equal to that calculated based perfect mixing between the fuel, nitrogen and air) and autoignites according to the homogeneous delay time required by ϕ_{PREMIX} for thermal runaway (although its reaction history, in terms of temperature increase and radical pool build-up at the shorter lengths due to the presence of and reaction at ξ_{MR}, will affect the eventual delay time). On the other hand, if ξ_{MR} exists, the dominant path towards autoignition will be through ξ_{MR} and autoignition is expected to occur closer to the injector, in what is termed the 'inhomogeneous phase'. This discussion concerning the possible mechanisms of autoignition will be continued in **Chapter 8**.

Autoignition at higher T_{air} and hence in the 'inhomogeneous phase', since at the higher T_{air} autoignition occurs at shorter L_{IGN} where ξ_{MR} exists, exhibits a shallower gradient in **Figure 6.6**. As the autoignition region moves closer to the injector the enhanced mixing causes the influence of temperature (and in other words the 'effect of chemistry') to diminish, with the eventual autoignition location much less affected by changes in T_{air}. This points towards an inhibiting effect of enhanced mixing on the chemistry, since closer to the injector there is higher u', $\frac{u'}{U}$, χ and $\chi|\xi = \xi_{MR}$. Note also that the gradient in the 'inhomogeneous phase' becomes approximately similar to that observed for acetylene and ethylene.

Figure 6.7(a) shows L_{MIN} and **Figure 6.7(b)** $\langle L_{MIN} \rangle$ for equal velocity hydrogen autoignition. Both measures of L_{IGN} decrease with increasing T_{air}. Consider first **Figure 6.7(a)**, showing a range of conditions with $U_{air} = 18.0$ – 27.0 m/s. The black lines were taken with traces of methane in the fuel stream and with the CCD camera. For $U_{air} = 18.0$ m/s it is confirmed that small quantities of methane in hydrogen ($Y_{CH4} = 0.05$ – 0.10) do not have as significant an effect on the autoignition lengths as that of T_{air} and U_{air}, similar to the results of Fotache et al. [1997b]. Then, it is possible to conclude that the '*CCD*' results for $U_{air} = 27.0$ m/s will be

close to L_{MIN} for $Y_{CH4} = 0$ and otherwise at the same conditions. Furthermore, the blue lines in **Figure 6.7(b)** should be close to $\langle L_{MIN} \rangle$ for $Y_{CH4} = 0$, again at the same conditions. Furthermore, in **Figure 6.7(a)** lines of constant U_{air} taken with $Y_{fuel} = 0.15$ and 0.28 collapse, so that there is almost no effect of Y_{fuel} in this range on L_{MIN}. This agrees with the results for the effect of fuel dilution from **Section 6.2.1** and **Figure 6.1** and results in the cumulative conclusion that, for $Y_{fuel} > 0.15$ the autoignition length of hydrogen is not considerably affected by its dilution.

Figure 6.7 also indicates that, unlike for the hydrocarbon fuels, for hydrogen the autoignition location exhibits a clear non-linear upstream shift as T_{air} is increased. This conclusion holds for both L_{MIN} and $\langle L_{MIN} \rangle$. The fact that the axial location of autoignition increases sharply as T_{air} decreases is consistent with the finding that the boundary between the 'No Ignition' and 'Random Spots' regimes was the least well defined for this fuel. On the other extreme, for every one of the curves shown flashback would have occurred for a temperature higher than the hottest point plotted by about 1 – 2 K, reflecting the fact that the boundary between the 'Random Spots' and 'Flashback' regimes is sharper.

6.2.3 Effect of Air Velocity

Each set of points in **Figure 6.8** corresponds to an experimental set with acetylene in which L_{MIN} (**Figure 6.8(a)**) and $\langle L_{MIN} \rangle$ (**Figure 6.8(b)**) were measured for fixed T_{air} and Y_{fuel}, while U_{air} ($\cong U_{fuel}$) was slowly increased. Both L_{MIN} and $\langle L_{MIN} \rangle$ increase monotonically with U_{air}. On average, the increase amounts to 8 – 15 mm per m/s of U_{air} over the range of tested conditions: (i) T_{air} = 815, 854, 868 and 895 K, $Y_{fuel} = 0.75$, $\upsilon_{fuel} = 0.90$, and, (ii) T_{air} = 896 K, $Y_{fuel} = 0.55$, $\upsilon_{fuel} = 1.00$. Similarly, **Figure 6.9** shows results for ethylene. Both L_{MIN} and $\langle L_{MIN} \rangle$ increase by 10 – 12 mm per m/s of U_{air} for fixed conditions of T_{air} = 1028 K, $Y_{fuel} = 0.75$, and, T_{air} = 1046 K, $Y_{fuel} = 0.70$, with υ_{fuel} set to 0.95 for all experiments. From these

figures directly, but also indirectly from lines of constant U_{air} in the temperature plots of **Figure 6.6** for n-heptane and **Figure 6.7** for hydrogen, it is evident that increasing U_{air} results in a significant downstream shift in the autoignition regions for all fuels and over all tested conditions. This is an important conclusion.

Each data set presented in this section was obtained from a series of experimental runs across which T_{air} and Y_{fuel} were constant, but U_{air} and U_{fuel} were changed from each run to the next in order to keep $\upsilon_{fuel} \cong 1$. Consider the following regarding the effect of temperature:

- The air temperature decreases linearly downstream of the injector because of heat losses, in way that has been measured (see **Section 3.3.1**). The axial decay of the mean temperature relative to T_{air}, i.e. $T_{air} - \langle T(r = 0, z)\rangle$ at a certain z, was found to improve (its modulus decreased) by 15% per 6 m/s increase in U_{air}. So, for a given T_{air} the temperature at a certain axial length *increased* with increasing U_{air}. At autoignition lengths, $z = L_{IGN}$:

$$\frac{\Delta T_{air}(r = 0, z = L_{IGN})}{T_{loss}|L_{IGN}} \quad \cong \quad 0.142\Delta U_{air} \tag{6.1}$$

  where $\Delta T_{air}(r = 0, z = L_{IGN})$ is the increase in local temperature at $(r = 0, z = L_{IGN})$ due to an increase ΔU_{air} in U_{air}, with T_{air} constant and $T_{loss}|L_{IGN}$ the typical temperature decay from T_{air} at $\frac{z}{M} = -8.7$ to $z = L_{IGN}$. For L_{IGN} of 30 – 160 mm (acetylene and ethylene extremes) and a decay of 10 K per 100 mm of tube in the 'jacketed' tube, $T_{loss}|L_{IGN} \cong 2$ – 16 K.

- Because of forced-convective heat transfer from the injector walls during the residence time of the fuel in the injector, T_{fuel} is generally not an independent parameter but a function of T_{air}, U_{air} and U_{fuel} (and various thermodynamic properties of the diluted-fuel mixture). For experiments in which T_{air} was held constant but $U_{air} \cong U_{fuel}$ was varied, an empirical fit to actual data can be

used based on the heat balance between the air and fuel flows:

$$\frac{\Delta T_{fuel}}{T_{fuel}} \cong \frac{0.021U_{fuel} + 0.919}{0.021(U_{fuel} + \Delta U_{fuel}) + 0.919} - 1 \tag{6.2}$$

to within ±0.04 and 95% confidence level (CL) for acetylene and ethylene *over the full range of conditions*, including T_{air} and Y_{fuel}.

Taking into account the above points, the conditional temperature of the most reactive mixture was estimated based on non-reacting (frozen) flow for given T_{air} and T_{fuel} and from an envelope of conditions spanning the experiments from which all the data in **Figures 6.8** and **6.9** were obtained. The range of $\langle T|\xi = \xi_{MR}\rangle$ is shown in **Figure 6.10**. The conditional temperature over a complete range of U_{air} (and hence U_{fuel}) is not affected by more than 5 K, even though T_{fuel} drops by up to 60 – 80 K. For a drop of 5 K in T_{air} the increase in L_{MIN} is 5 – 10 mm for acetylene and 5 – 15 mm, which cannot account for the corresponding 30 – 60 mm and 60 – 80 mm increases in L_{MIN} and $\langle L_{MIN}\rangle$ in **Figures 6.8** and **6.9**.

The downstream shift in all measures of L_{IGN}, even though the mean mixture fraction field remains largely unchanged (**Section 3.4.1**), *can* be explained well in terms of the increase in χ. As U_{air} increases, u'_{air} increases in order to keep the turbulence intensity, or $\frac{u'_{air}}{U_{air}}$, constant at 0.12 – 0.15 (**Section 3.2.1**), as do $\langle \xi'^2\rangle$ and $\langle\chi\rangle$. In fact, it has been shown in **Section 3.4.2**, that away from the injector, at representative autoignition lengths, $\langle\chi\rangle$ is well modelled by $\langle\chi\rangle \propto \frac{\langle\xi'^2\rangle}{\frac{L_{turb}}{u'}}$, with L_{turb} changing little with the conditions and $\frac{L_{turb}}{u'}$ not changing significantly with axial distance at the same conditions. More explicitly, recall from **Section 3.4.3** that in declaring that 'χ has increased', it has not only been stated that an increase in U_{air} increases $\langle\chi\rangle$, but also, it has been implied that $\langle\chi|\xi = \xi_{MR}\rangle$ increases at the same location, and, the values of the pdf$(\chi|\xi = \xi_{MR})$ decrease at lower values of $\chi|\xi = \xi_{MR}$ and increase at higher values of $\chi|\xi = \xi_{MR}$. It must be that the downstream shift in L_{IGN} is caused by the increase in $\chi|\xi = \xi_{MR}$.

6.2.4 Effect of Injector Size

The '3 mm' (d_{IN} = 2.24 mm) injector was chosen as the default injector and all results so far have been with this geometry. In additional experiments with acetylene, two smaller injectors with diameters 1.185 mm and 1.027 mm (28% and 21% of the '3 mm' injector area) were used. Autoignition with the smaller injectors was less bright and was associated with significantly smaller spots that seemed to decay faster and travel smaller distances before extinction. A higher pitched but less intense (loud) acoustic signature was observed, with $\overline{f}_{IGN}$ higher than that of the '3 mm' experiments. The effect of the injector size, d_{IN}, is described in **Figures 6.11**, **6.12** and **6.13** that show the results of an investigation into the effects of Y_{fuel}, T_{air} and U_{air} respectively on the autoignition lengths obtained with the small injectors and comparison (where possible) with *similar* results for acetylene obtained with the '3 mm' injector. In all experiments the condition $U_{fuel} \cong U_{air}$ was adhered to within ±20% as mentioned at the beginning of this section.

Figure 6.11 shows L_{MIN} and L_{MODE} taken with the d_{IN} = 1.027 mm injector at fixed T_{air} = 900 K, U_{air} = 29.7 m/s and υ_{fuel} = 1.20, as Y_{fuel} was increased from 0.61 to 0.85. The effect of fuel dilution is the same as with the '3 mm' results. An increase in Y_{fuel} causes the autoignition lengths to decrease. The decrease in both L_{MIN} and L_{MODE} is close to the slope obtained for the '3 mm' lifted flame data. Although the '3 mm' lifted flame situation is not directly representative of autoignition in the 'Random Spots' regime, the comparison shows that for the small injector the sensitivity of the autoignition location to changes in Y_{fuel} is similar to that of the lifted flames and thus, nearly half that observed for the '3 mm' geometry operating the 'Random Spots' regime.

Figures 6.12(a) and **6.12(b)** show results for L_{MIN} and L_{MODE} respectively taken with both the d_{IN} = 1.027 mm and d_{IN} = 1.185 mm injectors, at various fixed U_{air}, Y_{fuel} and υ_{fuel}, while varying T_{air} from about 880 to 920 K. A discussion

concerning the $\frac{z_M}{M} = 24$ and $\frac{z_M}{M} = 35$ data will be reserved for **Section 6.2.5** and so this data can be overlooked at this stage. The effect of temperature on L_{IGN} is the same as with the '3 mm' injector. An increase in T_{air} causes a decrease in L_{MIN} (**Figure 6.12(a)**) and L_{MODE} (**Figure 6.12(b)**). Furthermore, it appears from **Figure 6.12(a)** that L_{MIN} decreases non-linearly with increasing T_{air}.

The insert in **Figure 6.12(a)** compares the L_{MIN} trend-line comprising of $d_{IN} = 1.185$ mm injector data and taken at $U_{air} = 20.5$ m/s, $Y_{fuel} = 0.65$ and $\upsilon_{fuel} = 0.80$ (solid lines and square symbols), with two '3 mm' trend-lines taken from **Figure 6.4(a)** that bracket the small injector conditions with: (i) $U_{air} = 17.3$ m/s (dashed-dotted line and square symbols), and, (ii) $U_{air} = 24.8$ m/s (dashed-dotted line and diamond symbols); both with $Y_{fuel} = 0.60$ and $\upsilon_{fuel} = 1.00$. Firstly, stable 'Random Spots' autoignition with the small injector was possible for temperatures considerably higher than the '3 mm' injector flashback limit. Flashback was not possible with the small injector even at T_{air} higher by about 25 K (from between 880 – 900 K to 915 K) from that necessary to cause flashback with the '3 mm' injector. The 'Nothing–to–Spots' limit also shifts to higher temperatures. This amounts to a 30 K increase in T_{air} (from between 850 – 860 K to 885 K). Hence, autoignition in the 'Random Spots' regime shifts to higher temperatures with the use of smaller injector nozzle diameters. Secondly, it is interesting to compare the magnitude of L_{MIN} achieved with the different d_{IN}. At the lower temperature limit ($T_{air} = 880$ K) of the 'Random Spots' regime with the small injector, L_{MIN} was measured at around 30 mm. For the '3 mm' geometry at the same 'Nothing–to–Spots' limit (T_{air} between 850 – 860 K) L_{MIN} was between 70 and 90 mm, more than twice the small injector result. However, at the higher temperature limit, close to flashback, the '3 mm' injector reaches values of L_{MIN} ($\approx$ 20 – 30 mm) similar to those obtained with the small injector nozzles. It is clear that the range of achievable L_{MIN} decreases significantly for the small injector. The similar L_{MIN} at the 'Spots–to–Flame' transitions of the two injectors might also indicate that

for both nozzles there exists a limit of L_{MIN} below which stable autoignition is not possible. This limit seems to depend slightly on the conditions (U_{air}, υ_{fuel}) and geometry (d_{IN}). It is reasonable to try to explain this outcome in terms of the scalar dissipation rate being higher than a critical value close to the nozzles. Returning to the other extreme, the 'Nothing–to–Spots' limit of the smaller injector, with its associated higher T_{air} and much shorter L_{MIN} than for the '3 mm' nozzle, must be determined by the fact that more vigorous mixing, at least initially, leads quickly to a 'lack' of ξ_{MR}, or better to low values of pdf($\xi = \xi_{MR}$), resulting in autoignition in the 'imperfectly premixed phase' for which the delay time based on ξ_{PREMIX} (much leaner for the smaller d_{IN}) is longer than the residence time in the tube. It cannot be explained in terms of heat losses since, as mentioned above, the 'Nothing–to–Spots' limit of a smaller injector occurs at higher T_{air} than that of the '3 mm' injector. The degree of shortening of L_{MIN} with T_{air} is also dramatically reduced to about 1 mm per 4 K. Recall that the '3 mm' experiments showed drops of 1 – 2 mm/K. The slope of the '3 mm' data in **Figure 6.12(a)** is around 1.2 – 1.5 mm/K, at least 5 times the small injector slope.

Figure 6.13 directly investigates the effect of U_{air} on L_{MIN} and $\langle L_{MIN} \rangle$ for both small injectors, although this could have been deduced by the existing data in **Figure 6.12**. Again, the effect of increasing $\frac{z_M}{M}$ from 23 to 24 to 35 will be left for the following section. In **Figures 6.13(a)** and **6.13(b)** data are provided collectively spanning the range of U_{air} from about 10 to 30 m/s, various T_{air} between 855 and 885 K, with $Y_{fuel} = 0.65$ and 0.75, and $\upsilon_{fuel} = 1.20$, grouped in lines of near-constant T_{air}, Y_{fuel} and υ_{fuel}. **Figure 6.13(b)** compares runs of similar conditions between the $d_{IN} = 1.027$ mm and 2.24 mm injectors and contains data with similar $Y_{fuel} = 0.75$ throughout. In certain conditions it can be seen that with the smaller injectors it is possible to reduce U_{air} below the flashback limit for the larger injector (recall that flashback occurs at low U_{air}), all other conditions being the same. As with the '3 mm' injector, increasing U_{air} causes a monotonic increase in L_{MIN} and

$\langle L_{MIN} \rangle$. Yet, the autoignition lengths are much less sensitive to changes in U_{air}, similar to what was observed for the effects of Y_{fuel} and T_{air}. The slope of this increase amounts to 2 mm per 1 m/s increase in U_{air} and this should be compared with the 10 – 15 mm increase per 1 m/s observed with the '3 mm' injector. Finally, **Figure 6.13(b)** reveals that the magnitudes of L_{MIN} and $\langle L_{MIN} \rangle$ for the small injector experiments remain close to the values of the same lengths in the '3 mm' injector at near-flashback (low U_{air}) conditions, and that generally, the effect of increasing U_{air} at this limit is to increase the critical flashback length. This latter result ties in with the conclusion that close to flashback, autoignition might be occurring in regions associated with a critical scalar dissipation rate that does not allow L_{IGN} to occur at even shorter lengths.

6.2.5 Effect of Turbulence

Figures 6.12 and **6.13(a)** show results for the autoignition length observed with the two small injectors and also during experiments with these injectors in which the distance of injection from the grid was increased by means of a 36 mm 'injector extension', or from $\frac{z_M}{M}$ of 23 to 35. It has been shown with hot wire measurements (**Section 3.2.1**) that at the downstream locations ($\frac{z_M}{M} = 35$) u' decreases by 20 – 30% from its upstream ($\frac{z_M}{M} = 23$) value. Similarly L_{turb} increases by 10 – 20%. Recall from **Section 3.4** that in the Gaussian plume equation (**Equation 3.2**) that described the results for $\langle \xi \rangle$ in this apparatus well, σ scales with $\frac{u'}{U}$ for both 'long' and 'short lengths' from the injector. Furthermore, it was shown that it is possible to model $\langle \chi \rangle$ as being inversely proportional to a turbulent timescale, $\frac{L_{turb}}{u'}$, for $L_\chi = \frac{z}{d_{IN}} > 10$, or 22 mm. Then, the effect of the decrease in u' and (less so) increase in L_{turb} due to injection at a longer length from the grid, is for iso-contours of $\langle \xi \rangle$ to elongate axially with the characteristic plume width becoming narrower and for $\langle \chi \rangle$ to decrease by 30 – 50%.

Both L_{MIN} and L_{MODE} show a significant decrease in L_{IGN} when $\frac{z_M}{M}$ is increased. For example, consider the green/black line pair in **Figure 6.13(a)** at constant $T_{air} = 865$ K, $Y_{fuel} = 0.65$, $\upsilon_{fuel} = 1.20$, and with $d_{IN} = 1.19$ mm and $\frac{z_M}{M} = 23$. With an increase of $\frac{z_M}{M}$ to 35 and even with U_{air} higher by 10 m/s, the autoignition length falls to half the $\frac{z_M}{M} = 23$ value. Otherwise the effects of T_{air} and U_{air} on the measures of autoignition length remain the same as before, with increasing T_{air} causing a decrease in L_{MIN} and $\langle L_{MIN} \rangle$ and an increase in U_{air} causing an increase in the same lengths.

6.2.6 Summary

From the results of the current chapter the following conclusions are made, for autoignition lengths in the CTHC:

- The effect of an increase in Y_{fuel} was, in general, for L_{IGN} to decrease. Qualitatively, the trend was found to be similar for all geometries, fuels and for the various combinations of T_{air} and U_{air} tested, with two exceptions: (i) the insensitivity of hydrogen L_{IGN} to Y_{fuel} within the tested range of $Y_{fuel} > 0.15$, and, (ii) the (possible) non-linear trend of n-heptane, for which L_{IGN} increased with increasing Y_{fuel} for $Y_{fuel} < 0.76$, but decreased for pure fuel. For acetylene injected through the small injector the sensitivity of L_{IGN} to Y_{fuel} was approximately halved relative to the '3 mm' results.

- For all geometries, fuels and for all investigated conditions, the effect of increasing T_{air} was to cause a strong, monotonic decrease in all measures of L_{IGN}. Slight deviations from linearity were found for the hydrocarbon fuels, but for hydrogen the non-linearity was strong, with L_{IGN} levelling out at higher T_{air} and shorter L_{IGN}. For acetylene injected through the small injector L_{IGN} was less influenced (by a factor of 4 – 8) by changes to T_{air}.

- An increase in U_{air} (with $U_{fuel} \cong U_{air}$) caused a significant, non-linear increase in L_{IGN}. For acetylene injected through the small injector a similar trend was found, but the effect on L_{IGN} was lessened by a factor of 5 – 8. The increase in L_{IGN} cannot be explicated in terms of the slight decrease in T_{fuel} as U_{fuel} increased (together with U_{air}), nor in terms of the mean mixing field that was found not to be affected by U_{air}. Nevertheless, it can be explained in terms of an increase in $\chi|\xi = \xi_{MR}$ with U_{air}, and this refers to the increase in the mean $\langle\chi|\xi = \xi_{MR}\rangle$ together with a decrease in the value of pdf$(\chi|\xi = \xi_{MR})$ at low conditional dissipation.

- Autoignition in the 'Random Spots' regime shifted to higher T_{air} when using the smaller injectors. Higher T_{air} and lower U_{air} could be employed before flashback was achieved, relative to the '3 mm' injector. However, the 'Spots–to–Flame' limit was reached at similar L_{IGN} that depended slightly (and in the manner expected) on U_{air}, υ_{fuel} and d_{IN}, leading one to reason that the scalar dissipation could be above a critical value close to the nozzle. Far from flashback, such as at the 'Nothing–to–Spots' transition, the small injector L_{IGN} was considerably reduced from equivalent results obtained with the '3 mm' injector. Small injector results at the 'Nothing–to–Spots' limit indicate that lack of autoignition is possibly caused by low values of pdf$(\xi = \xi_{MR})$.

- The reduction in L_{IGN} could be augmented by injecting at longer distances from the grid, and hence, into a turbulent flow with reduced u', increased L_{turb} and lower χ, $\chi|\xi = \xi_{MR}$.

As a closing remark to this section, it is emphasized that the trends that have been observed and summarized above were reached by using a variety of different optical equipment and by analyzing the data with a variety of different techniques, and thus, it is possible to claim with a certain confidence that these conclusions are independent of the experimental methods used.

6.3 Confined Turbulent Co-Flows of Hot Air: Fuel Jet and Wake Flows

The effect on L_{MIN} of changing υ_{fuel} (or U_{fuel} since U_{air} is fixed) while keeping T_{air}, U_{air} and Y_{fuel} constant is shown in **Figure 6.14** for acetylene. Each group of data points corresponds to a line of constant T_{air}, U_{air} and Y_{fuel} conditions with: (i) $T_{air} = 870$ K, $Y_{fuel} = 0.70$ and $U_{air} = 20.6$, 22.1 and 23.4 m/s, (ii) $T_{air} = 903$ K, $Y_{fuel} = 0.70$ and $U_{air} = 21.5$, 23.1 and 24.7 m/s, and, (iii) $T_{air} = 904$ K, $Y_{fuel} = 0.75$ and $U_{air} = 23.9$ m/s. Hence, the range of investigated conditions for these experiments spans: $T_{air} = 870$ – 906 K[‡], $U_{air} = 20.6$ – 24.7 m/s and $Y_{fuel} = 0.70$ – 0.75. The normalized fuel velocity, υ_{fuel}, ranges from 0.40 to 1.50. For both wake and jet fuel flows, and for all seven combinations of T_{air}, U_{air} and Y_{fuel}, autoignition moves linearly downstream by an increase in υ_{fuel}. The typical downstream shift in L_{MIN} associated with an increase in υ_{fuel} of 0.10 is in the range 2 – 5 mm.

In the acetylene data of **Section 6.2** the range $\upsilon_{fuel} = 0.80$ – 1.20 was considered 'equal velocity' (although 90% of the '3 mm' measurements fall inside $\upsilon_{fuel} = 0.85 - 1.15$). At this stage it is possible to quantify the variations in L_{MIN} for acetylene *across data sets* of equal velocity experiments, but for which υ_{fuel} changes by ±20%. From the results in the previous paragraph, L_{MIN} should increase by 6 – 10 mm between the two extremes of $\upsilon_{fuel} = 0.80$ and 1.20. For the reason that this variation is not negligible, in the presentation (and plots) of results in **Section 6.2**, although all measurements were for equal velocity, the particular value of υ_{fuel} in each data set was given. Where a value of υ_{fuel} was supplied as a representative value for a particular data set this variable was not allowed to vary by more than ±0.02 inside that same data set. Hence, *within data sets* L_{MIN} varied by less than ±1 mm due to variations in υ_{fuel}.

[‡]It should be noted that throughout this thesis, where data sets have been shown for 'constant' T_{air}, an allowance was made within the same data set of ±1 K and in very few cases ±2 K from the stated conditions.

Returning to **Figure 6.14** (right plot), L_{MIN} for fuel wakes is around 31 mm at $\upsilon_{fuel} \cong 0.85$, for T_{air} = 903 K, U_{air} = 23.1 – 24.7 m/s and Y_{fuel} = 0.70. For the fuel jet with T_{air} = 904 K, U_{air} = 23.9 m/s and Y_{fuel} = 0.75, L_{MIN} = 27 mm at υ_{fuel} = 1.05. Assuming a reasonably linear variation of L_{MIN} with υ_{fuel} and extrapolating between υ_{fuel} = 0.85 and 1.05, the discrepancy between the wake and jet measures of L_{MIN} is approximately 10 mm. This difference can be explained purely in terms of the 1 K variation in T_{air} (recall from **Section 6.2.2** the 1 – 2 mm decrease in L_{MIN} per K), but more importantly the 0.05 variation in Y_{fuel} (recall from **Section 6.2.1** the 9 – 20 mm decrease in L_{MIN} per 0.1 increase in Y_{fuel}). These results were obtained for the same geometry and the same fuel and so based on this comparison the transition between wake and jet flows seems to be smooth.

The autoignition of hydrogen jets was also studied. **Figure 6.15** shows results for both L_{MIN} and L_{MODE} along constant U_{air}, U_{fuel} (and hence υ_{fuel}) lines, as a function of T_{air}, over a wide range of conditions spanning T_{air} from 970 – 1010 K, U_{air} from 20 – 32 m/s, and, U_{fuel} from 20 – 120 m/s. For all data Y_{fuel} was kept constant at 0.13. Thus, the data in **Figure 6.15** were obtained for jets with υ_{fuel} = 2.00 – 4.60. The trends in this figure are non-linear, with the axial location increasing sharply as T_{air} decreases, similar to the observed trends for the same fuel in the equal velocity experiments. The flashback T_{air} increases with U_{air} and U_{fuel}, while the length from the injector at which autoignition occurs just before flashback decreases at the higher velocities (and higher T_{air}). As with acetylene, the effect of U_{fuel} for a given U_{air} is to increase all measures of L_{IGN}, yet the displacement of L_{MIN} caused by a certain increase in υ_{fuel} is much less than that observed with acetylene. This leads to the expectation that in attempting to estimate a mean residence time from injection to L_{MIN}, τ_{MIN}, or indeed any measure of L_{IGN} and corresponding τ_{IGN} (explained in **Section 2.4.3**), one must account for the jet momentum (and specifically the jet density that is much lower for hydrogen) in order to collapse τ_{IGN} data taken at various υ_{fuel} but at the same U_{air}.

6.4 Confined Turbulent Annular Jets of Hot Air

In **Sections 4** and **5.3** it was shown that in the CTHAJ, with the exception of a few slow spotting conditions at long lengths, unsteady lifted flames were set up in the tube that extinguished and re-(auto)ignited, in what resembled pulsed combustor behaviour; qualitatively different to autoignition in the CHTC 'Random Spots' regime. Thus, in the current section L_{IGN} is no longer a strict autoignition length, but rather an amalgam of autoignition length and lift-off height. Nevertheless, the flow does exhibit the ability to 'autoignite' and so L_{IGN} was measured as a function of the conditions. The effect of various parameters on L_{IGN} will be examined.

Recall from **Section 2.3** that in this configuration the velocity and temperature fields were not characterized in this work. Instead, the literature was consulted, a brief overview of which makes up the following two paragraphs. It will be evident and explicitly emphasized that in the literature, a proper understanding of the flow in such a geometry has been approached predominantly through a suitably defined Reynolds number. In order to be able to relate the conditions during the experiments to the presented studies in the literature, but also because autoignition is expected to be strongly dependent, amongst other, on the mixing and hence the character of the flow, which is in turn described by the Reynolds number, for all results, plots, presentation and discussion thereof concerning autoignition in the CTHAJ, reference will be made to $\mathcal{R}e_{air}$, rather than U_{air}. It is straightforward to convert to a velocity from the definition of $\mathcal{R}e_{air}$, the supplied conditions (such as T_{air}) and the specifics of the geometry given in **Section 2.2.3**.

Much work has been done towards improving the understanding and ability to predict numerically the complex flows behind bluff-bodies. Studies of annular jets with various blockage ratios and forebody angles [Li and Tankin, 1987] and hot wire measurements in the annular jet shear layer [Huang and Lin, 2000], agree that transition to turbulence occurs for flows with $\mathcal{R}e > 750$. On the other hand, Laser

Doppler Anemometry (LDA) and smoke flow on a confined annular jet geometry with blockage ratio of 0.23 reported transition at $\mathcal{R}e > 2000$ [Sheen et al., 1997]. In the experiments presented in this thesis, turbulence in ensured by the perforated grid upstream of the injector and bluff-body. At high $\mathcal{R}e$, shear from the bluff-body is expected to augment, if not dominate, the turbulent character and hence mixing.

The aforementioned studies have also emphasized the importance of a suitably defined Reynolds number for the classification of the various types of flow and regimes in the wake of the bluff-body. At high $\mathcal{R}e$, the extent of the recirculation zone becomes independent of $\mathcal{R}e$ and depends on geometrical characteristics alone [Durão and Whitelaw, 1978, Li and Tankin, 1987]. For confined geometry, the recirculation length normalized with D_{BLUFF} was found to be elongated and widened by larger blockage ratios and bluff-body angles. The recirculation zone extended from the bluff-body to between 1 – 3 D_{BLUFF} downstream [Davies and Beér, 1971, Nicholson and Field, 1949].

Turbulence quantities have also been measured with LDA [Durão and Whitelaw, 1978] and substantial anisotropy was reported for lengths up to 8 D_{BLUFF}, after which the jet develops similar to a round jet. Minimum values of $\frac{u'}{U}$ of 30% were reported in the recirculation zone, decreasing with increasing blockage ratio, but not affected significantly by U_{air}. The axial and radial locations of the fluctuation peaks were also considered. In the axial direction, the fluctuations were most intense near the bluff-body and at the downstream end of the recirculation length, while radially u' was smaller in the recirculation region than the shear layer. The radial profiles consistently revealed maxima in the axial fluctuations at the shear layers of the jet.

Figures 6.16(a) and **6.16(b)** contain the main results in terms of autoignition location for the CTHAJ. In general, the stronger effect is that of T_{air}, but it can be seen that $\mathcal{R}e_{air}$ is also a controlling parameter. Irrespective (and over a relatively wide range) of U_{air} and υ_{fuel}, $\mathcal{R}e_{air}$ describes the data well for the two bluff-body/quartz tube geometry combinations used (**Section 2.2.3**). This is expected,

since the flow field and hence resulting mixing patterns are very well described in terms of $\mathcal{R}e_{air}$ and justifies the inspection of the data through this variable, rather than U_{air}. Given a value of $\mathcal{R}e_{air}$, the effect of increasing T_{air} is, as with the CTHC with the same fuel, to decrease both L_{MIN} and L_{MODE}.

In **Figure 6.16(a)** the possible downstream extent of the recirculation zone obtained from the literature is indicated. For short lengths from the injector, comparable to the recirculation zone extent, it may be noted that the trends for the two lengths begin to differ, with the earliest length, L_{MIN}, levelling out as T_{air} increases further (**Figure 6.16(a)**), but the overall autoignition region as seen through L_{MODE}, continuing to move closer to the injector/bluff-body (**Figure 6.16(b)**). This is especially apparent for the lower $\mathcal{R}e_{air}$ data that occupy the lower range in T_{air} at short L_{IGN}. During these experiments the autoignition region exhibited the 'Spot-Wake Interactions' behaviour described in **Section 4** and illustrated in **Figure 4.20**. The sudden, dangerous shift of the autoignition region to close distances from the injector leads to the short L_{MIN}. The inability to flashback and the return to stable spotting situations at longer lengths, results in PF averaged images with longer L_{MODE}, less affected by the short term deviations towards the injector.

Autoignition of a homogeneous ethylene–air mixture in a continuous flow reactor [Cowell and Lefebre, 1987] resulted in delay times of 5.5 ms for $T_{air} = 1042$ K and an equivalence ratio (ϕ) of 0.2. This value for ϕ is equal to that calculated based on hypothetical homogeneous conditions for the run, indicated by the arrow in **Figure 6.16(a)**, had the fuel and air been premixed and is denoted by ϕ_{PREMIX} (specifically from the fuel and air volumetric flow rates). This would have corresponded to an L_{MIN} of 100 mm (based on $U_{fuel} \cong U_{air} = 18.2$ m/s). So, the presence of inhomogeneities leads to delayed autoignition, relative to the homogeneous case. More straightforward comparison is possible with experiments in this apparatus, but without the bluff-body. For conditions with the same nitrogen-diluted ethylene and $T_{air} = 1042$ K, but equal air and injection velocity, $U_{fuel} \cong U_{air} = 18.2$ m/s,

L_{MIN} was measured at 130 mm; almost 40 mm upstream of those obtained here for the same U_{air} (see data point in **Figure 6.16(a)**). This comparison is only made possible thanks to the finding that υ_{fuel} does not seem to significantly affect L_{MIN} or L_{MODE} in the CTHAJ results presented in **Figure 6.16**.

It is indeed likely, as originally suspected, that the increased fluctuations of the velocity field in the CTHAJ are causing an additional delay in the inhomogeneous autoignition of ethylene, by causing an increase in $\chi|\xi = \xi_{MR}$, relative to the CTHC. This has already been observed in the CTHC apparatus for all fuels, in that an increase in U_{air} (and hence u'_{air}) resulted in a non-linear increase in all measures of L_{IGN}, but also in the mean residence time until autoignition, [Markides and Mastorakos, 2005] (more details in **Chapter 7**). Here, even with the same U_{air} and T_{air}, it is possible to conclude that the presence of the bluff-body alone leads to an increased L_{IGN}. It is repeated that, the comparisons and conclusions made in the last two paragraphs are made possible only because in the CTHAJ υ_{fuel} does not significantly affect L_{MIN} or L_{MODE} for a given $\mathcal{R}e_{turb}$.

6.5 Mean and Randomness of True Autoignition Length

In the current chapter, various means of quantifying L_{IGN} (i.e. L_{MIN}, $\langle L_{MIN} \rangle$, L_{MODE} and L_{MEAN}) were used. These were obtained from:

- Different imaging systems such as:
  - The intensified UV CCD imaging system, both with (denoted by '*OH*') and without (denoted by '*broad*') an additional optical OH^* filter, and,
  - Short (0.25 ms) and long (250 ms) exposure imaging with the un-intensified CCD system (denoted by '*CCD*'). In these measurements, only the 'blue' intensity component was considered.

- Different optical methods including:
  - Single length measurements from an AVG, STD or PF image generated by a large number of instantaneous snapshots during each run, and,
  - From a large number of time-series measures of $\widehat{L_{MIN}}$, where $\widehat{L_{MIN}}$ denotes an instantaneous measure of the minimum autoignition length.

An important outcome is that almost all *trends* are independent of the optical equipment and analysis technique. Thus, it may be said with confidence that the effects of the various parameters on the physical processes being measured is correctly captured in terms of the method of raw data generation, processing and analysis. The differences between the various measures of the autoignition lengths can be due to true randomness in the autoignition locations, but perhaps also due to non-convergence of the statistics, or indeed inherent to the choice of measurement technique. These possibilities are discussed below.

In the experiments presented in this chapter, L_{MEAN} was found to be equal to $0.95 - 1.25 L_{MODE}$ at 95% CL. At higher T_{air}, as $\overline{f}_{IGN}$ increased and L_{IGN} shortened, the pdfs of L_{IGN} became positively skewed (towards the injector), as in **Figure 6.17**. Then, L_{MEAN} was displaced increasingly downstream of L_{MODE}. This can be seen also in **Figures 6.2** and **6.4**. Note also that the images in **Figure 6.17** are not normalized. The intensity is reduced at lower T_{air}, as $\overline{f}_{IGN}$ decreases and L_{IGN} increases.

The shortest length is L_{MIN}. Considering all '*OH*' data generated with the ICCD and contained in the current chapter, it is possible to quantify the *random* discrepancy between all measures of L_{MIN} from the AVG, STD and PF averaged images. This is less than 15% (95% CL). In terms of *systematic* discrepancies, the STD and PF images agree well, with the STD usually shorter by *at most* 5%. The STD and PF images predicted L_{MIN} lengths ±8% to ±20% shorter than identical measurements made on AVG images from the same runs. Also, the random uncer-

tainty associated with measurement of L_{MIN} from AVG images in general were up to ±15% (obtained by comparison with STD and PF). Hence, AVG L_{MIN} measurements were not used. Where applicable (for hydrogen) the '*OH*' and '*broad*' images from the ICCD also agreed well; to within ±10%.

The '*CCD*' L_{MIN} results from AVG and PF images were no more than 3% apart, but were shorter than their '*OH*' equivalents. The AVG images were on average 20% shorter and the PF on average 10% shorter than their respective '*OH*' counterparts, with random variations about these values of 15% and 10% respectively. This prediction difference is consistent throughout and is not thought be due to the processing for two reasons. Firstly, it is in direct agreement with **Figure 4.6(a)** and the relevant discussion in **Section 4.2.1: Random Spots**, concerning the spectral emissions of acetylene during autoignition, where it was shown that the CH^* radical emits strongly in the 'upstream' autoignition regions, as opposed to OH^* that appears stronger further downstream. Secondly, in the processing of instantaneous '*CCD*' images, denoising was performed before thresholding to obtain L_{MIN}. This is in contrast to the '*OH*' processing, in which only the final AVG, STD and PF images were denoised. The effect of denoising is to decrease the 'background' noise level, and consequently the threshold that effectively defines L_{MIN}. Unless the absolute level of the noise intensity is constant for all images (which is not the case), it might be expected that the different processes of denoising in the '*OH*' and '*CCD*' cases are affecting the result.

Long exposure L_{MIN} measurements from individual '*CCD*' $\widehat{L_{MIN}}$ were 1.15 (±0.10) times shorter than short exposure L_{MIN} measurements from simultaneously recorded, short exposure '*OH*' averaged images of the same phenomena. As mentioned in **Section 4.4.3: Long Exposure Images**, long exposure measurements are better able to identify the earliest length as they are obtained from many realizations of $\widehat{L_{MIN}}$ from many *individual/instantaneous* images, as opposed to short exposure analyses which operate on a single *averaged* image per run. In addition,

the fact that for short exposure measurements L_{MIN} is the length from the injector to a rise height from the background of 3% relative to the maximum intensity, as opposed to the 1% rise height from the background in each long exposure image, enhances the small discrepancy. In a brief study *the same threshold* was used for short '*CCD*' measures of L_{MIN} from: (i) individual $\widehat{L_{MIN}}$, and, (ii) AVG or PF images. The L_{MIN} values from the former were on average 4% (±5% to 95% CL) times shorter than L_{MIN} from the latter, as expected.

Figure 6.2(a) shows the lengths L_{MIN} and $\langle L_{MIN} \rangle$ as calculated from: (i) *long exposure images* for acetylene and T_{air} = 903 K, U_{air} = 25.2 m/s, υ_{fuel} = 0.85, and, (ii) *short exposure images* for T_{air} = 875 K, U_{air} = 24.6 m/s, υ_{fuel} = 1.00. Consider first the long exposure results with the exposure fixed to 250 ms. It was stated in **Section 4.4.3** that at the slowest spotting conditions $\langle L_{MIN} \rangle$ should deviate from L_{MIN} towards the longer $\langle L_{TRUE} \rangle$. At these conditions, the gap between L_{MIN} and $\langle L_{MIN} \rangle$ is a rough measure of the true spread in autoignition locations. Here, $\langle L_{MIN} \rangle$ goes from $0.90L_{MIN}$ (2 mm) to $0.75L_{MIN}$ (9 mm) as L_{MIN} lengthens and $\overline{f}_{IGN}$ decreases. Hence, the randomness is autoignition location amounts in this case to about 25% of L_{MIN}. This is most probably an underestimate of the true spread, because t_{EXP} is long enough to require $\overline{f}_{IGN} \approx 1 - 10$ Hz before $\langle L_{MIN} \rangle \sim \langle L_{TRUE} \rangle$ and $\langle L_{MIN} \rangle - L_{MIN}$ is approximately equal the randomness in L_{TRUE}; $\overline{f}_{IGN}$ is estimated at more than 1 kHz for this data. In the short exposure images, $\langle L_{MIN} \rangle$ does *not* show the same behaviour. It does not tend any closer to L_{MIN} at the fastest spotting conditions (high Y_{fuel}) than had been established for slow spotting (low Y_{fuel}). This result is not a reflection of a physical reality, but rather a consequence of the imaging method and can be understood through the explanation offered in **Section 4.4.1: Frame Rates and Exposure Times**. There it was claimed that (strictly) for short exposure images, such as here, only the global autoignition region can be characterized (i.e. including the regions of post-ignition flame propagation). Both L_{MIN} and $\langle L_{MIN} \rangle$ follow the global region

irrespective of $\overline{f}_{IGN}$, so that even at slow spotting, $\langle L_{MIN} \rangle$ cannot deviate away from L_{MIN} in order to approach L_{TRUE}.

Nevertheless, another interesting result becomes apparent. From the short exposure data in **Figure 6.2** and irrespective of $\overline{f}_{IGN}$ or L_{MIN}, $\langle L_{MIN} \rangle$ consistently underestimates L_{MODE} by 10 mm, or 10 – 20%. This is important because it means that *if* short exposure $\langle L_{MIN} \rangle \approx \langle L_{TRUE} \rangle$, then these quantities will not be far from L_{MEAN} or L_{MODE} either. Such a scenario would be possible, if the distance of propagation of the flamelets was short relative to the autoignition lengths.

Figure 6.18 shows normalized pdfs of the true (earliest) autoignition regions and comparison with pdfs of global autoignition/propagation regions, measured during experiments spanning a range of conditions with n-heptane in the '3 mm' injector and the CHTC burner. The CMOS system was used to generate 5,000 short exposure images per run at 10 kHz. The resulting images were analysed in three ways, based on the methods and autoignition lengths used so far:

1. For each image $\widehat{L_{MIN}}$ was found as previously described and applied to long and short exposure images with the slow framing CCD and ICCD cameras (black lines). Recall that this variable is the instantaneous minimum length from the injector of any reaction (through OH^* emissions) in an image.

2. After tracking the propagating flamelets, L_{TRUE} was also recovered by reporting only on the initial sites of creation of any new flamelet based on a thresholding technique. The technique took into account representative propagation velocity behaviour and the size of the spot in each image with respect to its size in previous instances. Of the 5,000 original images, almost all of which contained signal from post-ignition flames, about 500 – 600 images were found to contain true, explosive, small-scale autoignition events.

3. The images were then used to compile a PF 'averaged' image, in the same way as was done with the short exposure images generated from the slow

framing cameras (red lines). Hence, from each image, a global autoignition (or autoignition and flame propagation) region was defined, relative to a threshold. Each image contributed equally to the two-dimensional '*PF*' image.

In **Figure 6.18** the data for L_{TRUE}, $\widehat{L_{MIN}}$ and L_{IGN} from the PF image are plotted by subtracting the mean of $\widehat{L_{MIN}}$, $\langle L_{MIN} \rangle$, and dividing by its standard deviation. The probabilities were normalized to unity. All lengths were normalized in the same way as, i.e. based on the mean and standard deviation of $\widehat{L_{MIN}}$, in order to show the upstream displacement of the pdfs relative to $\langle L_{MIN} \rangle$ and to be able to compare the spread of the distributions directly. The randomness of the autoignition location is equal to σ_{TRUE}, the standard deviation of L_{TRUE} by definition.

The overall reported L_{MIN} from the first method is near the vertical axis. For the PF method L_{MIN} is $2\sigma_{MIN}$ downstream, where σ_{MIN} is the standard deviation of $\widehat{L_{MIN}}$ and $\frac{\sigma_{MIN}}{L_{MIN}}$ was found to be 0.10 – 0.15 over all conditions. The pdf of $\widehat{L_{MIN}}$ is shifted by no more than $0.5 - 1.0\sigma_{MIN}$ downstream of the pdf of L_{TRUE}. Based on these results, a single realization of L_{MIN} can overestimate L_{TRUE} by 5 – 15%, but on average $\langle L_{MIN} \rangle$ overestimates $\langle L_{TRUE} \rangle$ by only 4% (±1%, 95% CL) or 3±1 mm. This is small for this data, given L_{MIN} of 60 – 100 mm, but is expected to be so in general. From the PF image, L_{MODE} overestimates $\langle L_{TRUE} \rangle$ by about $2\sigma_{MIN}$, or 20 – 30%. Also, L_{MEAN} from is not more than $1.00 - 1.25\sigma_{MIN}$, or 20% longer than L_{MODE}, which agrees very well with the measurements mentioned near the beginning of this section. In other words, it turns out that short exposure measurements of $\langle L_{MIN} \rangle$ are close to the equivalent measures of $\langle L_{TRUE} \rangle$, irrespective of $\overline{f}_{IGN}$ and that σ_{MIN} is approximately the same as σ_{TRUE}. Going a step further, L_{MEAN} and L_{MODE} are also reasonable estimates of $\langle L_{TRUE} \rangle$, overestimating the correct values by a factor of 1.25 – 1.35.

From the pdf of L_{TRUE}, the distance of L_{MIN} from $\langle L_{TRUE}$ characterizes the true spread in autoignition position in the tube. From the pdf of $\widehat{L_{MIN}}$, the distance

of L_{MIN} from L_{MODE} characterizes both the true spread in autoignition and the average distance that a spots travels during the exposure time. As such, as a measure of the randomness of autoignition, L_{MODE} - L_{MIN} can be said to be 'contaminated' by the post-ignition flamelets. The difference between the two spreads is about $0.4\sigma_{MIN}$, or 2 – 3 mm and for an exposure time of 0.1 ms leads this to a reasonable measure for the average axial, downstream propagation velocity of 20 – 30 m/s for the earliest flamelets. In addition to σ_{MIN} and the observed differences between L_{MIN}, $\langle L_{TRUE} \rangle$, $\langle L_{MIN} \rangle$ and L_{MODE}, the randomness of the autoignition location can also be quantified by L_{STD}, the standard deviation of L_{IGN} from the PF image. This quantity depends on the threshold level chosen, but can give reasonable results for the statistical spread in the autoignition. **Figure 6.18** shows that with a high enough threshold, L_{STD} overestimates σ_{TRUE} by a factor of 1.2 to 1.4 at most.

Hence, from the results of this chapter, but also the investigations of the frequency of the occurrence of autoignition in **Chapter 5**, there seems to be a real effect of the turbulent flow in the spatial distribution of the autoignition kernels, that cannot be completely attributed to the fluctuations of T_{air}, which were measured and found to range between 0.05% – 0.25% of T_{air}, or up to 2.5 K for the conditions here, but must be also attributed to the turbulent dispersion and spread in the plume, and (perhaps) the spatial randomness in $\chi|\xi = \xi_{MR}$.

6.6 Conclusions from Chapter 6

In this chapter results were presented of the location of autoignition in the 'Random Spots' regime for the CTHC and CTHAJ burners. The location of autoignition was measured in practice by making optical measurements with a variety of equipment and techniques based on chemiluminescent emissions from the autoigniting regions. The original (earliest) autoignition sites were difficult to investigate in isolation, due to the fact that post-ignition flames originating at these sites propagated across

the tube before they extinguished. Different versions of L_{IGN} were defined and measured, where possible, in order to best: (i) quantify the mean location of both the autoignition sites and the extent of post-ignition propagation, and, (ii) characterize the statistical spread in the appearance of autoignition. Depending on how heavily contaminated a particular measurement of L_{IGN} was by the post-ignition flames and what the exposure time was relative to the mean frequency of occurrence of autoignition, each one of these quantities was used to inspect different spatial aspects of the phenomenon. The absolute magnitudes of the different versions of L_{IGN} were different, but the observed trends were similar and independent of the optical equipment, analysis techniques and chosen definition of L_{IGN}.

For the CTHC:

- Autoignition in the 'Random Spots' regime shifted to higher T_{air} when using injector nozzles with smaller d_{IN}. Also, lower U_{air} could be employed before the flashback limit was reached.
- Far from the flashback 'Spots–to–Flame' transition for acetylene injected through the small injector, L_{IGN} was considerably reduced from equivalent results obtained with the '3 mm' injector. Small injector results at the 'Nothing–to–Spots' limit also indicate that lack of autoignition is possibly caused by low values of pdf($\xi = \xi_{MR}$).
- A further reduction in L_{IGN} could be achieved by injecting at longer distances from the grid and hence, into a turbulent flow with reduced u', increased L_{turb} and reduced χ, $\chi|\xi = \xi_{MR}$.
- The 'Spots–to–Flame' limit for the small and '3 mm' injectors was reached at similar L_{IGN} that depended slightly on U_{air}, υ_{fuel} and d_{IN}. Together with the observed insensitivity of L_{IGN} to T_{air} in the small injector experiments, this perhaps reveals that the scalar dissipation could be above a critical value close to the nozzle.

- Generally, L_{IGN} decreased as Y_{fuel} increased, except for hydrogen that was insensitive to Y_{fuel}, within the tested range of $Y_{fuel} > 0.15$ and the (possible) non-linear trend of n-heptane, for which L_{IGN} increased with increasing Y_{fuel} for $Y_{fuel} < 0.76$, but decreased for pure fuel. For acetylene injected through the small injector, the sensitivity of L_{IGN} to Y_{fuel} was approximately halved.

- The effect of increasing T_{air} was to cause a strong, monotonic decrease in all measures of L_{IGN}. For the hydrocarbons, slight deviations from linearity were found, but for hydrogen the non-linearity was obvious, with L_{IGN} levelling out at higher T_{air} (shorter L_{IGN}). For acetylene injected through the small injector, L_{IGN} was less affected by T_{air}.

- An increase in U_{air} (with $U_{fuel} \cong U_{air}$) caused a significant, non-linear increase in L_{IGN}. For acetylene injected through the small injector, a similar trend was found, but the effect on L_{IGN} was lessened. The increase in L_{IGN} cannot be explained in terms of the decrease in T_{fuel} as U_{fuel} increased (together with U_{air}), nor in terms of the mean mixing field that was not affected by U_{air}, but it can be explained in terms of the increase in $\chi|\xi = \xi_{MR}$.

- For a given T_{air}, U_{air} and Y_{fuel}, L_{IGN} increased with increasing U_{fuel} (and hence υ_{fuel}). The transition between wake ($\upsilon_{fuel} < 1$) and jet ($\upsilon_{fuel} > 1$) flows was smooth.

In the CTHAJ, L_{IGN} decreased almost linearly with increasing T_{air}, increased with increasing $\mathcal{R}e_{turb}$ and was insensitive to changes in υ_{fuel}. At high T_{air}, when L_{IGN} was such that the autoignition events appeared in the vicinity of the recirculation zone, the trends of the various measures of L_{IGN} were no longer identical.

It was uncovered that the original autoignition sites manifested in these flows with significant spatial randomness. The low magnitude of the fluctuations of T_{air}, leads to the conclusion that there is a real effect of the turbulent flow in the spatial appearance of the autoignition kernels.

6.7 Errors Associated with Data of Chapter 6

Each '*CCD*' data point in this chapter, corresponding to a particular run, was calculated from 100 – 4400 images. '*OH*' and '*broad*' results were from 200 – 1200 instantaneous images. A comparison has been carried out between the predictions of $\widehat{L_{MIN}}$ from CCD images and both ICCD '*OH*' and '*broad*' images. It was found that the absolute (systematic) discrepancy in the measurement due to the use of the different measurement equipment, the presence of the filter and processing methods was of the order of 5%. The relative (random) error within bands of similar data was also at ±5%.

The resulting systematic uncertainty in correctly locating the earliest flame front in each image and hence the reported values of L_{MIN} introduced by the flame front tracking is typically ±2 – 6 mm for images from the CCD and ±3 mm for ICCD images. The error worsens as the spatial resolution of the images decreases. The worst case uncertainty is 8 mm for measurements of n-heptane made with the CCD in the CTHC. In this case, the imaging window had to cover an axial length of about 0.4 m; long enough to make the measurements of L_{MIN} shown in **Figure 6.6**.

The worst case uncertainty introduced into the calculation of L_{MIN}, $\langle L_{MIN} \rangle$, L_{MODE} and L_{MEAN} due to the image processing is 4 mm or 5% for acetylene and hydrogen and 6 mm or 6% for ethylene. This error corresponds to the '*CCD*' images. For the '*OH*' and '*broad*' images with the ICCD, the error is reduced to approximately half this value from the improved pixel resolution and lens. Note that the attainment of L_{MIN} is invariably associated with more random error than $\langle L_{MIN} \rangle$, L_{MODE} and L_{MEAN}, because it depends on the processing of a single image.

6.8 Chapter 6 Figures

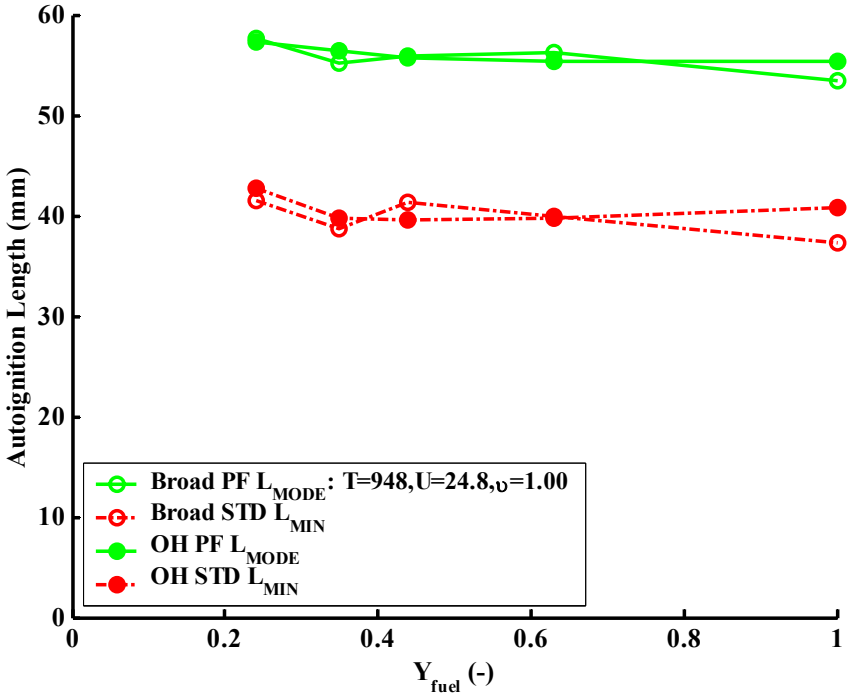

Figure 6.1: Hydrogen lengths: Effect of fuel dilution for equal velocity. '*OH*' denotes long exposure (1 – 5 ms) measurements with the ICCD camera, UV lens and additional OH^* filter. '*Broad*' denotes long exposure (1 – 5 ms) measurements with the ICCD camera, UV lens and no optical filter. L_{MIN} and L_{MODE} for constant T_{air}, U_{air} and υ_{fuel}.

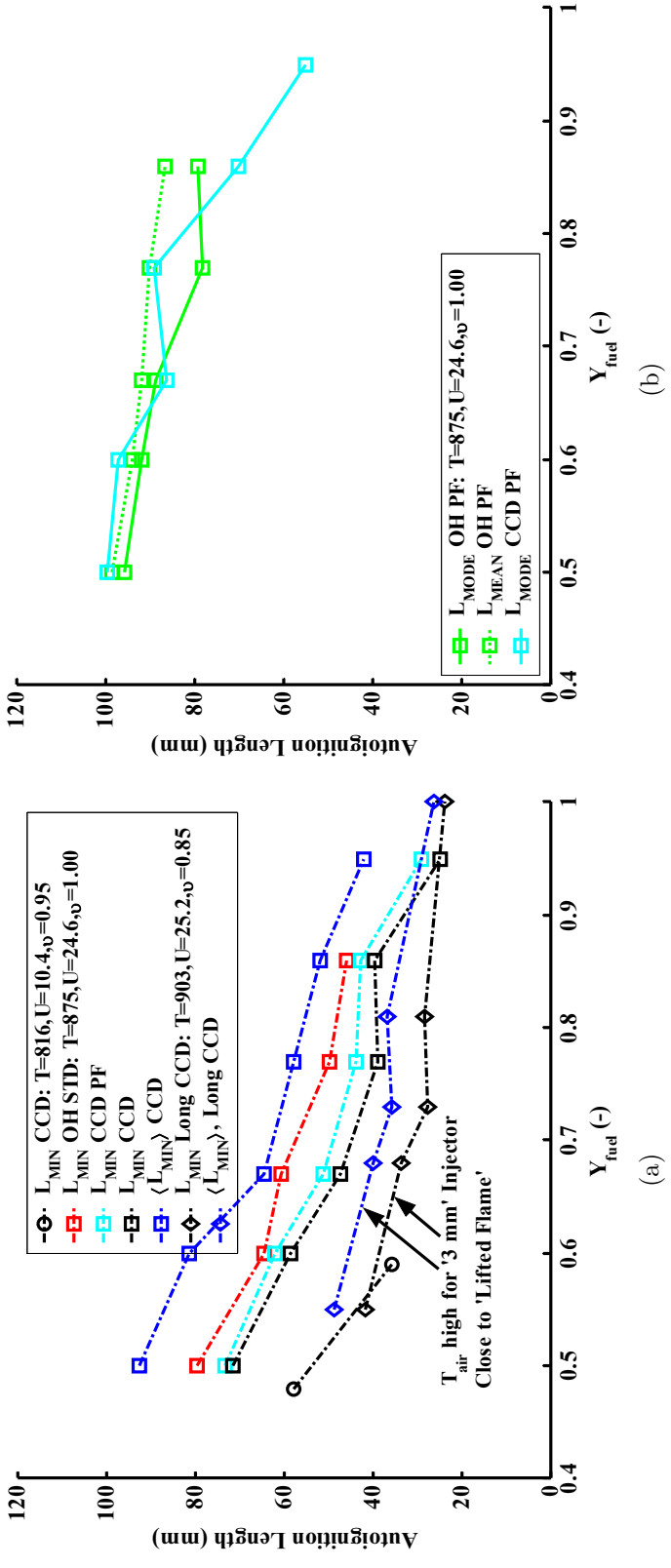

Figure 6.2: Acetylene lengths: Effect of fuel dilution for equal velocity. '*OH*' denotes long exposure (1 – 80 ms) measurements with the ICCD camera, UV lens and additional OH^* filter. Except were specifically stated, '*CCD*' denotes short exposure (0.25 ms) images taken with the un-intensified CCD camera and by considering the 'blue' intensity component only. (a) L_{MIN} and $\langle L_{MIN} \rangle$ as a function of Y_{fuel} for three sets of constant T_{air}, U_{air} and v_{fuel} conditions. Long exposure: $t_{EXP} = 250$ ms. (b) L_{MODE} and L_{MEAN} as a function of Y_{fuel} for constant T_{air}, U_{air} and v_{fuel}. Conditions corresponding to red/cyan/black lines and square markers in (a) with $T_{air} = 875$ K, $U_{air} = 24.6$ m/s and $v_{fuel} = 1.00$.

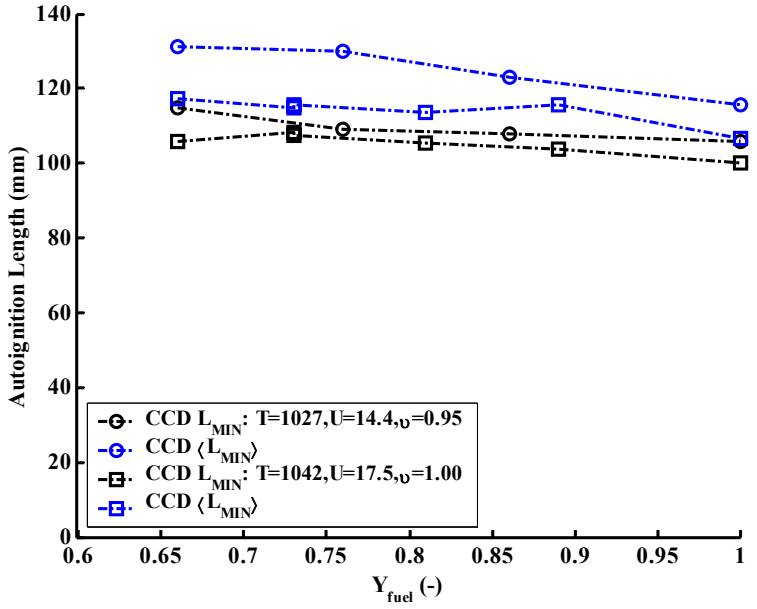

(a)

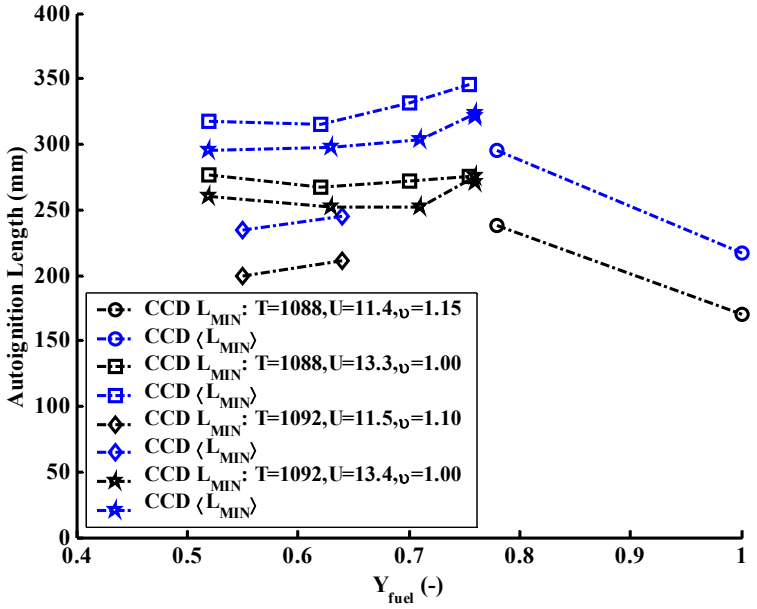

(b)

Figure 6.3: Ethylene and n-Heptane lengths: Effect of fuel dilution for equal velocity. '*CCD*' denotes long exposure (250 ms for both fuels) images taken with the unintensified CCD camera and by considering the 'blue' intensity component only. (a) Ethylene. L_{MIN} and $\langle L_{MIN} \rangle$ as a function of Y_{fuel} for two sets of constant T_{air}, U_{air} and υ_{fuel} conditions. (b) n-Heptane. L_{MIN} and $\langle L_{MIN} \rangle$ as a function of Y_{fuel} for four sets of constant T_{air}, U_{air} and υ_{fuel} conditions.

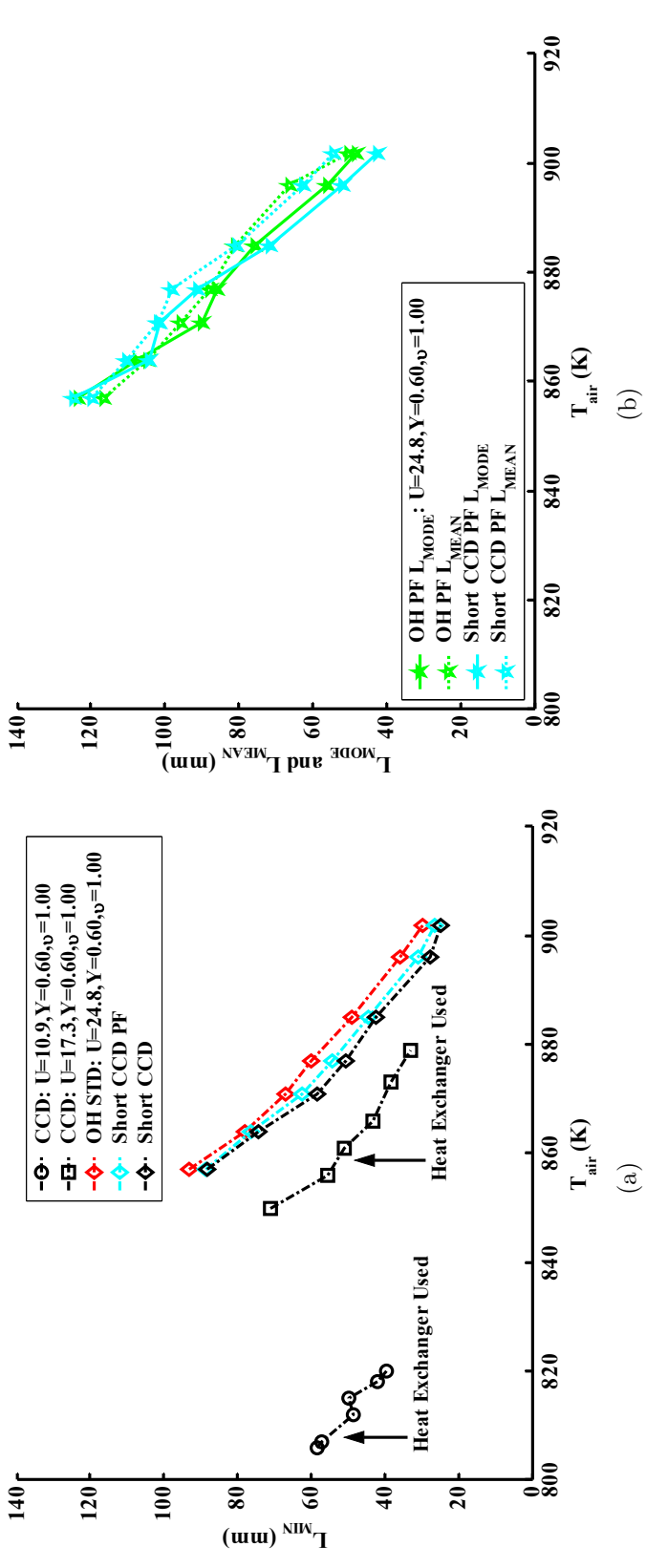

Figure 6.4: Acetylene lengths: Effect of air temperature for equal velocity. *'OH'* denotes long exposure (1 – 80 ms) measurements with the ICCD camera, UV lens and additional OH^* filter. Except were specifically stated, *'CCD'* denotes long exposure (250 ms) images taken with the un-intensified CCD camera and by considering the 'blue' intensity component only. (a) L_{MIN} as a function of T_{air} for three sets of constant U_{air}, Y_{fuel} and v_{fuel} conditions. Short exposure: $t_{EXP} = 0.25$ ms. (b) L_{MODE} and L_{MEAN} as a function of T_{air} for constant U_{air}, Y_{fuel} and v_{fuel}. Conditions corresponding to red/cyan/black lines and diamond markers in (a) with $U_{air} = 24.8$ m/s, $Y_{fuel} = 0.60$ and $v_{fuel} = 1.00$.

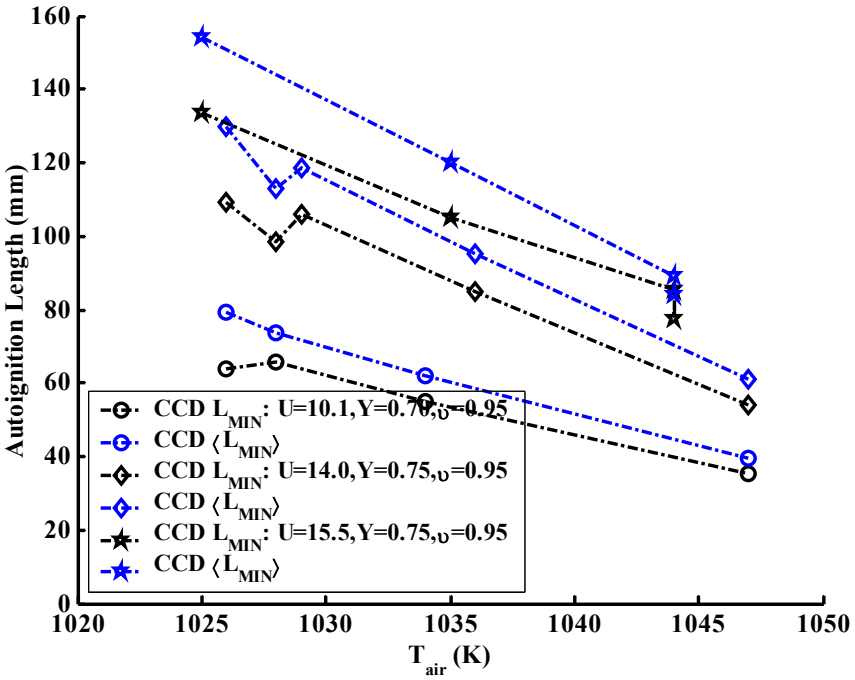

Figure 6.5: Ethylene lengths: Effect of air temperature for equal velocity. '*CCD*' denotes long exposure (250 ms) images taken with the un-intensified CCD camera and by considering the 'blue' intensity component only. L_{MIN} and $\langle L_{MIN} \rangle$ as a function of T_{air} for three sets of constant U_{air}, Y_{fuel} and υ_{fuel} conditions.

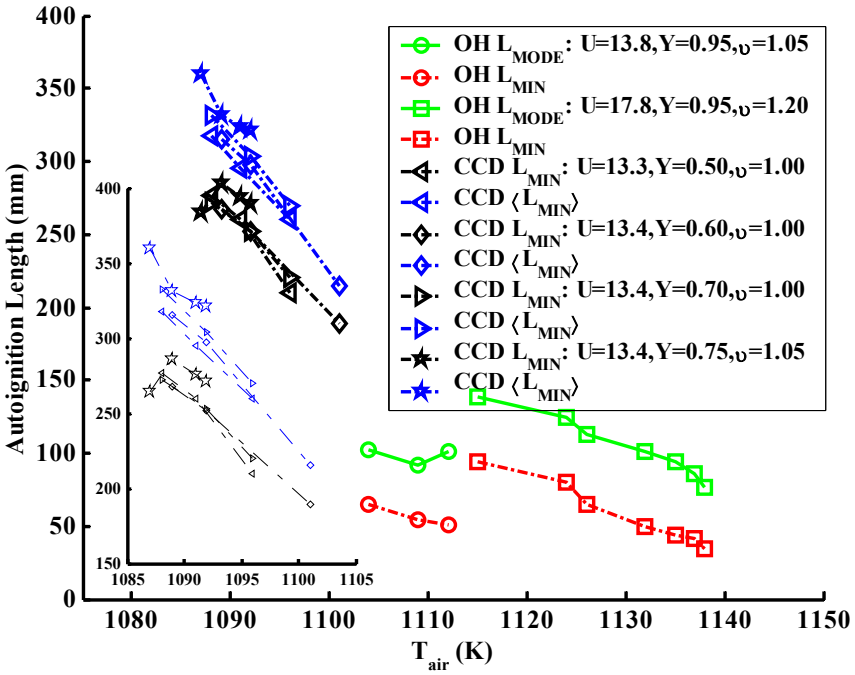

Figure 6.6: n-Heptane lengths: Effect of air temperature for equal velocity. '*OH*' denotes long exposure (5 ms) measurements with the ICCD camera, UV lens and additional OH^* filter. '*CCD*' denotes long exposure (250 ms) images taken with the un-intensified CCD camera and by considering the 'blue' intensity component only. L_{MIN}, $\langle L_{MIN} \rangle$, L_{MODE} and L_{MEAN} as a function of T_{air} for six sets of constant U_{air}, Y_{fuel} and υ_{fuel} conditions.

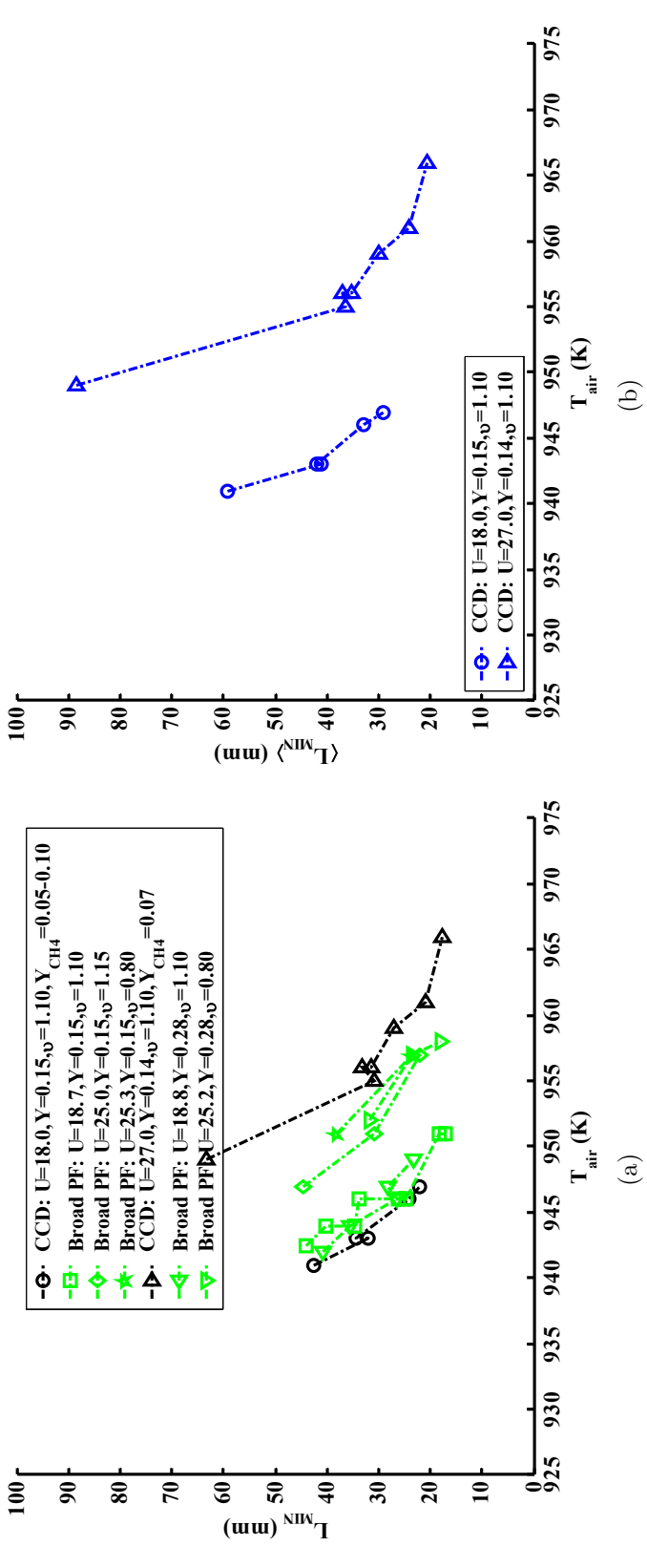

Figure 6.7: Hydrogen lengths: Effect of air temperature for equal velocity. '*Broad*' denotes short exposure (0.075 – 0.1 ms) measurements with the ICCD camera, UV lens and no optical filter. '*CCD*' denotes long exposure (250 ms) images taken with the un-intensified CCD camera and by considering the 'blue' intensity component only. For '*CCD*' experiments with hydrogen: $Y_{CH4} = 0.05 - 0.10$. (a) L_{MIN} as a function of T_{air} for seven sets of constant U_{air}, Y_{fuel} and v_{fuel} conditions. (b) $\langle L_{MIN} \rangle$ as a function of T_{fuel} for constant U_{air}, Y_{fuel} and v_{fuel}. Conditions corresponding to black lines in (a).

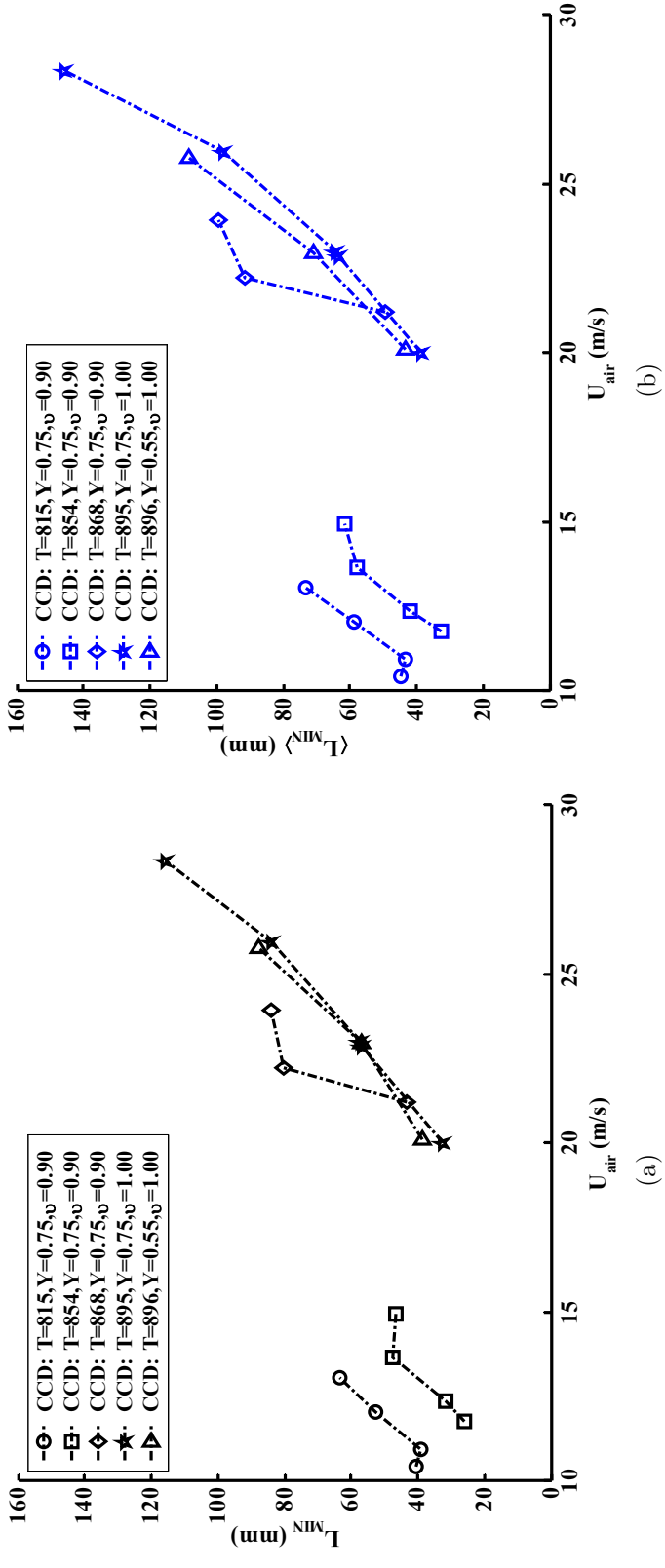

Figure 6.8: Acetylene lengths: Effect of bulk air co-flow velocity for equal velocity. '*CCD*' denotes long exposure (250 ms) images taken with the un-intensified CCD camera and by considering the 'blue' intensity component only. (a) L_{MIN} as a function of U_{air} for five sets of constant T_{air}, Y_{fuel} and v_{fuel} conditions. (b) $\langle L_{MIN} \rangle$ as a function of U_{air} for same five constant sets of T_{air}, Y_{fuel} and v_{fuel} as in (a).

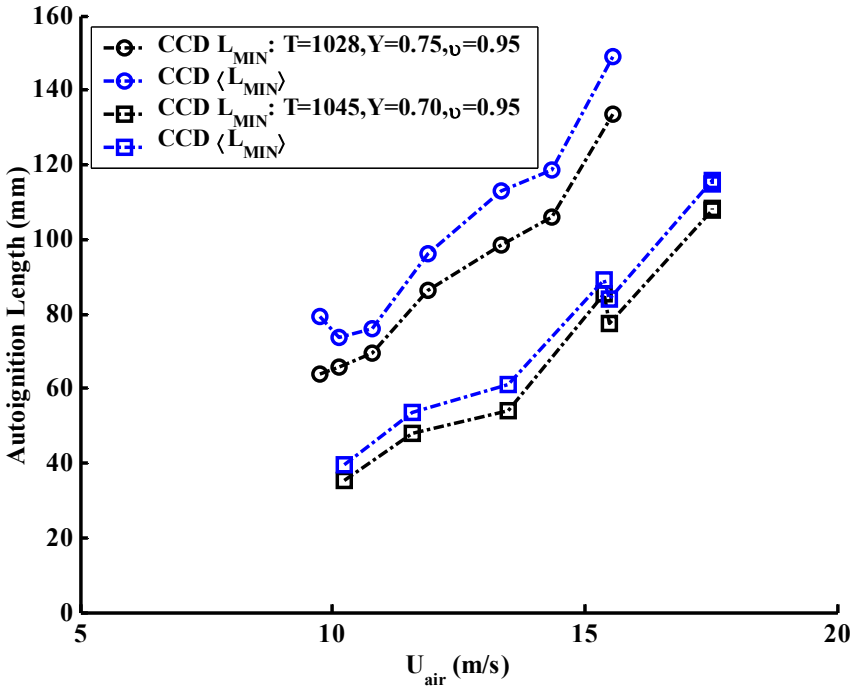

Figure 6.9: Ethylene lengths: Effect of bulk air co-flow velocity for equal velocity. '*CCD*' denotes long exposure (250 ms) images taken with the un-intensified CCD camera and by considering the 'blue' intensity component only. L_{MIN} and $\langle L_{MIN} \rangle$ as a function of U_{air} for two sets of constant T_{air}, Y_{fuel} and υ_{fuel} conditions.

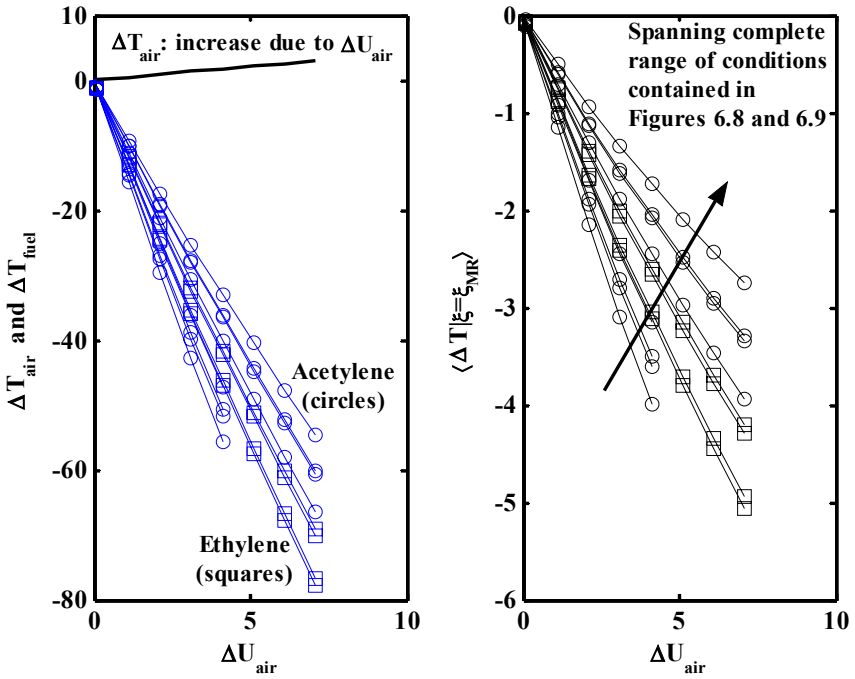

Figure 6.10: Estimation of temperature of most reactive mixture as a function of fuel mass flow. With constant T_{air} and Y_{fuel} conditions, the fuel mass flow changes, so as to keep $U_{fuel} \cong U_{air}$.

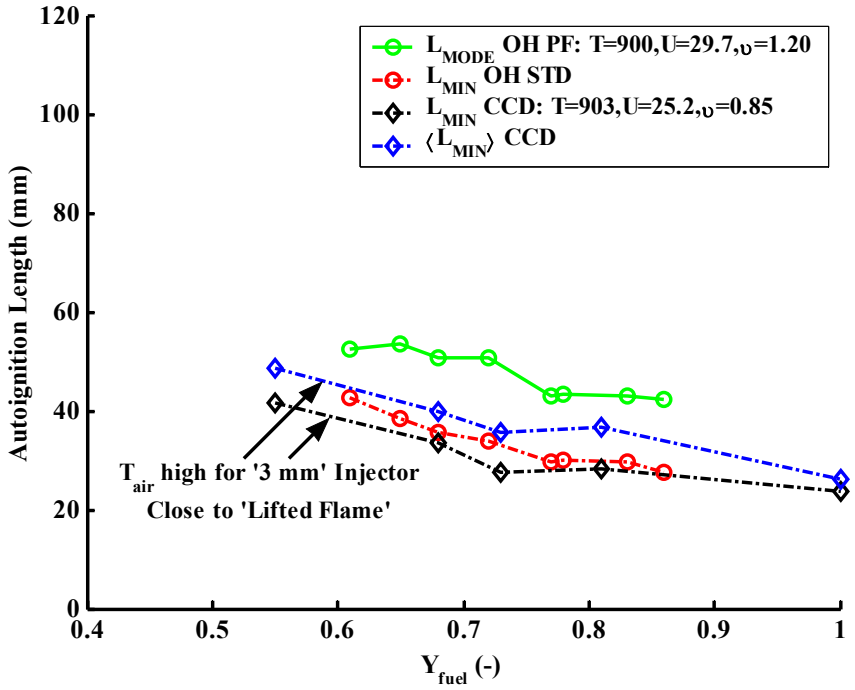

Figure 6.11: Ethylene lengths: Effect of injector size, turbulence and fuel dilution for equal velocity. '*OH*' denotes long exposure (1 – 40 ms) measurements with the ICCD camera, UV lens and additional OH^* filter. L_{MIN} and L_{MODE} as a function of Y_{fuel} for constant T_{air}, U_{air} and υ_{fuel} as given in the legend (green and red lines), with the 1.027 mm small injector. Comparison with *similar* conditions taken with the '3 mm' injector from **Figure 6.2**: black/blue lines and diamond markers with $T_{air} = 903$ K but $U_{air} = 25.2$ m/s and $U_{fuel} = 20.2$ m/s rather than $U_{air} = 29.7$ m/s and $U_{fuel} = 35.6$ m/s as here.

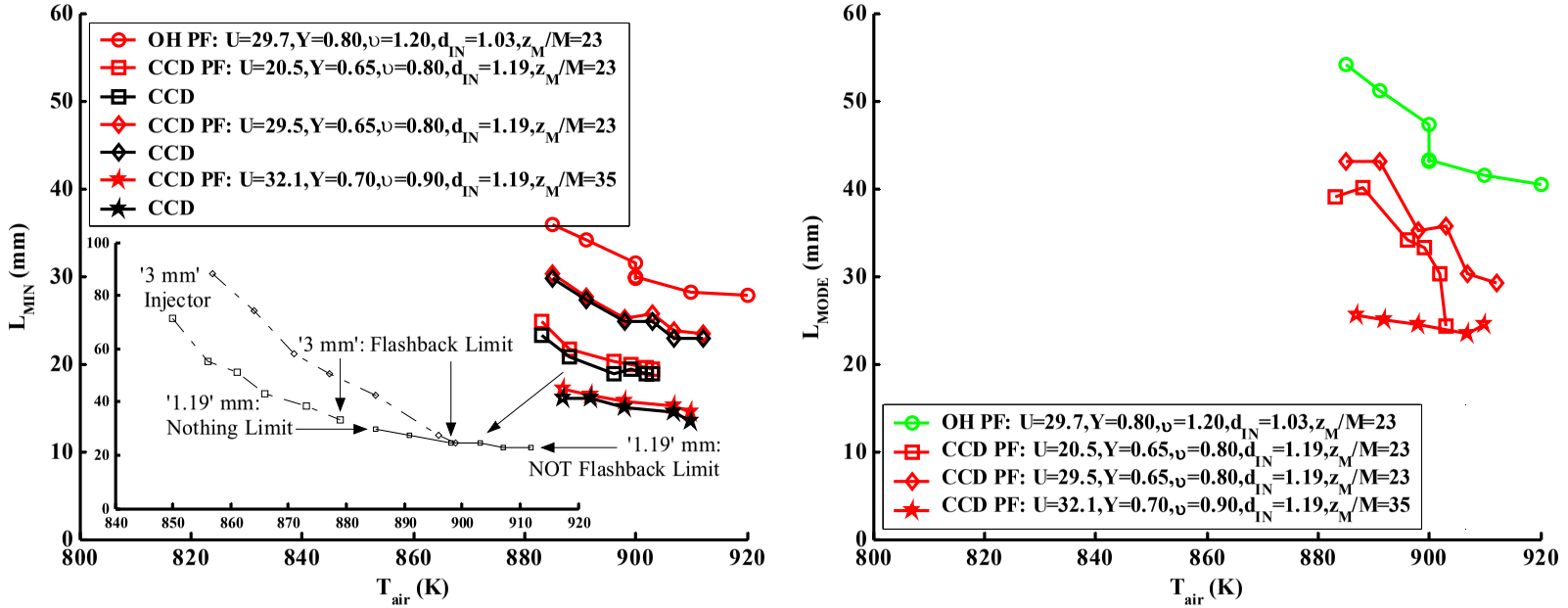

Figure 6.12: Acetylene lengths: Effect of injector size, turbulence and air temperature for equal velocity. '*OH*' denotes long exposure (1 – 40 ms) measurements with the ICCD camera, UV lens and additional OH^* filter. '*CCD*' denotes short exposure (0.25 ms) images taken with the un-intensified CCD camera and by considering the 'blue' intensity component only. (a) L_{MIN} as a function of T_{air} for four sets of constant U_{air}, Y_{fuel} and υ_{fuel} conditions. The insert compares the small injector square data points (U_{air} = 20.5 m/s, Y_{fuel} = 0.65, υ_{fuel} = 0.80) with *similar* conditions taken with the '3 mm' injector from **Figure 6.4(a)**: (i) black line and square markers with U_{air} = 17.3 m/s, Y_{fuel} = 0.60, υ_{fuel} = 1.00, and, (ii) black line and diamond markers with U_{air} = 24.8 m/s, Y_{fuel} = 0.60, υ_{fuel} = 1.00. (b) L_{MODE} as a function of T_{air} for four sets of constant U_{air}, Y_{fuel} and υ_{fuel} conditions, corresponding to those in (a). For both (a) and (b) also showing d_{IN} (mm) and $\frac{z_M}{M}$ (-), where d_{IN} the injector nozzle inner diameter, z_M the axial distance from the grid to the injector nozzle and M the grid hole diameter, all in mm.

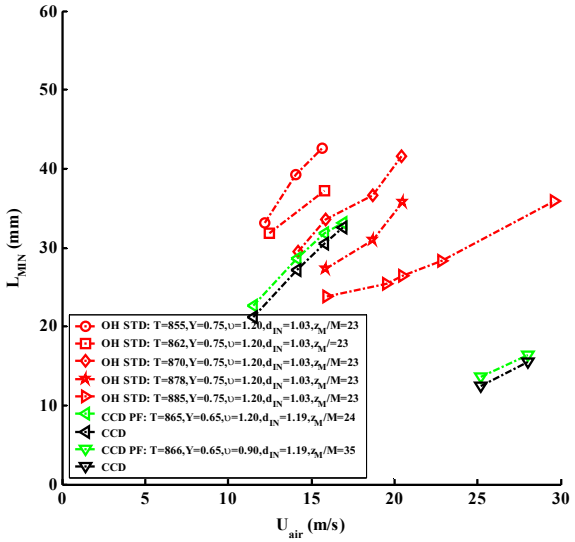

(a)

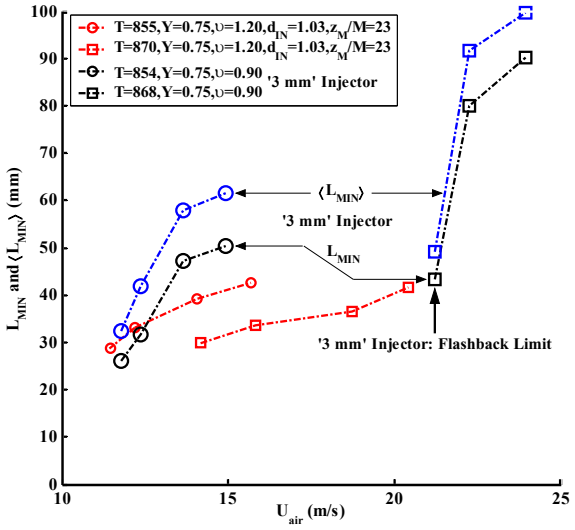

(b)

Figure 6.13: Acetylene lengths: Effect of injector size, turbulence and bulk air co-flow velocity for equal velocity. '*OH*' denotes long exposure (10 – 40 ms) measurements with the ICCD camera, UV lens and additional OH^* filter. '*CCD*' denotes short exposure (0.25 ms) images taken with the un-intensified CCD camera and by considering the 'blue' intensity component only. (a) L_{MIN} as a function of U_{air} for seven sets of constant T_{air}, Y_{fuel} and υ_{fuel} conditions. (b) L_{MIN} and $\langle L_{MIN} \rangle$ as a function of U_{air} for three sets of constant T_{air}, Y_{fuel} and υ_{fuel} conditions. Comparison with *similar* conditions with '3 mm' injector taken from **Figure 6.6**: black/blue lines and larger markers. For both (a) and (b) also showing d_{IN} (mm) and $\frac{z_M}{M}$ (-), where d_{IN} the injector nozzle inner diameter, z_M the axial distance from the grid to the injector nozzle and M the grid hole diameter, all in mm.

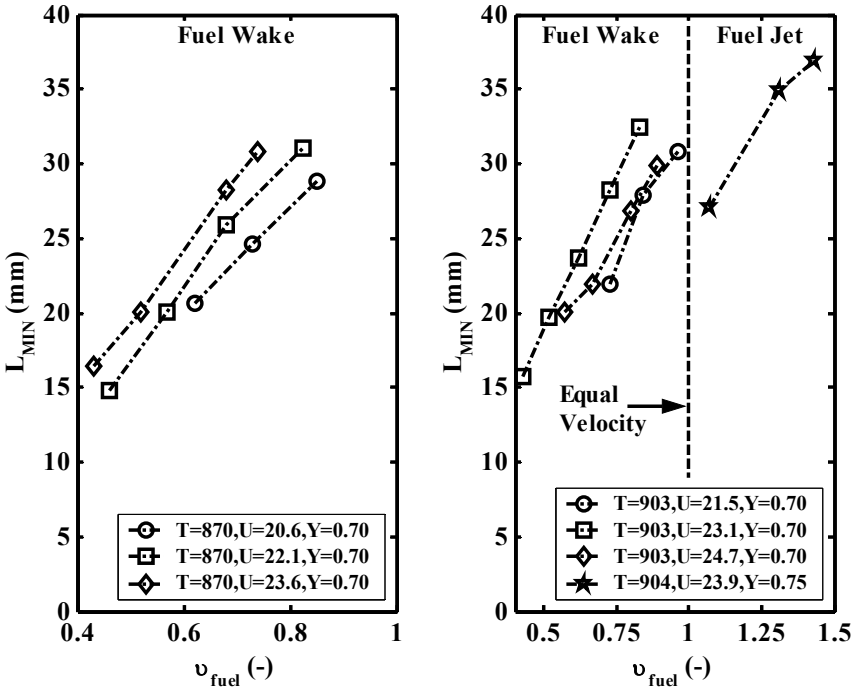

Figure 6.14: Acetylene lengths: Effect of bulk fuel injection velocity. Acetylene wakes and jets. All data from long exposure (50 – 250 ms) images taken with the un-intensified CCD camera. L_{MIN} as a function of υ_{fuel} for seven sets of constant T_{air}, U_{air} and Y_{fuel} conditions, at lower temperature $T_{air} = 870$ K (left) and higher temperature $T_{air} = 903$ – 904 K (right).

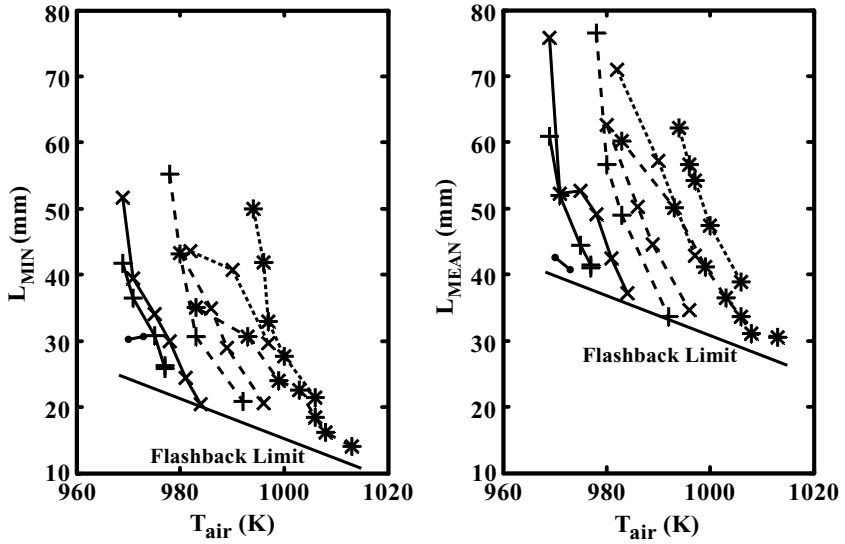

Figure 6.15: Hydrogen lengths: Effect of bulk fuel injection velocity and air temperature. Hydrogen jets. All data from short exposure (0.05 – 0.15 ms) measurements with the ICCD camera, UV lens and additional OH^* filter. L_{MIN} (left) and L_{MEAN} (right) as a function of T_{air} for eight sets of conditions with constant $Y_{fuel} = 0.13$ throughout. Lines for data points with constant U_{air}: solid (20 m/s), dashed (26 m/s) and dotted (32 m/s). Markers for data points with constant U_{fuel}: '•' (40 m/s), '+' (70 m/s), '×' (100 m/s) and '∗' (120 m/s).

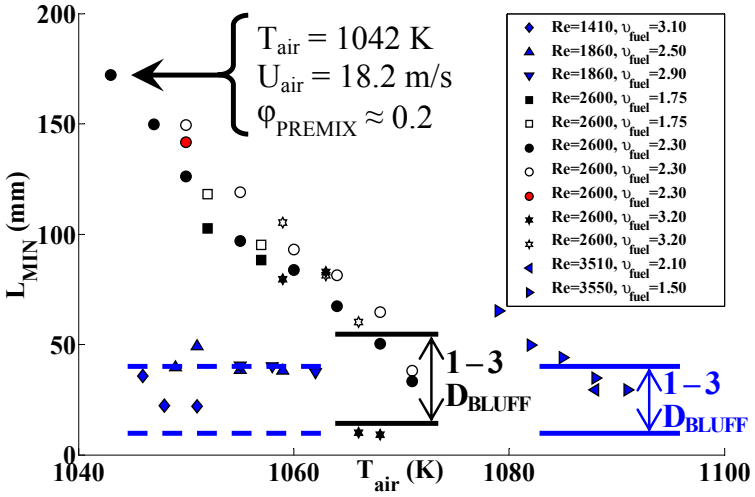

(a)

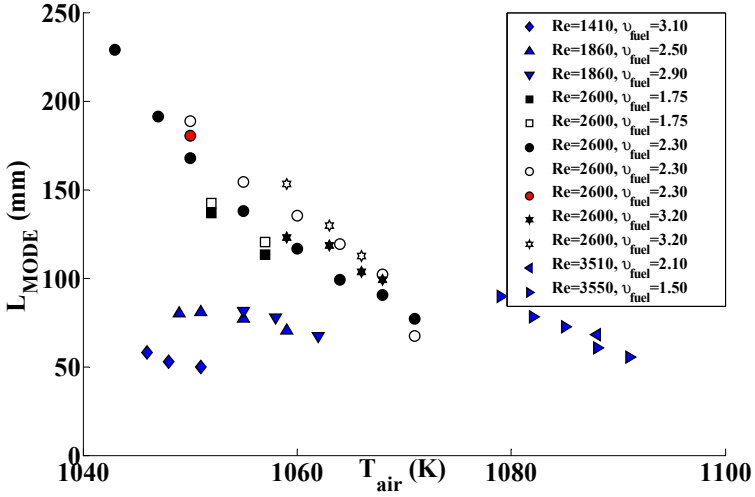

(b)

Figure 6.16: Bluff-Body/Ethylene lengths: Effect of air temperature in CTHAJ. Data from both short (0.5 ms) and long exposure (1 – 8 ms) measurements with the ICCD camera, UV lens and additional OH^* filter. (a) L_{MIN} from STD image as a function of T_{air} for various $\mathcal{R}e_{air}$ and $\upsilon_{fuel} = \frac{U_{fuel}}{Uair}$. Blue symbols are for the smaller tube/bluff-body geometry. Empty and filled symbols are from different runs but for the same conditions to check repeatability. The red symbol is from the PF image corresponding to the same instantaneous sequence. ϕ_{PREMIX} from Cowell and Lefebre [1987] (see discussion in **Section 6.4**). (b) L_{MODE} from the PF image as a function of T_{air} for various conditions. Blue symbols are for the smaller tube/bluff-body geometry. Empty and filled symbols are from different runs but for the same conditions to check repeatability. The red symbol is from the STD image corresponding to the same instantaneous sequence.

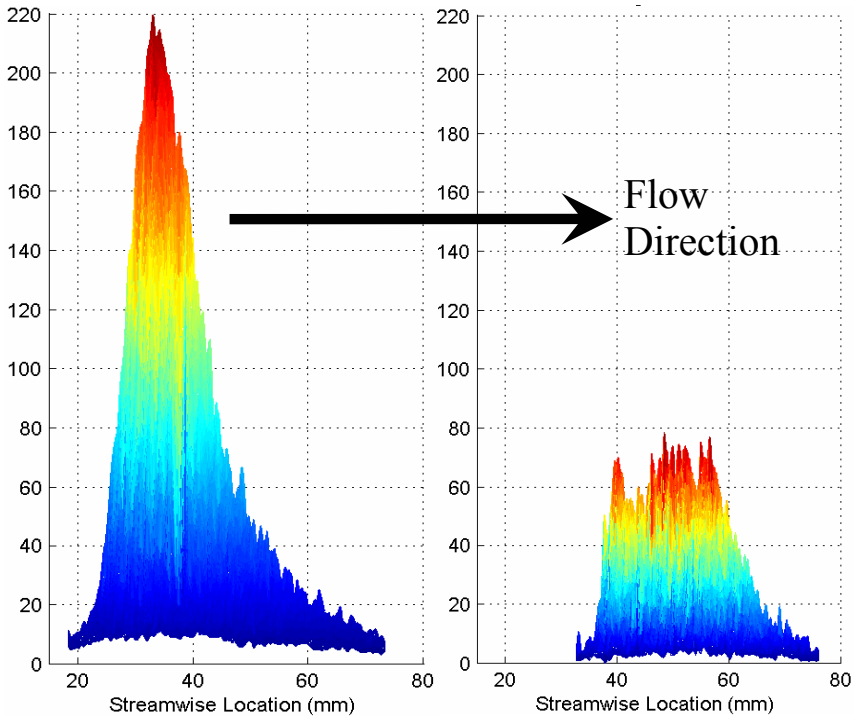

Figure 6.17: Typical two-dimensional (not normalized) PF images viewed from the side, showing tails and relation between L_{MODE} and L_{MEAN} as autoignition (reacting) region moves from relatively short (left) lengths to longer ones (right). Injector to the left.

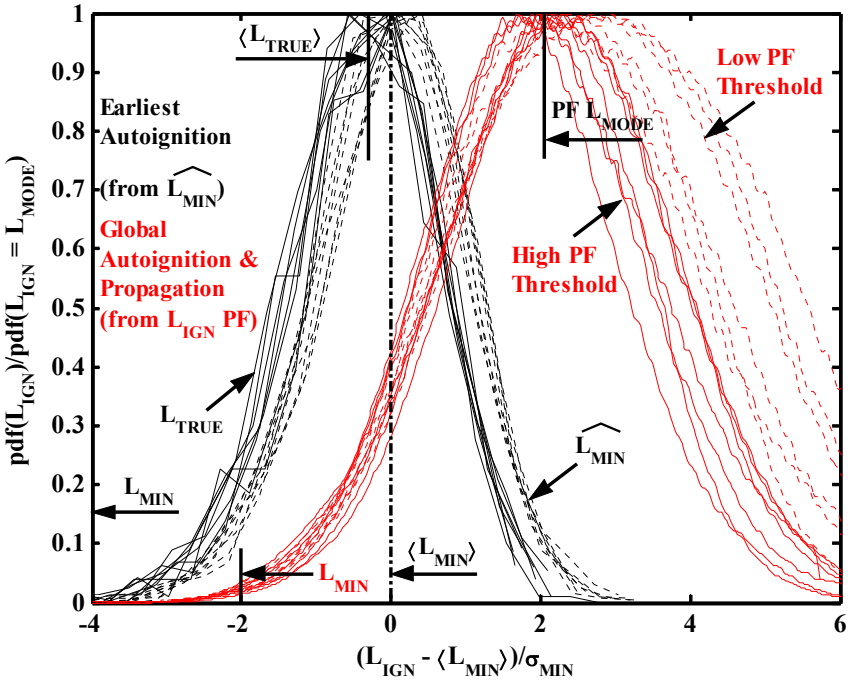

Figure 6.18: Normalized pdfs of true autoignition length and comparison with minimum length measurements of the earliest autoignition regions and measurements of the global autoignition regions from PF images that contain both autoignition and flame propagation. Injector to the left. $\frac{\sigma_{MIN}}{L_{MIN}} \cong 0.10 - 0.15$ over all conditions.

Chapter 7

Results — III: Autoignition Delay Time

7.1 Objectives of Chapter 7

This chapter presents data taken in the CTHC burner, with the '3 mm' and small injectors, that has mostly already been shown in **Chapter 6**. There, autoignition was inspected spatially, which allowed the results to be seen directly in terms of the turbulent mixing fields that had been previously measured in this apparatus.

Measurements of autoignition length, L_{IGN}, were used to estimate corresponding autoignition delay times, τ_{IGN}, by the procedure described in **Section 2.4.3**. For equal velocity data, $\upsilon_{fuel} \cong 1$, a mean residence time from injection to autoignition was estimated based on the bulk air velocity, U_{air}, as $\frac{L_{IGN}}{U_{air}}$. For fuel jets and wakes, the momentum of the jet being injected into the co-flow (and hence ρ_{fuel} and U_{fuel}) was taken into account when calculating a mean residence time along the centerline from **Equation 2.22**. The experimental uncertainty associated with the data in this chapter is exactly the same as that in the data of **Chapter 6**. The additional error introduced by the time delay estimation has been discussed in **Section 2.4.3**.

The current chapter seeks to question the trends of **Chapter 6** in terms of a mean lagrangian 'autoignition delay time'. The effects of the main independent parameters, such as air temperature and velocity, fuel composition and injection velocity on the autoignition delay time results are investigated. The chapter is divided into two main sections. **Section 7.2** deals with measurements taken with the '3 mm' and small injectors for equal velocity in the CTHC. In **Section 7.3** the restriction on the velocities is relaxed and measurements from a variety of wake and jet injected fuel flows are shown and discussed. As with the autoignition length chapter, results are shown for hydrogen, acetylene, ethylene and prevaporized n-heptane, with varying degrees of dilution with excess nitrogen. The chapter closes with a brief overview of the main findings.

7.2 Equal Velocity Kinematic Condition

Experiments with the '3 mm' injector are shown first for the various fuels. The effects of bulk air temperature (**Section 7.2.1**) and bulk air velocity (**Section 7.2.2**) will be investigated. Following this, small injector data will be presented. In **Section 7.2.3** an attempt to understand the effect of changing the injector geometry (through d_{IN}) is made. This section also revisits experimental data taken with the small injector placed at a different (increased) distance from the turbulence generating grid, with emphasis on the effect of the altered turbulence levels (intensity and lengthscales) and mixing quantities (mixture fraction and scalar dissipation).

7.2.1 Effect of Temperature

Figures 7.1 to **7.4** contain all data that is relevant to this section, for: ethylene, n-heptane, acetylene and hydrogen, in this order. The temperatures necessary for a certain autoignition delay time were found to be in the sequence that would

have been required for uniform mixtures. The easiest (in terms of T_{air}) fuel to ignite was acetylene, followed by hydrogen, ethylene and n-heptane (refer to Colket and Spadaccini [2001] for Arrhenius plots of hydrogen, ethylene and n-heptane and Varatharajan and Williams [2001], Wang [1999] for acetylene and a comparison with other hydrocarbons). A qualitative difference with these homogeneous mixtures, that has already been mentioned, was the limited range of temperatures for which 'Random Spots' autoignition is possible; in the low temperate limit due to the onset of the 'No Ignition' regime and at high temperatures because of the propensity for flashback. The range of temperatures and velocities for which 'Random Spots' was possible (in both the 'Nothing–to–Spots' and 'Spots–to–Flame' transition limits) was different for the various fuels. The measured autoignition delay times were inside the range 0.6 – 30 ms and as such, were at least of the order of the outer turbulent timescale of the flow, that was estimated as varying between 0.6 and 4 ms.

The data is presented in the form of Arrhenius plots, with the natural logarithm of the measure of autoignition delay time, $\ln(\tau_{IGN})^*$, plotted against an inverse temperature, $\frac{1000}{T_{air}}$, such that the gradient is proportional (by a factor of 1,000) to an 'equivalent activation temperature', T_{act}. Arrhenius plots are commonplace in homogeneous chemistry studies (including studies of autoignition/oxidation) because complex chemistry reveals itself in the form of deviations from straight lines on these plots and thus, an inability to define a single T_{act}. It is stressed that in choosing this form of data presentation here, it has *not* been implied (indeed a major conclusion from this work is directly opposed to such an interpretation) that the phenomena can be understood and predicted in terms of chemistry *alone*.

Firstly, on inspection of all figures, one notes that the behaviour is non-linear and a single T_{act} cannot be defined. For n-heptane (**Figure 7.2**), acetylene (**Figure 7.3**) and hydrogen (**Figure 7.4**) that span a large enough temperature range, the

*Note that the notation on the vertical axes, denotes the taking of the logarithm of time in units of ms. The logarithmic quantity itself is non-dimensional.

non-linearity is clear, but even in the limited ethylene data (**Figure 7.1**) the possibility exists of a slight deviation from one-step chemistry. Secondly, the nature of the non-linearity itself is different between the hydrocarbons and hydrogen. For the former, the slope (i.e. T_{act}) decreases slightly with decreasing T_{air} (or increasing $\frac{1000}{T_{air}}$; moving towards the right in the plots) and corresponding longer τ_{IGN}, especially when considering τ_{MODE} and τ_{MEAN} for acetylene in **Figures 7.3(b)**. On the other hand, for hydrogen there is a tendency for T_{act} to increase at lower T_{air} and longer τ_{IGN}. Thermal feedback has been shown to be a prerequisite for the autoignition of hydrogen [Kreutz and Law, 1996]. Yet, this conclusion cannot be made with certainty here, because the hydrogen/nitrogen data spans a short temperature range, which cannot be extended due to the limits set by the 'Nothing–to–Spots' and 'Spots–to–Flame' limits, while the hydrogen/nitrogen/methane data is associated with the additional uncertainty introduced by the presence of methane in the fuel stream. Nevertheless, it is apparent that the acceleration of the chemistry at higher temperatures (and shorter τ_{IGN}) observed through the raising of T_{act} with the hydrocarbons is not mirrored for hydrogen.

The crossover temperature, T_c, for hydrogen chemistry is defined as the temperature at which the chain branching and recombination rates are equal and is approximately 925 K at 1 atm from Pellett et al. [2002] and 930 K at 1 atm from Kreutz and Law [1998]. The rate of chain branching reactions for hydrogen chemistry increases with temperature. On the other hand, since the radical recombination steps require a third body, the rate of these reactions decreases with increasing temperature. An example of an elementary recombination reaction for homogeneous mixtures, is the removal of active hydrogen atoms by oxygen molecules in three-body recombination reactions of the type, [Colket and Spadaccini, 2001]:

$$H + O_2 + M \rightleftharpoons HO_2 + M \tag{7.1}$$

As mentioned, the formation of the HO_2 radical is kinetically favoured at lower temperatures and higher pressures. Once formed, HO_2 does not participate in (the necessary for oxidation) chain propagation reactions and so, as the temperature in the experiments increases from T_c to higher temperatures, chain branching will be increasingly allowed to dominate the overall reaction. This would lead to a rapid increase in the reaction rate and an increased ability for explosive oxidation. Hence, this explains the acceleration in the chemistry at temperatures higher than T_c that has been observed by numerous investigators [Bozhenkov et al., 2003, Colket and Spadaccini, 2001, Craig, 1966, Wang et al., 2003]. For the hydrogen experiments in this work, the air temperatures employed were between 940 and 970 K and were thus in the vicinity of the second explosion limit for the hydrogen–air system and higher, but not considerably so, than the crossover temperature.

Returning to the observations of T_{act} concerning all fuels, in the theoretical treatment of inhomogeneous, turbulent autoignition, the concept of a single T_{act} is overly simplistic and is not expected to be capable of capturing the physical processes under investigation, unless the effects of turbulent mixing and complex chemistry are small enough to be neglected. In such a case, linear Arrhenius plots would be observed. The conclusion that can be drawn from the observed non-linear Arrhenius behaviour is that, either:

1. The mixing field, or,
2. Issues of complex chemistry, or,
3. Turbulent mixing and real chemistry interactions

are affecting the phenomenon. From the known conditions (temperature at atmospheric pressure) of the experiments, all hydrocarbon fuels used in these experiments will exhibit linear Arrhenius behaviour. Even n-heptane is not expected to show its well known negative temperature behaviour inside the range of tested conditions, i.e. above 1080 K at 1 atm. N-heptane begins to show non-linearity below

940 K, [Ciezki and Adomeit, 1993, Colket and Spadaccini, 2001, Curran et al., 1998, Fieweger et al., 1994, Held et al., 1997, Horning, 2001, Peters et al., 2002]. Hence, complex chemistry effects are most likely absent from the observed phenomena, at least for the hydrocarbon fuels. This is significant, since a non-linear Arrhenius plot is likely to reveal an effect of turbulent mixing, rather than of complex chemistry. The ability of turbulent mixing to cause non-linearity in Arrhenius plots, even with one-step chemistry, has been demonstrated by Mastorakos et al. [1997b].

The advantage of these measurements over DNS studies for example, is that the latter have limitations in treating the full chemistry at representative Reynolds numbers. Experiments such as these have the advantage of dealing *de facto* with real chemistry and so it was not required to assume at any stage that the effects of complex chemistry are not important. Nevertheless, the author holds the view that the main *trends* in the results contained in this thesis can and should be understood in terms of mixing and *simple* chemistry, and, that there are little to no complex effects of chemistry, at least for the hydrocarbon fuels, that reveal themselves in these experiments. The understanding that they are not, at least in the investigated cases and with the possible exception of hydrogen (see below), has been arrived at *a posteriori* from considerations of the data. This is a significant result in itself.

The observed acceleration of chemistry at the higher temperatures for hydrogen can be explained by one of the following possibilities:

1. Either the hydrogen chemistry is affected by the addition of methane such that at higher temperatures the slow thermal decomposition of methane introduces radicals that cause the recombination reactions to pick up, or,

2. If the presence of methane can be neglected with regards to altering the dominant chemical pathways towards oxidation (and hence autoignition), it is possible that the complex kinetic behaviour of hydrogen is itself responsible, in the manner expected and explained above, or,

3. By the fact that this fuel autoignites closer to the injector than what has been experienced with the hydrocarbons and is hence influenced to a different extent by the turbulence. Note that for all fuels, including hydrogen, above $\ln(\tau_{MIN}) \approx 0.5$ the shape of the Arrhenius plots is actually similar. Looking closely at **Figure 7.4**, it is not unreasonable to deduce that at the observed increase in T_{act} is limited to the highest U_{air} (and hence turbulence levels), and lowest τ_{MIN} (and hence eddy turnover times) when autoignition can be achieved at shorter delay times (below $\ln(\tau_{MIN}) \approx 0.5$) and at higher T_{air}. Above $\ln(\tau_{MIN}) \approx 0.5$ it is difficult to argue for an acceleration of the chemistry, through an increased T_{act}.

In the first two cases, the change in T_{act} is a definite manifestation of an effect of real chemistry. In order to consider the final one in more detail, all τ_{MIN} data for hydrogen, ethylene and n-heptane that have been shown in this section for the temperature dependence of the phenomena are plotted in the form of an inverse Damköhler number, defined as $\mathcal{D}a = \frac{\tau_{turb}}{\tau_{MIN}} = \frac{L_{turb}}{\tau_{MIN} u'_{air}}$ in **Figure 7.5**. The turbulence quantities u'_{air} and L_{turb} were estimated as follows: $u'_{air} \cong 0.14 U_{air}$ for the U_{air} of each data point and $L_{turb} \cong M$. The normalized temperature plotted on the dependent axis in **Figure 7.5(a)** is the inverse of T_{air} shifted *vertically only* so that lines containing data of similar U_{air}, Y_{fuel} and υ_{fuel} pass through zero at unity $\mathcal{D}a$. The values of $\mathcal{D}a_{MIN}$ after this shift are preserved, as are the gradients of any lines of constant U_{air}, Y_{fuel} and υ_{fuel}. In such a figure, homogeneous autoignition delay times would appear as straight lines with constant (but dissimilar for the various fuels and hence different T_{act}) gradient, independent of $\mathcal{D}a$ and proportional to $\frac{1}{T_{act}}$. In **Figure 7.5(b)** an attempt was made to account for the T_{act} of the different fuels. Acetylene data is added to the data already contained in **Figure 7.5(a)** and the dependent variable in now made proportional to $\frac{T_{act}}{T_{air}}$, with data groups of similar U_{air}, Y_{fuel} and υ_{fuel} shifted vertically as before. Hence, the results can be compared across the different fuels, irrespective of their T_{act}, since for any fuel homogeneous autoignition would

result in straight lines with constant (and similar) gradient independent of $\mathcal{D}a$ and T_{act} (choice of fuel).

Note in **Figure 7.5** the order of the chemical timescales with respect to τ_{turb}. At low $\mathcal{D}a_{MIN}$, when the chemical timescales τ_{MIN} are large, the effect of temperature is high, seen by the steeper gradient. It may be said that the effect of mixing here is minimized and the eventual autoignition delay time (which is the same as the chemical time) will be mostly (but not necessarily completely) determined by the chemical temperature dependence. As the chemistry becomes faster, τ_{MIN} decreases and $\mathcal{D}a_{MIN}$ increases. The gradient of the trend-line decreases and the turbulent mixing starts to increasingly affect the outcome. Seen otherwise, the chemical timescale approaches the characteristic eddy turnover time, and the phenomena become increasingly insensitive to changes in temperature and dominated by the mixing, for example by high dissipation at short lengths. This is direct proof of the ability of the turbulence to actively affect the chemistry. The collapse of the gradients of data bands with different U_{air} *after* normalization by the turbulent timescale is interesting and suggests that the T_{act} experienced in the measurements for different fuels and over a wide range of conditions is strongly determined by the kinetic behaviour of each fuel *and* the extent to which this is modified by the turbulent mixing as accounted for by τ_{turb}, and hence $\mathcal{D}a_{MIN}$.

7.2.2 Effect of Air Velocity

The delaying effect of mixing on the chemical timescale of autoignition can also be seen in terms of the increase in τ_{IGN} with all conditions kept constant, but with an increase in U_{air}. It has already been shown that the higher U_{air} flows are associated with higher u'_{air} and $\chi|\xi = \xi_{MR}$. **Figures 7.6** and **7.7** show, for acetylene and ethylene, τ_{MIN} and $\langle\tau_{MIN}\rangle$ data as a function of U_{air}, in lines representing data groups of constant T_{air}, Y_{fuel} and υ_{fuel} (but changing T_{fuel} as discussed previously).

For both fuels an increase in U_{air} causes delayed autoignition. The increase in L_{IGN} reported for the same data in **Figure 6.5** is non-linear and does not collapse to a constant residence time when normalized by the mean velocity. Such a collapse would have been expected for example for a uniform mixture, in which case the effect of turbulence is only important in the form of the fluctuations of temperature, T'_{air}, that are known to be small in these experiments (about 0.08 – 0.10% of T_{air}) and also uncorrelated with the turbulent velocity fluctuations u'_{air}. It is unlikely that the delay evident in **Figures 7.6** and **7.7** can be described through T'_{air}. Then, it seems that the enhanced turbulent mixing at higher U_{air}, with the higher $\chi|\xi = \xi_{MR}$, is causing a real delay in autoignition in terms not only of its location, but also in terms of the residence time (or chemical timescale) until autoignition.

This was not necessarily expected. In DNS studies [Mastorakos et al., 1997a] the increase in u'_{air} caused not only an increase in $\langle\chi|\xi = \xi_{MR}\rangle$, but also an *increase* in the conditional variance $\langle\chi''^2|\xi = \xi_{MR}\rangle$, such that the probability of having instantaneous, low conditional scalar dissipation rates at the most reactive mixture, pdf$(\chi|\xi = \xi_{MR})$, actually minimally *increased*. For this reason the DNS have shown only a weak dependence of τ_{IGN} on u'_{air}, with τ_{IGN} decreasing slightly with increased u'_{air}. In the experiments presented here, the value of the conditional $\langle\chi|\xi = \xi_{MR}\rangle$ has been measured (**Section 3.4.3**) and found to increase at the same physical location, i.e. L_{IGN}, for an increase in U_{air}. It was also found that this quantity increased even when viewed in a lagrangian sense, i.e. for the same τ_{IGN}. Furthermore, as U_{air} increased, the values of pdf$(\chi|\xi = \xi_{MR})$ were found to decrease at low $\chi|\xi = \xi_{MR}$ and increase at high $\chi|\xi = \xi_{MR}$. This completely clarifies the seeming discrepancy between the results obtained here and those from the DNS. In the end, both these experiments and the DNS agree on the basic finding that the effect of turbulence on autoignition can be understood in terms of the history of pdf$(\chi|\xi = \xi_{MR})$, even though due to different initial conditions the observed results concerning the effect of u'_{air} on τ_{IGN} in these studies were dissimilar.

7.2.3 Effect of Injector Size and Turbulence

Figures 7.8 and **7.9** contain the same data as in **Figures 6.12** and **6.13(a)** for experimental runs with the small injector nozzle, during which T_{air} and U_{air} were varied respectively, but with all other variables kept approximately unchanged. As an aside, it is noted that in the small injector experiments the changes in T_{fuel} as U_{fuel} was varied (along with U_{air}) were lower than what was experienced with the larger injector, because of the reduced mass flows through the injector that kept T_{fuel} consistently closer to T_{air}. This is not expected to affect the main conclusions, for the same reason as before; the conditional temperature of the most reactive mixture is little affected by T_{fuel} and mostly determined by T_{air}, which is kept approximately constant. In the plots here, the data is presented in terms of τ_{MIN}. Consider first the results for $\frac{z_M}{M} = 23$ and 24.

Figure 7.8 is an Arrhenius plot for acetylene with the small injector, similar to **Figure 7.3** for the same fuel with the '3 mm' injector. It can be seen that τ_{MIN} is generally shorter than that measured with the '3 mm' injector, and that the slopes are shallower than those in **Figure 7.3**, so that even with the same fuel, T_{act} is lower for this geometry. Again, this is a direct effect of turbulent mixing on the chemistry. There exists a trend for $\ln(\tau_{MIN})$ (and consequently τ_{MIN}) to increase with decreasing T_{air} (or increasing $\frac{1000}{T_{air}}$), with possible, but small, deviations from straight line behaviour.

Figures 7.9(a) and **7.9(b)** contain plots of τ_{MIN} and τ_{MODE} respectively as functions of U_{air}, similar to **Figure 7.6** for acetylene in the '3 mm' injector. The trends are qualitatively different to those observed in **Figure 7.6**, with τ_{MIN} remaining approximately constant and independent from U_{air} and τ_{MODE} showing a small decrease with increasing U_{air}. These results are unusual in the light of the aforementioned result for τ_{IGN} to increase with U_{air} in the larger injector. An attempt to explain this outcome is given below.

It is known from the mixture fraction measurements that with the small injector $\langle\chi|\xi = \xi_{MR}\rangle$ is initially higher, but decays faster with axial distance from injection, quickly reaching lower values than those obtained with the '3 mm' injector. If a critical value of dissipation controls the ability to autoignite, we would expect the earliest extent of the range of possible L_{IGN} with the small injector to shift to shorter lengths. The maximum extent of the range of possible L_{IGN} is not determined by heat losses, since with higher temperatures compared to the '3 mm' injector, the small injector still results in shorter global autoignition regions. However, it must be determined by the fact that regions with finite pdf($\xi = \xi_{MR}$), or 'significant' presence of most reactive mixture, and within which it is reasonable to expect 'inhomogeneous phase' autoignition, will shift to shorter lengths with the small injector. This reasoning might explain the shorter autoignition lengths, delay times and global autoignition regions observed with the small injector nozzle. Furthermore, the existence of initially higher $\langle\chi|\xi = \xi_{MR}\rangle$ might explain the higher T_{air} required for autoignition in the small injector. Now assume that due to the initially higher $\langle\chi|\xi = \xi_{MR}\rangle$ autoignition occurs far downstream within the region of finite pdf($\xi = \xi_{MR}$). There, the distance from the injector is longest, the residence time is maximized and the local $\langle\chi|\xi = \xi_{MR}\rangle$ is reduced. In this scenario, an increase in U_{air} would not change the mean mixing field, but would increase $\langle\chi|\xi = \xi_{MR}\rangle$ and push the L_{IGN} even further downstream. Indeed, it was observed that higher U_{air} resulted in L_{IGN} being slowly displaced downstream. The manner in which L_{IGN} increases can also be understood by realizing that due to the fast decay of $\langle\chi|\xi = \xi_{MR}\rangle$ and autoignition far downstream within the region of presence of ξ_{MR}, turbulent mixing would have little time and space to affect the chemistry, resulting in vigorous mixing early on with little influence on the eventual locations of autoignition downstream, which would then be affected mostly by the chemistry (as long as the presence of finite ξ_{MR} can be guaranteed). Then, it would be expected for L_{IGN} to increase, but for τ_{IGN} to remain approximately constant, as U_{air} increases.

The effect of the injecting farther away from the grid can be seen with the $\frac{z_M}{M} = 35$ data in **Figures 7.8** and **7.9**. The autoignition delay time is considerably shorter than before, by a factor of 4 – 5 in τ_{MIN} and 3 – 4 in τ_{MODE}, but the insensitivity to U_{air} is again apparent. This is in line with the discussion in the previous paragraph because the regions of presence of finite most reactive mixture should be closer to the injector for $\frac{z_M}{M} = 35$.

7.3 Fuel Jet and Wake Flows

Figure 7.10 shows the effect of changing υ_{fuel} while keeping all other variables constant, with the exception of T_{fuel}. The data is for acetylene in the CTHC with a '3 mm' injector, reproduced from **Figure 6.14**, but plotted in terms of τ_{MIN}. This variable spans the range of about 1.1 – 1.6 ms in this data. For all sets of conditions and both for wakes and jet flows, once finds that autoignition is delayed by an increase in υ_{fuel}. The residence time until autoignition takes into account the decay in the centreline velocity. The observation that this has not collapsed the data, points towards the fact that as υ_{fuel} is increased, turbulent mixing is enhanced. As before with U_{air}, this in turn delays autoignition.

Hydrogen jet flows were more extensively tested for a range of conditions that have already been presented in **Figure 6.15** and discussed in **Section 6.3**. In **Figure 7.11** each line contains a set of data points with the same U_{air}, Y_{fuel} and υ_{fuel} and changing T_{air}. Each type of line (solid, dashed, etc.) corresponds to a particular U_{air} and the symbols used to a particular U_{fuel}. It can be seen that τ_{MIN} varies by an order of magnitude from about 0.15 – 1.5 ms and is of the order of the turbulent timescale. After plotting τ_{MIN} as calculated from L_{MIN}, U_{air}, U_{fuel} and ρ_{fuel} it becomes apparent that the data seems to collapse approximately in bands of constant U_{air}. The bands of different U_{air} clearly do not collapse and again it can be said that the phenomena cannot be simply kinetically controlled,

but that the turbulence and mixing are playing an active role in determining the location of autoignition. The fact that for the same T_{air} a higher U_{air} results in delayed autoignition reveals a delaying effect of the turbulent air stream on the phenomenon, consistent with Blouch and Law [2003].

7.4 Conclusions from Chapter 7

For autoignition in the 'Random Spots' regime with the CTHC burner:

- The measured τ_{IGN} were in the range 0.6 – 30 ms and as such were at least of the order of τ_{turb}. Arrhenius plots of τ_{IGN} are non-linear and a single T_{act} cannot be defined, revealing an effect of turbulent mixing rather than of complex chemistry. For the hydrocarbons, T_{act} decreases with decreasing T_{air}, whereas for hydrogen there is a tendency for T_{act} to decrease at shorter τ_{IGN} and higher T_{air}. This difference can perhaps be explained by the magnitude of τ_{IGN} relative to τ_{turb}. When $\tau_{IGN} \gg \tau_{turb}$ the effect of temperature is significant and the effect of mixing is minimized. Hence, the eventual autoignition delay time (which is the same as the chemical time) will be mostly determined by the chemical temperature dependence. As τ_{IGN} becomes of the order of τ_{turb} the mixing starts to increasingly affect (delay) the phenomenon.

- The increase in L_{IGN} that was noted in **Chapter 6** was *not* successfully collapsed by the increased U_{air} when obtaining τ_{IGN}. In other words, an increase in U_{air} caused a delay in autoignition (increased τ_{IGN}) that cannot be explained by considerations of a homogeneous autoignition delay time, but only through the increase in $\chi|\xi = \xi_{MR}$.

- For injection from smaller injectors, τ_{IGN} decreased and became less sensitive to changes in T_{air} and U_{air}. Similar conclusions were reached for injection farther away from the grid. The effect of increasing υ_{fuel} was to delay τ_{IGN}.

7.5 Chapter 7 Figures

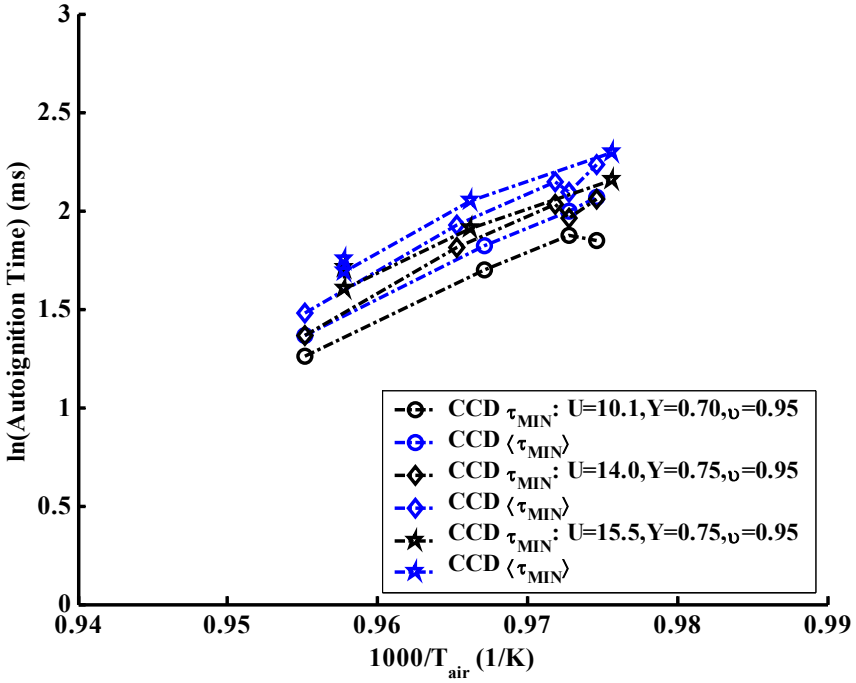

Figure 7.1: Ethylene delay times: Effect of air temperature for equal velocity. Time data corresponds exactly to lengths in **Figure 6.5**. Natural logarithm of τ_{MIN} and $\langle\tau_{MIN}\rangle$ (in ms) as a function of $\frac{1000}{T_{air}}$ for constant U_{air}, Y_{fuel} and υ_{fuel}.

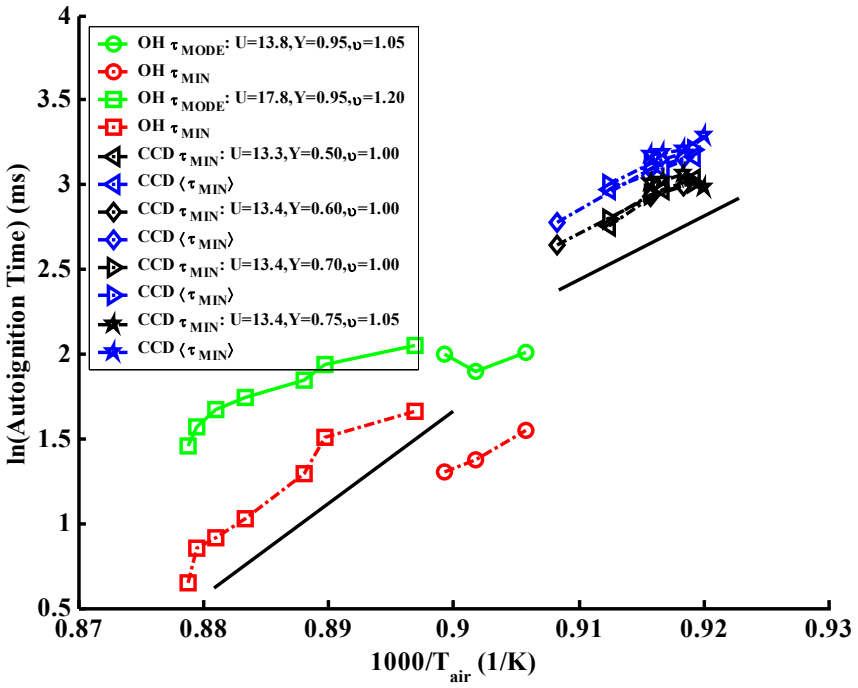

Figure 7.2: n-Heptane delay times: Effect of air temperature for equal velocity. Natural logarithm of τ_{MIN} and $\langle\tau_{MIN}\rangle$ (in ms) as a function of $\frac{1000}{T_{air}}$ for constant U_{air}, Y_{fuel} and υ_{fuel}. Time data corresponds exactly to lengths in **Figure 6.6**. Showing linear fits for τ_{MIN} (black and red).

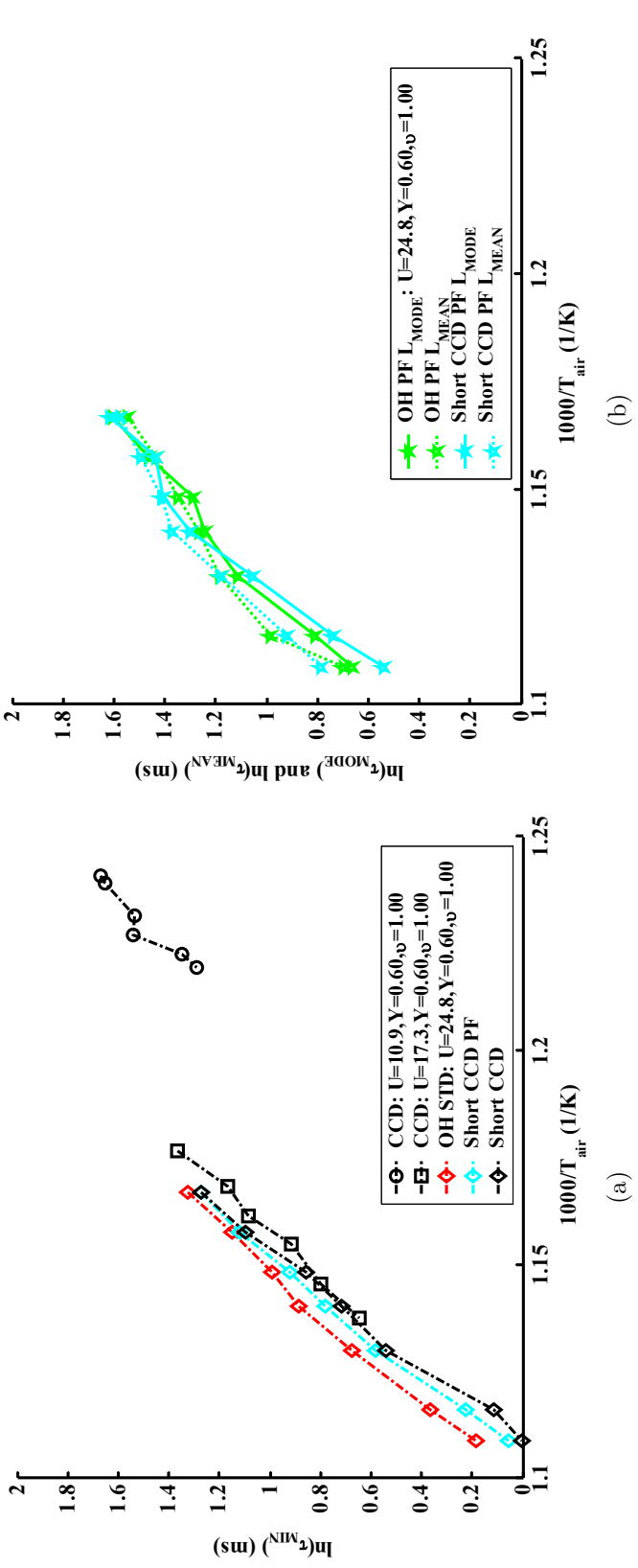

Figure 7.3: Acetylene delay times: Effect of air temperature for equal velocity. Time data corresponds exactly to lengths in **Figure 6.4**. (a) Natural logarithm of τ_{MIN} (in ms) as a function of $\frac{1000}{T_{air}}$ for constant U_{air}, Y_{fuel} and v_{fuel}. (b) Natural logarithm of τ_{MODE} (in ms) as a function of $\frac{1000}{T_{air}}$ for selected data in (a).

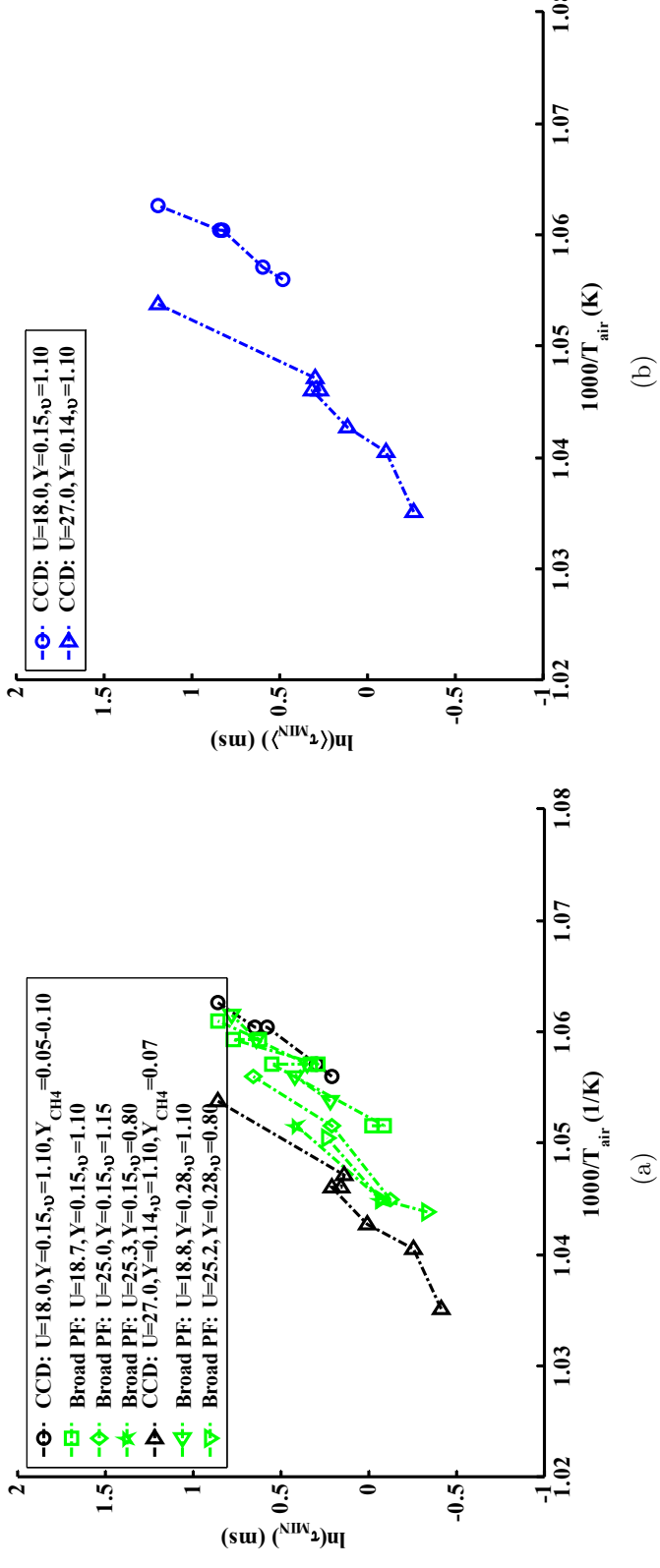

Figure 7.4: Hydrogen delay times: Effect of air temperature for equal velocity. Time data corresponds exactly to lengths in **Figure 6.7**. (a) Natural logarithm of τ_{MIN} (in ms) as a function of $\frac{1000}{T_{air}}$ for constant U_{air}, Y_{fuel} and v_{fuel}. (b) Natural logarithm of $\langle \tau_{MIN} \rangle$ (in ms) as a function of $\frac{1000}{T_{air}}$ for constant U_{air}, Y_{fuel} and v_{fuel}.

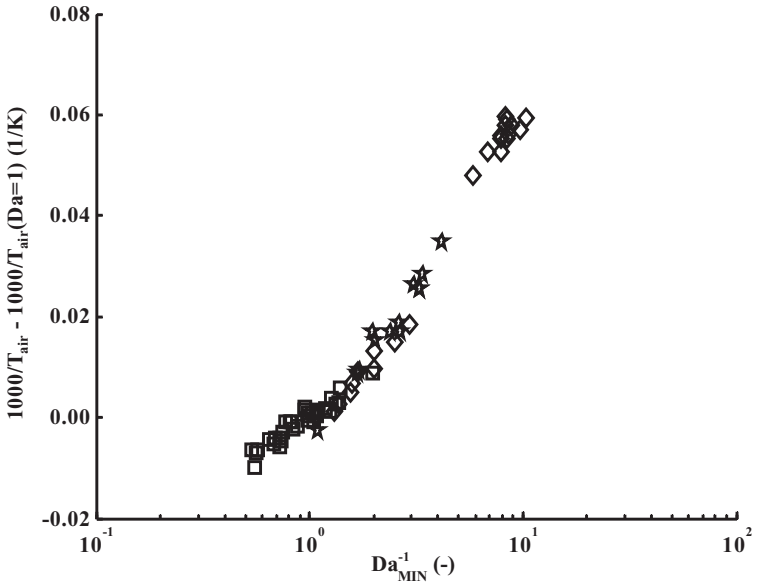

(a)

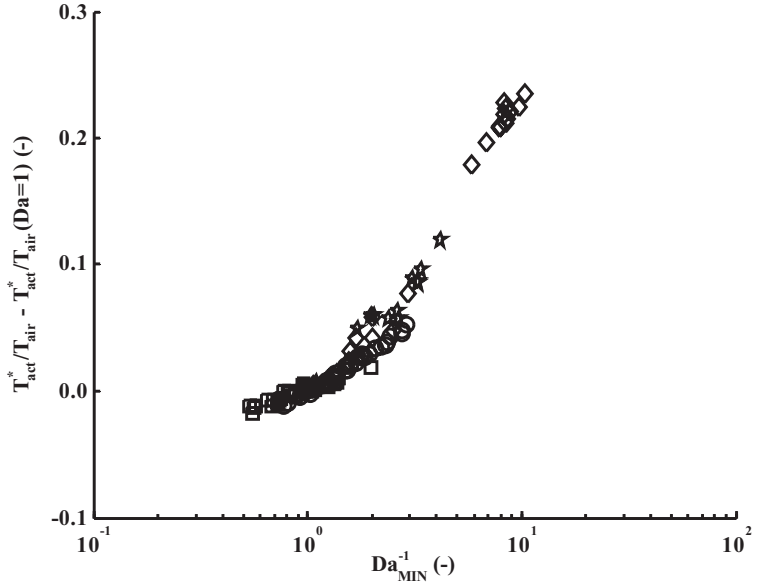

(b)

Figure 7.5: Damköhler plots for all fuels in '3 mm' injector CTHC apparatus as a function of normalized air temperature. $\mathcal{D}a$ is defined as τ_{turb} over τ_{MIN}. (a) $\mathcal{D}a^{-1}$ against $\frac{1000}{T_{air}} - \frac{1000}{T_{air}(\mathcal{D}a=0)}$, or the inverse temperature shifted by its value at unity $\mathcal{D}a$. Data points are from all experiments concerning the effect of temperature on τ_{MIN} of hydrogen, ethylene and n-heptane. (b) $\mathcal{D}a^{-1}$ against $\frac{T^*_{act}}{T_{air}} - \frac{T^*_{act}}{T_{air}(\mathcal{D}a=0)}$, the temperature normalized by the activation temperature ($T^*_{act} = 198.72\frac{T_{act}}{1000}$) for the particular fuel, shifted by its value at unity $\mathcal{D}a$. Data points are from all experiments concerning the effect of temperature on τ_{MIN} of all fuels including acetylene.

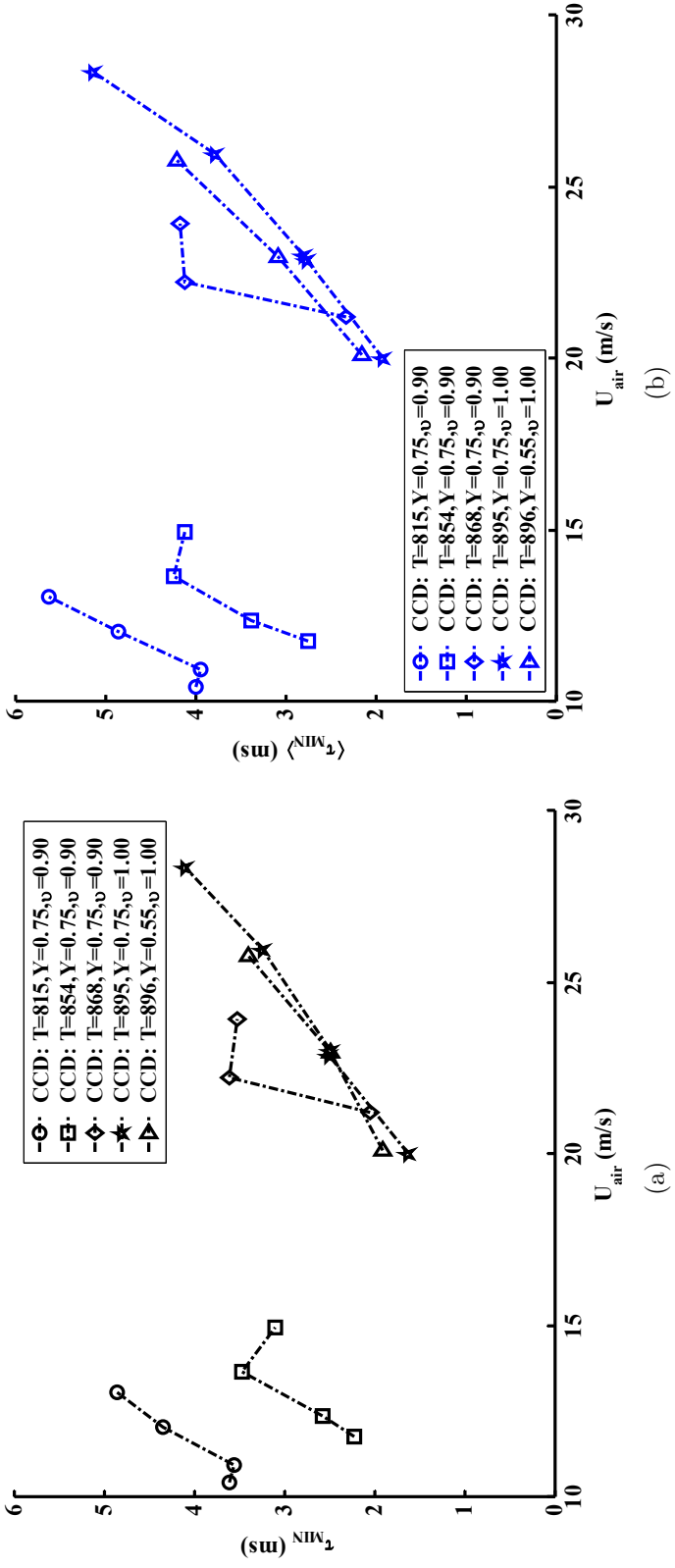

Figure 7.6: Acetylene delay times: Effect of bulk air co-flow velocity for equal velocity. Time data corresponds exactly to lengths in **Figure 6.8**. (a) τ_{MIN} as a function of U_{air} for constant T_{air}, Y_{fuel} and v_{fuel}. (b) $\langle \tau_{MIN} \rangle$ as a function of U_{air} for the same constant T_{air}, Y_{fuel} and v_{fuel}. All conditions corresponding to black lines in (a).

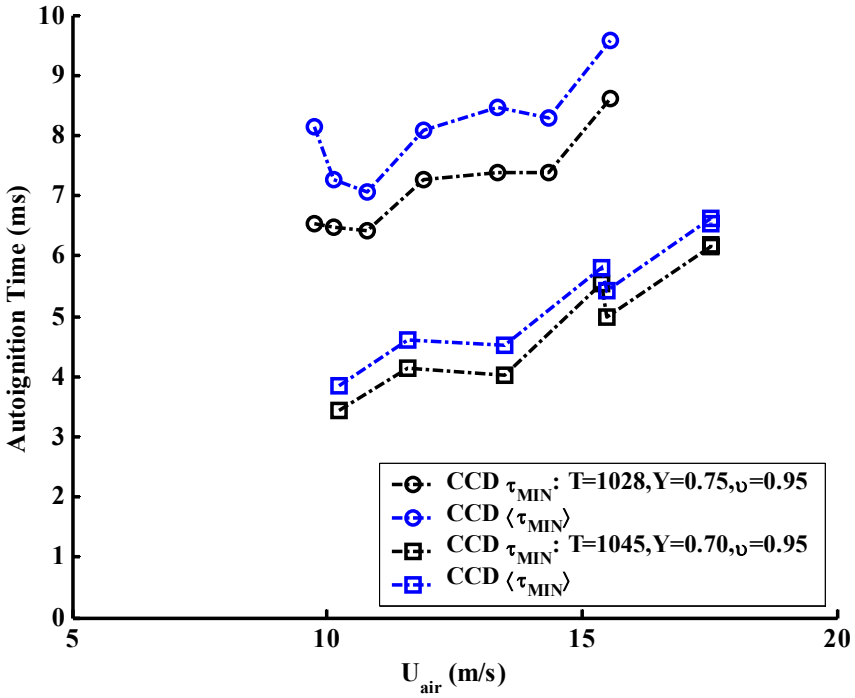

Figure 7.7: Ethylene delay times: Effect of bulk air co-flow velocity for equal velocity. Time data corresponds exactly to lengths in **Figure 6.9**. τ_{MIN} and $\langle\tau_{MIN}\rangle$ as a function of U_{air} for constant T_{air}, Y_{fuel} and υ_{fuel}.

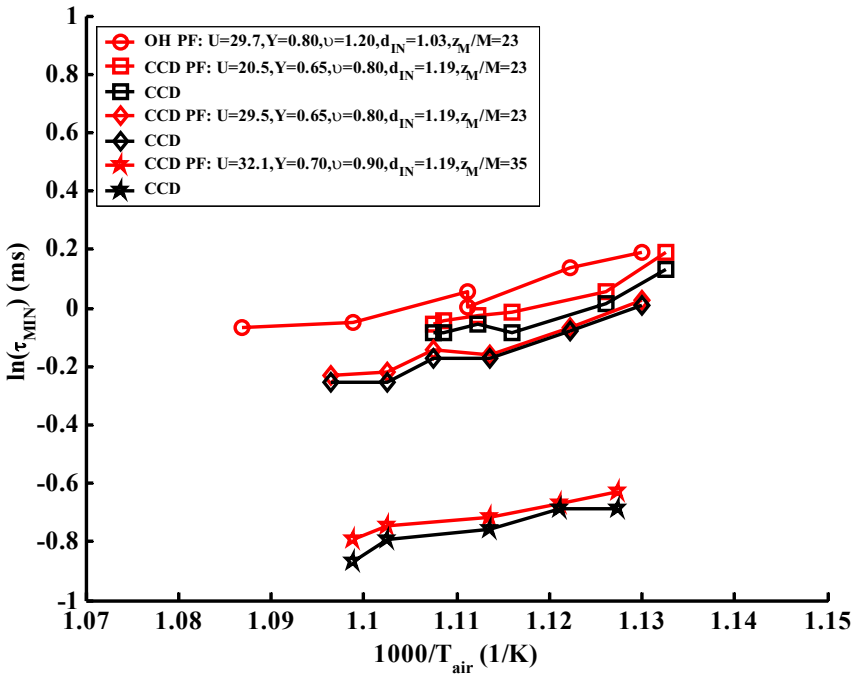

Figure 7.8: Acetylene delay times: Effect of injector size, turbulence and air temperature for equal velocity. Time data corresponds exactly to lengths in **Figure 6.12**. (a) Natural logarithm of τ_{MIN} (in ms) as a function of $\frac{1000}{T_{air}}$ for constant U_{air}, Y_{fuel} and υ_{fuel}. Also showing d_{IN} (mm) and $\frac{z_M}{M}$ (-), where d_{IN} the injector nozzle inner diameter, z_M the axial distance from the grid to the injector nozzle and M the grid hole diameter, all in mm.

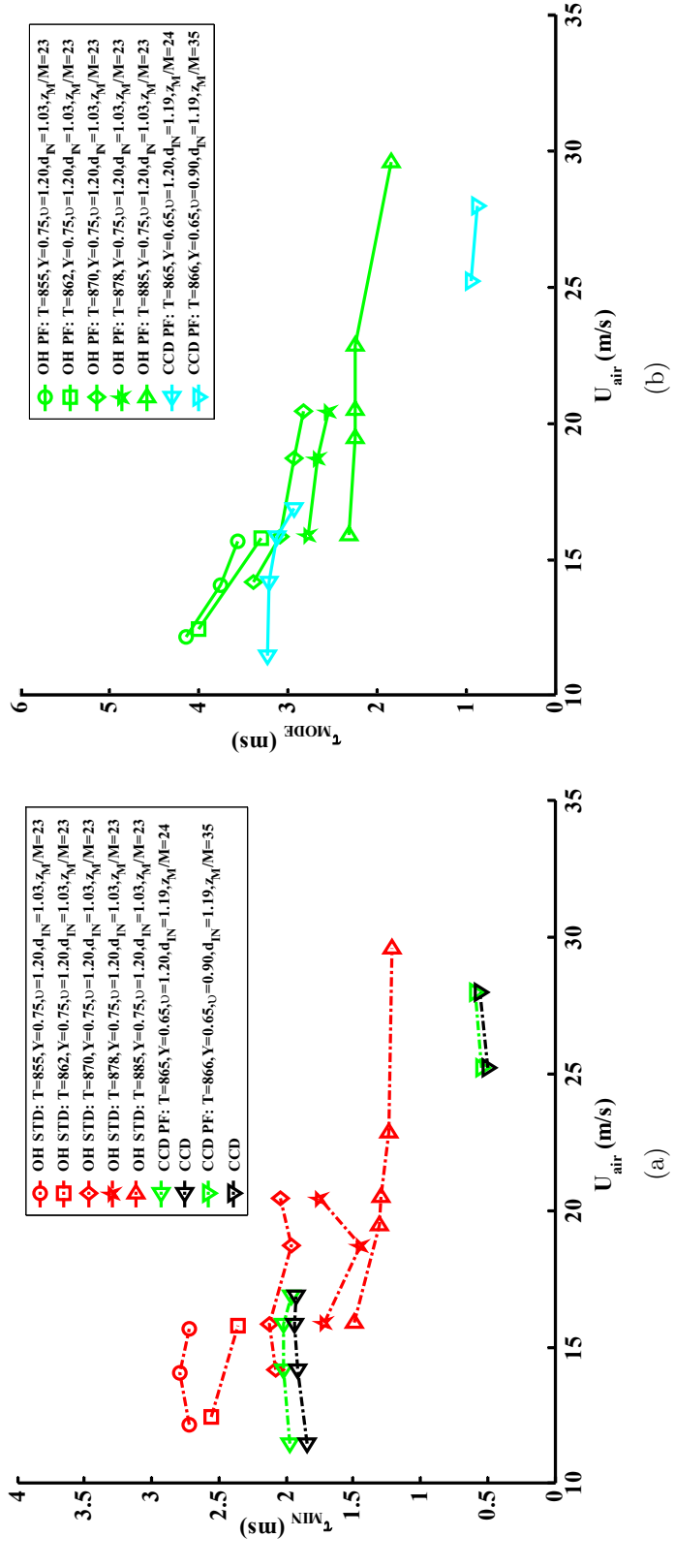

Figure 7.9: Acetylene delay times: Effect of injector size, turbulence and bulk air co-flow velocity for equal velocity. (a) Time data corresponds exactly to lengths in **Figure 6.13(a)**. τ_{MIN} as a function of U_{air} for constant T_{air}, Y_{fuel} and v_{fuel}. (b) Data not presented in **Chapter 6**. L_{MODE} as a function of U_{air} for same constant T_{air}, Y_{fuel} and v_{fuel} as in (a). Also showing d_{IN} (mm) and $\frac{z_M}{M}$ (-), where d_{IN} the injector nozzle inner diameter, z_M the axial distance from the grid to the injector nozzle and M the grid hole diameter, all in mm.

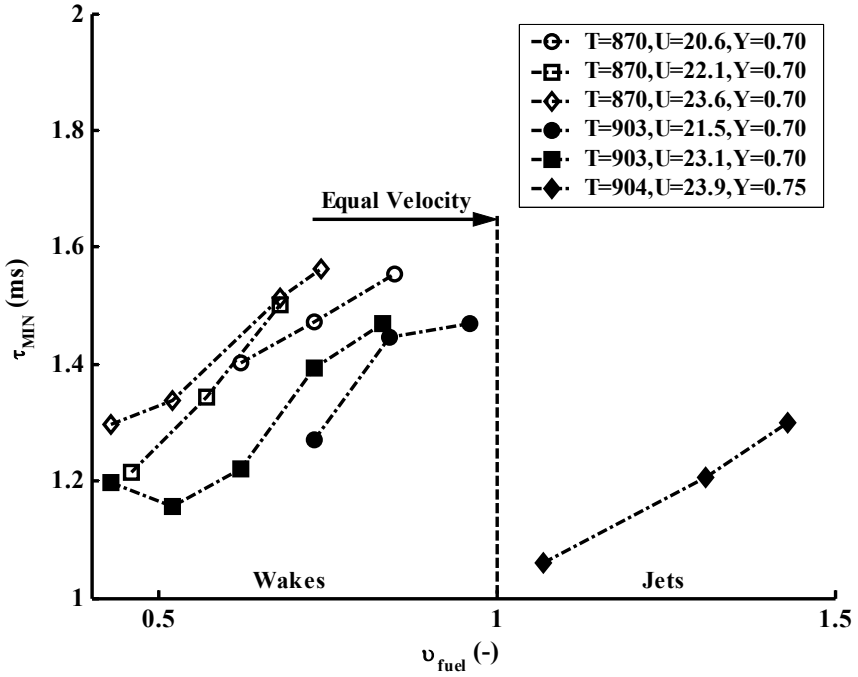

Figure 7.10: Acetylene delay times: Effect of bulk fuel injection velocity. Acetylene wakes and jets. Time data corresponds exactly to lengths in **Figure 6.14**. τ_{MIN} as a function of υ_{fuel} for constant T_{air}, U_{air} and Y_{fuel} conditions.

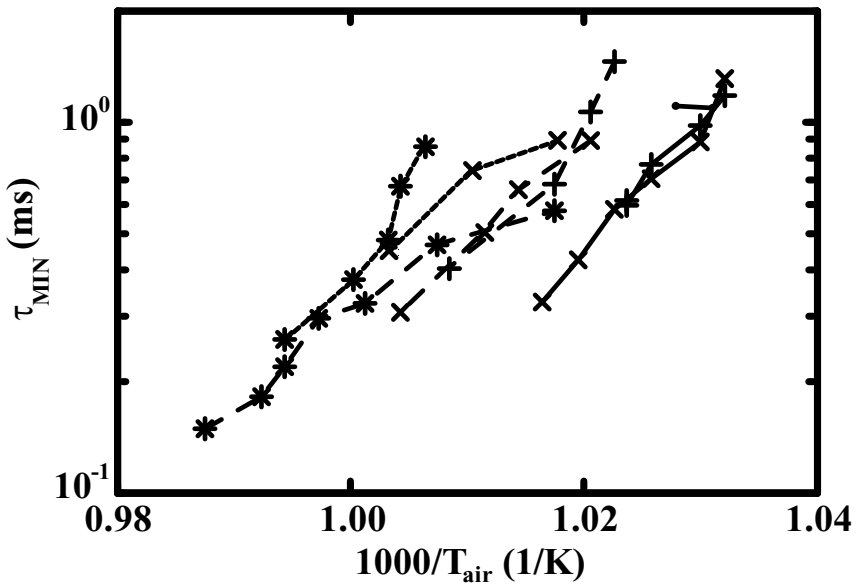

Figure 7.11: Hydrogen delay times: Effect of bulk fuel injection velocity and air temperature. Hydrogen jets. Time data corresponds exactly to lengths in **Figure 6.15**. L_{MIN} as a function of $\frac{1000}{T_{air}}$ for constant $Y_{fuel} = 0.13$ throughout. Lines for data points with constant U_{air}: solid (20 m/s), dashed (26 m/s) and dotted (32 m/s). Markers for data points with constant U_{fuel}: '$\bullet$' (40 m/s), '+' (70 m/s), '$\times$' (100 m/s) and '$*$' (120 m/s).

Chapter 8

Conclusions and Further Discussion

8.1 Conclusion Chapter Objectives

In this final chapter, the main results from this work are re-iterated and final conclusions are drawn. Also included is a discussion of certain points that, due to their more speculative nature, could not form part of the main results chapters, but are considered important nonetheless. Some of these points have been mentioned only briefly in **Chapters 6** and **7**, mainly to offer possible explanations for the observed experimental findings. The purpose of the discussion in this chapter is to bring these points together and through this to strenuously state the importance of the turbulent mixing field in determining the eventual location and time of autoignition. It will be demonstrated that considerations of chemistry alone, conclusively fail to explain certain key qualitative observations concerning the possibility or not of autoignition in the apparatus. Moreover, it will established that knowledge of homogeneous delay times (as for example from shock tubes, etc.) cannot be used to predict accurately the observed autoignition locations and delay times, or even the correct trends of autoignition that have been established experimentally in this study. The understanding and ability to predict autoignition in turbulent inhomo-

geneous flows, through the existence of a most reactive mixture and the critical effect of the scalar dissipation rate, gained theoretically though analytical and DNS studies is reinforced.

8.2 Conclusions

Experiments of turbulent, inhomogeneous autoignition have been carried out in concentric, co-flowing fuel plumes confined in a well-insulated quartz tube, formed by the continuous injection of a pure or nitrogen-diluted fuel into a uniform, turbulent, preheated co-flow of air, without (referred to as CTHC burner) and with (referred to as CTHAJ burner) a 45° bluff-body at the end of the injector. Hydrogen, acetylene, ethylene and n-heptane have been used as fuels. Two injector nozzles with different inner diameters were used, as were two bluff-body/quartz tube combinations. In addition, for certain experiments the quartz tube was further insulated by placing a heat exchanger over its length in order to ascertain any effect of heat losses. The conditions of the experiments were such that the autoignition, or chemical, timescales were of the order of the outer (integral) turbulent timescales.

The background co-flow has been inspected for and found to be uniform in terms of the mean and turbulent fluctuations of the velocity (at cold conditions) and the mean and fluctuations of temperature. The heat losses from the tube were measured, both by axial and radial profiles of the mean temperature. It was found that the presence of the heat exchanger halved the axial decay of mean temperature in the tube, but no considerable differences in the results concerning autoignition were found. The fluctuations of temperature were found to be small. Uniform profiles of mean velocity were also obtained at hot conditions, as was the magnitude of the rms of the turbulent fluctuations of the velocity. The turbulent character of the velocity field was inspected further, by measuring the integral and Kolmogorov lengthscales and by compiling pdfs and power spectra of the velocity fluctuations

(at cold conditions). The measured Kolmogorov lengthscales from the turbulent dissipation were close to the estimates of this quantity from the integral lengthscale. Both the integral timescale and Kolmogorov lengthscale were found to be reasonably uniform in the radial direction and to increase slightly in the axial direction. The pdfs and power spectra were as expected for a confined pipe flow, at regions downstream of a turbulence generating grid. Pdfs and power spectra of the temperature fluctuations showed that these were small and well characterized by a random process, suggesting that the temperature at the inlet is steady and not turbulent. This was confirmed by measurements of the cross-correlation of the fluctuations of velocity and temperature, which were also found to be small.

The mixing field was measured by acetone PLIF at low (but not ambient) temperatures. It was found that, for injection of fuel with equal bulk velocity as that of the air, the mean mixing patterns resembled well the behaviour expected from the analytic treatment of diffusion from a point source. The radial profiles of mean mixture fraction were Gaussian, scaling as expected with downstream distance and bulk velocity. The axial profiles tended to a -2 power-law decay downstream of the (finite sized) injector and were unchanged by changes to the bulk velocities. The variance of the mixture fraction and mean scalar dissipation rate were also considered and these were found to be well related by a timescale ratio of '2.0' along the centreline, except close to the injector. The effect of increasing the air bulk velocity or the non-dimensional fuel injection velocity, was to increase both the mixture fraction variance and mean scalar dissipation. The effect of increasing the non-dimensional fuel injection velocity was to shift the mixing patterns (mean and fluctuations of the mixture fraction and mean scalar dissipation rate) downstream. Detailed considerations of the point statistics of these variables revealed that, for the equal velocity case, the probability of having a most reactive mixture rises from zero at the injector to a maximum value and decays downstream. The effect of increasing the bulk velocities, or a richer choice of most reactive mixture, is to decrease the probability

of having the most reactive mixture. The mean conditional scalar dissipation rate at the most reactive mixture decays monotonically downstream. An increase in air velocity increases the unconditional and conditional mean of the scalar dissipation rate at the same location and decreases the probability of having low conditional scalar dissipation rate at the most reactive mixture.

Autoignition was achieved in the tube with all fuels and in all configurations. Depending on the inlet velocity and temperature of the air and fuel and the degree of dilution of the fuel stream with nitrogen, a variety of phenomena have been observed in the CTHC that have been grouped into operation regimes, namely: 'No Ignition', 'Random Spots', 'Flashback' and 'Lifted Flame'. In all cases autoignition occurred followed by inevitable post-ignition flames that propagated in the tube. The conditions for which transition occurred between regimes was briefly investigated. Generally, 'No Ignition' was observed at lower temperature and higher velocities, 'Flashback' was possible at higher temperatures and lower velocities and 'Lifted Flames' at high temperatures and high velocities. In the 'Random Spots' regime autoignition manifested visually in the form of repeated 'spotty flashes', each one of which was audibly associated with a 'popping' sound. In addition, complex behaviour was possible in the 'Random Spots' regime in the CTHAJ that involved unsteady, igniting and extinguishing pulsed-combustor type lifted flames, *perhaps* due to interactions of autoignition with acoustics or the turbulent flow, but more probably due to a strong interaction between autoignition and the recirculation zone in bluff-body wake and organized shear flow in the annular jet.

In the 'Random Spots' regime autoignition spots appeared both as a consequence of independent events of autoignition and from events which were caused by propagating flames originating from earlier events elsewhere in the flow. Due to the extinction of the post-ignition flamelets in relative closeness to the original autoignition sites, autoignition was inspected in the 'Random Spots' regime, in terms of chemiluminescence emissions, frequency of occurrence, acoustics, location and an

estimate of the autoignition delay time from injection. From the study of chemiluminescence emissions from the autoigniting regions in the flow, the OH^* radical was chosen as a suitable candidate for optical measurements for all fuels and both in the CTHC and CTHAJ.

In the CTHC the autoignition lengths decreased with increasing temperature, decreasing air velocity, decreasing non-dimensional fuel injection velocity and decreasing dilution (except for hydrogen that was not affected in the tested envelope of conditions and n-heptane that showed a non-linearity). A decrease was also observed for autoignition with the smaller diameter injector nozzles and for injection farther downstream of the grid (i.e. at lower turbulence levels). With the exception of small injector results concerning the effect of air velocity, all aforementioned conclusions were unchanged even when viewed in terms of an estimated mean residence time until autoignition (autoignition delay). Specifically, the autoignition delay time decreased with increasing temperature, decreasing air velocity, decreasing non-dimensional fuel injection velocity and decreasing dilution. It also decreased for autoignition with the smaller injector and for injection farther downstream of the grid. With the small injectors, the air velocity was found not to affect the autoignition delay time. In the CTHAJ, the autoignition lengths decreased with increasing temperature and decreasing Reynolds number. The effect of the non-dimensional fuel injection velocity was not found to be significant for the tested conditions.

In the CTHC the mean frequency of occurrence of autoignition was found to decrease exponentially with increasing autoignition length from the injector and considerable spread was observed in the autoignition locations with all conditions fixed. The randomness in the occurrence of autoignition, both temporally but also spatially, cannot be completely explained in terms of the (minimal) randomness in the initial temperature, but must be attributed to the randomness in the scalar mixing field, including the turbulent dispersion of the scalar, and possibly, the variation in the conditional scalar dissipation.

The most important conclusions from this work are that:

- Most of these phenomena can be explained in terms of mixing and simple chemistry and that, in general, turbulent, inhomogeneous autoignition cannot be predicted from chemical delay times obtained from homogeneous experiments. The ability to understand and predict the majority of autoignition phenomena in these flows does not rest primarily on an improved understanding of the complex chemical kinetics of autoignition chemistry, but rather on a deeper knowledge surrounding the effect of turbulent mixing on the preignition chemistry.

- The effect of enhanced turbulence (increased fluctuations of the velocity) is to cause a decrease in the probability of having low conditional scalar dissipation rates at the most reactive mixture, which in turn causes a delay in autoignition. From a broader point of view, both these experiments and the DNS of [Mastorakos et al., 1997a] agree on the basic finding that:

  - *For inhomogeneous autoignition, the effect of turbulence in determining the eventual emergence of autoignition can be understood in terms of pdf($\xi = \xi_{MR}$) and the history of $\chi|\xi = \xi_{MR}$*, and that,
  - *The randomness in the location of autoignition can be understood in terms of the spatial randomness of the regions containing finite pdf($\xi = \xi_{MR}$), and perhaps, of $\chi|\xi = \xi_{MR}$.*

8.3 Further Discussion

The inability to autoignite highly-strained inhomogeneous counterflows has been theoretically and experimentally confirmed, both in laminar and turbulent flows and for a wide range of fuels (see **Section 1.2**). The outcome is 'intuitive', because in this configuration the 'effective residence time' (or time for which the two streams are allowed to mix and react) is determined directly by the rate at which the reactants are brought together by the opposed velocities before flowing radially outwards, which is in turn directly affected by the aerodynamic strain rate (or the bulk χ).

In the case of parabolic co-flowing mixing layers and plumes, such as here, the scalar mixing processes are fundamentally different from those in elliptic counterflows. More specifically, barring an external limitation on the allowable time-span of the mixing, the time available for mixing and chemical reaction in the layer can be made arbitrarily long, independent of the velocities of the two streams. The possible existence of a critical χ in turbulent co-flow mixing layers has only *theoretically* been demonstrated with CMC. Based on observed situations of failed autoignition for sustained high χ, one can envision the likely existence of a critical limit of χ (χ_{CRIT}) that can delineate between the propensity for autoignition, or lack thereof. A situation in which the heat released (and radicals generated) by the chemical reactions is balanced by the severe heat losses (and diffusion of active species away from the radical pool) incurred due to high dissipation would, after all, be nothing more than a *local* manifestation of one of the strongest results concerning autoignition of homogeneous mixtures.

Interestingly, DNS did not reveal such a possibility, but perhaps, this was so due to the transient nature of the calculations, with χ inevitably decaying in the numerical domain, leading to an inability of maintaining high levels of this variable for too long. This outcome in the DNS arises because the fuel–oxidizer interface cannot be specified with arbitrarily fine resolution, thus limiting the initializing

values of χ. In any case, the emergence of χ_{CRIT} for autoignition in a parabolic flow has never been demonstrated experimentally. In the experiments with both the CTHC and CTHAJ, the existence of 'No Ignition' regimes were uncovered, although what was actually observed was a lack of autoignition *within the residence time allowable* by the tube length and the flow velocities and so it is intriguing to reflect on the consequences of the observation of failed autoignition in the 'No Ignition' regime of operation.

Consider the mixing flow in the experimental configuration in terms of pdf(ξ) as shown in **Figure 8.1**.

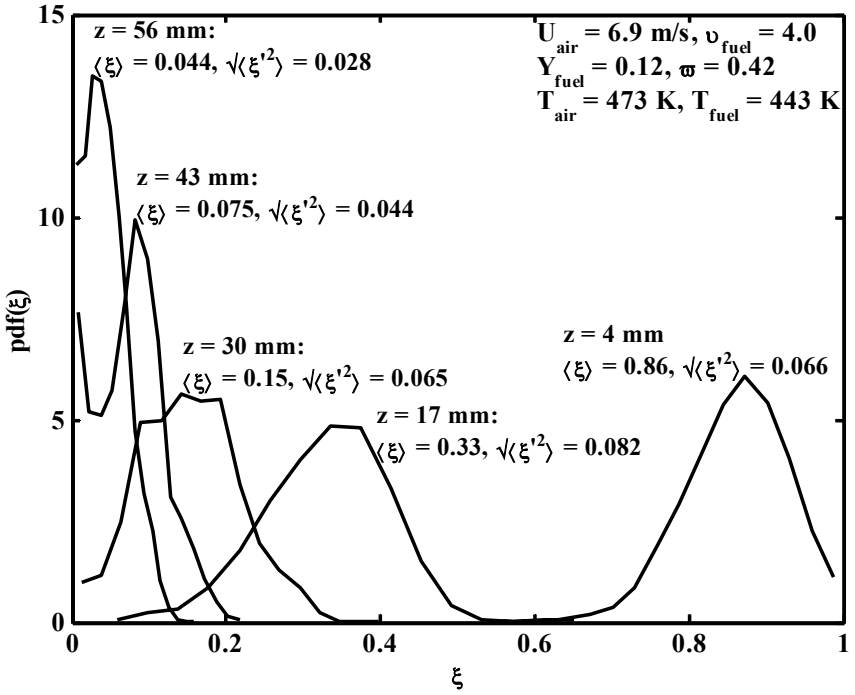

Figure 8.1: Probability density functions of mixture fraction at various axial distances along the centreline

Moving downstream from the injector, say along the centreline, pdf(ξ) shifts from strongly bi-modal at zero and unity ξ (pure air and fuel) near the injector, tending gradually at long lengths (and times) towards a delta function at a lean value of the mixture fraction that is denoted by $\xi_{PREMIX} \neq \xi_{MR}$. In terms of pdf($\xi = \xi_{MR}$),

Figure 3.22(a) reveals that this variable begins from zero at $z = 0$ (and $\frac{z}{U} = 0$), increases to a maximum value and decreases at long lengths (and times) towards zero. Then, after a 'sufficiently long' time the air and fuel streams are mixed, creating a mixture with $\xi_{PREMIX} \neq \xi_{MR}$, such that $\text{pdf}(\xi = \xi_{MR}) \rightarrow 0$.

Based on this knowledge, *assume* that given 'sufficiently vigorous' mixing in the tube relative to its length, the flow can be separated into two 'regions':

1. A 'most reactive' region, defined by finite $\text{pdf}(\xi = \xi_{MR})$.
2. An 'imperfectly premixed' (or 'mixed') region, defined by 'negligibly small' $\text{pdf}(\xi = \xi_{MR})$.

The concept of a 'negligibly small' $\text{pdf}(\xi = \xi_{MR})$ is arbitrary, but not un-physical. Such a reasoning can be based on the requirement that for autoignition to occur at ξ_{MR}, a critical quantity of mixture at ξ_{MR} must exist. This critical value of $\text{pdf}(\xi)$ can also be thought of as a threshold (pdf_{THRESH}) and is routinely used in CMC modelling of autoignition, where for $pdf(\xi) < pdf_{THRESH}$ the equations are not solved.

The 'mixed' region is generally characterized by a more uniform mixing state than that of the 'most reactive', but nonetheless, the distinction between 'most reactive' and 'mixed' regions does not imply a sharp transition between two physical regimes, or a discontinuity in the mixing character of the flow, in terms of ξ or χ. On the contrary, both the ξ and χ decay asymptotically, towards ξ_{PREMIX} and zero respectively, downstream and away from the injector. Rather, there is a gradual change from one regime to the other as the gradients decay smoothly in the downstream distance and the value of $\text{pdf}(\xi = \xi_{MR})$ disappears. It is the definition of pdf_{THRESH} that forces the demarcation between the regimes.

The corollary of accepting this assumed point of view is illustrated in **Figure 8.2**.

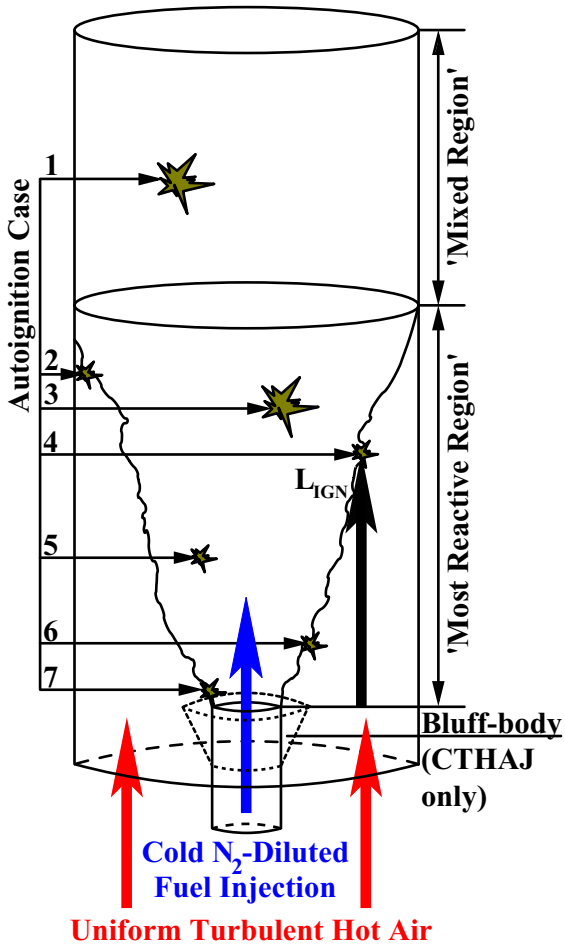

Figure 8.2: Modes of autoignition in the Turbulent, Co-flow Mixing Layer

It is the author's view that an interpretation of the results in terms of the the existence of these two regions is significant, because the location of autoignition (or lack of) can be accounted for by different arguments, depending on where it occurs with respect to these. Eventually, the possibility (or not) of autoignition in the full length of the tube, will be a result of the competition between the inhomogeneous autoignition processes in the 'most reactive' length and the 'imperfectly premixed' autoignition processes in the 'mixed', as described below.

Upstream, ξ_{MR} always exists in the 'most reactive' portion of the tube, by definition and by virtue of the fact the flows are continuous. As long as this condition is satisfied, current understanding of autoignition leads to the conclusion that, if the flow autoignites here, then it will do so somewhere along the loci of points of most reactive chemistry. In **Figure 8.2** inhomogeneous autoignition occurs at ξ_{MR} in the 'most reactive' region for Points "2" – "7". Failure of autoignition in this region, in the light of the existence of ξ_{MR}, such as in 'No Ignition', must be attributed to a situation in which reacting kernels are possible and do occur, but are unable to evolve from the pre-ignition chemistry of lower temperatures and slower radical build-up to the explosive, large-scale flame chemistry typically associated with 'successful' autoignition. At the same time, this inability to realize complete thermal runaway, renders the detection of the on-going processes by a sharp rise in some global variable (e.g. temperature or pressure) impossible. These slowly reacting radical pools can also be referred to as 'kernels that failed to autoignite' and are discussed in [Echekki and Chen, 2003]. For all practical purposes it can be said that this is a case of 'unsuccessful' autoignition.

From this point of view, the precise cause of the failed autoignition behaviour in the 'most reactive' region can only be hypothesized upon, assisted by indirect experimental evidence, since the existence of and value of χ_{CRIT} are not known. The view is held here that the capability of a turbulent inhomogeneous mixing flow to autoignite, depends on the various characteristics of both the mixing field and the chemistry as illustrated in **Figure 8.3**.

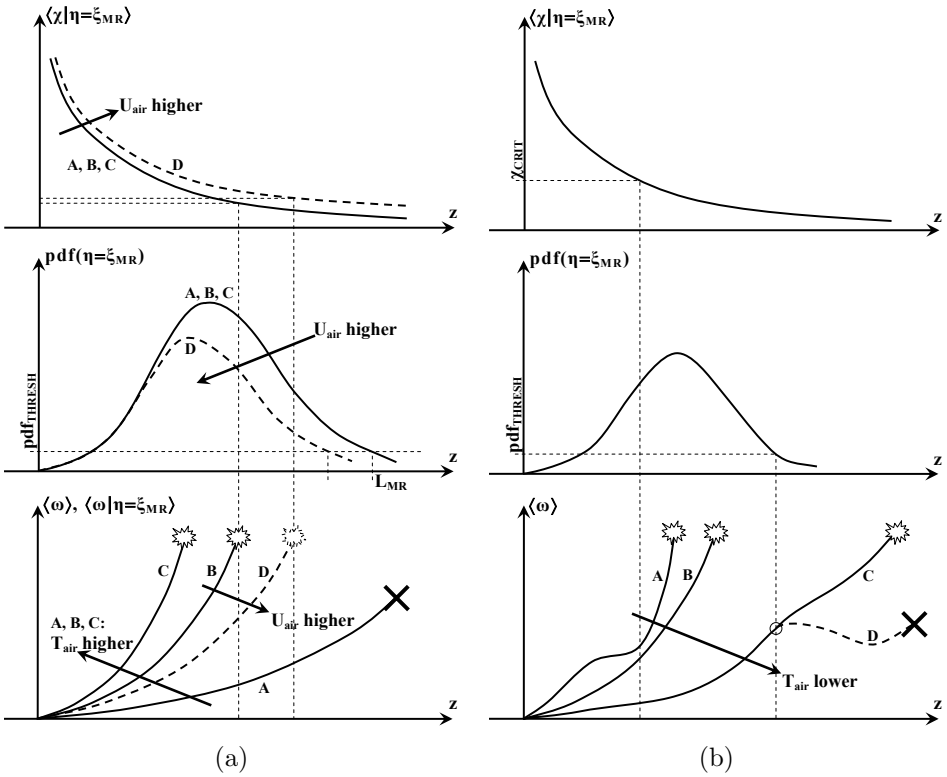

Figure 8.3: Illustrated explanation of the autoignition modes

Consider the situation corresponding to case "A" in the sketch in **Figure 8.3(a)**. If T_{air} is too low for the given $\langle\chi|\xi = \xi_{MR}\rangle$ (or equivalently if $\langle\chi|\xi = \xi_{MR}\rangle > \chi_{CRIT}$), the initial reaction rate will be everywhere slow, as will the mean conditional reaction rates, $\langle\dot{\omega}|\xi = \xi_{MR}\rangle$. So, even at ξ_{MR} for which the reaction rates are optimum (fastest) for autoignition, reaction will be too slow to evolve the kernels *within* the 'most reactive' length, denoted by L_{MR}. Seen otherwise, if the magnitude of $\chi|\xi = \xi_{MR}$ is high relative to the slow chemistry (and thus low χ_{CRIT}), this would lead to situations whereby even though the chemical reaction rates are fast, they are not fast enough to cause autoignition *within* L_{MR}, or the lagrangian time available to the mixture in the domain. Comparison can be made with a DNS simulation in which the run time is not enough to successfully autoignite the mixing field at any location, given initial conditions of low temperature.

For higher T_{air}, case "B" in **Figure 8.3(a)** is reached. For the given U_{air} and $\langle\chi|\xi=\xi_{MR}\rangle$, $\langle\dot{\omega}|\xi=\xi_{MR}\rangle$ increases until autoignition is achieved inside L_{MR}. Equivalently, χ_{CRIT} has increased so that $\langle\chi|\xi=\xi_{MR}\rangle$ drops below χ_{CRIT} within L_{MR}. Case "C" is for even higher T_{air}. For a higher U_{air} (but same T_{air}, χ_{CRIT}), or for richer ξ_{MR}* (such as due to a higher T_{fuel} relative to T_{air}, lower T_{act} or lower Y_{fuel}) and hence also higher $\langle\chi|\xi=\xi_{MR}\rangle$, the values of pdf($\xi=\xi_{MR}$) decrease so that L_{MR} is closer to the injector. In addition, the effective lagrangian 'mixing and reaction' time inside the L_{MR} region decreases. These outcomes have been verified experimentally (**Figures 3.22(a)** and **3.22(b)**). Also, it is expected that $\langle\dot{\omega}|\xi=\xi_{MR}\rangle$ and χ_{CRIT} decrease. This results in scenario "D". Now:

1. If the downstream shift in autoignition length required by the decreased $\langle\dot{\omega}|\xi=\xi_{MR}\rangle$ is longer than the shortening of L_{MR}, autoignition will not occur, for reasons similar to those outlined for case "A". In another case, if pdf($\xi=\xi_{MR}$) falls below pdf_{THRESH}, autoignition could fail due to the non-attainment of a critical concentration of ξ_{MR}, or in other words, too small a number of fast reacting autoignition kernels and a very small probability of autoignition.

2. It is possible that one is operating in conditions that inhibit autoignition because of excessive removal of heat and radicals way from the kernel cores, such as for example a situation of too high scalar gradients, with $\langle\chi|\xi=\xi_{MR}\rangle > \chi_{CRIT}$. Case "A" in **Figure 8.3(a)** shows the inhibition of autoignition when $\langle\chi|\xi=\xi_{MR}\rangle$ does not drop below χ_{CRIT} so that autoignition is not possible at all inside L_{MR}. The difference between this and the situation in case "D" in **Figure 8.3(a)**, is that autoignition would fail in the former due to low χ_{CRIT}, whereas in the latter due to high $\langle\chi|\xi=\xi_{MR}\rangle$, even for very long L_{MR}. This case is of great fundamental importance and if true would give rise to critical conditions for the possibility (or not) of autoignition in these types of flow.

*At a given physical location, richer ξ_{MR} would increase the local $\langle\chi|\xi=\xi_{MR}\rangle$, even if U_{air} remained unchanged, as demonstrated by **Figures 3.22(c)**, **3.22(d)** and **3.23(a)**.

In other circumstances, for certain fuels and conditions, autoignition can be delayed until Point "1" in **Figure 8.2**, beyond the 'most reactive' region and into the 'mixed' portion of the tube (case "C" in **Figure 8.3(b)**). This will be a case of (imperfectly) premixed autoignition and the chemistry will play a more dominant role. In the absence of autoignition in the 'most reactive' length upstream, a lack of autoignition here (case "D" in **Figure 8.3(b)**) can only be explained by too long a τ_{CHEM} (or too low a homogeneous chemical reaction rate of ξ_{PREMIX}) relative to the τ_{RES} made available by the length of tube. The necessary τ_{CHEM} for explosive autoignition is controlled by the chemical reaction rates and consequently the premixed mixture (ξ_{PREMIX}) and temperature (and pressure). Any effect of turbulence on autoignition will be through the fluctuations of the temperature.

Going a step further, if ξ_{PREMIX} is not very different from ξ_{MR}, case "C" in **Figure 8.3(b)** is likely, with only an inflection point at the downstream edge of L_{MR}, whereas if ξ_{PREMIX} is very different from ξ_{MR}, case "D" is possible with a dramatic drop of reaction rate as soon as the mixture begins to react in an 'imperfectly premixed' mode. This conjecture could be used to explain the inability for certain fuels to autoignite within the whole length of the tube, as discussed in **Section 4.2.1: 'Nothing–to–Spots' or 'Pre-Ignition Reactions' Transition**. In fact, ξ_{PREMIX} has been evaluated for the conditions of the experiments and it was found that for hydrogen (which showed discontinuous autoignition behaviour) ξ_{PREMIX} was up to 2 orders of magnitude lower than ξ_{MR}, as opposed to n-heptane (that autoignited along the whole length of the tube) for which ξ_{PREMIX} was only a factor of 4 – 40 lower than ξ_{MR}.

Contrary to common practice in the traditional treatment of inhomogeneous autoignition, *in general* it is not strictly correct to decouple the chemical from the mixing processes, although it *may* be possible to make such a simplification *under certain circumstances*. The argument by which autoignition can be envisaged in terms of a 'chemical' and 'mixing' time and explained by splitting the total

autoignition delay into a mixing and chemical delay is indeed in direct contrast to one of the major conclusions of this thesis. Consider the following experimental procedure:

Initially: The quartz tube has been insulated externally by the heat-exchanger and the temperature drop along the tube is about 3 – 4 K per 100 mm (or 4 D_{TUBE}) of tube. All inlet conditions are fixed and with a continuous flow of pure acetylene through the injector, no ignition is observed in the tube. It has been confirmed that mixing between the air–mixture feeds is vigorous enough so that there are no large-scale inhomogeneities, with low χ and pdf($\xi = \xi_{MR}$), exist after 10 D_{TUBE} from injection (the tube has a length of 20 D_{TUBE}) and call this the 'most reactive length', L_{MR}.

Transition: T_{air} is raised incrementally (by 1 – 2 K) and autoignition events are observed visually and audibly at a mean vertical distance of about 5 D_{TUBE} from the injector.

Firstly, the failure to explain this sudden transition in terms of de-coupling and treatment of the problem in terms of a homogeneous chemical delay time will be illustrated. Ignoring any effect of the heat losses to the walls would result in the following train of thought:

Initially: τ_{MIX} is about half of the total τ_{RES} (because the 'most reactive' length is half of the tube length) and τ_{CHEM} must be larger than the remainder of the total τ_{RES} for a lack of autoignition in the tube.

Transition: As T_{air} is raised, autoignition is expected to occur at the longest τ_{res}, somewhere near the exit the tube, far downstream and to approach the injector continuously (but non-linearly) as the temperature is raised further.

No complex, non-linear kinetic effects can be thought of influencing the results for this fuel (but even for n-heptane, the conditions were away from negative temper-

ature coefficient behaviour) and so this explanation does not suffice. The outcome can only be explained as follows:

Initially: The mixing patterns in the tube vary from a 'most reactive' region stretching from the injector to about half the tube length and a 'mixed' region occupying the downstream half of the tube. In the 'mixing' region ξ_{MR} exists. The lack of autoignition here reflects the fact that kernels are not able to sustain large-scale autoignition events ('unsuccessful' autoignition), for reasons already outlined above and illustrated in **Figure 8.3**. In the 'mixed' region the acetylene–air mixture has been 'imperfectly premixed' resulting in a certain value of ξ_{PREMIX} or $\phi_{PREMIX} = \frac{AFR_{stoic}}{1/\xi_{PREMIX}-1}$. For this equivalence ratio, autoignition in the temperature and pressure conditions is slow relative to τ_{res} in the tube. Overall, with failure of autoignition in both regions, this situation corresponds to case "D" in **Figure 8.3(b)**.

Transition: The mixing patterns in the tube are virtually unaffected by the incremental temperature increase. The value of ξ_{MR} decreases slightly, but the reaction rate increases. In terms of **Figure 8.3(b)** this would be a transition from case "D" to "B". At this higher temperature autoignition becomes possible in the 'most reactive' regions of the tube, due to the fact that the reaction rate has increased (and also, perhaps but not necessarily, the value of χ_{CRIT} itself might have increased) to allow autoignition to proceed *in the 'mixing' length of the tube.*

Although the above explanations are hypothetical, mainly due to a lack of definite knowledge concerning these processes (e.g. the existence or not of χ_{CRIT}), they do offer possible explanations to the situation of sharp change in autoignition behaviour for which the conventional arguments, based on homogeneous chemical delay times, fail conclusively.

8.4 Future Work

In **Section 8.3** it was hypothesized that the decay of pdf($\xi = \xi_{MR}$) downstream of the injector in the axisymmetric co-flow was of importance, because it allowed for two distinct physical mechanisms that could lead to the eventual emergence of autoignition. On the one hand, this allowed for a wide range of phenomena and lead to the discussion concerning the possible autoignition modes that can be expected from such a configuration. On the other, it introduces a further critical factor for autoignition, thus removing a certain amount of focus from the effects of $\chi|\xi = \xi_{MR}$. In *planar* co-flowing mixing layers, high values of pdf($\xi = \xi_{MR}$) can be sustained for longer lengths and so this configuration can offer a fresh look at some of the scenarios that have been described above. The planar geometry also facilitates optical measurements, should allow a greater flexibility for setting the fuel temperature (because the splitter plate can be insulated) and offers the added advantage of allowing measurements in flows that have been considered, at least to some extent, previously in the literature. The planar flows will be: (i) directly comparable to the studies of laminar co-flow mixing layers, and, (ii) qualitatively closer to the investigated flows studied by the DNS. The planar configuration can be approached in a similar manner as was done here for the axisymmetric case.

Irrespective of the flow configuration it will be interesting to experimentally measure the value of the most reactive mixture (ξ_{MR}) and to examine the effect of $\chi|\xi = \xi_{MR}$ on this variable. This will have to be done with simultaneous heat release and mixture fraction measurements, that need not have to be two-dimensional. For point measurements the investigated position can be shifted, say along the centreline. Then the conditional reaction rate can be plotted at various locations (and hence at various times and values of $\chi|\xi = \xi_{MR}$). Another, simpler measurement would be for simultaneous PLIF of OH^* and acetone (or NO). From the former the location of autoignition can be determined, such that the conditional statistics of the turbulent

mixing field, including $\chi|\xi = \xi_{MR}$ (and the pdf of $\xi = \xi_{MR}$ for the axisymmetric flow), can be inspected in the locality of the autoignition events. It cannot be known, at this stage, to what degree the presence of the tracers will affect the autoignition chemistry.

'Spot-wake interactions' in the CTHAJ burner showed the possibility of dangerous deviations from the mean behaviour leading to an increased propensity for flashback. The velocity field and more specifically the pdfs of the velocity fluctuations in the recirculation zone can be inspected, to try to obtain greater insight into this regime of operation.

•

As planned, my journey continues
I arrive at the foot of the mountain
That stands firm between me and the otherside
There, I meet the wise man in his dwelling
Who has been to the otherside many times before
Who has guided all the others that have made their passage
Who have warned me to take his counsel;

And I speak to him
He advises me that I must pass the mountain
He advises me that there are only two ways to pass
To climb and to go around
And he tells me all that he knows
To those who know me, it would seem but a simple choice
For mostly I cannot escape myself;

And I am now on the otherside
I am aware that it has taken more
But I have come to know the mountain better
All cold stone and density and depth
Even if I did not need it to pass
I am proud to have bored though
And no-one can take this away from me;

And now?

Nothing.
Sometimes we must go alone
and wait for the world to follow.

"Humanity has advanced, when it has advanced,
not because it has been sober, responsible, and cautious,
but because it has been playful, rebellious, and immature."
Tom Robbins (1936 –)

Hopkinson Laboratory, Cambridge
Wednesday, 29$^{\underline{\text{th}}}$ of June, 2005 *Christos Markides*

Bibliography

R.A. Antonia and J. Mi.
Temperature dissipation in a turbulent round jet.
J. Fluid Mech., 280:179–197, 1993.

G.K. Batchelor.
The effect of homogeneous turbulence on material lines and surfaces.
Proc. R. Soc. Lond., A 213:349–366, 1952.

S.W. Benson.
The kinetics and thermochemistry of chemical oxidation with application to combustion and flames.
Prog. Energy Combust. Sci., 7:125–134, 1981.

J.D. Blouch, J.-Y. Chen, and Law C.K.
A joint scalar PDF study of nonpremixed hydrogen ignition.
Combust. Flame, 135(3):209–225, 2003.

J.D. Blouch and C.K. Law.
Effects of turbulence on nonpremixed ignition in heated counterflow.
Combust. Flame, 132(3):512–522, 2003.

J.D. Blouch, C.J. Sung, C.G. Fotache, and C.K. Law.
Turbulent ignition of non-premixed hydrogen by heated counterflowing atmospheric air.
Proc. Combust. Inst., 27:1221–1228, 1998.

D.G Bogard and K.A. Thole.
13: The handbook of fluid dynamics, chapter Wall-bounded shear flows, pages 13(49)–13(63).
CRC Press, Boca Raton, FL, U.S.A., 1^{st} edition, 1998.

S.A. Bozhenkov, S.M. Starikovskaia, and A. Yu. Starikovskii.
Nanosecond gas discharge ignition of H_2- and CH_4- containing mixtures.
Combust. Flame, 133:133–146, 2003.

C. Brackmann, J. Nygren, X. Bai, Z. Li, and H. Bladh.
Spectrochimica Acta Part A, 2003.

D. Bradley, A.K.C. Lau, and M. Missaghi.
Response of compensated thermocouples to fluctuating temperatures: computer simulations, experimental results and mathematical modeling.
Combust. Sci. and Tech., 64:119, 1989.

H.H. Bruun.
Hot wire anemometry: principles and data analysis.
Oxford University Press, 1995.
ISBN 0198563426.

K.A. Buch and W.J. Dahm.
Experimental study of the fine-scale structure of conserved scalar mixing in turbulent shear flows.
J. Fluid Mech., 364:1–29, 1998.

W.G. Burwell and D.R. Olson.
The spontaneous ignition of isooctane air mixtures under steady flow conditions.
SAE Paper, (650510):839–849, 1965.

R. Cabra, T. Myhrvold, J.Y. Chen, R.W. Dibble, A.N. Karpetis, and R.S. Barlow.
Simultaneous laser raman-rayleigh-LIF measurements and numerical modeling results of a lifted turbulent H_2/N_2 jet flame in a vitiated coflow.
Proc. Combust. Inst., 29:1881–1888, 2002.

A. Caldeira-Pires and M.V. Heitor.
Temperature and related statistics in turbulent jet flames.
Exp. Fluids, 24:118–129, 1998.

R.H. Chan, C-W. Ho, and M. Nikolova.
Salt-and-Pepper noise removal by median-type noise detectors and detail-preserving regularization.
Accepted for publication by IEEE Trans. Image Proc., 2004.

H. Chen, S. Chen, and R.H. Kraichnan.
Probability distribution of a stochastically advected scalar field.
Phys. Rev. Lett., 63(24):2657–2660, 1989.

C.-C. Chiao.
Characterization of natural illuminants in forests and the use of digital video data to reconstruct illuminant spectra.
J. Opt. Soc. Am. A., 17(10):1713–1721, 2000.

H.K. Ciezki and G. Adomeit.
Shock-tube investigation of self-ignition of n-heptane–air mixtures under engine relevant conditions.
Combust. Flame, 93:421–433, 1993.

M.B. III Colket and L.J. Spadaccini.
Scramjet fuels autoignition study.
J. Prop. Power, 17(2):315–323, 2001.

D.C. Collis and M.J. Williams.
Two dimensional convection from heated wires at low Reynolds number.
J. Fluid Mech., 6:357, 1959.

L.H. Cowell and A.H. Lefebre.
Influence of pressure on autoignition characteristics of gaseous hydrocarbon–air mixtures.
SAE Paper, 6(860068):1–11, 1987.

R.A. Craig.
A shock tube study of the ignition delay of hydrogen–air mixtures near the second explosion limit.
Technical Report AFAPL-TR-66-74, WPAFB, OH, U.S.A., 1966.

H.J. Curran, P. Gaffuri, W.J. Pitz, and C.K. Westbrook.
A comprehensive modeling study of n-heptane oxidation.
Combust. Flame, 114:149–177, 1998.

B.B. Dally, A.N. Karpetis, and R.S. Barlow.
Structure of turbulent non-premixed jet flames in a diluted hot co-flow.
Proc. Combust. Inst., 29:1147–1154, 2002.

P.A. Davidson.
Turbulence: an introduction for scientists and engineers.
Oxford University Press (2004), Oxford, U.K., 1^{st} edition, 2004.

T.W. Davies and J.M. Beér.
Proc. Combust. Inst., 13:631–638, 1971.

P. Domingo and L. Vervisch.
Proc. Combust. Inst., 26:233–240, 1996.

F. Ducourneau.
Inflammation spontanée de mélanges riches air–kérosène.
Entropie, 59:11–18, 1974.

D.F.G. Durão and J.H. Whitelaw.
J. Fluid Mech., 85:369–385, 1978.

T. Echekki and J.Y. Chen.
Direct numerical simulation of autoignition in non-homogeneous hydrogen air mixtures.
Combust. Flame, 134:169–191, 2003.

C.F. Edwards, D.L. Siebers, and D.H. Hoskin.
A study of the autoignition process of a diesel spray via high speed visualization.
SAE Paper, (920108):187–204, 1992.

P. Ferrão and M.V. Heitor.
Probe and optical diagnostics for scalar measurements in premixed flames.
Exp. Fluids, 24:389–398, 1998.

J.R. Fienup, D. Griffith, L. Harrington, A.M. Kowalczyk, J.J. Miller, and J.A. Mooney.
Comparison of reconstruction algorithms for images from sparse-aperture systems.
In *Proc. SPIE 4792-01*, Seattle, WA, U.S.A., July 2002. Image Reconstruction from Incomplete Data II.

K. Fieweger, R. Blumenthatl, and G. Adomeit.
Shock-tube investigations on the self-ignition of hydrocarbon–air mixtures at high pressures.
Proc. Combust. Inst., 25, 1994.

C.G. Fotache, T.G. Kreutz, and C.K. Law.
Ignition of counterflowing methane versus heated air under reduced and elevated pressures.
Combust. Flame, 108:442–470, 1997a.

C.G. Fotache, T.G. Kreutz, and C.K. Law.
Ignition of hydrogen-enriched methane by heated air.
Combust. Flame, 110(4):429–440, 1997b.

C.G. Fotache, T.G. Kreutz, D.L. Zhu, and C.K. Law.
An experimental study of ignition in nonpremixed counterflowing hydrogen versus heated air.
Combust. Sci. Tech., 109:373–393, 1995.

C.G. Fotache, C.J. Sung, C.J. Sun, and C.K. Law.
Mild oxidation regimes and multiple criticality in nonpremixed hydrogen–air counterflow.
Combust. Flame, 112(3):457–471, 1998.

C.G. Fotache, H. Wang, and C.K. Law.
Ignition of ethane, propane, and butane in counterflow jets of cold fuel versus hot air under variable pressures.
Combust. Flame, 117:777–794, 1999.

J.H. Frank, K.M. Lyons, D.F. Marran, M.B. Long, S.H. Stårner, and R.W. Bilger.
Mixture fraction measurements in turbulent nonpremixed hydrocarbon flames.
Proc. Combust. Inst., 25:1159, 1994.

A.G. Gaydon and H.G. Wolfhard.
Flames: their structure, radiation and temperature.
Chapman & Hall (January, 1979), London, U.K., 3^{rd} edition, 1970.
ISBN 0470264810.

F.B. Gessner and G.L. Moller.
Response behaviour of hot wires in shear flow.
J. Fluid Mech., 47:449–468, 1971.

J.B. Ghandhi and P.G. Felton.
On the fluorescence of ketones at high temperatures.
Exp. Fluids, 21:143–144, 1996.

S.S. Girimaji.
On the modelling of scalar diffusion in isotropic turbulence.
Phys. Fluids A, 4(11):2529–2537, 1992.

N. Graf, J. Gronki, C. Schulz, and T. Baritaud.
SAE Paper, (2001-01-1924), 2001.

J.F. Griffiths and S.K. Scott.
Thermokinetic intercations: fundamentals of spontaneous ignition and cool flames.
Prog. Energy Combust. Sci., 13:161–197, 1987.

M. V. Heitor, A.M.K.P. Taylor, and J.H. Whitelaw.
Simultaneous velocity and temperature measurements in a premixed flame.
Exp. in Fluids, 3:323–339, 1985.

T.J. Held, A.J. Marchese, and F.L. Dryer.
A semi-empirical reaction mechanism for n-heptane oxidation and pyrolysis.
Combust. Sci. Tech., 123:107–146, 1997.

B.T. Helenbrook, H.G. Im, and C.K. Law.
Theory of radical-induced ignition of counterflowing hydrogen versus oxygen at high temperatures.
Combust. Flame, 112:242–252, 1998.

N.A. Henein and J.A. Bolt.
Kinetic considerations in the autoignition and combustion of fuel sprays in swirling air.
ASME Paper, (72-DGP-8), 1972.

R. Hilbert and D. Thevenin.
Combust. Flame, 128(1-2):22–37, 2002.

J.O. Hinze.
Turbulence.
McGraw-Hill (1975), New York, NY, U.S.A., 2^{nd} edition, 1975.

J.P. Holman.
Experimental methods for engineers.
Thomas Casson, New York, NY, U.S.A., 7^{th} edition, 2001.
ISBN 0073660558.

D.C. Horning.
A study of the high-temperature autoignition and thermal decomposition of hydrocarbons.
Report TSD-135, Stanford University, Stanford, CA, U.S.A., 2001.

R.F. Huang and C.L. Lin.
J. Wind Eng. Ind. Aerodyn., 85:31–45, 2000.

S. Humer, R. Seiser, and K. Seshadri.
Non-premixed and premixed extinction and autoignition of C_2H_4, C_2H_6, C_3H_6, and C_3H_8.
Proc. Combust. Inst., 29:1597–1604, 2002.

H.G. Im, J.H. Chen, and C.K. Law.
Proc. Combust. Inst., 27:1047–1056, 1998.

F.E. Jørgensen.
How to measure turbulence with hot-wire anemometers – a practical guide.
Dantec Dynamics, Skovlunde, Denmark, February 2002.

Y. Ju and T. Niioka.
Combust. Flame, 99:240, 1994.

M. Katsuki, Y. Mizutani, and Y. Matsumoto.
An improved thermocouple technique for measurement of fluctuating temperatures in flames.
Combust. Flame, 67:27–36, 1987.

L. Koopmans, R. Ogink, and I. Denbratt.
Visualization (PLIF) of intermediates generated in the negative valve overlap of an HCCI operated engine.
Joint Meeting of the Scandinavian-Nordic and Italian Sections of the Combustion Institute, pages 1–4, Ishia, Naples, Italy, 18–21st September, 2003 2003.

T.G. Kreutz and C.K. Law.
Ignition in nonpremixed counterflowing hydrogen versus heated air: computational study with detailed chemistry.
Combust. Flame, 104:157–175, 1996.

T.G. Kreutz and C.K. Law.
Ignition in nonpremixed counterflowing hydrogen versus heated air: computational study with skeletal and reduced chemistry.
Combust. Flame, 114:436–456, 1998.

T.G. Kreutz, M. Nishioka, and C.K. Law.
The role of kinetic versus thermal feedback in nonpremixed ignition of hydrogen versus heated air.
Combust. Flame, 99:758–766, 1999.

X. Li and R.S. Tankin.
Combust. Sci. Tech., 52:173–206, 1987.

A. Liñán.
The asymptotic structure of counterflow diffusion flames for large activation energies.
Acta Astronaut., 1:1007–1039, 1974.

A. Liñán and A. Crespo.
An asymptotic analysis of unsteady diffusion flames for large activation energies.
Combust. Sci. Tech., 14:95–117, 1976.

A. Liñán and F.A. Williams.
Combust. Flame, 95:31, 1993.

P.M. Ligrani and P. Bradshaw.
Subminiature hot-wire sensors: development and use.
J. Phys. E: Sci. Instrum., 20:323–332, 1987a.

P.M. Ligrani and P. Bradshaw.
Spatial resolution and measurement of turbulence of turbulence in the viscous sublayer using miniature hot-wire probes.
Exp. in Fluids, 5:407–417, 1987b.

J.S. Lim.
Two-dimensional signal and image processing.
Prentice Hall, Englewood Cliffs, NJ, U.S.A., 1990.
ISBN -.

S. Liu, J.C. Hewson, J.H. Chen, and H. Pitch.
Effects of strain rate on high-pressure nonpremixed n-heptane autoignition in counterflow.
Combust. Flame, 137:320–339, 2004.

M.B. Long, S.H. Stårner, and R.W. Bilger.
Differential diffusion in jets using joint PLIF and Lorenz-Mie imaging.
Combust. Sci. and Tech., 93:209, 1993.

A. Lonzano, S.H. Smith, M.G. Mungal, and R.K. Hanson.
Concentration measurements in a transverse jet by planar laser-induced fluorescence of acetone.
AIAA J., 32:218–221, 1993.

A. Lonzano, B. Yip, and R.K. Hanson.
Acetone: a tracer for concentration measurements in gaseous flows by planar laser-induced fluorescence.
Exp. Fluids, 13:369–376, 1992.

C.N. Markides and E. Mastorakos.
An experimental study of hydrogen autoignition in a turbulent co-flow of hot air.
Proc. Combust. Inst., 30:883–891, 2005.

S.D. Mason, J.H. Chen, and H.G. Im.
Effects of unsteady scalar dissipation rate on ignition of non-premixed hydrogen/air mixtures in counterflow.
Proc. Combust. Inst., 29:1629–1636, 2002.

A.R. Masri, R. Cao, S.B. Pope, and G.M. Goldin.
PDF calculations of turbulent lifted flames of H_2/N_2 issuing into a vitiated co-Flow.
Combust. Theory Modelling, 8:1–22, 2004.

E. Mastorakos.
Turbulent combustion in opposed jet flows.
PhD thesis, Imperial College of Science, Technology and Medicine, London, U.K., July 1993.

E. Mastorakos.
Modelling autoignition in turbulent flows: a review.
In 4^{th} *GRACM Congress on Computrational Mechanics*, Patra, Greece, June 2002.

E. Mastorakos, T.A. Baritaud, and T.J. Poinsot.
Numerical simulations of autoignition in turbulent mixing flows.
Combust. Flame, 109:198–223, 1997a.

E. Mastorakos and R.W. Bilger.
Second-order conditional moment closure for the autoignition of turbulent flows.
Phys. Fluids, 10(6):1246–1248, 1998.

E. Mastorakos, C.N. Markides, and Y.M. Wright.
Hydrogen autoignition in a turbulent duct flow: experiments and modelling.
In *12th International Conference on Fluid Flow Technologies*, Budapest, Hungary, 3–6 September 2003. Conference on Modelling Fluid Flow.

E. Mastorakos, A. Pirez da Cruz, T.A. Baritaud, and T.J. Poinsot.
A model for the effects of mixing on the autoignition of turbulent flows.
Combust. Sci. Tech., 125:243–282, 1997b.

G. McKay.
The gas-phase oxidations of hydrocarbons.
Prog. Energy Combust. Sci., 3:105–126, 1977.

J.D. Mellado, A.L. Sánchez, J.S. Kim, and A. Liñán.
Branched-chain ignition in strained mixing layers.
Combust. Theory Modelling, 4:265–288, 2000.

Y. Mizutani and T. Takada.
Effects of velocity, turbulence and wall impingement on the ignition of fuel sprays perpendicularly injected into a heated air stream.
In *17th ICDERS*, 1999.

R.J. Moffat.
Describing the uncertainties in experimental results.
Exp. Therm. Fluid Sci., 1:3–17, 1988.

J.A. Muss, R.W. Dibble, and L. Talbot.
A helium-hydrogen mixture for the measurement of mixture fraction and scalar gradient in non-premixed reacting flows.
In *AIAA Paper 94-0612*, Reno, NV, U.S.A., January 1994. 32th AIAA Meeting.

T. Ni, J.A. Pinson, S. Gupta, and R.J. Santoro.
Two-dimensional imaging of soot volume fraction by the use of laser-induced incandescence.
Applied Optics, 34(30):7083–7091, 1995.

H.M. Nicholson and J.P. Field.
Proc. Combust. Inst., 3:44–68, 1949.

R. Obertacke, H. Wintrich, F. Wintrich, and A. Leipertz.
A new sensor system for industrial combustion monitoring and control using UV emission spectroscopy and tomography.
Combust. Sci. and Tech., 121:133–151, 1996.

S. Pedersen and B. Qvale.
A model for the physical part of the ignition delay in a diesel engine.
SAE Paper, (740716), 1974.

G.L. Pellett, C. Bruno, and W. Chinitz.
Review of air vitiation effects on scramjet ignition and flameholding combustion processes.
In *AIAA Paper 2002-3880*, pages 1–37, Indianapolis, IN, U.S.A., July 2002. 38^{th} AIAA/ASME/SAE/ASEE Joint Propulsion Conference and Exhibit.

A.E. Perry.
Hot-wire anemometry.
Oxford University Press, 1982.
ISBN 0198563272.

N. Peters.
Turbulent combustion.
Cambridge Monographs on Mechanics. Cambridge University Press, Cambridge, U.K., 3^{rd} edition, 2000.

N. Peters, G. Paczko, R. Seiser, and K. Seshadri.
Temperature cross-over and non-thermal runaway at two-stage ignition of n-heptane.
Combust. Flame, 128:38–59, 2002.

B.E. Poling, J.M. Prausnitz, and J.P. O'Connell.
The properties of gases and liquids.
McGraw-Hill (2001), New York, NY, U.S.A., 5^{th} edition, 2001.
ISBN 0070116822.

J. Portilla, V. Strela, M. Wainwright, and E.P. Simoncelli.
Image denoising using scale mixtures of Gaussians in the wavelet domain.
IEEE Trans. Image Proc., 12(11):1338–1351, November 2003.

G.F.C. Rogers and Y.R. Mayhew.
Engineering thermodynamics: work and heat transfer.
Addison Wesley Longman, Harlow, Essex, U.K., 4^{th} edition, 1992.
ISBN 0582045665.

Y. Sakai, T. Watanabe, S. Kamohara, T. Kushida, and I. Nakamura.
Int. J. Heat Fl. Flow, 22:227–236, 2001.

A.L. Sánchez.
Nonpremixed spontaneous ignition in the laminar wake of a splitter plate.
Phys. Fluids, 9(7):2032–2044, 1997.

A.L. Sánchez, I. Iglesias, and A. Liñán.
An asymptotic analysis of chain-branching ignition in the laminar splitter plate separating streams of hydrogen and oxygen.
Combust. Theory Modelling, 2:259–271, 1998.

A.L. Sánchez, A. Liñán, and F.A. Williams.
J. Eng. Math., 31:119, 1997.

A.L. Sánchez, A. Liñán, and F.A. Williams.
Chain-branching explosions in mixing layers.
SIAM J. Appl. Math., 59(4):1335–1355, 1999.

A. Sbaibi, P. Paranthoen, and Lecordier J.C.
Frequency response of fine wires under simultaneous radiative–convective heat transfer.
J. Phys. E: Sci. Instrum., 22:14–18, 1989.

J.M. Seitzman, M.F. Miller, T.C. Island, and R.K. Hanson.
Double-pulse imaging using simultaneous OH/acetone PLIF for studying the evolution of high-speed, reacting mixing layers.
Proc. Combust. Inst., 25:1743–1750, 1994.

H.J. Sheen, W.J. Chen, and J.S. Wu.
J. Fluid Mech., 350:177–188, 1997.

J.M. Simmie.
Detailed chemical knetic models for the combustion of hydrocarbon fuels.
Prog. Energy Combust. Sci., 29:599–634, 2003.

L.J. Spadaccini.
Autoignition characteristics of hydrocarbon fuels at elevated temperatures and pressures.
J. Eng. Power, Trans. ASME, pages 83–87, 1977.

L.J. Spadaccini and J.A. TeVelde.
Autoignition characteristics of aircraft-type fuels.
Combust. Flame, 46:283–300, 1982.

S. Sreedhara and K.N. Lakshmisha.
Direct numerical simulation of autoignition in a non-premixed, turbulent medium.
Proc. Combust. Inst., 28:25–34, 2000.

S. Sreedhara and K.N. Lakshmisha.
Autoignition in a non-premixed medium: DNS studies on the effects of 3-dimensional turbulence.
Proc. Combust. Inst., 29:2051–2059, 2002.

S.H. Stårner and R.W. Bilger.
Mixture fraction imaging in a lifted methane jet flame.
Combust. Flame, 107:307–313, 1996.

F.W. Stringer, A.E. Clarke, and J.S. Clarke.
The spontaneous ignition of hydrocarbon fuels in a flowing system.
Proc. Instn. Mech. Engrs., 184(3J):212–225, 1969.

L.K. Su.
Measurements of the three-dimensional scalar dissipation rate in gas-phase planar turbulent jets.
Ctr annual research briefs, Centre for Turbulence Research, Stanford University, Stanford, CA, U.S.A., 1998.

L.K. Su and N.T. Clemens.
The structure of fine-scale scalar mixing in gas-phase planar turbulent jets.
J. Fluid Mech., 488:1–29, 2003.

N.P. Tait and D.A. Greenhalgh.
2D laser induced fluorescence imaging of parent fuel fraction in nonpremixed combustion.
Proc. Combust. Inst., 24:1621–1628, 1992.

J.R. Taylor.
An introduction to error analysis.
University Science Books (March, 1997), Sausalito, CA, U.S.A., 2^{nd} edition, 1997.
ISBN 0935702423.

M.C. Thurber.
PhD thesis, Stanford University, Stanford, CA, U.S.A., March 1999.

M.C. Thurber, F. Grisch, B.J. Kirby, M. Votsmeier, and R.K. Hanson.
Measurements and modelling of acetone laser-induced fluorescence with implications for temperature imaging diagnostics.
Opt. Lett., 22:251–253, 1997.

M.C. Thurber, B.J. Kirby, and R.K. Hanson.
Double-pulse imaging using simultaneous OH/acetone PLIF for studying the evolution of high-speed, reacting mixing layers.
In *AIAA Paper 98-0397*, Reno, NV, U.S.A., January 1998. 36^{th} AIAA Meeting.

C. Treviño and A. Liñán.
Combust. Flame, 103:129, 1995.

C. Trevino.
Progress in Astronautics and Aeronautics, AIAA, 131:19, 1991.

M.S. Tsurikov and N.T. Clemens.
The structure of dissipative scales in axisymmetric turbulent gas-phase jets.
In *AIAA Paper 2002-0164*, Reno, NV, U.S.A., January 2002. 40^{th} AIAA Meeting.

A. Tsuzura and T. Yanagi.
In *20^{th} Symposium on Combustion of Japan*, page 266. Japanese Section of the Combustion Institute, 1982.

B. Varatharajan and F.A. Williams.
Ignition times in the theory of brached-chain and thermal explosions.
Combust. Flame, 121:551–554, 2000.

B. Varatharajan and F.A. Williams.
Chemical-kinetic descriptions of high-temperature ignition and detonation of acetylene–oxygen–diluent systems.
Combust. Flame, 125:624–645, 2001.

B.L. Wang, H. Olivier, and H. Grönig.
Ignition of shock-heated H_2–air–steam mixtures.
Combust. Flame, 133:93–106, 2003.

H. Wang.
A comprehensive kinetic model of ethylene and acetylene oxidation at high temperatures.
Progress report, University of Delaware, Newark, DE, U.S.A., 1999.

W. Wentzel.
Ignition process in diesel engines.
Technical Memorandum 979, NACA, 1936.

Z. Wu, S.H. Stårner, and R.W. Bilger.
Lift-off height of turbulent H_2/N_2 jet flames in a vitiated co-flow.
Presentation, The University of Sydney, Sydney, Australia, December 2003.

J.C. Wyngaard.
Measurement of small-scale turbulence structure with hot wires.
J. Phys. E: Sci. Instrum., 1:1105–1108, 1968.

A. Yoshida, S. Kubozuka, and S. Nakamura.

Compensation of thermocouple signals by digital FIR filters for temperature measurement in turbulent premixed flames.
Combust. Sci. and Tech., 65:317, 1989.

X.L. Zheng, J.D. Blouch, D.L. Zhu, T.G. Kreutz, and C.K. Law.
Ignition of premixed hydrogen/air by heated counterflow.
Proc. Combust. Inst., 29:1637–1643, 2002.

X.L. Zheng and C.K. Law.
Ignition of premixed hydrogen/air by heated counterflow under reduced and elevated pressures.
Combust. Flame, 136:168–179, 2004.

G. Zizak.
Flame emission spectroscopy: fundamentals and applications.
Lecture given at the ICS Training Course on Laser Diagnostics of Combustion Processes, NILES, University of Cairo, Egypt, 18–22 November 2000.

Appendix A

Thermocouple Corrections

A.1 Overview

The Biot number, $\mathcal{B}i = (\mathcal{N}u/2)(k_{gas}/k_{metal})$, where $\mathcal{N}u$ is the Nusselt number, and k_{gas}, k_{metal} are the thermal conductivities of the gas and thermocouple metal, in these experiments obeys $\mathcal{B}i < 10^{-2}$ always and $\mathcal{B}i \sim 10^{-3}$ usually, so that it is possible to say that $\mathcal{B}i \ll 1$. This allows the assumption of temperature uniformity of the thermocouple bead [Fotache et al., 1995]. In addition, there can be no catalysis on the thermocouples because they are placed in either pure air or pure fuel. It is then the case that, a balance of convection, radiation and conduction heat transfers will completely determine the measured raw thermocouple temperature:

$$\dot{Q}_{conv} = \dot{Q}_{rad} + \dot{Q}_{cond} \tag{A.1}$$

whereby the heat transferred to the thermocouple by convective processes ($\dot{Q}_{conv}$) is lost by radiative means ($\dot{Q}_{rad}$) to the surrounding solid walls and conductive means ($\dot{Q}_{cond}$) through the thermocouple wires themselves to the walls in which they are embedded. The balance refers to the wire joints at the thermocouple tips, pointed out in **Figure 2.9(b)** by T_{air}^{raw} in the case of the air thermocouple and in **Figure 2.9(c)** by T_{fuel}^{raw} in the case of the fuel one.

A simple solution to **Equation A.1** is not possible in this form. The convection term is linear in temperature, the radiation term is a fourth order in temperature and the conduction term involves a second order differential (spatial gradients of temperature). In the approach adopted here, firstly, the assumption $\frac{\dot{Q}_{cond}}{\dot{Q}_{rad}} < 1$ is made to decouple **Equation A.1** and consider the effect of the radiative heat losses only. After a correction has been made for these losses, an additional correction is

made for the losses by conduction.

A.2 Radiation

The radiative losses are dealt with first. Assuming $\frac{\dot{Q}_{cond}}{\dot{Q}_{rad}} < 1$ and thus ignoring the conduction term in **Equation A.1** at this stage leaves:

$$\begin{aligned} \dot{Q}_{conv} &= \dot{Q}_{rad} \\ \dot{Q}_{conv} &= hS_{t/c}(T_\infty - T_{raw}) \end{aligned} \tag{A.2}$$

where h is the convective heat transfer coefficient and $S_{t/c}$ is the surface area of the thermocouple, denoted thus in order to distinguish it from the cross-sectional area of the thermocouple wires, $A_{t/c}$, that is used for the heat conduction treatment in **Section A.3**.

Radiation from the hot gases (e.g. the air, fuels and nitrogen) can be safely ignored, but radiation from flames is a more complex matter [Rogers and Mayhew, 1992]. In the case of the vast majority of the autoignition experiments contributions from the relatively low luminosity autoignition events can be neglected, because of the small amounts of emitting matter and the non-luminous flame chemiluminescence involved. Only in the case of intense autoignition close to the injector were larger (of the order of 0.1 m), high luminosity flames observed (see **Chapter 4** and specifically **Figure 4.10**). Nevertheless, even in this case, the reading from both thermocouples was checked and found to be unaffected as the flames were introduced after fuel injection was initiated. Thus, both the radiation of the gases and any autoignition in the tube downstream have been neglected.

In terms of the radiative heat transfer, it is implied in **Equations A.1** and **A.2** that $\dot{Q}_{rad}$ is the *net, resultant* heat flow due to radiation from the thermocouple to the surrounding solid walls; a radiation 'loss'. It is assumed that the surface area of the air thermocouple wire is much smaller than that of the stainless steel grid and mixer wall and that the surface area of the fuel thermocouple wire is much smaller than that of the injector. Then, the surroundings are modelled as follows (see also **Figure 2.9**):

Air thermocouple Stainless steel grid and mixer walls with $S_{steel} \gg S_{t/c}$ and quartz tube walls with $S_{quartz} \gg S_{t/c}$. The thermocouple tip cannot 'see itself' and so, by conservation of energy, the radiation shape or view factor obeys $F_{t/c-steel} + F_{t/c-quartz} = 1^*$, and,

*$F_{t/c-i}$ is used in the conventional sense, i.e. fraction of radiative energy leaving surface 't/c'

Fuel thermocouple Stainless steel injector walls with $S_{injector} \gg S_{t/c}$. Again, the thermocouple tip cannot 'see itself' and so, $F_{t/c-injector} = 1$.

The radiative heat exchange network involving the air thermocouple, the grid, mixer and quartz tube in terms of heat flows is given by:

$$\begin{aligned} \dot{Q}_{rad} &= \epsilon_{t/c} S_{t/c} \sigma \Big[(T_{air}^{raw})^4 \\ &\quad - F_{t/c-steel}(T_{steel})^4 - F_{t/c-quartz}(T_{quartz})^4 \Big] \\ \Rightarrow \dot{Q}_{rad} &= \epsilon_{t/c} S_{t/c} \sigma \Big[(T_{air}^{raw})^4 \\ &\quad - F_{t/c-steel}(T_{steel})^4 - (1 - F_{t/c-steel})(T_{quartz})^4 \Big] \end{aligned} \tag{A.3}$$

where σ is the Stefan–Boltzmann constant and is equal to $5.669\text{x}10^{-8}$ W.m^{-2}.K^{-4}, $F_{t/c-i}$ are radiation shape factors (see footnote on previous page) and $\epsilon_{t/c}$ the grey body emissivity of the thermocouple metal.

Similarly, for the fuel thermocouple:

$$\begin{aligned} \dot{Q}_{rad} &= \epsilon_{t/c} S_{t/c} \sigma \Big[(T_{fuel}^{raw})^4 - F_{t/c-injector}(T_{injector})^4 \Big] \\ \Rightarrow \dot{Q}_{rad} &= \epsilon_{t/c} S_{t/c} \sigma \Big[(T_{fuel}^{raw})^4 - (T_{injector})^4 \Big] \end{aligned} \tag{A.4}$$

Effectively, the the grid, mixer, tube and injector act as black bodies, not because $\epsilon \to 1$, but because $\frac{S_{t/c}}{S} \to 0$. Substitution of $\dot{Q}_{rad}$ into **Equation A.2**, gives the final form of the radiation correction expressions:

$$\begin{aligned} T_{air}^{rad} &= T_{air}^{raw} + \frac{\epsilon_{t/c}\sigma}{h} \Big[(T_{air}^{raw})^4 \\ &\quad - F_{t/c-steel}(T_{steel})^4 - (1 - F_{t/c-steel})(T_{quartz})^4 \Big] \end{aligned} \tag{A.5}$$

$$\begin{aligned} T_{fuel}^{rad} &= T_{fuel}^{raw} + \frac{\epsilon_{t/c}\sigma}{h} \Big[(T_{fuel}^{raw})^4 \\ &\quad - (T_{injector})^4 \Big] \end{aligned} \tag{A.6}$$

Here, T_{rad} is not yet T_{corr} because the effect of heat conduction has not been considered.

---

and reaching surface 'i'.

A.3 Conduction

Returning to **Equation A.1**, the conduction term is given by:

$$\dot{Q}_{cond} = -k_{metal} A_{t/c} \frac{dT(l)}{dl} \tag{A.7}$$

where k_{metal} is the thermal conductivity of the thermocouple metal and l a (variable) dimension along the thermocouple length. Neglecting $\dot{Q}_{rad}$ and with the boundary conditions $T(l \rightarrow \infty) \equiv T_{\infty} \equiv T_{corr}$ and $T(l = 0) \equiv T_{wall}$, the one-dimensional steady-state solution to the ordinary differential equation is:

$$\frac{T_{corr} - T_{wall}}{T_{corr} - T_{raw}} = \cosh(mL_{t/c}) + \left(\frac{h}{mk_{metal}}\right) \sinh(mL_{t/c}) \tag{A.8}$$

$$m = 2\sqrt{\frac{h}{k_{metal} d_{t/c}}}$$

where $L_{t/c}$ and $d_{t/c}$ are the immersed length and conductive diameter of the thermocouple wire. Re-arranging to separate out the correction term:

$$T_{corr} = T_{raw} + \frac{T_{raw} - T_{wall}}{[\cosh(mL_{t/c}) + (\frac{h}{mk_{metal}}) \sinh(mL_{t/c})] - 1} \tag{A.9}$$

The factors $(mL_{t/c})$ and $(\frac{h}{mk_{metal}})$ reduce to:

$$mL_{t/c} = 2f_{t/c}\sqrt{\frac{L_{t/c}}{d_{t/c}}} \tag{A.10}$$

$$\frac{h}{mk_{metal}} = \frac{1}{4} mL_{t/c} \times \left(\frac{L_{t/c}}{d_{t/c}}\right)^{-1} = \frac{1}{2} f_{t/c} \frac{1}{\sqrt{\frac{L_{t/c}}{d_{t/c}}}} \tag{A.11}$$

$$f_{t/c} = \sqrt{L_{t/c}}\sqrt{\frac{h}{k_{metal}}} \tag{A.12}$$

The 0.25 mm R-Type air thermocouple has $\sqrt{L_{t/c}} = 0.1$ and $\frac{L_{t/c}}{d_{t/c}} = 36$. A conservative 'effective' immersed length, $L_{t/c}$, of about 0.05 m for the 0.25 mm K-Type fuel thermocouple gives $\sqrt{L_{t/c}} \cong 0.2$ and $\frac{L_{t/c}}{d_{t/c}} \cong 200$. For both thermocouples

$\sqrt{h/k_{metal}} > 3.7$ for all velocity and temperature conditions used in this thesis. Thus, $f_{t/c} > 0.37$ for the air, and $f_{t/c} > 0.74$ for the fuel thermocouple. Note that from **Section 2.2.4**, $h = (k_{metal}/d_{t/c})\mathcal{N}u(\mathcal{R}e, \mathcal{P}r)$, so that the factors $\sqrt{h/k_{metal}}$ and consequently $f_{t/c}$ are strongly determined by the flow $\mathcal{R}e$. Hence, unlike the radiation case, the normalized conduction correction itself is strongly influenced by both the magnitude of the velocities flowing over the thermocouples and the temperature of those flows.

Figure A.1 examines $g_{cond} = \{[\cosh(mL_{t/c}) + (\frac{h}{mk_{metal}})\sinh(mL_{t/c})] - 1\}^{-1}$, the inverse of the denominator in **Equation A.9**, as a function of $f_{t/c}$ and $\frac{L_{t/c}}{d_{t/c}}$. In order to gain insight into the magnitude of the conduction correction term, one also needs an idea of the wall temperature T_{wall} and a postulate is put forward with respect to this, that: $\frac{T_{wall}}{T_\infty} \approx c$, with c a constant of proportionality. Physical justification may be drawn from thinking about the self-similarity of the thermal boundary layer on the wall. Substituting into **Equation A.9** (with $T_{corr} \equiv T_\infty$ by definition) and re-arranging for the normalized conduction correction:

$$\begin{aligned} \frac{\Delta T_{cond}}{T_{corr}} &= \frac{T_{corr} - T_{raw}}{T_{corr}} = \frac{1-c}{1+g_{cond}^{-1}} \\ g_{cond} &= \{[\cosh(mL_{t/c}) + (\frac{h}{mk_{metal}})\sinh(mL_{t/c})] - 1\}^{-1} \end{aligned} \tag{A.13}$$

The correction term of **Equation A.13** represents the normalized (relative) error introduced into the raw thermocouple measurement due to conduction losses.

For the fuel thermocouple, with $g_{cond}^{-1} \gg 10^4$ from **Figure A.1**, it is possible to conclude that the error in not treating the losses due to conduction is infinitesimal. However, for the air thermocouple g_{cond} has a value of approximately 0.025 at flow conditions which require the greatest correction. Also, the temperature boundary layer near the mixer wall has been measured and it was found that $c \approx T_{mixer}/T_\infty = 0.80 \pm 0.03$, so that **Equation A.13** gives a correction of $(0.20 \pm 0.03)/(1 + g_{cond}^{-1})$. Hence, the greatest correction due to conduction, ΔT_{cond}, amounts to about 0.5% of T_{corr}. This correction was not ignored in this work. Re-writing the final form of the correction equation (**Equation A.9**) in the case of the air thermocouple, with $T_{wall} \equiv T_{mixer}$:

$$T_{air}^{corr} = T_{air}^{raw} + \frac{T_{air}^{raw} - T_{mixer}}{[\cosh(mL_{t/c}) + (\frac{h}{mk_{metal}})\sinh(mL_{t/c})] - 1} \tag{A.14}$$

Equation A.14 was solved to provide the best possible prediction of T_{corr}.

A.4 Appendix A Figures

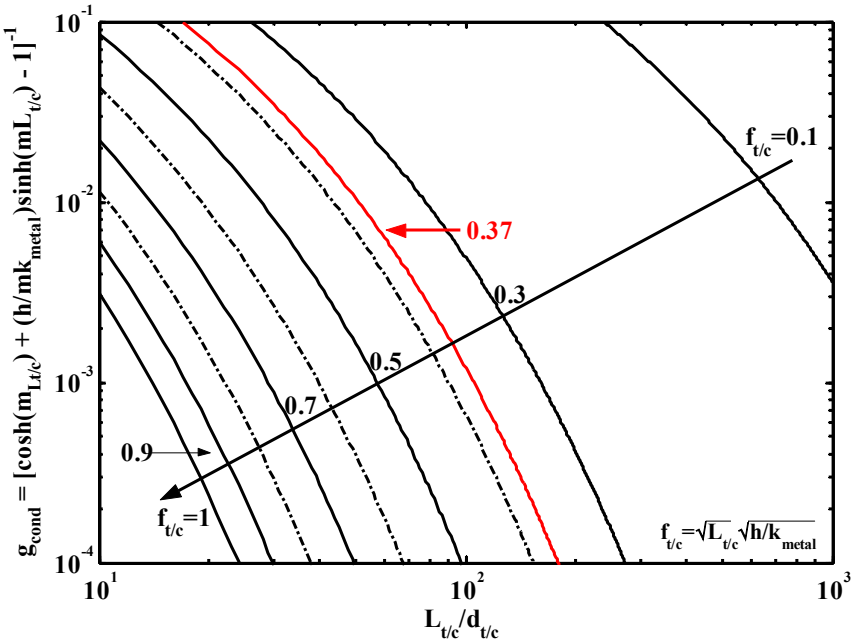

Figure A.1: Errors in raw thermocouple temperature due to conduction heat losses along the thermocouple wire.

Appendix B

Fine Thermocouple Compensation

B.1 Overview

Heitor et al. [1985], Katsuki et al. [1987], Mastorakos [1993], Sbaibi et al. [1989] model the effect of the thermal inertia of the thermocouple wire as acting on the measured temperature in the form of a first-order filter of the form:

$$\begin{aligned} T_{air} &= T_{wire} + \tau_{wire}\frac{dT_{wire}}{dt} \\ \Leftrightarrow \mathbb{F}[T_{air}] &= (1 + i \cdot \omega\tau_{wire})\mathbb{F}[T_{wire}] \end{aligned} \tag{B.1}$$

Here, T_{air} is the 'true' temperature of the air being measured, T_{wire} the lagging temperature of the thermocouple wire and τ_{wire} the thermocouple time constant. The symbol $\mathbb{F}[\ldots]$ denotes the Fourier transform. As mentioned in Mastorakos [1993], the two forms of **Equation B.1** are entirely equivalent and, in theory, the time domain and frequency domain compensation techniques based on these forms should yield similar results. In actual fact, the time domain technique has to deal with issues concerning the numerical differentiation of the time varying wire temperature, whereas the frequency domain technique must address issues relating to the correct estimation and convergence of the resulting power spectra. A brief overview of relevant literature for both techniques is given in Caldeira-Pires and Heitor [1998]. In addition, the choice of sampling frequency is important, as on the one hand good time resolution is required, and on the other high sampling rates allow more noise into the signal [Bradley et al., 1989, Yoshida et al., 1989]. This is especially true for the time domain approach that directly involves differentiating a noisy signal. In order to circumvent this problem, the signal frequency content can be first inspected in the Fourier space before re-sampling at an appropriate frequency.

Because it was felt that the noise could be rigorously filtered out in the frequency domain and that this could be done in the absence of such strict requirements on the sampling frequency (apart from the Nyquist–Shannon criterion), the frequency approach was adopted. The fastest temperature timescale was assumed to be (at most) of the order of the fastest velocity timescale and so sampling was done at 100 kHz, with hardware low-pass filtering at 50 kHz. Convergence of the spectra (see **Equation 2.18**) was ensured by measuring for long times (up to 100 s) and averaging a large number of spectra (up to 1000). In a few cases both methods were used with the same time constant to inspect any differences introduced into the results by the method alone. The time domain method was used with a three-point central difference, as in Mastorakos [1993]. The discrepancy was found to be <10%.

First-order phase-lead software compensation was employed in the Fourier space with a 'compensation time constant', τ_{comp}, not necessarily equal to τ_{wire} as pointed out by Katsuki et al. [1987]:

$$\mathbb{F}[T_{comp}] \;=\; (1 + i \cdot \omega\tau_{comp})\mathbb{F}[T_{wire}] \tag{B.2}$$

It is evident from the right-hand-side of **Equation B.2**, that compensation preferentially amplifies the higher frequencies and therefore will also strongly amplify any noise present in the signal. For this reason, the power spectra of the measured signal prior to compensation, $\mathbb{F}[T_{wire}]$, were examined for a cut-off frequency where the signal became indistinguishable from the noise. The signal was numerically low-pass filtered at this frequency before proceeding.

From **Equation B.1** and **B.2**, the compensated and 'true' air temperatures, T_{comp} and T_{air}, are related by:

$$\mathbb{F}[T_{comp}] \;=\; \frac{(1 + i \cdot \omega\tau_{comp})}{(1 + i \cdot \omega\tau_{wire})}\mathbb{F}[T_{air}] \tag{B.3}$$

and the aim is to set $\tau_{comp} \cong \tau_{wire}$.

B.2 Approach

A practical problem faced for the compensation process arises from the dependence of τ_{wire} on the instantaneous wire film temperature $T_{film} = \frac{T_{wire}+T_{air}}{2}$ and local velocity U_{air} [Tsuzura and Yanagi, 1982]. At the relatively low temperatures involved (i.e. 900 – 1000 K) the radiation losses are small enough to approximate $T_{air} \cong T_{wire}$ to within less than 0.1 – 0.2%. Furthermore, in the work described in this thesis

the measurements were made in steady flowing, pre-heated air and not in turbulent flames as in the literature. As a result, the view of Mastorakos [1993] is taken, that the calculation of a constant τ_{wire} based on the mean air properties around the thermocouple will be both adequate and more accurate than the measurements in the references. It is then straightforward to attempt a best estimate for τ_{wire} and this is dealt with next.

Considering the full energy balance for the temperature of a long wire in radiative and convective heat transfer Sbaibi et al. [1989] represented the overall time constant of the wire as having contributions from both the radiative and convective transfer modes:

$$\begin{aligned}
\tau_{wire} &= \frac{1}{\frac{1}{\tau_{rad}}+\frac{1}{\tau_{conv}}} \\
\tau_{rad} &= \tau_o \frac{1}{4\epsilon\sigma T_{wire}^3} \\
\tau_{conv} &= \tau_o \frac{d_{wire}}{k_{air}\mathcal{N}u} \\
\tau_o &= \frac{(d\rho c_p)|_{wire}}{4} \\
\Rightarrow \tau_{wire} &= \tau_o \left(\frac{d_{wire}}{k_{air}\mathcal{N}u}\right)\left[1+\frac{4\epsilon\sigma T_{wire}^3 d_{wire}}{k_{air}\mathcal{N}u}\right]^{-1} \\
&= \tau_{conv}\underbrace{\left[1+\frac{4\epsilon\sigma T_{wire}^3 d_{wire}}{k_{air}\mathcal{N}u}\right]^{-1}}_{\mathcal{S}_{rad} \equiv \text{ deviation from } \tau_{conv}}
\end{aligned} \tag{B.4}$$

where the subscript '*wire*' denotes wire properties so that d, $\rho = 8825$ kg.m^{-3} and $c_p = 485.7$ J.kg^{-1}.K^{-1} are the diameter, density and specific heat capacity of the wire. Also, ϵ is the emissivity of the wire metal, σ the Stefan-Boltzmann constant, k_{air} the thermal conductivity of the air and $\mathcal{N}u$ can be expressed in many ways.

Both Heitor et al. [1985], Mastorakos [1993] neglected the term $\mathcal{S}_{rad}$. By effectively setting $\mathcal{S}_{rad}$ to unity, they compared the estimation for the time constant τ_{conv} with that measured by monitoring the temperature decay after applying a heating pulse to the thermocouple and found good agreement. No measurements of time constants were made in this work. Caldeira-Pires and Heitor [1998], Ferrão and Heitor [1998] have carefully quantified this agreement for a similar set-up and compensation method, reporting a $\pm 10\%$ uncertainty in the value of τ_{wire}. With this error in the time constant, they specify a subsequent $\pm 20\%$ uncertainty in the variance of the temperature fluctuations after compensation. The final error in T'_{air} was then equal to the error in τ_{wire}, i.e. $\pm 10\%$. In the references mentioned in this

paragraph, a simple empirical relation from Collis and Williams [1959] was employed for the forced-convective heat transfer from the wire:

$$\mathcal{N}u \;=\; 0.24 + 0.56\mathcal{R}e_{wire}^{0.45} \tag{B.5}$$

valid in the range $0.02 < \mathcal{R}e_{wire} < 44$, with $\mathcal{R}e_{wire}$ the Reynolds number based on U_{air}, d_{wire} and the air kinematic viscosity ν_{air}.

The procedure of theoretically estimating τ_{conv} in this thesis was taken directly from Heitor et al. [1985], Mastorakos [1993], with the heat transfer correlation of Collis and Williams [1959] (**Equation B.5**). The methods differ, in that here an estimate for τ_{wire} was attempted by considering the full form of **Equation B.4**; including $\mathcal{S}_{rad}$. Depending on the conditions, the values of τ_{wire} so calculated were estimated as being in the range 35 – 50 ms, decreasing with increasing velocity and temperature.

The term $\mathcal{S}_{rad}$ is plotted in **Figure B.1** as a function of $T_{wire} \cong T_{air}$ for various ϵ in the range 0.47 ± 0.29. As explained in the caption, the mean measured temperature during the fine thermocouple temperature measurements did not exceed $T_{air} \cong 950$ K for the lowest velocities ($U_{air} = 13.5$ m/s), or, $T_{air} \cong 990$ K for the highest ($U_{air} = 26.6$ m/s). Then, the error that would have been associated with neglecting this term, which effectively would have neglected the radiative contribution to the time constant, would not have exceeded 7%. Additional contributions to the overall error in τ_{wire} arise from d_{wire}, the various air transport properties and $\mathcal{N}u$, but these are much smaller than the 60% uncertainty in ϵ. On this basis, an attempt to utilize a more precise or comprehensive (and hence more complicated) empirical correlation for $\mathcal{N}u$ than that of Collis and Williams [1959] was considered unjustified. After including the best estimate of $\epsilon = 0.47$ into the expression for $\mathcal{S}_{rad}$, the uncertainty in this variable is reduced to $\sim$2%, which is approximately the same (if not less) than that introduced by Ferrão and Heitor [1998] by neglecting this term (see **Figure B.1** caption). As a result, it is fair to expect that the final error in both: (i) τ_{wire} including that associated in the use of **Equation B.4**, and, (ii) T'_{air}, will also be close to (if not less than) the $\pm$10% error of the same reference. These conjectures are also assisted by the larger uncertainties associated with the evaluation of the local flame gas properties in Caldeira-Pires and Heitor [1998], Ferrão and Heitor [1998], Heitor et al. [1985], Mastorakos [1993] and the fact that the high-frequency energy content of the spectra is expected to be much higher in the presence of a flame.

B.3 Appendix B Figures

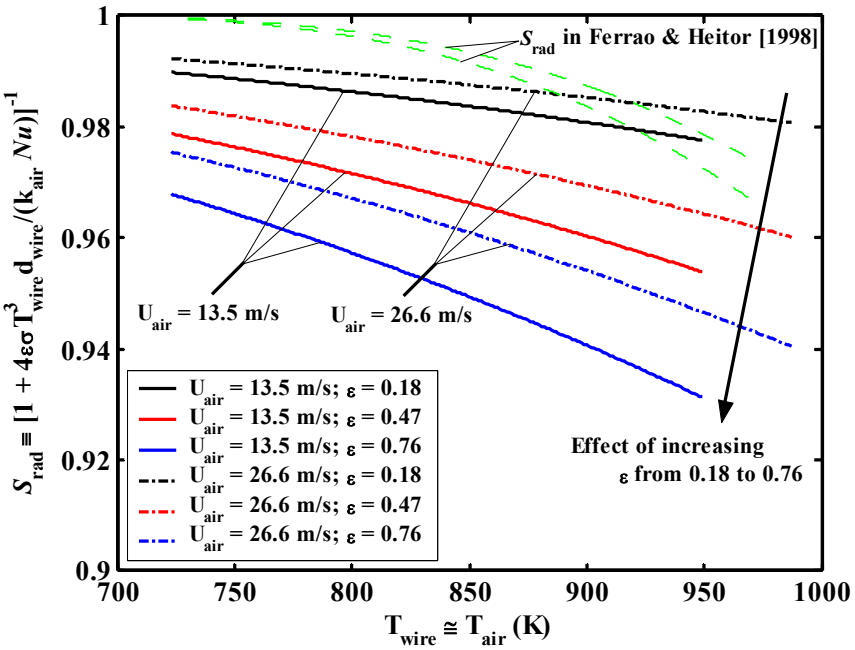

Figure B.1: Theoretical variation of the time constant deviation term ($\mathcal{S}_{rad}$) of **Equation B.4**. The mean measured temperature during the fine thermocouple temperature measurements did not exceed $T_{air} \cong 950$ K for the lowest velocities with $U_{air} = 13.5$ m/s, or, $T_{air} \cong 990$ K for the highest with $U_{air} = 26.6$ m/s. This covers all fine thermocouple data. Also included, in the region between the green lines is the range of S_{rad} calculated based on the data from Ferrão and Heitor [1998] for a 40 μm R-Type thermocouple ($\epsilon = 0.09$), U_{air} between 20 and 40 m/s and T_{air} between 300 and 1600 K. Note that the temperature scale is not correct for the data of Ferrão and Heitor [1998], because in this case the full range of T_{air} was shifted and scaled to fit into the existing x-axis range.

Appendix C

Mixture Fraction Image Processing

C.1 Median Smoothing in the Physical Domain

The first stage in the mixture fraction image processing was aimed at removing 'salt-and-pepper' [Chan et al., 2004] or shot noise, mostly caused by the image intensifier and the technique by which photons are amplified in the Micro-channel Plates, or MCPs (see **Section 2.4.2: Intensified Charge Coupled Device Camera**). Median smoothing is a non-linear operation that is generally accepted as being an efficient approach to the removal of this type of noise when edge preservation is necessary [Lim, 1990]. It was only employed inside the 'mixing window'.

C.2 Wiener Filtering in the Frequency Domain

The Wiener filter is the optimal Mean Square Error (MSE) stationary linear filter for images degraded by additive noise and blurring. Calculation of the Wiener filter requires the assumption that the signal and noise processes are second-order stationary (in the random process sense). For most realistic scenarios the linear Wiener filter will have a slight advantage over non-linear Most Likelihood (ML) algorithms. At moderate Signal-to-Noise Ratios (SNRs), such as here, Poisson does not dominate over Gaussian noise, making the Wiener filter most appropriate. This is a result of the combined effects of: (i) detector noise, which is commonly assumed to be Gaussian-distributed, and, (ii) the fact that the raw images of acetone fluorescence are relatively low contrast. The assumption of Gaussian-distributed detector noise was investigated (see **Figure C.1**) and it was found that in the absence of intensifier

noise (examined with the ICCD intensifier set to very low gains) this assumption is valid. At higher SNRs both classes of algorithm give similar results irrespective of the type of noise present. Given the simpler computational requirements of the Wiener filter it would ordinarily be preferred [Fienup et al., 2002].

This stage of image processing was used for the removal of signal content smaller than the 'mixing window'. Here, the Wiener filter was used in the frequency domain, as implemented by Matlab's `wiener2` function. Matlab function `wiener2` uses a pixel-wise adaptive Wiener method based on statistics estimated from a local neighbourhood of each pixel and assuming constant power additive (Gaussian) noise. It is an adaptive filter tailoring itself to the local image variance. Where the variance is large it performs little smoothing, while where it is small the smoothing is enhanced, thus preserving edges and other high-frequency parts. The neighbourhood over which Wiener low-pass filtering was performed was set equal to the 'mixing window'. At the end of this process the autocovariance of the noise was used as an input into the final stage described in **Section C.3**. The instantaneous image obtained after this stage of filtering had incurred little processing and is termed the 'first mixture fraction image', ξ_1.

C.3 BLS-GSM Denoising in the Wavelet Domain

Application of optimal linear filtering techniques in the wavelet domain is being proven to outperform frequency domain implementations [Portilla et al., 2003]. The final denoising stage was made with this considerations in mind. Further removal of signal content within the 'mixing window' by a custom wavelet technique, based on "Bayesian Least Squares – Gaussian Scale Mixture" (BLS-GSM) denoising algorithms [Portilla et al., 2003]. Here a brief outline of the inputs to the BLS-GSM code* used in this work is given.

A non-blind denoising approach was employed with a shift-invariant pyramid of orthogonal Haar wavelets, or Daubechies wavelets of order 1. The number of scales used for the pyramidal representation was adapted to the image size with 3 orientations for two-dimensional separable wavelets. No neighbourhood parent coefficient was employed. Boundary mirror extension was allowed for in order to avoid boundary artifacts.

The 'full steerable pyramid' wavelet transform was also tried, with 5 scales, 8 orientations and the utilization of a parent, resulting in equally good denoised image SNR and Peak Signal-to-Noise Ratio (PSNR), but at increased computational cost. As with conventional orthogonal wavelet decompositions, the steerable pyramid is implemented by recursively splitting an image into a set of oriented sub-bands, and a

*Refer also to *http://decsai.ugr.es/∼javier*.

low-pass residual band which is sub-sampled by a factor of two along the horizontal and vertical axes. Yet, unlike conventional orthogonal wavelet decompositions, the oriented bands are not sub-sampled, and the sub-sampling of the low-pass band does not produce aliasing artifacts, as the low-pass filter is designed to obey the Nyquist–Shannon sampling criterion.

For the estimation method the BLS-GSM model included the full covariance matrix without assuming uncorrelated Gaussian vectors in describing both the noise and signal. This takes into account the fact that the coefficients in the image representation are strongly correlated, both because of inherent spectral features of the image (the wavelet decomposition is performed on the image in its Fourier domain representation) and in the case of the steerable pyramid because of the redundancy induced by the over-complete representation. Both the full Bayesian least squares and two-step MAP-Wiener solutions were obtained for comparison, with the former chosen to obtain the results presented in this thesis. The neighbourhood of spatial neighbours within the same sub-band was based on the 'mixing window'. At the end of the post-processing one obtains the 'second mixture fraction image', ξ_2.

C.4 Appendix C Figures

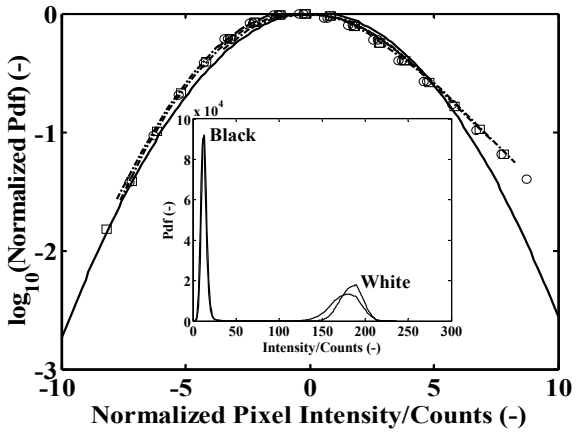

(a)

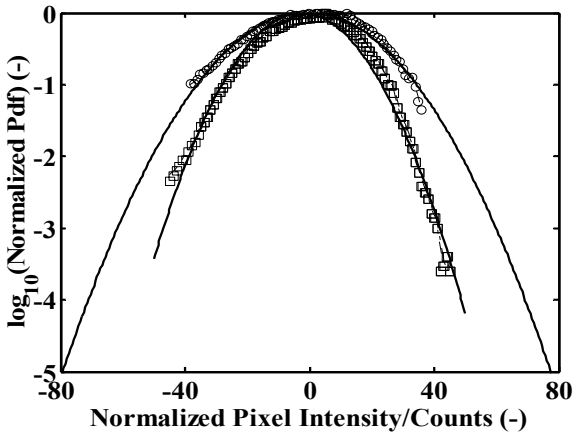

(b)

Figure C.1: Optical system detection characterization with ICCD camera at low gain. (a) Normalized 'black' and (b) 'white' signal pdfs of the complete optical system from dark and bright image respectively to saved file. In (a) the inset is of same pdfs, but not normalized and plotted linearly.